Electronic transfers in lanthanides complexes : from the electronic structure to the reactivity

Arnaud Jaoul

NNT : 2017SACLS043

Thèse de doctorat de l'Université Paris-Saclay préparée à l'Ecole Polytechnique

Ecole doctorale n°571
Molécules, Matériaux, Instrumentation et Biosystèmes
Spécialité de doctorat : Chimie

par

M. Arnaud Jaoul

Transferts d'électron dans des complexes de lanthanide: une étude combinée de chimie expérimentale et théorique

Thèse présentée et soutenue à l'Ecole Polytechnique, le 19 Septembre 2017.

Composition du Jury :

M.	Philippe Maître	Directeur de recherche au CNRS Université Paris Sud	(Président du Jury)
M.	Nicolas Mézailles	Directeur de recherche au CNRS Université Paul Sabatier	(Rapporteur)
M.	Marc Walter	Professeur assistant Technische Universität Braunschweig	(Rapporteur)
Mme	Hélène Gérard	Professeur des Universités Université Pierre et Marie Curie	(Examinatrice)
M.	Grégory Nocton	Chargé de recherche au CNRS Ecole Polytechnique	(Directeur de thèse)
Mme.	Carine Clavaguéra	Chargée de recherche au CNRS Université Paris Sud	(Directrice de thèse)

Electron Transfer induced by Lanthanide complexes: a combined experimental and theoretical study

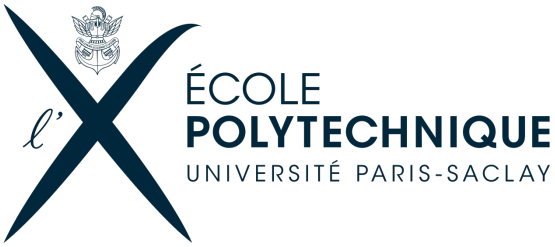

Arnaud Jaoul

Chemistry

Ecole Polytechnique, Université Paris-Saclay

A thesis submitted for the degree of

Doctor of Philosophy

September 2017

À Aurélie,
Un rayon de vie
Passé trop vite de l'autre côté...

Acknowledgements

Remettons les choses à leur place: une thèse est autant le travail de l'étudiant que de l'ensemble des personnes avec qui il a pu échanger et qui ont pu lui offrir leur savoir (scientifique ou non). Ces personnes là sont en partie responsable de ces travaux et je veux ici profiter d'un moment pour les remercier. Bien sur, la tâche sera difficile, puisqu'il m'a été donné l'occasion de cotoyer de nombreuses personnes tout au long de mon séjour sur le campus de l'Ecole ainsi que dans les couloirs du Latimer Hall à Berkeley. Le campus est grand, mais c'est, en quelque sorte, au détour d'un couloir dans un projet *a priori* sans importance, que j'ai eu la chance de rencontrer Greg et Carine. Un duo de chercheur étonnant mêlant chimie expérimentale et théorique.

C'est Greg qui tout d'abord m'a mis sur le chemin de la chimie des éléments f, en me conseillant d'aller voir du côté de Brighton si l'herbe y était plus verte. Je veux te remercier Greg d'avoir su m'accompagner et de m'avoir fait partager ton expérience et ton savoir faire de la chimie des éléments f. C'est par ton dévouement et ton amour de la chimie que j'ai pu évoluer librement tout au long de ma thèse.

C'est ensuite Carine qui m'a emmené doucement vers le côté obscur en me donnant goût à chercher des réponses à toutes mes questions (même (souvent) les plus absurdes). Je n'ai jamais vu une directrice de thèse si dévouée et à l'écoute, toujours à répondre à ces emails, même (souvent) après 22h. Merci de ton écoute et de ta disponibilité au cours de ces trois ans, nos discussions vont me manquer.

Par leur aide, ainsi que grâce à l'amabilité de Martin Head Gordon, j'ai pu obtenir une bourse Fulbright et m'envoler vers le nouveau continent. Je remercie chaleureusement le groupe de Martin et notamment Hudi, Eloy, Daniel, Jérôme et Matthias pour m'avoir donné des coups de mains techniques quand j'en avais besoin. Merci également à Dick pour nos échanges parfois longs sur la chimie et sur la culture américaine.

Leur aide a également été précieuse dans la complexe tâche de sélection d'un jury de thèse ("quid du nombre de cadre A par rapport aux cadres B et d'extérieurs par rapport aux intérieurs"). Merci à N. Mézailles, M. Walter, H. Gérard, et P. Maître pour avoir pris le temps de juger le travail qui a été effectué au cours de ces trois ans.

Ce travail est également le fruit de discussions et d'échanges au sein du Laboratoire de Chimie Moléculaire et je remercie bien sûr l'ensemble de ces membres permanents ou non d'avoir pris part à ma formation tant sur le point de vue humain que sur le point de vue intellectuel. Duncan, nos conversations anglaises vont me manquer, je savais toujours qui aller voir lorsque j'avais besoin d'entendre chanter cet accent britannique. Bibi, merci pour ton franc parler et tes questions existentielles, cela met toujours de la bonne humeur dans nos repas quotidiens. Elodie, merci de ta gentillesse et de la dévotion que tu voues à aider tout le monde. Merci à Marie pour avoir été là (presque) depuis le départ, et de m'avoir fait une place dans la salle RX pour faire moi même (de temps en temps) mes structures, ou pour avoir été à l'écoute de mes sautes d'humeur (peu) fréquentes. Merci également

à Thérèse, Anne-Flo, Cindy, Corinne, Audrey, Gilles F., Gilles O., Sophie, Stéphane, Christophe, Adrien, Edith ("On ne court pas dans les couloirs"), Ségolène, Svetlana, Sofia, et Cédric pour nos discussions passionnés.

Je crois que le travail auquel j'ai eu la chance de participer pendant trois ans n'aurait pas pu être accompli sans l'aide et la formation que m'a apporté Louis Ricard. Nos conversations de geek sur la compilation de tel utilitaire en utilisant telle version de gcc et telle version de openmpi ("mais fais attention, elle n'est pas bien compilé sur phymath, je vais la recompiler pour toi") ou sur le changement de RAM du cluster (parce que bon les erreurs de mémoire ça va un moment) ainsi que nos discussions endiablées sur mes réactions vont me manquer.

Merci bien évidemment à toute la Greg's team. Merci à Thibault (même si techniquement tu n'en fais pas partie) pour m'avoir montré les ficelles de la chimie des éléments f, et pour nos sorties au Lacanal (même si je n'étais pas souvent là). Merci à Augustin avec qui il fait toujours bon discuter chimie que ce soit à Paris ou à SF (et pour m'avoir fait découvrir Jupiter's pizza). Merci à Mathieu pour nos discussions scientifiques et aussi (souvent) très polytechnicienne ("je veux pas vieux chouffiser mais bon les Prex c'est quand même des tos"). Merci à Violaine pour sa joie de vivre (vous avez compris vous pourquoi elle rigole tout le temps?) et pour sa détermination. Merci également aux stagiaires Alex, François, Varunesh, Enzo, Marie, et Punam.

Il va bien sûr de soi, qu'un travail de thèse ne peut s'effectuer sans lier des liens d'amitié avec les autres doctorants du laboratoire. Aike, merci d'avoir su mettre de l'ambiance à nos remplissage d'hélium ("et mince il y a un bouchon de glace", "comment ça il n'y a pas d'hélium dans le dewar"). Alice, merci pour ta bonne humeur et ton esprit d'équipe qui nous ont permis d'explorer Milan pratiquement intact. Yingxiao, même si tu étais tête en l'air ("Attention Yingxiao est resté à l'arrêt de tram") merci pour l'attention que tu as pu porter aux choses. Deniz, merci d'avoir toujours eu à cœur d'écouter les déboires des autres sans trop te plaindre. Yann, merci pour ton humour toujours coloré et pour ton optimisme sans faille, tu as su, par ta présence, faire sortir du noir le labo1. Louis M., merci pour m'avoir fait rêvé à de nouvelles startup et pour ta bonne humeur, je t'attend pour monter Bro'Do. Mathias, merci d'avoir partagé mon bureau pour une journée, et d'avoir été l'un des meilleurs attaquant de notre équipe de foot. Merci, finalement, à ma petite Irene pour m'avoir accompagné lors de ce long périple, et avoir su par sa présence et son sourire me redonner espoir dans les moments où il me manquait. Merci également à Brendan, Lucille, Geoffroy, Chris, Vincent, Matthias M. (et toute l'équipe @phdmooc) et bien d'autres pour avoir partagé ma vie de thésard.

Je voudrais également remercier mes parents, Véro, Mathieu, Julien et Mylène pour avoir fait le déplacement jusqu'à Paris pour m'écouter parler un langage qu'ils ne parlaient pas. Leur présence en ces quelques semaines mouvementées de ce début de mois de septembre montre leur attachement sans faille à notre grande famille Jaoul-Vianey-Casadella.

Enfin, je voudrais remercier Sophie pour avoir su être à mes côtés tout au long de cette épopée. Elle n'a eu de cesse de corriger mes discours et mes doutes, et a toujours été une source d'inspiration. Merci de me faire rêver.

Contents

List of Abbreviations

bph . . . . . Benzophenone

bipy . . . . . Bipyridine

bpm . . . . . Bipyrimidine

CASPT2 . . . . Complete Active Space Perturbation Theory

CASSCF . . . . Complete Active Space Self Consistent Field

Cp* . . . . . Pentamethyl-cyclopentadienyl

Cp^{ttt} . . . . . Tris-tertbutyl-cyclopentadienyl

DFT . . . . . Density Functional Theory

DKH . . . . . Douglass Kroll Hess

DME . . . . . Dimethoxyethane

dppz . . . . . Dipyrido[3,2-a:2',3'-c]phenazine

EPR . . . . . Electron Paramagnetic Resonance

HF . . . . . Hartree-Fock

HOMO . . . . . Highest Occupied Molecular Orbital

Ind . . . . . 2-(2-pyrimidil)benzimidazolate

LUMO . . . . . Lowest Occupied Molecular Orbital

NMR . . . . . Nuclear Magnetic Resonance

Ortep . . . . . Oak-Ridge Thermal Ellipsoid Plot

phen . . . . . Phenanthroline

SOMO . . . . . Single Occupied Molecular Orbital

taphen . . . . . Tetra-azaphenanthrene

tempo . . . . . (2,2,6,6-Tetramethylpiperidin-1-yl)oxyl

THF . . . . . Tetrahydrofurane

TMS . . . . . Trimethylsillyl

ZORA . . . . . Zeroth Order Regular Approximation

There's nothing insightful in saying that work's more fun and satisfying when you're surrounded by good and supportive people. But, though I obviously can't render an unbiased judgment, I believe it's especially important in academia and scientific research. By its very nature, science is both a collaborative and intimate vocation. It's one that relies on flashes of creative insight and that for most is more than just a job, it's a passion and an identity. And yet, it's one whose central currency is peer critique. Add those up, and the right social environment – one that pushes, supports, inspires, stabilizes and forgives – is more likely to both forge scientific breakthroughs and keep people in the game to do it again.

— Prof. Alan Townsend *Blog post*

Introduction

In recent years, the transition from industrial-only to ecology-friendly governments has accentuated the importance of scientific research. Two fields have been impacted significantly by this "green" evolution: the energy and the chemistry sectors[1]. While oil and gas companies are still relying on their exploitations, they increased their development in sustainable energy productions. For instance, Total has been spending high amounts of money in solar energy, and has just recently acquired Saft a battery manufacturer. In chemistry, green catalytic processes have been developed by creating new processes[2] more respectful of the environment, and by recycling polluting molecules such as carbon dioxyde.

In order to envision these innovations, biological systems have been taken as an inspiration[3]. For millennials, these systems have been able to gather energy, or to recycle polluting molecules[4]. Photosynthesis creates energy by absorption of light. This process has been relying on the quantum mechanics electronic structure of certain molecules that can absorb light and promote electron transfer towards biological molecules of interest[5]. Better understanding of this concept for biological system passed through the use of both experimental and theoretical analyses of the molecules at stake. The knowledge acquired has led to improvements in the development of solar cells or to recycle polluting molecules. The rise of new catalyst capable of selectively promote an electron transfer to small molecules has led to greener catalysis that are capable of reproducing, in a way, biological systems[6].

For biological systems, electron transfers are of central importance. They maintain the cohesion of the systems and make them perform efficiently[7]. Understanding the processes of electron transfer for biological molecules is difficult as they require to study the synergy

between hundreds of molecules. Smaller systems are used as case studies to get knowledge on the behaviour of electron transfers in solution[8]. Exploiting electron transfer in order to promote certain type of reactivity has been the fundamental concept on which chemistry has been developed. However, the understanding of these processes is challenging as it involves several intermediate species that are often delicate to isolate.

In both fields, the systematic use of experimental and theoretical evidences in order to understand key systems has been extremely successful in increasing the understanding of electron transfer processes. In this field, divalent lanthanide molecules are getting a lot of attention as they can reduce selectively molecules and stabilise key intermediates. Lanthanide ions have been mostly studied for their magnetic and luminescence properties in their trivalent oxydation states, and used for a small number of examples in organic reactions in their divalent states, where an electron transfer is exploited[9]. Despite recent efforts, their behaviour towards molecule reduction and further reactivity is still difficult to analyse.

For these molecules, the ambiguity between two electronic structures for the lanthanide ion $4f^n5d^0$ or $4f^{n-1}5d^1$ is of importance for getting information into the bonding interaction with the different molecules involved, and into the process of electron transfer itself. Improving the methodology currently used to study these molecules could have significant impact in both lanthanide chemistry and electron transfer reactivity.

The recent improvement in quantum chemistry software made possible the systematic usage of all-electron relativistic calculations for lanthanide molecules. This methodology is perfectly adapted to study electron transfers with these molecules, and to get improved results compared to relativistic effective core potentials that only compute valence electrons. Moreover, benchmark studies comparing experimental and computational results is of growing need in order to exactly know what the limitations of the different computational methods are.

This manuscript will be interested into the relationship between electronic structure and chemical reactivity with lanthanide complexes. After recalling the latest developments in the lanthanide field, and detailing electronic structure examples of samarium and ytterbium complexes, the electronic structure of organic radical complexes of samarium will be investigated using both the experimental and the theoretical tools. The knowledge acquired will be used to further study the reactivity of these complexes towards organic molecules or

persistent radicals. Finally, the electron transfer will be pushed forwards with the development of new bimetallic complexes that link a transition metal and a lanthanide with a bridging radical ligand. The use of these molecules for further reactivity and the importance of the ligand design will be detailed.

Generalities about lanthanides

Lanthanide elements are the fifteen elements located after lanthanum and until lutetium ($57 \leqslant Z \leqslant 71$)[10]. These elements are present in mainly three oxidation states: 0, +II, and +III. In their 0^{th} oxidation state, their electronic configuration has been determined and varies from $4f^n5d^06s^2$ to $4f^{n-1}5d^16s^2$ depending on the position of the atom on the periodic table (Table 1).

Lanthanide	La	Ce	Pr	Nd	Pm	Sm	Eu	Gd
Configuration	$4f^05d^16s^2$	$4f^15d^16s^2$	$4f^35d^06s^2$	$4f^45d^06s^2$	$4f^55d^06s^2$	$4f^65d^06s^2$	$4f^75d^06s^2$	$4f^75d^16s^2$
$E^o(Ln^{3+}/Ln^{2+})$	-3.1	-3.2	-2.7	-2.6	-2.6	-1.6	-0.4	-3.9
Lanthanide	Tb	Dy	Ho	Er	Tm	Yb	Lu	
Configuration	$4f^95d^16s^2$	$4f^{10}5d^16s^2$	$4f^{11}5d^06s^2$	$4f^{12}5d^06s^2$	$4f^{13}5d^06s^2$	$4f^{14}5d^06s^2$	$4f^{14}5d^16s^2$	
$E^o(Ln^{3+}/Ln^{2+})$	-3.7	-2.5	-2.9	-3.1	-2.3	-1.0	/	

Table 1: Lanthanide electronic configuration[11] and calculated redox potentials[12] (V) relative to the standard oxidation potential of the normal hydrogen electrode

The electronic configuration of the atom gives indications about the stable oxidation state of the atom itself. As a result, cerium is $4f^15d^16s^2$ and has four stable oxidation states: +II, +III, and +IV, while ytterbium is $4f^{14}5d^06s^2$ and has two stable oxidation states +II and +III. Overall, the most stable oxidation state for every lanthanide is +III, which is made possible by the removal of the two 6s electrons and one 4f electron to achieve an electronic configuration of $4f^{n-1}5d^06s^0$. The 4f orbitals are very contracted, and removing more than one electron from the 4f orbitals requires a huge amount of energy[11] which explains the tendency for lanthanide to prefer being in their +III oxidation state. In their trivalent state, lanthanide have powerful luminescent properties, *e.g.* gadolinium complexes are used as contrast agents in MRI[13]. The oxidation state +II is stabilised for several atoms (Table 1 for redox potentials, and see David paper for a recent comparison of different estimations[14]).

Europium and ytterbium have in their +II oxidation state an electronic configuration $4f^7$ and $4f^{14}$ respectively, which stabilise Eu^{+II} and Yb^{+II}. Samarium has an intermediate redox potential (1.53 V) which is due in part to its almost half-filled 4f shell, which stabilise its +II oxidation state. Other lanthanides such as Nd, Dy, and Tm have also been used in their +II oxidation state, but their redox potential is high which limits their usability.

The 4f orbitals are quasi-degenerate, and contrary to Transition Metals (TM), the spin-orbit effect is more important than the crystal field splitting for the removal of this degeneracy (Figure 1)[15]. The energy difference between the electronic configuration $4f^n$ and a $4f^{n-1}5d^1$ is then of high importance, as the 5d orbitals will be impacted strongly by the crystal field splitting, enhancing the bonding interaction with the lanthanide ion, while the 4f orbitals will favour an ionic interaction. This electronic structure difference has recently been analysed by Evans *et al.*[16] but it is still difficult to know exactly the impact of either electronic structure on the bonding interaction with lanthanide complexes.

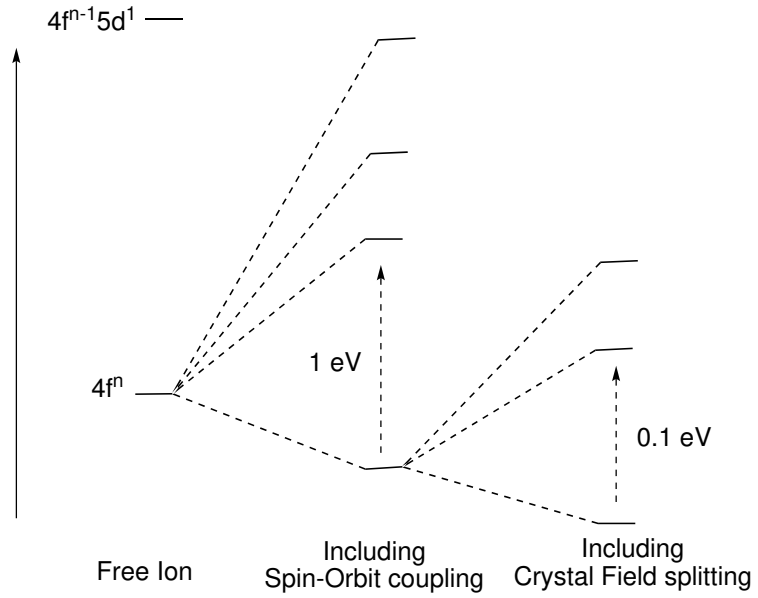

Figure 1: Effect of spin-orbit coupling and crystal field splitting for trivalent lanthanide ions, with the approximate energies for each effect between different states[15]

Synthesis of divalent organolanthanide complexes and applications

Synthesis, and type of ligand used

Divalent organolanthanides have a low redox-potential which can be used for further electron transfer reactions[17]. In this field the development by Kagan[18,19] of SmI_2 reactions has been of tremendous importance for the use of divalent lanthanide in organic synthesis. Recently, organic reactions have also been carried out with more reducing lanthanide such as dysprosium[20], neodymium[21] and thulium, but their use in this domain is still scarce[22].

The use of lanthanide in organometallic synthesis can be traced back to the first synthesis of Cp_3Ln by Wilkinson[23]. Since then, cyclopentadienyl (Cp) analogues in this type of chemistry have been vastly explored, especially by the group of Evans[24] and Andersen[25]. In the Pearson theory of Hard and Soft Acid and Base[26], lanthanides are classified as hard acid. Therefore, alkoxydes or amides which behave like hard donors are well fitted to stabilise the formation of molecular complexes of lanthanides[27]. Cp ligands, that are not considered as hard donors, stabilise importantly the lanthanide complex as they occupy a large part of its coordination sphere.

The synthesis of divalent lanthanide complexes can be achieved through several ways. The divalent LnI_2 can be made easily for samarium, ytterbium and europium. Starting from this complex, salt metathesis can transfer the ligand to the metal coordination sphere. The use of basic ligands such as hexamethyldisilazane (HMDS) can also enable the easy coordination of protonated ligands. For derivative where the divalent iodide salt is not very stable (Nd, or Dy), passing by the trivalent lanthanide complex could be easier[28]. The trivalent lanthanide molecule can then be reduced to form divalent lanthanide complexes.

The sterics of the ligand has an effect on the stabilisation of the divalent species (Figure 2 for different ligand examples). As a result, Cp analogues containing methyl[29,30], tert-butyl[31] or trimethylsilanes groups have been extensively studied, as they enable the solubilisation of the complexes, and stabilise intermediate species. In this domain, the use of phosphorous or arsenide analogues of Cp ligands has been explored by F. Nief in our lab[28,32]. Phosphorous analogues can present different coordination compared to Cp ligands, as they can bind

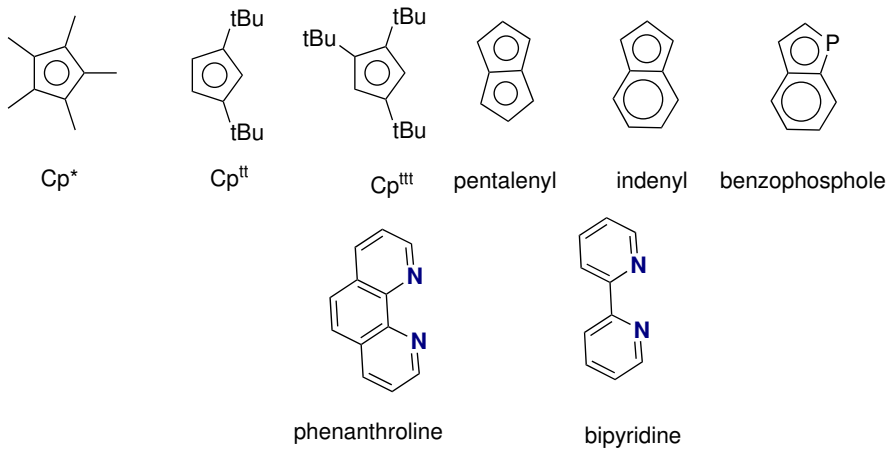

Figure 2: Different ligands used in lanthanide chemistry and two examples of heterocycle

to the lanthanide either in η^1 or η^5 coordination. The equilibrium between this two coordination modes has been recently studied by our group with imminophosphorane ligands[33]. Moreover, they can stabilise very reactive intermediates such as divalent thulium complexes[34,35]. Finally, increasing the π system of Cp can also produce interesting ligands such as indenyl[36,37] or benzophosphole[38] which were used in the 1990s and pentalene which has been used recently to synthesise bimetallic complexes[39,40].

Reduction of small molecules, and isolation of reactive +II derivatives

This process has been used recently by the group of Evans to synthesise every divalent lanthanide (except Pm) starting from a trivalent lanthanide complex, and reducing it with potassium graphite (KC_8)[16,41]. They were able to show that upon reduction the 5d orbitals were populated except in the case of Sm, Eu, Tm, and Yb where the 4f orbitals were occupied. This fluctuation could explain the stability difference observed between Sm, Eu, Tm and Yb and all the other lanthanides in the +II oxidation state.

Apart from their use in organic chemistry that will be further detailed in Chapter 2, divalent lanthanide selective reductions have been used by several groups for the activation of small molecules of interest such as carbon dioxyde (CO_2, CO, N_2). The group of Evans has led the implementation of new methodologies to reduce this kind of molecules. Early on, in the 1980s, they presented one example of N_2 reduction by Cp^*_2Sm[42] (Figure 3). Synthesising *in situ* divalent lanthanides also led to the formation of activated dinitrogen

molecules bridging two lanthanides[43], which presented for terbium complexes slow magnetic relaxation[44,45]. They also studied the reduction of carbon dioxyde by samarium complexes and were able to rationalise the reaction pathways[46] by using computational chemistry[47].

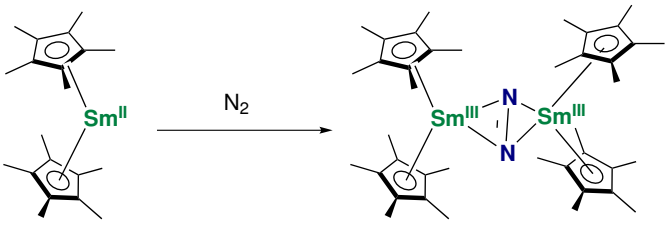

Figure 3: Activation of N_2 by samarium complexes as described by Evans *et al.*[42]

Covalency in lanthanide complexes

The use of computational chemistry has been of particular importance in understanding the covalency issues of lanthanide complexes. Since the seminal work of Wilkinson[23], lanthanide molecules have been supposed to interact only in an ionic fashion with other molecules, which is directly linked to the 4f orbitals vicinity of the nuclei. But, after the work of Fischer *et al.*[48,49], a debate fractioned the scientific community: was there a part of covalency between the lanthanide ion and its ligands?

The work on Cp_3Eu in the early 1990s by the group of Long[50] showed that the Mösbauer spectroscopy was not in agreement with neither an Eu^{+II} nor an Eu^{+III} oxidation state. This character was associated with the covalent character of the europium ion on the Cp ligands. The same kind of behaviour was also observed a few years ago for Cp_3Yb[51,52]. The authors concluded that a charge transfer from the ligand to the lanthanide was involved and that this was creating covalency between the moieties. This type of electronic structure was extended recently by the group of Andersen for $Cp^*_2Yb(bipy)$[53–56], which was analysed as neither an Yb^{+II} nor an Yb^{+III}[57,58]. The propension for ytterbium to have holes in its 4f population was analysed for different substituted bipyridine and was linked to the redox potential of the ligand[59]. The difficulty encountered by ytterbium to reduce a molecule leads to a multiconfiguration ground state for the whole molecule: a mixed configuration between $4f^{14}\pi^{*0}$ and $4f^{13\uparrow}\pi^{*\downarrow}$ (Figure 4).

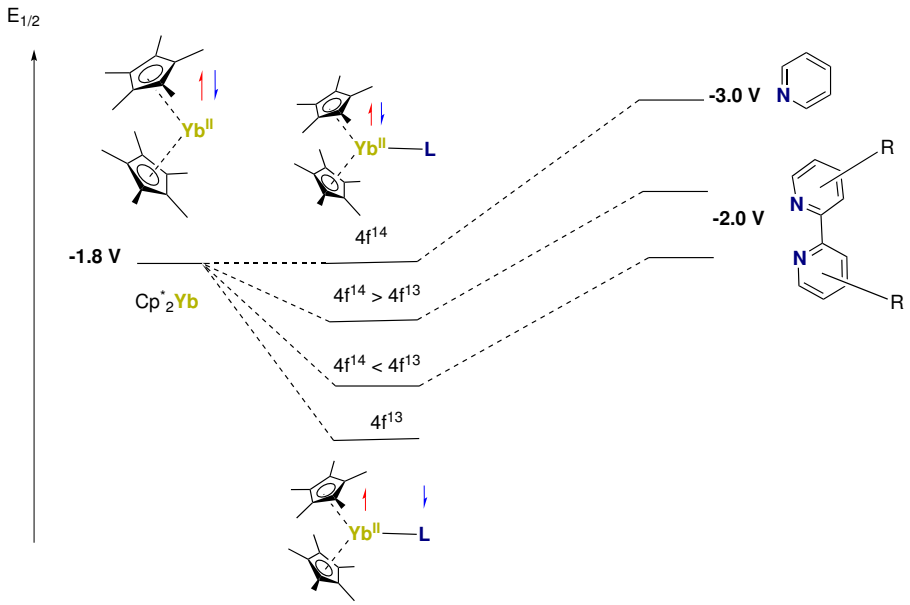

Figure 4: Scheme extracted from ref[59], the $4f^{13}$: $4f^{14}$ ratio depends on the redox potential of the ligand reduced

Objectives of the project

From this short bibliographical overview, the diversity of lanthanide radical transfer reactivity can be evaluated. However, the understanding of such transfers is limited, and getting information into the behaviour of lanthanide molecules towards electron transfer could have significant impact in the field of organic or organometallic chemistry. The project was designed around electron transfer. As a result, the journey of electrons in lanthanide reactivity will be undertaken from the reduction of organic molecule, to reactivity of such radicals with organic molecules or permanent radicals, and finally towards the transfer of electrons directly to a transition metal organometallic complex.

To deeply understand electron transfers with lanthanide molecules, the first step is to recognise the importance of relativistic effects in these compounds, and to perceive that their electronic structure can be different from what could be expected.

Then, reduction of organic molecules can be investigated (Figure 5). Phenanthroline complexes of lanthanide (samarium and ytterbium) were previously studied experimentally[60,61]. The experimental thermodynamic data will serve as a point of comparison for benchmark studies in order to find the appropriate methodology to treat complexes of lanthanide. The use of density functional theory in that matter will give the possibility to extract information from the electron density of the whole molecules, and further assess the C-C σ bond created for samarium complexes. The physical properties of phenanthroline complexes of lanthanide will be compared to quantum chemistry electronic structure of the complex, in order to understand the close behaviour of samarium, thulium and ytterbium complexes of phenanthroline. The knowledge gained from this study will be used on simple ketone reduction by SmI_2, and the equilibrium in this case between the σ dimer and the radical monomer will be studied in pyridine.

Once the electron is transferred on the ligands, it can be used to complete radical reactivity. In that sense, phenanthroline radical complexes of samarium will be reacted with a persistent radical, tempo, and with benzophenone. The reactivity will be studied both experimentally and theoretically.

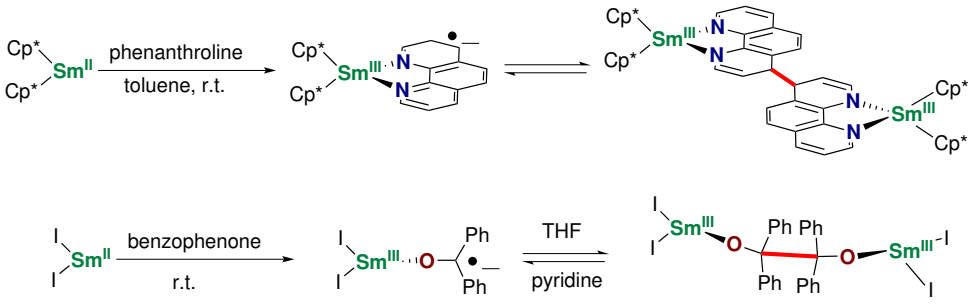

Figure 5: C-C σ bond reversible coupling

Finally, the electron was transferred to TM organometallic fragments (Figure 6). The design and characterisation of new molecules will be detailed and the reactivity of these species for stabilisation of Pd^{+IV} intermediates will be assessed. The importance of the ligand for such stabilisation will be explained and the rational design of a new ligand will be investigated using experimental knowledge as well as computational data.

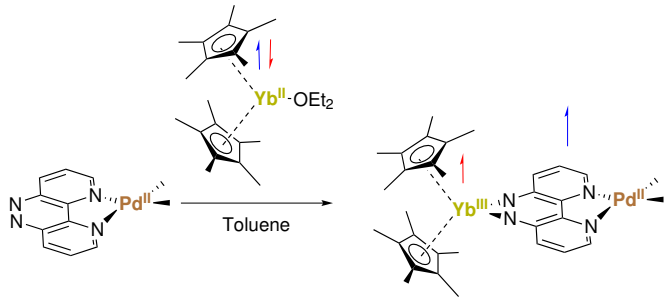

Figure 6: Synthesis of new bimetallic complexes

These different views of electron transfer are significantly similar, and bringing them together can trigger important conclusion for the radical reaction field.

References

[1] J. Spevacek, *Nat. Rev. Chem.* **2017**, *1*, 1–3.

[2] J. M. Clomburg, A. M. Crumbley, R. Gonzalez, *Science* **2017**, *355*, aag0804.

[3] Editorial, *Nat. Chem.* **2014**, *6*, 841–841.

[4] W. B. Tolman, *Activation of small molecules: organometallic and bioinorganic perspectives*, Wiley VCH, **2006**.

[5] K. Szaciłowski, W. Macyk, A. Drzewiecka-Matuszek, M. Brindell, G. Stochel, *Chem. Rev.* **2005**, *105*, 2647–2694.

[6] J. Michl, *Nat. Chem.* **2011**, *3*, 268–269.

[7] V. Balzani, *Electron Transfer In Chemistry*, Wiley & sons, **2008**.

[8] H.-B. Kraatz, N. Metzler-Nolte, *Concepts and Models in Bioinorganic Chemistry*, Wiley-VCH, **2006**.

[9] S. Cotton, *Lanthanide and Actinide Chemistry*, (Ed.: W. Sons), John Wiley & Sons, **2006**.

[10] IUPAC, *Pure and Applied Chemistry* **1988**, *60*, 431–436.

[11] P. F. Lang, B. C. Smith, *J. Chem. Edu.* **2010**, *87*, 875–881.

[12] L. J. Nugent, R. D. Baybarz, J. L. Burnett, J. L. Ryan, *J. Phys. Chem.* **1973**, *77*, 1528–1539.

[13] A. de Bettencourt-Dias, *Luminescence of Lanthanide Ions in Coordination Compounds and Nanomaterials*, John Wiley & Sons, **2014**.

[14] F. H. David, *Radiochimica Acta* **2008**, *96*, 135–144.

[15] L. Sorace, C. Benelli, D. Gatteschi, *Chem. Soc. Rev.* **2011**, *40*, 3092–3104.

[16] M. E. Fieser, M. R. MacDonald, B. T. Krull, J. E. Bates, J. W. Ziller, F. Furche, W. J. Evans, *J. Am. Chem. Soc.* **2015**, *137*, 369–382.

[17] S. Kobayashi, R. Anwander, *Lanthanides: Chemistry and Use in Organic Synthesis*, Springer Science & Business Media, **1999**.

[18] H. B. Kagan, J. L. Namy, P. Girard, *Tetrahedron* **1981**, *37*, 175–180.

[19] H. B. Kagan, *Tetrahedron* **2003**, *59*, 10351–10372.

[20] W. J. Evans, N. T. Allen, J. W. Ziller, *J. Am. Chem. Soc.* **2000**, *122*, 11749–11750.

[21] A. A. Fagin, T. V. Balashova, D. M. Kusyaev, T. I. Kulikova, T. A. Glukhova, N. P. Makarenko, Y. A. Kurskii, W. J. Evans, M. N. Bochkarev, *Polyhedron* **2006**, *25*, 1105–1110.

[22] M. Szostak, D. J. Procter, *Angew. Chem. Int. Ed. Engl.* **2012**, *51*, 9238–9256.

[23] G. Wilkinson, J. M. Birmingham, *J. Am. Chem. Soc.* **1954**, *76*, 6210–6210.

[24] W. J. Evans, *J. Alloys Compd.* **2009**, *488*, 493–510.

[25] T. D. Tilley, R. A. Andersen, B. Spencer, H. Ruben, A. Zalkin, D. H. Templeton, *Inorg. Chem.* **1980**, *19*, 2999–3003.

[26] R. G. Pearson, *J. Am. Chem. Soc.* **1963**, *85*, 3533–3539.

[27] F. T. Edelmann, *Coord. Chem. Rev.* **2016**, *318*, 29–130.

[28] F. Jaroschik, PhD thesis, Ecole polytechnique, **2007**.

[29] W. J. Evans, J. W. Grate, H. W. Choi, I. Bloom, W. E. Hunter, J. L. Atwood, *J. Am. Chem. Soc.* **1985**, *107*, 941–946.

[30] W. J. Evans, I. Bloom, W. E. Hunter, J. L. Atwood, *Organometallics* **1985**, *4*, 112–119.

[31] G. Nocton, L. Ricard, *Dalton Trans.* **2014**, *43*, 4380–4387.

[32] F. Jaroschik, F. Nief, X.-F. Le Goff, L. Ricard, *Organometallics* **2007**, *26*, 3552–3558.

[33] T. Cheisson, A. Auffrant, G. Nocton, *Organometallics* **2015**, *34*, 5470–5478.

[34] F. Nief, D. Turcitu, L. Ricard, *Chem. Commun.* **2002**, 1646–1647.

[35] F. Jaroschik, F. Nief, X.-F. Le Goff, *Polyhedron* **2009**, *28*, 2744–2748.

[36] W. J. Evans, T. S. Gummersheimer, T. J. Boyle, J. W. Ziller, *Organometallics* **1994**, *13*, 1281–1284.

[37] W. J. Evans, T. S. Gummersheimer, J. W. Ziller, *App. Organomet. Chem.* **1995**, *9*, 437–447.

[38] F. Nief, L. Ricard, *J. Organomet. Chem.* **1994**, *464*, 149–154.

[39] A. Kilpatrick, F. G. Cloke, *Dalton Trans.* **2017**, *46*, 5587–5597.

[40] O. T. Summerscales, S. C. Jones, F. G. N. Cloke, P. B. Hitchcock, *Organometallics* **2009**, *28*, 5896–5908.

[41] M. R. MacDonald, J. E. Bates, J. W. Ziller, F. Furche, W. J. Evans, *J. Am. Chem. Soc.* **2013**, *135*, 9857–9868.

[42] W. J. Evans, T. A. Ulibarri, J. W. Ziller, *J. Am. Chem. Soc.* **1988**, *110*, 6877–6879.

[43] M. E. Fieser, J. E. Bates, J. W. Ziller, F. Furche, W. J. Evans, *J. Am. Chem. Soc.* **2013**, *135*, 3804–3807.

[44] J. D. Rinehart, M. Fang, W. J. Evans, J. R. Long, *Nat. Chem.* **2011**, *3*, 538–542.

[45] J. D. Rinehart, M. Fang, W. J. Evans, J. R. Long, *J. Am. Chem. Soc.* **2011**, *133*, 14236–14239.

[46] S. Labouille, F. Nief, L. Maron, *J. Phys. Chem. A* **2011**, *115*, 8295–8301.

[47] L. Castro, C. E. Kefalidis, D. McKay, S. Essafi, L. Perrin, L. Maron, *Dalton Trans.* **2014**, *43*, 12124–12134.

[48] D. R. Fischer, H. Fischer, *J. Organomet. Chem.* **1965**, *4*, 412–414.

[49] D. R. Fischer, H. Fischer, *J. Organomet. Chem.* **1967**, *8*, 155–175.

[50] F. Grandjean, A. F. Williams, G. J. Long, *J. Am. Chem. Soc.* **1994**, *116*, 5999–6000.

[51] R. G. Denning, J. Harmer, J. C. Green, M. Irwin, *J. Am. Chem. Soc.* **2011**, *133*, 20644–20660.

[52] M. Coreno, M. de Simone, J. C. Green, N. Kaltsoyannis, R. Coates, C. Hunston, N. Narband, A. Sella, *Dalton Trans.* **2014**, *43*, 5134–5141.

[53] M. D. Walter, M. Schultz, R. A. Andersen, *New J. Chem.* **2006**, *30*, 238–246.

[54] M. D. Walter, D. J. Berg, R. A. Andersen, *Organometallics* **2006**, *25*, 3228–3237.

[55] M. Schultz, PhD thesis, University of California, Berkeley, **2000**.

[56] M. Schultz, J. M. Boncella, D. J. Berg, T. D. Tilley, R. A. Andersen, *Organometallics* **2002**, *21*, 460–472.

[57] C. H. Booth, M. D. Walter, D. Kazhdan, Y.-J. Hu, W. W. Lukens, E. D. Bauer, L. Maron, O. Eisenstein, R. A. Andersen, *J. Am. Chem. Soc.* **2009**, *131*, 6480–6491.

[58] C. H. Booth, D. Kazhdan, E. L. Werkema, M. D. Walter, W. W. Lukens, E. D. Bauer, Y.-J. Hu, L. Maron, O. Eisenstein, M. Head-Gordon, R. A. Andersen, *J. Am. Chem. Soc.* **2010**, *132*, 17537–17549.

[59] G. Nocton, C. H. Booth, L. Maron, R. A. Andersen, *Organometallics* **2013**, *32*, 5305–5312.

[60] G. Nocton, W. W. Lukens, C. H. Booth, S. S. Rozenel, S. A. Medling, L. Maron, R. A. Andersen, *J. Am. Chem. Soc.* **2014**, *136*, 8626–8641.

[61] G. Nocton, L. Ricard, *Chem. Commun.* **2015**, *51*, 3578–3581.

Come to the dark side, we have cookies

1 Relativistic calculations with lanthanide complexes

Quantum chemistry treatment of molecular systems has been under massive development over the last decades. For small organic systems, near-exact calculations can be performed, but for large organic systems and transition metal complexes, calculations rely on several approximations. As a result, computational chemists need to know what approximations they can make, and more importantly which ones they cannot.

In this context, computational chemists have been depending on two main approximations that are based on different ways of solving the Schrödinger equation[1]. But, if they consider heavy-elements such as lanthanides, they also need to take into account the relativistic effects that affect core-electrons[2]. Consequently, another layer of approximations needs to be made.

For several years, the systematic treatment of heavy-elements compounds with relativistic effective core potential has led to successful characterisations of complexes of these molecules[3]. The understanding of their electronic structure has permitted the development of new reactivity, and has improved the knowledge of their interaction with organic molecules.

The advancement of computer systems, and the development of new algorithmic procedures to reduce the computational cost of all-electron calculations have led to the availability of these techniques for lanthanide molecular systems[4]. These calculations have been relying on the implementation of relativistic approximations such as Douglass-Kroll-Hess (DKH) or

Zeroth Order Regular Approximation (ZORA), implemented in several electronic structure software such as ORCA[5], TURBOMOLE[6], MOLCAS[7], or ADF[8]. In this context, the QChem[9] software is very attractive as it possess powerful *ab initio* methods, but neither the ZORA or DKH approximations are implemented in this code. As a result an implementation of ZORA in QChem was performed in the group of M. Head-Gordon (Berkeley, USA), in order to investigate the use of these techniques on lanthanide molecular complexes.

Relativistic approximations are still under massive research, and while new approximations have been made such as the eXact 2-Component (X2C)[10], the systematic use of relativistic Hamiltonian for the study of heavy-element compounds is still limited to a few research groups. This indicates that there is a need for deep investigation into the use of systematic ZORA or DKH for heavy-element molecules.

For commercial reasons (Non-Disclosure Agreement), the ZORA implementation in Qchem cannot be discussed , but the theories behind relativistic all-electron calculations will be described. In order to understand the Dirac equation a short general introduction to non-relativistic methodologies will be discussed. Then, the different relativistic approximations will be detailed, with a specific focus on the ZORA Hamiltonian. Finally, two application examples of the use of ZORA and DKH approximations will be showed, introducing the concept of topological QTAIM, ELF and NCI analyses.

1.1 Generalities on electronic structure calculations

1.1.1 Solving the Schödinger equation

Non-relativistic quantum calculations are based on solving the Schrödinger equation[11] using different approximations[12]. The time independent Schrödinger equation links the wave-function to the total energy of a system. Its expression can be written as :

$$\hat{\mathrm{H}}\ |\psi\rangle = \mathrm{E}\ |\psi\rangle$$

where E is the stationary energy, $\hat{\mathrm{H}}$ is the Hamiltonian, and ψ the wave-function for a system of N nuclei and n electrons.

For this system, neglecting the relativistic effects, the Hamiltonian can be written as

$$\hat{H} = \hat{T}_e + \hat{T}_n + \hat{V}_{Ne} + \hat{V}_{ee} + \hat{V}_{NN}$$

where $\hat{T}_e$ is the electron kinetic energy, $\hat{T}_n$ the nuclei kinetic energy, $\hat{V}_{Ne}$ the interaction between the nuclei and the electron, $\hat{V}_{ee}$ the interaction between the electrons and $\hat{V}_{NN}$ the interaction between the nuclei.

Several terms in this equation are not known analytically, or are difficult to evaluate. As a result, different approximations were developed in the 1930s in order to solve this equation for small systems. First, the Born-Oppenheimer approximation was able to decrease the size of the equation by considering the nuclei as fixed particles (for an overview on non-Born-Oppenheimer calculations read the recent review from Adamowicz[13]). Then, the wave-function was expressed as a Slater determinant of n spin-orbitales.

At this stage one term is still not known analytically : V_{ee}. As a result, two hypotheses have been developed in order to solve the Schrödinger equation: wave-function theories (or *ab initio* methods) and Density Functional Theory (DFT).

1.1.2 *Ab initio* methods

Wave-function theory is based on the Hartree-Fock (HF) formalism[12]. In this formalism, the wave-function is described as a single Slater determinant, and the electron-electron interaction is averaged to a mean field potential described as a Coulomb and an exchange potential. The Coulomb force corresponds to the classic Coulomb interaction between two charges, while the exchange potential is related to the interaction of one electron of spin α with an electron of spin β. The set of HF equations has to be solved by an iterative procedure as it depends on a set of orbitals that are not known exactly. After resolution of the equations, a better expression for the orbital is injected back into the equations themselves in order to achieve self consistency (this procedure is called Self Consistent Field (SCF)).

This type of SCF cycle is the basic equation that is solved by quantum chemistry softwares. The resulting HF energy does not reproduce the exact energy of the system. The correlation is defined as the energy difference between the exact energy and the HF energy. This correlation energy comes from two[14] different factors that are not treated by HF calculations :

- **Dynamic correlation**: there is a correction for the interaction between two anti-parallel spins in the exchange potential. However, there is no contribution from the interaction between parallel spins.

- **Static correlation** : the form of the wave-function has been chosen as a single Slater determinant. But, this is an approximation that might not be accurate for systems with quasi-degenerated energies, like open-shell molecules or during bond breaking where the wave-function of the system is evolving as a combination of two wave-functions.

These problems encountered within the HF approximation lead to inaccurate energy and electronic structure evaluations. Dynamic correlation can be added to the HF energy by a perturbation treatment, which lead to Möller-Plesset theory (MP)[15]. MP2 energies is the perturbation at the second order and one of the most used correction[16] to HF to account for the dynamic correlation. Another improvement over HF for dynamic correlation includes the use of the first, second and third excited states into the calculation of the wave-function. This can be done using Coupled-Cluster[17] Single Double and Triple (CCSDT) which is often used in order to achieve chemical precision (error of only a few kcal/mol) for closed-shell systems. This technique is partially accounting for the static correlation, such as for bond-breaking systems[18]. This type of method can be extended in order to study excited states of molecules with methods such as Equation of Motion Coupled Cluster (EOM-CCSD)[19] or Coupled Cluster Single and Double (CC_2)[20].

The static correlation is corrected with the use of multi-determinantal theories. In theories such as the Complete Active Space Self Consistent Field (CASSCF)[21] (for a recent overview on CASSCF read the book from Roos[22] or the review from Shepard[23]), the ground state wave-function is described as a combination of multiple Slater determinants. The main idea behind CASSCF is to select an active space of molecular orbitals for which to perform the multi-determinantal calculation (Figure 1.1). However, the number of active orbitals is limited (18 electrons in 16 orbitals). The development of new techniques such as Restricted Active Space SCF[24], Generalised Active Space SCF[25,26], Density Matrix Renormalisation Group[27,28] have been able to push the limits of the active space to 18, 22 and 50 orbitals, respectively. These methods correct the static correlation but do not include

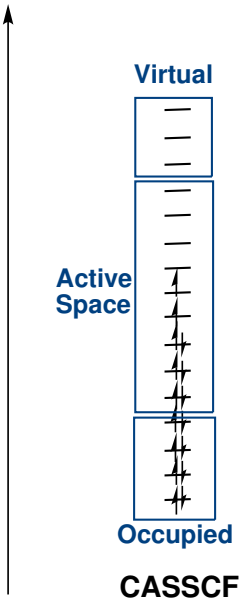

Figure 1.1: Scheme of a fictitious triplet system and representation of the different domains of CASSCF; the active space is composed of 8 electrons in 9 orbitals CAS(8,9)

dynamic correlation. To add the dynamic correlation effects, perturbation theory can be added to the CASSCF wave-function. The same methodology than MP2 can be adapted to CASSCF, and the resulting CAS Perturbation Theory 2 (CASPT2)[29] calculation restores the dynamic correlation that was not included from the CASSCF calculation. Other perturbations such as N-Electrons Valence Perturbation Theory 2 (NEVPT2)[30] can also be used, but there is no significant difference with CASPT2 in terms of accuracy or computational expanses[31,32].

Ab initio calculations at the HF, MP2, or CCSD level present the disadvantages of being computationally demanding and not applicable for Transition Metal (TM) or lanthanide as HF orbitals suffer from the non inclusion of correlation. In this domain, methods based on the Density Functional Theory present certain advantages such as a partial dynamic correlation inclusion.

1.1.3 Density Functional Theory

The electron density could be a better variable for solving the Schrödinger equation than the coordinates of the electron itself. Indeed, the electron density only depends of the three spatial coordinates, while in wave-function theories each electron is described with three spatial coordinates. According to theorems of Hohenberg and Kohn[33], the energy is a functional of

the density. In order to solve analytically the density dependant Schrödinger equation, Kohn and Sham (KS) proposed[34] an *ansatz* that consists in replacing the electronic system in interaction with a system of independent electrons in an external field. The fictitious system has the same energy as the real one, and the total energy of the real system can be written as

$$E = T_{KS}[\rho] + V_{Ne}[\rho] + J[\rho] + E_{xc}[\rho]$$

where T_{KS} correspond to the kinetic energy and J is the Coulomb interaction of the fictitious system and E_{xc} is the Exchange-Correlation potential. It can be shown that the Coulomb interaction of the fictitious system is responsible for the Self Interaction Error (SIE): for a system of one electron this Coulomb interaction does not vanish. The last term of the equation is the only one not known analytically. As a result, several expressions for this term have been developed over the years[35,36]. Firstly, the Local Density Approximation (LDA) expressed the exchange correlation potential as a function of the electron density. This kind of functionals gives accurate results for system close to the homogeneous electron gaz. However as soon as there is heterogeneity, *e.g.* when there is strong interactions between atoms, LDA gives incorrect results. Expanding the expression of the exchange correlation potential as a function of both the electron density and its gradient (Generalised Gradient Approximation (GGA)), or of the electron density, its gradient and its kinetic energy (meta-GGA), or of the electron density, its gradient and an inhomogeneity parameter[37] (Non-separable Gradient Approximation (NGA)), led to a large variety of functionals and the enhancement in the evaluation of the electronic structure and energies of molecules.

The development of these approaches has separated two streams of theoretical chemists: one that designs new density functionals by fitting the parameters of the functional to several databases[38] and the other that uses physical results from which they can extract the parameters[39]. The number of GGA functionals today is very important, and there is no functional designed for a specific use. As such, the consistent evaluation of functionals for specific cases is crucial. These functionals have been able to evaluate the electronic structure of a massive amount of chemical systems. But, their main disadvantage relies on the SIE, which stabilises delocalised states and leads to errors.

The exact exchange contribution can be evaluated using the HF theory. As a result, the HF exchange can be used in a satisfactory way for the exchange part of the exchange-correlation functional. In most functionals a fixed HF exchange percentage has been used (from 5 to 50%) and this kind of mixing between (meta-)GGA exchange and HF exchange reduces the SIE and gives accurate energies. Moreover, at long distances the HF exchange gives a good evaluation of the exchange potential. As a result, long range corrected functionals[40] have been designed, and account for 100% HF exchange at long distances while at short distances this exchange is small (0%). Even more, double-hybrid functionals[41] have been developed by combining MP2 and GGA functionals, *i.e.* by combining the HF and the GGA exchange and the MP2 and the GGA correlation.

Finally, the choice of the functional needs to be a compromise between different factors: the number of parameters inside the density functional, the computational cost, the calculated properties, the accuracy desired, and the size of the system under study. Depending on the type of calculation undertaken, different functionals will be used.

In addition to the choice of the functional, another important effect is not accurately treated by DFT Functionals: the dispersion interactions. That is why, several dispersion correction models have been developed[42]. The first one is based on the work of Grimme *et al* and consists in the addition on the energy of a semi-empirical correction of the form $\frac{C_6}{r^6}$ (D3 approximation[43]). The second one has been developed by the group of van Voorhis and consists in the addition in the exchange correlation functional of a non-local potential that account for the dispersions effects. This has been used recently in the design of a new type of functionals based on the non-local part of the functional developed by van Voorhis[44]. The third way to include dispersion effects is to fit the parameters of the functional using a dataset including systems with significant dispersions interactions. This type of functional has been developed by the group of Truhlar for the past decade[38].

DFT can be used to compute excited states with methods such as the Time Dependant Density Functional Theory (TDDFT)[45] or approximations to TDDFT like the Tamm Dancoff Approximation (TDA)[46]. These theories have been used on open-shell and closed shell molecules alike. Recently, these theories have been extended with a fast simplified

version[47,48] that can be used on large-size molecules and that could have significant impact for excitation spectra of biologic molecules.

1.2 Relativistic approximations: from the Dirac equation to ZORA and DKH models

For elements located lower in the periodic table than the 3rd row, relativistic effects are important and must be taken into account when performing the theoretical calculations[49,50]. The core electrons tend to approach the speed of light, and as a result, relativistic effects become important for these electrons. Valence electrons are deeply influenced by this effect on core electrons. Two ways exist for the treatment of these relativistic effects. The first one involves the use of Relativistic Effective Core Potential (RECP), while the second one uses relativistic Hamiltonians.

1.2.1 RECP

The use of RECPs in quantum chemistry is not new. It has been described for more than two decades by Dolg *et al* for lanthanide molecules[51] and used in countless examples. The principle applied is very easy to understand: core electrons can be replaced by a potential describing their influence on the valence electrons. Indeed, core electrons are not useful in reactivity, and thus are not of tremendous importance when performing computational chemistry. On the contrary, valence electrons must be treated exactly[3].

ECPs have been used for more than a decade on Transition Metal (TM) chemistry, but in recent years with the improvement of density fitting techniques such as the Resolution of the Identity (for non-hybrid functional[52,53], and MP2[54]), the Cholesky decomposition[55] for CASSCF calculations especially[56,57], the Resolution of the Identity Chain of Sphere[58], and others[59,60], computational methods have become faster without any loss in accuracy on the energy evaluation (a comparison between these fitting techniques have been recently published by Pedersen *et al*[61]). In this context, the use of all-electron calculations have become feasible, and the computational cost of all-electron calculations with density fitting techniques has been substantially similar to ECP calculations (Figure 1.2).

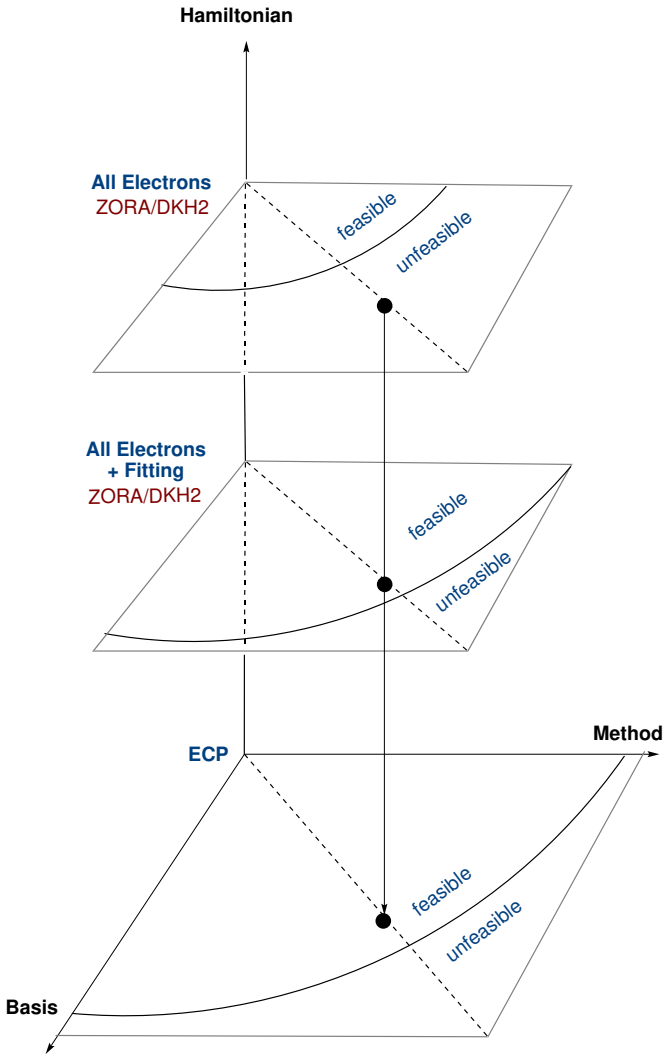

Figure 1.2: Scheme extracted from Dolg *et al.*[3] and improved for the purpose of this manuscript

It is then a good idea to deeply investigate the use of all-electron calculations with heavy-element compounds. That is why only all-electron calculations will be performed for this study, and that the all-electron relativistic methods will be deeply investigated in the current section[62,63].

1.2.2 Dirac Equation

In the non-relativistic case, the Schödinger equation needs to be solved. In the relativistic case, applying the Born-Oppenheimer approximation, the Dirac-Coulomb one electron equation[64] needs to be solved and can be written as:

$$\mathbf{h}_i^D \psi_i = (\boldsymbol{\beta} c^2 + c\boldsymbol{\alpha}.\mathbf{p} + \mathbf{V_{ee}} + \mathbf{V_{eN}})\psi_i = (\boldsymbol{\beta} c^2 + c\boldsymbol{\alpha}.\mathbf{p} + \mathbf{V})\psi_i = \epsilon_i \psi_i \qquad (1.1)$$

$$\text{where} \begin{cases} \boldsymbol{\beta} & = \begin{bmatrix} I_2 & 0 \\ 0 & -I_2 \end{bmatrix} \\ \\ \boldsymbol{\alpha_j} & = \begin{bmatrix} 0 & \sigma_j \\ \sigma_j & 0 \end{bmatrix} \end{cases} \quad \text{j is 1, 2 and 3 and } \sigma \text{ are the Pauli matrices}$$

and V is the sum of the electron-electron and the electron-nuclei interactions; p is the momentum operator and c the light celerity, and the Pauli matrices can be written as:

$$\boldsymbol{\sigma_1} = \begin{bmatrix} 0 & 1 \\ 1 & 0 \end{bmatrix} \quad \boldsymbol{\sigma_2} = \begin{bmatrix} 0 & -i \\ i & 0 \end{bmatrix} \quad \boldsymbol{\sigma_3} = \begin{bmatrix} 1 & 0 \\ 0 & -1 \end{bmatrix}$$

In this equation, the wave-function can be described accurately as 4-dimension vector that can be decomposed in small and large components. The relativistic HF (Dirac-Fock) and the DFT[35] equations can then be transcribed into the Dirac equation, by changing the potential in the equation depending on the method used. Solving the Dirac equation relies on solving a set of coupled equations between the small and the large components of the 4-dimension wave-function vector.

Even if performant algorithms have been developed to solve the full 4-components Hamiltonian, this type of calculation is limited to small systems, and time consuming. Approximations were developed in order to speed up the calculation by decoupling the two sets of equations.

1.2.2.1 ZORA Hamiltonian

A specific relationship between the small and the large components can be exploited in order to express the energy as a function of a two-component vector. This relationship is based on the development at the zeroth order of $\frac{\epsilon_i}{c^2 - V}$. This leads to the Zeroth Order Regular Approximation (ZORA) equation[65]:

$$\epsilon_i^{ZORA}\, \psi_i = (V\mathbf{I_2} + \frac{\mathbf{p^2}}{2} + \boldsymbol{\sigma}.\mathbf{p}\, \frac{v(r)}{2c^2 - V}\, \boldsymbol{\sigma}.\mathbf{p})\, \psi_i \tag{1.2}$$

This expression can be divided into the non-relativistic Hamiltonian and the ZORA correction to the kinetic energy. This corrective term depends on the inverse of V which means that a shift in the potential will not lead to a shift in the energy. This gauge dependance

could result in unrealistic geometry structures, or wrong electron affinity. Different ways exist in order to remove this gauge dependance:

- **Scaled ZORA**: the increase in the development order leads to a satisfactory removal of gauge dependance. First Order Regular Approximation and Scaled ZORA techniques are based on this principle. A less computational demanding method, the Electrostatic Shift Approximation(ESA)[66], uses a scaled ZORA Hamiltonian and approximations to the energy differences between molecules to accelerate the calculation.

- **Approximation of the potential**: the gauge dependance relies on the potential V. Expressions of this potential can be approximated using the Sum of Atom Potential Approximation[67] (SAPA), or a Model Potential[68], and thus remove altogether the gauge dependance.

- **Utilisation of the Resolution of the Identity**(RI): RI can be used in order to modify the formulation of the ZORA expression[69,70]. This has been done for *ab initio* methods, but the large basis set needed to obtain accurate calculations discouraged the use of ZORA for *ab initio* methods (even if some recent methodologies could be of interest in this field[71–73])

Each quantum chemistry software that will be used for the quantum chemistry described in this manuscript contain one specific version of ZORA. As an example, in the ADF package[8] the ZORA-ESA/SAPA method is implemented while in the ORCA package[5] a scaled ZORA-MP is. The two methods do not have significant differences[68] and have been used uniformly throughout the manuscript.

1.2.2.2 Douglass-Kroll-Hess Hamiltonian

The Douglass-Kroll-Hess (DKH) Hamiltonian[74,75] relies on another approximation for the evaluation of the Hamiltonian. The idea is to use an unitary transformation $\hat{U}$ that decouples the large and the small component, relying on the Foldy-Wouthuysen transformation. This transformation can be described as :

$$\hat{U}\hat{H}_D\hat{U}^{-1} = \begin{bmatrix} \hat{H}_+ & 0 \\ 0 & \hat{H}_- \end{bmatrix} \tag{1.3}$$

The exact expression of $\hat{U}$ is not known, but this matrix can be decomposed in a infinite set of unitary transformations. The decomposition using n unitary transformations is called DKHn, and it uses n unitary transformation for the Hamiltonian, in order to get an approximate decoupling between the small and the large component. DKH2 is the most used version of the Hamiltonian and it has been used in combination with DFT and *ab initio* methods alike to compute energies and electronic structure. This type of Hamiltonian is standardly used in the MOLCAS software for CASSCF calculations with heavy elements[76].

Improvement on the ZORA or DKH model are under study today with new methods such as the exact two component (X2C)[77] which is almost as precise as the full 4-component calculation.

1.3 Lanthanide molecules calculations

The relativistic effects are of tremendous importance in the electronic structure of heavy-elements such as lanthanides. Indeed, the large number of electrons and the open-shell nature of these molecules require the use of adapted methodologies.

1.3.1 DFT or CASSCF?

Open-shell systems are the most common ones for TM or lanthanide complexes. In these systems the Hamiltonian expression derived previously does not have much sense. In the context of unrestricted calculations, a set of α and β equations needs to be solved independently. Unrestricted determinants are not eigenfunction of S^2 as it was the case for restricted calculations. As a result, unrestricted calculations never evaluate a doublet as exactly a doublet[12]. This means that the wave-function is contaminated by higher multiplicity components. The evaluation of the spin contamination of an unrestricted calculation will give the percentage of contamination by higher spin states.

This spin contamination issue has been a very delicate problem of HF theory for a long period of time[78–80]. It is not occurring as much in DFT as in *ab initio* calculations. In

DFT, the use of techniques to remove spin contamination has made a lot of debates[81–83]. But as DFT is not as much prone to spin contamination as HF theory, no improvement over this kind of behaviour was developed except for constrained-DFT that constrains the spin to be exact[84].

This competence for DFT calculations not to be prone to this high level of spin contamination might be related to the inclusion of correlation into the functional, which might correct the lack of static correlation issues encountered using HF wave-functions. As a result, DFT is often the best way to evaluate lanthanide molecules, as it is fast and provides reliable results for energies and electron densities. However, the lanthanide 4f orbitals (Figure 1.1) are not accurately described by DFT, as the 4f orbitals are degenerate and are only evaluated properly using multi-determinantal techniques such as CASSCF. This specificity is important in some cases[85,86], while in other traditional DFT methods can be used[87,88].

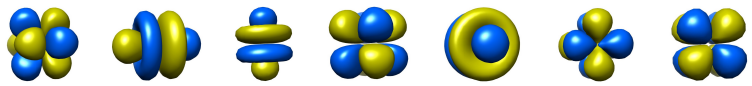

Table 1.1: 4f atomic orbitals of lanthanide atoms

CASSCF is not a panacea: the small number of orbitals that can be included in the active space is often the limiting step for lanthanide. In addition to the seven 4f orbitals that need to be taken into the active space, orbitals from the ligand or 5d orbitals might be important for the final evaluation of the electronic structure of the complex. CASSCF studies of lanthanide molecules have recently been performed by Le Guennic *et al.*[86]. The involvement of the seven 4f orbitals in the active space was not able to reproduce accurately in all the situations the magnetic behaviour of the molecules, which might indicate that the active space size needs to be augmented.

In his seminal book on CASSCF calculations[22], Roos also recommended the use of the 4f, 5d, 6s and 6p in the active space for lanthanide molecules. Indeed, building such an active space is not possible. However future investigations using DMRG[28] could permit such a large active space and improve the accuracy of quantum calculations on lanthanide molecules.

In most cases, DFT calculations are enough to reproduce accurately the energy difference between molecules, and can successfully design reaction mechanisms. This has been the

work of Maron *et al*[89–93] that involved the massive use of DFT calculations to study reaction mechanisms in lanthanide chemistry. Most of their work used ECPs, and as a matter of comparison, the effect of relativistic approximations on the mechanism could be of huge interest.

This work has been done using both methods. CASSCF calculations were performed using a DKH2 Hamiltonian, and a large gaussian basis set ANO-RCC-VDZP[94,95], when lanthanides were involved (DKH2). Otherwise, when only organic molecules were involved, CASSCF calculations were performed using an ANO-VTZP basis set.

DFT calculations were performed at three distinctive levels of theory:

- ZORA1: single point calculations using the ADF[8] chemistry software and a ZORA-SAPA/ESA Hamiltonian in combination with an all-electron Slater TZP basis set
- ZORA2: geometry optimisation using the ORCA[5] chemistry software and a scaled ZORA-MP Hamiltonian in combination with an all-electron Gaussian SVP basis set[96]
- ZORA3: single point calculations using the ORCA[5] chemistry and a scaled ZORA-MP Hamiltonian in combination with an all-electron Gaussian TZVP basis set[96]

Most optimisations were performed using the PBE-D3(BJ) ZORA2 level of theory, while single point calculations were performed at the PBE0-D3 ZORA1. Unless otherwise noted, the density functional used for the optimisation is therefore PBE-D3(BJ), and for single point calculations PBE0-D3. Energy comparisons were performed at the PBE0-D3(BJ) ZORA3 level of theory, unless otherwise noted.

Relativistic ECPs were also used during this study. Two types of relativistic ECP exist for lanthanide atoms: Small Core ECP (SC-ECP)[97] with the 4f electrons out-of-the-core of the pseudopotential and a Large Core ECP (LC-ECP)[98] with the 4f electrons in-the-core of the pseudopotential. Two LC-ECPs exist depending on the electronic configuration of the lanthanide, *i.e.* depending on the oxidation state of the lanthanide (+II or +III).

These two types of ECPs (LC-ECP, and SC-ECP) were used with their associated basis set for samarium[99], and a 6-31G(d,p) for the other atoms such as C, N, O, H (BS1).

Calculations were also done using palladium[100] and iodide atoms[101] ECPs, LC-ECP for ytterbium and a 6-31G(d,p) basis set for C, H and N (BS2). These ECPs were also used in combination with an extended large core basis set for ytterbium[102], a def2-QZVP[103] basis set for Pd and I, and a 6-311G++** for C, N, and H (BS3).

1.3.2 DFT and lanthanides

A couple of groups has been interested in studying the electronic structure and the reaction mechanisms of lanthanide with DFT. Maron's group has become an expert in the field of reaction mechanism for lanthanide complexes. Their recent collaborations with the group of Procter led to interesting conclusions for mechanisms of basic electron transfer reactions with SmI_2[93].

The group of Kaltsoyannis on the other hand has been interested in using specific DFT tools such as the Quantum Theory of Atoms In Molecules (QTAIM) and the Electron Localisation Function (ELF) methods in order to deeply investigate the density extracted from a DFT calculation in actinide calculations[104–106]. Their work mainly focussed on actinide elements (even if he is involved in lanthanide chemistry as well[107]) but these two methodologies can be used as well with lanthanides.

1.3.2.1 QTAIM

The topological analysis of the electronic density was formulated by Bader as a Theory of Atoms In Molecules[108]. A *critical point* is defined as a point in which the gradient of the density is the zero vector. In this sense, four types of *critical point* can exist depending on the sign of the three components of the density laplacian :

- Nuclear Critical Point (NCP): if the three derivatives are negative, this point is a local maximum in the bond path
- Bond Critical Point (BCP): if only two derivatives are negative, this point is a maximum in a plane and a minimum on a vector in the bond path
- Ring Critical Point (RCP): if only two derivatives are positive, this point is a minimum in a plane and a maximum on a vector in the bond path

- Cage Critical Point (CCP): if the three derivatives are negative, this point is a local minimum in the bond path

At these critical points, the value itself of the electron density laplacian is important. If the laplacian is positive, the bonding is ionic : the density is going towards the two atoms, and is not stable at this position. On the other hand, if the laplacian is negative, the bonding is covalent: the density is going to the plane orthogonal to the bonding. Moreover, the density at the critical point can give information into the bonding itself: a density superior to 0.20 involves a strong interaction[109].

QTAIM is a tool to study the influence of the bonding strength between a metal and a ligand, or in organic molecules[110]. But, there is still debate in the literature[109] towards the use of QTAIM for TM complexes, as it is not clear that the value of interest for bonding interactions is the laplacian. This method is believed to be density functional independent and the addition of implicit solvent models such as COSMO does not have a significant impact on its values[111].

QTAIM has been extended recently to be used with ZORA all-electron calculations, and has been implemented in the ADF software[112]. This version was used to compute QTAIM data presented in this manuscript.

1.3.2.2 ELF

A complementary tool on which computational chemists have been relying to study the density itself is the Electron Localisation Function[113,114]. This function is evaluating the probability for an electron to be in the neighbourhood of another electron of the same spin. This function is evaluated between 0 and 1.0, 0 corresponding to a delocalised system, 0.5 to the homogeneous gaz and 1.0 to a perfect localisation of the electrons.

The topological analysis of the ELF function partitions the space into different basins on which the attractors define a kinetic energy space where the Pauli principle is minimum. The basin close from the nuclei is called a core basin, while the others are called valence basins. The presence of a simple bond between two atoms implies a connection between two core basins and one valence basin: this is a *disynaptic* basin.

Recently, the development of ELI-D[115], an extension of the ELF function, has been performed and has been successfully applied to TM[116] and actinides[117] in order to study their bonding interactions.

1.3.2.3 Non Covalent Interaction

Another tool that can be used is the Non-Covalent-Interaction (NCI)[118] mapping. This NCI method is calculated as the different points in which there are singularities for the reduced density gradient. At these points, the density is analysed using the gradient laplacian.

Three types of points can be found depending on laplacian second component (second derivative of the density along the orthogonal plane to the interatomic vector, λ_2) : hydrogen bonds, when $\lambda_2 < 0$, repulsive forces, when $\lambda_2 > 0$ and van der Waals interactions when $\lambda_2 \approx 0$.

1.3.2.4 Energy Decomposition Analysis

A fourth tool has been used to study the interactions between TM complexes and their ligand: the Energy Decomposition Analysis. Developed initially by Morokuma[119,120], and improved by Ziegler and Rauk[121] this tool calculates energy between fragments of a molecules (for a recent review on this subject see the work from Hopffgarten[122]), and decomposes this energy between the electrostatic interaction, *i.e.* the charge distribution difference with the isolated molecules, the Pauli repulsion, *i.e.* the exchange potential resulting from the interaction between the two fragments, the orbital interaction, *i.e.* the orbital interactions between the fragments (donation, retro-donation and electronic overlap).

Using the decomposition scheme implemented in ADF is not suited for calculations with open-shell compounds, as ADF only does interaction energy between restricted fragments. In order to get rid of this issue, the ADF decomposition scheme was used, in addition to a single point calculation on the different fragments in an unrestricted fashion as recommended in the ADF manual[123].

New developments in the field of energy decomposition analysis involve Natural Energy Decomposition Analysis[124], Symmetry-Adapted Perturbation Theory[125,126], DLPNO-CCSD-EDA[127] or the Absolutely Localised Molecular Orbital EDA[128] that has recently achieve the analysis of bonding interactions[129,130].

Until now, these recent developments have never been used for lanthanide complexes, and the use of such decomposition schemes with lanthanide could estimate the orbital interaction importance in the bond strength for lanthanide molecules.

1.4 Electron transfer and electronic structure of lanthanide complexes

Understanding electron transfer for lanthanide molecules relies on the use of both experimental expertise, and a broad range of theoretical methods. Experimental results often cannot be interpreted easily without the use of quantum chemistry, and quantum chemistry results, especially with lanthanide molecules, are difficult to understand without experimental data. Both facets of chemistry are needed for improving the knowledge about electron transfer with lanthanide complexes.

Analysing the differences between lanthanide molecules using QTAIM, ELF and EDA methodologies brings to the experimental chemist ideas on why the bonding interaction is different for different lanthanides. One of this example is with samarium and ytterbium complexes of tetramethylbiphosphinine. This moiety is easily reduced by samarium, while ytterbium cannot reduce it. The two compounds possess different electronic structures which involves more orbital interaction in the samarium case than in the ytterbium case.

Moreover, while electron transfer with lanthanide complexes is often considered as a transfer of a single electron from a divalent lanthanide complex to an organic moiety, the reverse reaction can also happen especially with ytterbium. Indeed, this property is often not considered when discussing the reactivity of ytterbium but could be of significant importance. Comparing ytterbium (Yb^{+III}) and the nearest 5d element, lutetium (Lu^{+III}), was able to explain why ytterbium does not activate C-H bonds while lutetium does.

These two examples will be detailed shortly for the reader to consider the difficulty to understand electron transfer with lanthanide molecules.

1.4.1 Tetramethylbiphosphinine complexes of ytterbium and samarium

Tetramethylbiphosphinine complexes of ytterbium and samarium was investigated using both the experimental and the theoretical tool. The results indicate that the bonding interaction is

less strong in the case of the ytterbium than in the case of the samarium. The EDA analysis indicated that the orbital interaction between the lanthanide and the ligand was stronger for samarium than for ytterbium. The ELF analysis was in agreement with this result as the valence basins were more deformed by the interaction with the ligand in the case of samarium than in the case of ytterbium. The result from this work has been published in 2016 in the *New Journal of Chemistry*[131] and is provided in this manuscript.

NJC

PAPER

View Article Online
View Journal | View Issue

Cite this: *New J. Chem.*, 2016, 40, 6643

Electron transfer in tetramethylbiphosphinine complexes of Cp^*_2Yb and Cp^*_2Sm†

Arnaud Jaoul, Carine Clavaguéra* and Grégory Nocton*

Received (in Victoria, Australia) 17th February 2016,
Accepted 25th May 2016

DOI: 10.1039/c6nj00527f

www.rsc.org/njc

This article reports the synthesis and the characterization of two Cp^*_2Ln (Ln = Sm and Yb) fragments containing the tetramethylbiphosphinine (tmbp) ligand in equatorial position. The solid-state data indicate the reduction of the tmbp ligand with the decamethylsamarocene fragment along with the oxidation of the metal center, while the metrical parameters highlight a more dubious electronic structure for the tmbp adduct of the decamethylytterbocene fragment. ^1H and ^{31}P NMR have been recorded for both complexes and show the unambiguous oxidation of the samarium complex. On the other hand, the NMR data for $Cp^*_2Yb(tmpb)$ exhibit weakly shifted paramagnetic resonances along with a weak effective moment in solution; a situation that is neither in agreement with a divalent metal center and a neutral ligand, nor with an oxidized ytterbium ion and a radical tmbp ligand. In addition to these experimental data, theoretical calculations were performed on both complexes. DFT calculations highlight a large orbital contribution and an f occupation of 5.4 for the samarium complex, which is to compare to an f occupation of 13.8 and less orbital interactions in the ytterbium complex.

1. Introduction

The reaction of lanthanides fragments with redox non-innocent ligands such as bipyridine and phenanthroline led recently to interesting developments for the understanding of strong electron correlation in lanthanide complexes as well as for the rationalization of the reactivity of these complexes.[1–11] The electronic structure of both $Cp^*_2Yb(bipy)$ and $Cp^*_2Yb(phen)$ is of particular interest since these two molecules, which look very similar, do not have the same electronic ground state and do not follow the same reactivity patterns; $Cp^*_2Yb(bipy)$ is stable as a monomer[2,12] and $Cp^*_2Yb(phen)$ dimerizes in solution at the 4(7) position (the position located in *para* to the N-atom).[1] The electronic ground state of $Cp^*_2Yb(bipy)$ is intermediate valent, which means that two resonant structures compose the ground state: a closed-shell f^{14}, neutral bipyridine situation and an open-shell singlet f^{13}, bipy radical anion. The ratio between both structures is given by n_f that defines as the hole occupancy and therefore relates to the amount of trivalent ytterbium: if n_f is 1, ytterbium is trivalent, if n_f is 0, ytterbium is divalent. The n_f value of $Cp^*_2Yb(bipy)$ is 0.85 and is measured by L_{III}-edge XANES and computed by Complete Active Space Self-Consistent Field (CASSCF) calculations.[2] On the other hand, $Cp^*_2Yb(phen)$ has a triplet ground state.[1] Because both bipy and phen ligands have very similar redox potential, the reason for such a different electronic structure between both complexes was rationalized with the symmetry orbital in which the electron is transferred. In bipyridine, the LUMO is of b_1 symmetry (C_{2v} label) and is of a_2 symmetry in phenanthroline. Since the a_2 symmetry is not adapted for electron correlation because very little coefficients are present on the N atom, the density moves away from the metal center and it is what triggers the C–C bond formation.[1,13]

From these recent developments, we started a series of experiments in the idea of getting a better understanding of the mechanism of these electrons transfers. In bipyridine adducts with the Cp^*_2Yb fragment, the methyl substitution of the protons located on the bipy ligand leads to drastic modifications of the ground state electronic structure and both the sterics and the electronics may play a role.[3] The NCCN torsion angle is an important variable for the redox potential of methyl substituted bipy ligands and the latter increases when the torsion angle increases. The result of this observation is that the 3,3′-Me_2bipy adduct of Cp^*_2Yb has a small n_f of 0.17, indicative of an intermediate-valent ground state with a large contribution of the closed-shell f^{14}-bipy^0 and the ligand is not as reduced as other methyl substituted bipyridine ligands.[14]

In 2014, some of us described the steric influence of samarium complexes in this electron transfer event using bulky ligands such as Cp^{ttt} (tris-*tert*-butylcyclopentadienyl) and have shown that the redox potential net value was to take cautiously when it comes to single electron transfer in lanthanides complexes.[15] Both the steric hindrance and the orientation of the ligand on

LCM, CNRS, Ecole Polytechnique, Université Paris-Saclay, 91128 Palaiseau, France. E-mail: greg.nocton@polytechnique.edu

† Electronic supplementary information (ESI) available: NMR, magnetism, X-ray data for **1** and **2** and DFT calculations. CCDC 1452180 (**1**) and 1452181 (**2**). For ESI and crystallographic data in CIF or other electronic format see DOI: 10.1039/c6nj00527f

the metal center may play a role and can prevent the electron transfer from occurring. This is important since a better understanding of the electron transfer mechanism will lead to a better selectivity for the reactivity, including the activation of small molecule of importance, and also to the stabilization of new original divalent lanthanides complexes.

A last contribution, not yet entirely understood, is the role of the f-orbitals in these electron transfers. Although the participation of the 4f-orbitals in the chemical bonding is usually very small in lanthanide complexes, recent work show that these orbitals are likely to induce spin density alteration at the ligand and that they contribute to the bonding.[16]

To continue the story of these molecules and to bring more insights in the understanding of conditions needed for the electron transfer to occur or not, we turned our attention toward 2,2′-biphosphinine ligands, the phosphorus analogues of the bipyridine ligands. These remarkable ligands were synthetized in the beginning of the 90's by Le Floch *et al.*[17] and constitute very interesting tools for our studies since phosphorus is bigger than nitrogen but also more polarizable, so that the redox potential of the tetramethyl-2,2′-biphosphine ligand (tmbp) is higher than the one of the bipyridine ligand despite a PCCP torsion angle having a similar value than that of the 3,3′-Me_2bipy.[18] Herein, we wish to report the synthesis, experimental and theoretical analysis of adducts of the tmbp ligands with the Cp^*_2Yb and Cp^*_2Sm fragments. This paper stresses a new mechanism for an electron transfer to occur showing the importance of local redox potential.

2. Results and discussion

2.1. Synthesis and X-ray crystal structures

Addition of tetramethylbiphosphinine (tmbp) to a toluene solution of $Cp^*_2Sm(OEt_2)$ leads to the immediate formation of a dark brown solution. Addition of pentane to this solution in a 1 : 1 ratio and cooling the mixture at −40 °C leads to the formation of X-ray suitable dark brown crystals of the complex $Cp^*_2Sm(tmbp)$, **1**. An ORTEP of the crystal structure is shown in Fig. 1 with the principal metrical parameters in the caption and Table 1.

Table 1 Metric parameters for **1**, **2** and $Dtp_2Tm(tmbp)$[11]

Distance (Å) and angle (°)	1	2	$Dtp_2Tm(tmbp)$
M–Cp(Ctr)	2.42(1)	2.36(1)	2.44(1)
M–P	2.92(1)	2.872(2)	2.84(2)
		2.938(2)	
C–C	1.439(10)	1.464(9)	1.44(1)
PCCP	2	21	12

The complex $Cp^*_2Yb(tmbp)$, **2**, is prepared in a similar way with $Cp^*_2Yb(OEt_2)$ and tmbp in toluene, leading to a brown mixture as well. The brown mixture is let stand at room temperature to yield X-ray suitable dark brown crystals of **2**. The ORTEP of the crystal structure is shown in Fig. 2 and main metrical parameters in the caption. In both structures, the two Cp* ligands are coordinated in η^5 fashion and the mean M–C(Cp*) distances are 2.71(2) Å and 2.64(1) Å for **1** and **2**, respectively, while the M–Cp*(ctr) distances are 2.42(1) Å and 2.36(1) Å for **1** and **2**, respectively. The Yb–C(Cp*) distance is close to the distance reported for the divalent complex $Cp^*_2Yb(thf)_2$ of 2.66 Å[19] and may imply that the metal center remained at the divalent state in **2**. In **1**, the Sm–C(Cp*) distances are 0.15 Å shorter to those reported for the divalent complex $Cp^*_2Sm(thf)_2$ of 2.86(3) Å[20] in agreement with the oxidation of the samarium metal center.

The Sm–P distances are 2.909(2) Å and 2.927(2) Å and are rather close to each other so that a mean distance of 2.92(1) Å is meaningful. The latter compares with the Tm–P mean distance of 2.84(2) Å found in $Dtp_2Tm(tmbp)$.[11] The difference of 0.08 Å accounts for the lanthanide contraction of the ionic radius from Sm to Tm and is therefore in agreement with a similar electronic situation in **1** and in $Dtp_2Tm(tmbp)$. The C–C distance between the two phosphinine cycles is 1.439(10) Å and is very similar to the distance of the radical anionic free ligand of 1.440(2) Å.[18] Moreover, the PCCP torsion angle is 2° and testifies of a rather flat tmbp ligand in agreement with the presence of a radical anion delocalized over the entire ligand. These data taken together are in good agreement with a trivalent metal center and a reduced ligand that is, $Cp^*_2Sm(III)(tmbp^{\bullet -})$ for **1**.

On the other hand, in **2**, the Yb–P(1) and Y–P(2) distances are 2.872(2) Å and 2.938(2) Å, respectively, which feature a dissymmetrical coordination of the tmbp ligand. The PCCP torsion angle is 21°, that is rather large but lower than the

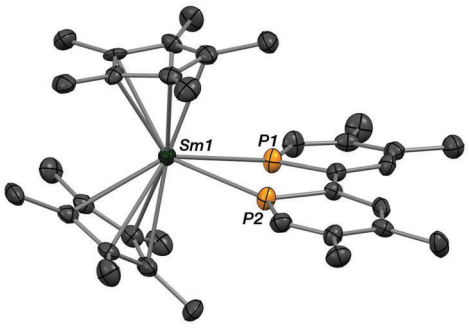

Fig. 1 ORTEP of $Cp^*_2Sm(tmbp)$. Carbon atoms are in grey and phosphorus atoms in orange. Thermal ellipsoids are represented at 50% level and hydrogen atoms are removed for clarity. Selected distances and angles: Sm–P(1), 2.909(2) Å, Sm–P(2), 2.927(2) Å; Sm–C(Cp*) (mean), 2.71(2) Å; Sm–Cp*(ctr), 2.42(1) Å; PCCP, 2°.

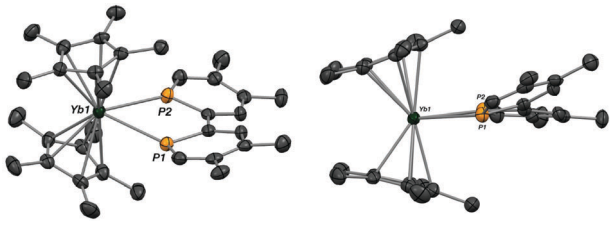

Fig. 2 ORTEP of $Cp^*_2Yb(tmbp)$. Carbon atoms are in grey and phosphorus atoms in orange. Thermal ellipsoids are represented at 50% level and hydrogen atoms are removed for clarity. Selected distances and angles: Yb–P(1), 2.872(2) Å; Y–P(2), 2.938(2) Å; Yb–Cp* (mean), 2.64(1) Å; Sm–Cp*(ctr), 2.36(1) Å; PCCP, 21°.

torsion angle of 46.6° reported by Le Floch for the cisoid neutral structure of tmbp.[18] This large angle as well as the dissymmetry observed in the P-atom coordination is interpreted as a difficulty to reduce the tmbp ligand. The Yb–P distances are large compare to that of the Dtp_2Tm(tmbp) complex (2.84(2) Å) (Table 1),[11] although Tm is the closest neighbor of Yb. The C–C distance between the two phosphinine cycles is 1.464(9) Å, very close to the distance obtained when bonded to the $Cr(CO)_4$ complex (1.471(5) Å) although it is rather smaller than in the free neutral cisoid tmbp ligand (1.490(8) Å).[18] Solid-state data are in agreement with a reduced tmbp ligand in the samarium case but not in the case of the ytterbium Cp^*_2Yb fragment. At first glance, it could make sense because Sm and Tm are much better reductants than ytterbium.[21] However, this is in contradiction with the redox potential of the first electron transfer of the tmbp ligand that is known to be higher than the one of the bipyridine ligand (−2.34 V *vs.* Fc^+/Fc compared to −2.62 *vs.* Fc^+/Fc for bipy). This means that the tmbp ligand is a better π-acceptor than the bipyridine ligand.[18] Following the redox potential only, the tmbp ligand should be reduced by Cp^*_2Yb. The result is therefore surprising. To some extent, this relates to the results that some of us reported in 2014 which concerned the non-reduction of a series of N-heterocycle ligands by the samarium fragment of the crowded tris-*tert*-butylcyclopentadienyl ligand (Cp^{ttt}_2Sm)[15] although the redox potential is the same than that of Cp^*_2Sm, that is capable of reducing pyridine.[22] In the latter work, a large steric hindrance of the Cp^{ttt}_2Sm fragment did not allow a close coordination of the N-heterocycle ligands and therefore did not favor electron transfer. In the case of the complex we present herein, the steric hindrance is not large. However, the torsion angle observed between the two phosphinine cycles in **2** is large and could therefore be at the origin of this result. In order to get insights in this new singularity, we turned to solution NMR and to theoretical calculations, the object of the next two paragraphs.

2.2. Solution NMR and effective moments

The solution analysis of the Cp^*_2Sm(tmbp) complex shows 5 peaks at room temperature in deuterated toluene in agreement with a C_{2v} symmetry. The resonance found at 2.83 ppm accounts for 30 protons and is attributed to the methyl resonance of the Cp* ligand. Its chemical shift is close to the expected diamagnetic chemical of Cp* (range from 1.8 to 1.9 ppm) and is in good agreement with a trivalent samarium nature being only weakly temperature independent paramagnetic in high temperature range.[23] The four other resonances are found at 185.8 ppm, 95.8 ppm, 17.1 ppm and −67.9 ppm in a 6 : 6 : 2 : 2 ratio and can be attributed to two methyl resonances and two aromatic proton resonances of the tmbp ligand. No phosphorus resonance has been detected in ^{31}P NMR in agreement with the presence of a paramagnetic center close to the phosphorus atoms. The large chemical shift of these resonances is in good agreement with the presence of a radical ligand and the principal contribution to the chemical shift is likely to be Fermi contact. Indeed very little dipolar contact contribution is expected from the samarium(III) center as shown by the slight shift of the methyl resonances of the Cp* ligands. The ^1H NMR spectrum is therefore in excellent agreement with the observations made in the solid-state and confirms the reduced nature of the tmbp ligand. The effective magnetic moment was measured by the Evans method in solution and is found to be 2.1 μ_B (0.55 cm^3 K mol^{-1}), in agreement with the presence of a samarium(III) (usually χT values range from 0.25 to 0.35 cm^3 K mol^{-1}) and a radical ligand (0.35 cm^3 K mol^{-1}). The magnetic data recorded in the solid state are close to those reported by Morris *et al.* for terpyridine complexes of samarium, complexes in which the same argument of a reduced ligand was made.[6] However, despite our efforts, the combustion analysis was not obtained for the Cp^*_2Sm(tmbp) complex and the value of the effective moment needs to be taken cautiously (see ESI†).

The ^1H NMR spectrum of the Cp^*_2Yb(tmbp) complex was recorded in deuterated toluene solution and shows 5 resonances as well in agreement with a C_2 symmetry in solution. In the solid state, the X-ray crystal structure exhibits a large torsion angle between the two phosphinine rings. However, in solution it is not possible to distinguish from an average C_{2v} symmetry or a C_2 symmetry. Therefore, it is not possible to tell if this bent structure is retained in solution. However, several points have to be noted. The resonances of the ligand appear only slightly shifted from their diamagnetic position, at 9.33 ppm (broad triplet), at 7.57 ppm, at 1.76 ppm and 0.73 ppm. This tends to show a very weak paramagnetism and therefore an intermediate valence situation, in which the n_f value (hole occupancy) is very small. The variable temperature data confirmed that these resonances are temperature dependent and have therefore a very small paramagnetic isotropic shift. Dissolving the Cp^*_2Yb(tmbp) complex in thf-d_8 at the same temperature leads to the immediate displacement of the tmbp ligand and to the formation of the divalent $Cp^*_2Yb(thf)_2$ complex. This allow us to estimate the paramagnetic isotropic shift for Cp^*_2Yb(tmbp) by subtracting the values obtained in toluene and in thf ($\delta^{para} = \delta^{obs} - \delta^{dia}$). The values of 0.88 ppm and 0.42 ppm for the protons and 0.66 ppm and 1.69 ppm for the methyl groups have been obtained. These very small isotropic shifts are to be compared to those found in the $Cp^*_2Yb(3,3'\text{-}Me_2bipy)$[14] and **2** is likely to exhibit a similar electronic structure that is an intermediate-valent situation with a large contribution of the divalent resonance structure. In the later complex, the redox potential is getting decreased upon methyl substitution on the 3,3′ position of the bipy and this induces such an electronic structure with a very small n_f.[14] On the other hand, when the bipyridine possesses methyl positions in the 6,6′ positions, the n_f value of the Cp^*_2Yb adduct is also very small. In this case the proximity between the methyl groups and the metal center increases significantly the Yb–N distances, which disadvantages the electron transfer.[15]

In our case, the redox potential is higher for the tmbp ligand than for the bipyridine ligand (−2.34 V *vs.* Fc^+/Fc compared to −2.62 *vs.* Fc^+/Fc for bipy), which shows that the redox potential of the ligand itself is probably not the reason of the situation found in Cp^*_2Yb(tmbp) (**2**). The fact that Cp^*_2Sm(tmbp) (**1**) exhibits a reduced ligand tends to show that steric hindrance seems not to affect too much the reduction of the ligand

although samarium is larger than ytterbium but reduction with the smaller thulium ionic radius has precedents.[11] Therefore, the fact that ytterbium is not a better reducer than Sm and Tm is therefore likely to better explain the situation. The beginning of an answer is probably lying in the dissymmetry observed in the Yb–P distances of $Cp^*_2Yb(tmbp)$ (2.872(2) Å and 2.938(2) Å, for Yb–P(1) and Yb–P(2), respectively). The PCCP torsion angle formed by the tmbp ligand does not allow a symmetrical coordination and this should affect the mechanism of the electron transfer. In the case of a symmetrical structure, the electron is transferred in the LUMO of the bipyridine that is delocalized on the entire ligand. In our case, the orientation of the lone pairs of the phosphorus that will accept the electron are not likely to be both well oriented in order to both accept electron from the metal center. This dissymmetry created by the large PCCP torsion angle is likely to modify greatly the local redox potential. In such a situation the metal must have the redox potential for the reduction of one phosphinine cycle only. If true, this situation would explain why the ytterbium complex has such a large contribution of its divalent structure and why samarium and thulium complexes are able to reduce the ligand. Once reduced, the energy of the ligand reorganizes and this leads to a symmetrical planar ligand. In order to have more insights in the nature of this electron transfer and on the electronic structure of the two complexes, we decided to perform a theoretical analysis that is described in the next paragraph.

2.3. Theoretical calculations

The calculations were first investigated at the DFT level. In the crystallographic structures, only few packing interactions were found. Therefore, the crystal structures were used as a starting point for the geometry optimization. In our hands, the geometry optimization was found to be not trivial. The reason for such a difficulty that was not expected may come from the singular electronic structure discussed in previous paragraphs and led us to complete the analysis by the use of several methods. The reproducibility of the PCCP torsion angle of the tmbp ligand in both **1** and **2** (*i.e.*, 1.7° for **1** and 21.4° for **2**) with the same couple of functional and basis set was not possible. The Tables 2 and 3 present the geometrical parameters of the calculated geometry of **2** and **1**, respectively, obtained from using the GGA functional PBE with the D3 dispersion correction. The scalar relativistic effects have been taken into account by using the ZORA Hamiltonian.

The problem lies in the reproduction of the torsion angle PCCP. The calculations do not reproduce the situation found in the crystal structure since this angle is small in **1** and large in **2** as they are both large in the theoretical calculations. Of course, this problem can have a large impact on the electronic structure of the molecule since a flat PCCP angle would allow a better electron transfer. However, the potential energy surface is almost flat for both complexes since the energy difference between an angle of 0° and an angle of 30° is only about 1 kcal mol^{-1} (see Fig. S5, ESI†). These results explain why the optimization of this molecule is not trivial and why the PCCP and the Ln–P distances are easily modified. The other couples of functional and basis set that have been tested led to a similar behaviour of the potential energy surface and problematic geometry optimizations. This also indicates that the symmetry in solution is likely to be C_{2v} since the rotation of the two phosphinines ring seems easily allowed. Yet, it does not explain why the tmpb ligand is reduced in **1** and not in **2**.

Using the PBE-D3 optimized geometry, further calculations were performed at the B3LYP-D3/TZ2P level in order to elucidate the electronic structure differences between the two complexes. The decomposition analysis of the binding energy between the lanthanide center and the ligands points out a large difference of the total bonding energy from Yb (−542 kcal mol^{-1}) to Sm (−854 kcal mol^{-1}) (see Table 4). Incontestably, this difference comes mainly from orbital interactions and the ratio between orbital and electrostatic contributions is twice higher for Sm. Similar conclusions can be drawn by looking at the HOMO of the complexes (Fig. 3). The HOMO of the Yb complex corresponds to a large contribution of 4f orbitals (82%) while the one for the Sm complex is a clear mixing of 4f (40%) and ligand orbitals. From these orbitals, it is clear that the samarium extents well the 4f orbitals and combines them with the LUMO of the tmbp that is of b_1 symmetry (in C_{2v}) (large coefficients on the lone pairs of the P atom). In this picture, because the small torsion angle is not reproduced (26.8°), it is clearly seen that the allowance of such a combination between the ligand orbitals and the metal f orbitals necessary implies a large extension of the 4f orbital in order to accommodate the misdirection of the lone pairs of the P atoms. To push further this model, topological analyses have been performed.

Table 2 Metric parameters for **2** (calculated, PBE-D3/ZORA *vs.* experimental)

Angle (°)/distance (Å)	DFT	X-ray
PCCP	26.8	21
Yb–P	2.91	2.872(2)
	2.9	2.938(2)
Yb–Cp*(ctr)	2.35(5)	2.36(1)

Table 3 Metric parameters for **1** (calculated, PBE-D3/ZORA *vs.* experimental)

Angle (°)/distance (Å)	DFT	X-ray
PCCP	23.8	1.9
Sm–P	2.95	2.919(2)
	2.97	2.927(2)
Sm–Cp*(ctr)	2.45(5)	2.42(1)

Table 4 B3LYP-D3/TZ2P energy decomposition analysis of the $Cp^*_2Yb(tmbp)$ and $Cp^*_2Yb(tmbp)$ complexes with respect to Yb/Sm, Cp* and tmbp fragments. The % Orb corresponds to the ratio between orbital interactions and the sum of electrostatic plus orbital interactions

EDA (kcal mol^{-1})	Yb	Sm
Pauli repulsion	208.08	226.42
Electrostatic	−533.46	−502.22
Orbital interactions	−179.27	−545.85
Dispersion	−37.09	−32.72
Total bonding energy	−541.75	−854.36
% Orb	25.2	52.1

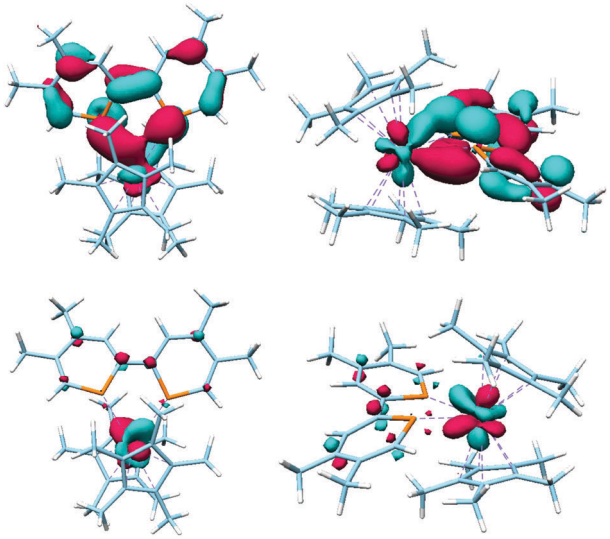

Fig. 3 Two views of the HOMO orbitals of $Cp^*_2Sm(tmbp)$ (**1**) (top) and $Cp^*_2Yb(tmbp)$ (**2**) (bottom).

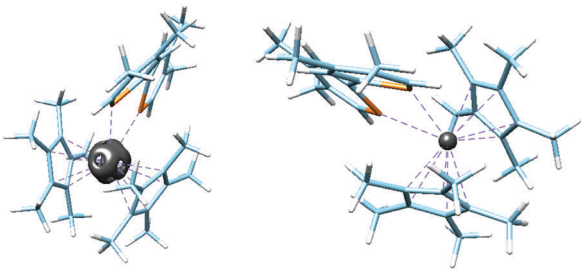

Fig. 4 ELF topologic analysis of $Cp^*_2Sm(tmbp)$ (**1**) (left) and $Cp^*_2Yb(tmbp)$ (right) (**2**).

The ELF analysis provides a localized picture of the electron pairs, especially localization valence domains between two atoms.[24] We pay attention to the disynaptic domains around the lanthanide center (Fig. 4). In both complexes, disynaptic basins exist between the lanthanide and P and/or C atoms. However, only a large deformation of Sm valence basins is observed. Furthermore, the number of electrons present in these basins are different, *i.e.* 7.1 for the Sm complex and 5.1 for the Yb one. These results are in agreement with the energetic and orbital analyses that highlight a stronger interaction in the Sm complex.

As expected, the CASSCF calculations indicate that the valence in the ytterbium complex **2** is intermediate, although a very large contribution of 97% after renormalization of the divalent (close-shell singlet) nature of the metal center was computed. This fits well the experimental data that indicated a low paramagnetism at room temperature and metrical parameters in agreement with a neutral tmbp and divalent ytterbium.

3. Conclusions

In conclusion, we reported the synthesis of two new complexes of tmbp with decamethylsamarocene and decamethylytterbocene. Both compounds have been characterized by X-ray diffraction and by solution NMR spectroscopy. These data are in agreement with a picture in which the tmbp is reduced by the samarium fragment while it is not (or very little) reduced with the ytterbium fragment. This comes as a singularity since tmbp is more easily reduced than bipyridine and the ytterbium fragment is known to reduce bipyridine. In order to better understand this problem, theoretical calculations have been performed at the DFT level. The difficulty in the reproduction of the solid-state geometry of **1** in the gas phase lies in a very flat potential energy surface between two configurations: a flat tmbp ligand (PCCP is close to zero) and a torqued tmbp ligand (PCCP is above 20°). However, these geometric arguments allow the better understanding of both electronic structures. (i) In the samarium complex significant orbital interactions are built with the ligand, which allows an overlap with both P lone pairs; the electron is transferred, the tmbp ligand becomes flat. (ii) In the ytterbium complex, less orbital interactions are noted and the dissymmetric coordination of the tmbp ligand with a large PCCP angle modifies locally the redox potential of the tmbp ligand, the electron principally remains on the metal center, the ligand remains torqued. Topological analyses confirmed this point. This work comes to the conclusion that the electron transfer in lanthanide complexes is not a trivial problem. Both electronic and steric contributions are involved and it is somewhat difficult to separate both in an easy way. Moreover, it challenges the net redox potentials that are given from electrochemistry for the free ligand and the metallic fragments: in a previous work, although the redox potential of two metallic fragments were similar, one of them only was reducing pyridine; in this work although Cp^*_2Yb fragment reduce bipyridine, it does not reduced tmbp, a better π-accepting ligand.

4. Experimental section

4.1. General considerations

All reactions were performed using standard Schlenk-line techniques or in a drybox (MBraun). All glassware was dried at 130 °C for at least 12 h prior to use. Toluene, pentane and diethyl ether were dried over sodium. Toluene-d_8 was dried over sodium while thf-d_8 was dried and stored over molecular sieves. All the solvents were degassed prior to use. ^{1}H NMR spectra were recorded on Bruker Avance II or III-300 MHz. ^{1}H chemical shifts are in ppm relative to TMS. Magnetic susceptibility measurements were made for all samples at 1, 5 and 40 kOe in a 7 T Cryogenic SX600 SQUID magnetometer. Sample containment and other experimental details have been described previously.[25] Diamagnetic corrections were made using Pascal's constants. The tetramethyl-2,2′-biphosphinine (tmbp) ligand was sublimed before use and the $Cp^*_2Sm(OEt_2)$ and $Cp^*_2Yb(OEt_2)$ complexes were synthetized according published procedures.[19]

4.2. X-ray

Single crystals of $Cp^*_2Sm(tmbp)$ (**1**) and $Cp^*_2Yb(tmbp)$ (**2**), were mounted on a kapton loop using Paratone® oil and cooled to

150 K in a nitrogen stream for X-ray structure determination. The loop was transferred to a Nonius Kappa diffractometer using Mo K_α (λ = 0.71073 Å) X-ray source, a graphite monochromator and a Brucker APEX-II detector. Preliminary orientation matrixes and cell constants were determined by collection of 10 s frames, followed by spot integration and least-squares refinement. Data were integrated and corrected for Lorentz and polarization effects. The crystal structures were solved using SHELXS and refined in SHELXL-97[26] by full-matrix least-squares using anisotropic thermal displacement parameters for all non-hydrogen atoms. All hydrogen atoms were placed at geometrically calculated positions. ORTEP drawings were produced using Mercury. CCDC 1452180 (**1**) and 1452181 (**2**).

4.3. Syntheses

Synthesis of $Cp^*_2Sm(tmbp)$ (1). A toluene solution (2 mL) of previously sublimed tmbp ligand (35 mg, 0.143 mmol) was added to a toluene solution (1 mL) of $Cp^*_2Sm(OEt_2)$ (71 mg, 0.143 mmol), yielding a dark brown solution. After the solution was stirred for 2 h, pentane (3 mL) was added to the solution and the mixture was let stand −40 °C yielding to the crystallization of dark brown X-ray suitable crystals. 71 mg (75%) of these crystals were collected by filtration and were dried under reduced pressure. ^{1}H NMR (δ, 295 K, toluene-d_8) 185.8 (6H, s, Me, tmbp), 95.8 (6H, s, Me, tmbp), 17.06 (2H, s, tmbp), 2.83 (30H, Cp*), −67.9 (2H, s, tmbp). No signals observed in ^{31}P NMR (δ, 295 K, toluene-d_8). No combustion analysis has been obtained despite several attempts.

Synthesis of $Cp^*_2Yb(tmbp)$ (2). A toluene solution (2 mL) of previously sublimed tmbp ligand (45 mg, 0.182 mmol) was added to a toluene solution (1 mL) of $Cp^*_2Yb(OEt_2)$ (94 mg, 0.182 mmol), yielding a dark brown solution. After the solution was stirred for 15 min, the solution was let stand at room temperature yielding to the crystallization of dark brown X-ray suitable needles. 101 mg (81%) of these crystals were collected by filtration and were dried under reduced pressure. ^{1}H NMR (δ, 295 K, toluene-d_8) 9.33 (2H, broad t, J_{PH} = 18 Hz, tmbp), 7.57 (2H, s, tmbp), 2.12 (30H, Me, Cp*), 1.76 (6H, Me, tmbp), 0.73 (6H, Me, tmbp). ^{31}P NMR (δ, 295 K, thf-d_8) 191.6 ppm (s). ^{1}H NMR (δ, 295 K, thf-d_8) 8.45 (q, 2H, AA′XX′, $(^2J_{P(1),H} + {}^5J_{P(2),H})$ = 39 Hz, free tmbp, $H_{6,6'}$), 7.15 (2H, massif, free tmbp, $H_{3,3'}$), 2.42 (12H, Me, free tmbp), 1.86 (30H, s, Cp* of $Cp^*_2Yb(thf)_2$). ^{31}P NMR (δ, 295 K, toluene-d_8) 178.2 ppm (s, free tmbp). No combustion analysis has been obtained despite several attempts.

4.4. Calculations

The geometries of the complexes were optimized at the DFT level of theory using PBE density functional (Perdew–Burke–Ernzerhof functional) associated to dispersion corrections in the D3 framework proposed by Grimme[27,28] and double zeta DZ basis sets. Scalar relativistic effects were taken into account using the zero-order regular approximation (ZORA).[29] Using the PBE-D3 optimized geometries, energy decomposition analysis (EDA)[30] and bonding properties were obtained at the B3LYP-D3/TZ2P level. These calculations have been performed with the ADF2014 program package.[31] Topology analyses were performed from the electron localization function (ELF) to provide a spatial localization of electron pairs from the B3LYP-D3 ADF results with the DGrid 4.6 program package.[32] Complete active space SCF (CASSCF) calculations were carried out using the SCF orbitals with the MOLPRO 2010.1 package.[33] Various active spaces were used to distribute 4f electrons in 4f orbitals and π^* orbitals of tmbp.

Acknowledgements

We thank CNRS, Ecole polytechnique and the French National Research Agency, ANR, for funding (grant #, ANR-15-CE29-0019). Dr Nicolas Mézailles is thanked gratefully for providing us the tmbp ligand. We thank Xavier Le Goff for help in recording the crystal structure of **2**. AJ is grateful to Ecole polytechnique for PhD fellowship. This work was granted access to the HPC resources of CINES and IDRIS under the allocation X2015086830 made by GENCI.

References

1 G. Nocton, W. L. Lukens, C. H. Booth, S. S. Rozenel, S. A. Melding, L. Maron and R. A. Andersen, *J. Am. Chem. Soc.*, 2014, **136**, 8626–8641.
2 C. H. Booth, M. D. Walter, D. Kazhdan, Y.-J. Hu, W. W. Lukens, E. D. Bauer, L. Maron, O. Eisenstein and R. A. Andersen, *J. Am. Chem. Soc.*, 2009, **131**, 6480–6491.
3 C. H. Booth, D. Kazhdan, E. L. Werkema, M. D. Walter, W. W. Lukens, E. D. Bauer, Y.-J. Hu, L. Maron, O. Eisenstein, M. Head-Gordon and R. A. Andersen, *J. Am. Chem. Soc.*, 2010, **132**, 17537–17549.
4 A. A. Trifonov, E. A. Fedorova, V. N. Ikorskii, S. Dechert, H. Schumann and M. N. Bochkarev, *Eur. J. Inorg. Chem.*, 2005, 2812–2818.
5 A. A. Trifonov, E. A. Fedorova, G. K. Fukin, N. O. Druzhkov and M. N. Bochkarev, *Angew. Chem., Int. Ed.*, 2004, **43**, 5045–5048.
6 J. M. Veauthier, E. J. Schelter, C. N. Carlson, B. L. Scott, R. E. Da Re, J. D. Thompson, J. L. Kiplinger, D. E. Morris and K. D. John, *Inorg. Chem.*, 2008, **47**, 5841–5849.
7 E. J. Schelter, R. Wu, J. M. Veauthier, E. D. Bauer, C. H. Booth, R. K. Thomson, C. R. Graves, K. D. John, B. L. Scott, J. D. Thompson, D. E. Morris and J. L. Kiplinger, *Inorg. Chem.*, 2010, **49**, 1995–2007.
8 C. J. Kuehl, R. E. Da Re, B. L. Scott, D. E. Morris and K. D. John, *Chem. Commun.*, 2003, 2336–2337.
9 R. E. Da Re, C. J. Kuehl, M. G. Brown, R. C. Rocha, E. D. Bauer, K. D. John, D. E. Morris, A. P. Shreve and J. L. Sarrao, *Inorg. Chem.*, 2003, **42**, 5551–5559.
10 C. N. Carlson, C. J. Kuehl, R. E. Da Re, J. M. Veauthier, E. J. Schelter, A. E. Milligan, B. L. Scott, E. D. Bauer, J. D. Thompson, D. E. Morris and K. D. John, *J. Am. Chem. Soc.*, 2006, **128**, 7230–7241.
11 L. Jacquot, M. Xémard, C. Clavaguéra and G. Nocton, *Organometallics*, 2014, **33**, 4100–4106.

12 M. Schultz, J. M. Boncella, D. J. Berg, T. D. Tilley and R. A. Andersen, *Organometallics*, 2002, **21**, 460–472.
13 G. Nocton and L. Ricard, *Chem. Commun.*, 2015, **51**, 3578–3581.
14 G. Nocton, C. H. Booth, L. Maron and R. A. Andersen, *Organometallics*, 2013, **32**, 5305–5312.
15 G. Nocton and L. Ricard, *Dalton Trans.*, 2014, **43**, 4380–4387.
16 S. Labouille, C. Clavaguera and F. Nief, *Organometallics*, 2013, **32**, 1265–1271.
17 P. Le Floch, D. Carmichael, L. Ricard and F. Mathey, *J. Am. Chem. Soc.*, 1991, **113**, 667–669.
18 P. Le Floch, D. Carmichael, L. Ricard, F. Mathey, A. Jutand and C. Amatore, *Organometallics*, 1992, **11**, 2475–2479.
19 T. D. Tilley, R. A. Andersen, B. Spencer, H. Ruben, A. Zalkin and D. H. Templeton, *Inorg. Chem.*, 1980, **19**, 2999–3003.
20 W. J. Evans, I. Bloom, W. E. Hunter and J. L. Atwood, *J. Am. Chem. Soc.*, 1981, **103**, 6507–6508.
21 W. J. Evans, *Inorg. Chem.*, 2007, **46**, 3435–3449.
22 S. Labouille, F. Nief, X.-F. Le Goff, L. Maron, D. R. Kindra, H. L. Houghton, J. W. Ziler and W. J. Evans, *Organometallics*, 2012, **31**, 5196–5203.
23 O. Kahn, *Molecular Magnetism*, John Wiley & Sons, 1993.
24 A. D. Becke and K. E. Edgecombe, *J. Chem. Phys.*, 1990, **92**, 5397–5403.
25 M. D. Walter, M. Schultz and R. A. Andersen, *New J. Chem.*, 2006, **30**, 238–246.
26 G. Sheldrick, *Acta Crystallogr., Sect. A: Found. Crystallogr.*, 2008, **64**, 112–122.
27 S. Grimme, *J. Comput. Chem.*, 2004, **25**, 1463–1473.
28 S. Grimme, J. Antony, S. Ehrlich and H. Krieg, *J. Chem. Phys.*, 2010, **132**, 154104.
29 M. Filatov and D. Cremer, *Mol. Phys.*, 2003, **101**, 2295–2302.
30 K. Morokuma, *Acc. Chem. Res.*, 1977, **10**, 294–300; T. Ziegler and A. Rauk, *Inorg. Chem.*, 1979, **18**, 1755–1759.
31 ADF2014, Theoretical Chemistry, Vrije Universiteit, Amsterdam, The Netherlands, http://www.scm.com, 2014.
32 M. Kohout, *version 4.6*, Radebeul, 2011.
33 H.-J. Werner, P. J. Knowles, G. Knizia, F. R. Manby and M. Schütz, *Wiley Interdiscip. Rev.: Comput. Mol. Sci.*, 2012, **2**, 242–253.

This comparison has given a clear picture of the bonding trend between two lanthanides, samarium and ytterbium. Yet, if ytterbium molecules are behaving in an ionic way, the differences between ytterbium and lutetium should be insignificant. But, the latter activate the C — H bonds of methane while the former does not. In order, to understand in what ways these two elements behave differently, a complete study involving DFT and CASSCF calculations has been undertaken on Cp^*_2YbMe.

1.4.2 Comparison of lutetium and ytterbium complexes towards C-H activation

Early transition metals and lanthanides have been successful in performing C-H bond activations. It is the case for example of yttrium[132], scandium[133] or lutetium[134–137]. These metals are known to activate methane under mild conditions.

These molecules have been a topic of interest for computational chemists trying to elucidate what the actual mechanism of the methane activation reaction was. Two types of mechanism can be possible[138]: one is the normal three center σ bond methatesis, and the other passes through a tuck-in complex[139,140] (Figure 1.3). In this context, the group of Cramer has been studying both mechanisms with DFT. Their results show that the tuck-in situation is unlikely –except in the case of scandium where the two mechanisms are in competition– and that the mechanism involves a σ bond metathesis, with a three center transition state.

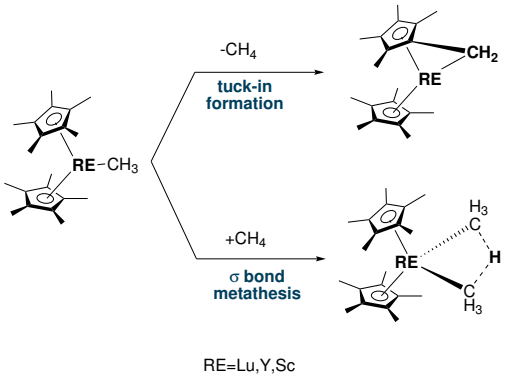

Figure 1.3: Two different types of mechanisms for the C-H activation for group 3 complexes RE=Lu,Y,Sc as detailled by Cramer *et al*[139,140]

C-H activation has also been attempted with lanthanide complexes. Cerium is known to activate C-H bonds[141] and samarium has been investigated successfully as well[142]. On the other hand complexes of ytterbium decomposes very easily without performing C-H bond activation[143]. Study on non-solvated complexes has been undergone by Andersen *et al* and, even if no decomposition occurred, no activation of methane was observed for Cp^*_2YbMe.

A quantum chemistry comparison between the different lanthanides and scandium and yttrium was done by the group of Eisenstein[89]. They concluded that the ionic radii size of the metal has an influence in the activation barrier of the reaction: the more important the size, the less important the activation energy is. One question remains: if the size of the ionic radii at stake is the only consideration, how to explain the fact that the ytterbium complex does not enable a C-H activation? In order to answer these questions, an in depth analysis and comparison of the C-H activation in the case of lutetium and ytterbium was done using the quantum chemistry tool.

1.4.2.1 Reaction mechanisms investigation

In the literature, attempts have been made to study the equilibrium by means of DFT[89,139,140]. The reported activation energy was identical for ytterbium and lutetium. The calculations were performed without the use of the whole Cp* molecule, instead preferring the smaller Cp molecule; moreover, the calculation used a small basis set (6-31G*), and a LC-ECP (avoiding the explicit treatment of the 4f electrons). In light of these concerns, an all-electron DFT study was performed using different density functionals.

In order to access the activation barrier, the distance $(CH_3)C-H(CH_4)$ inside the $Cp^*_2Ln(CH_3)(CH_4)$ molecule was varied from 2.52 to 1.11 Å. The graphs presented in Figure 1.4 give the variation of the energy following the C-H distance in the ytterbium complex. The same concept was applied to the lutetium complex and the results are presented in Figure 1.5.

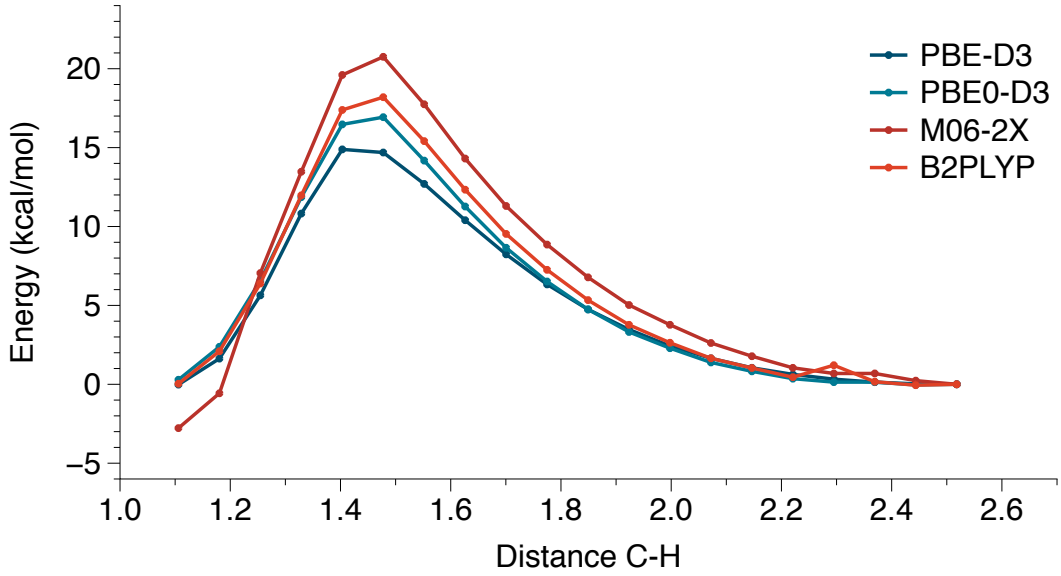

Figure 1.4: Energy depending on the distance $(CH_3)C-H(CH_4)$ in the complex $Cp^*_2Yb(CH_3)(CH_4)$; geometry optimisation was performed in the PBE-D3(BJ)/SVP and single point evaluations were performed using B2PLYP, M06-2X and PBE0-D3 functionals

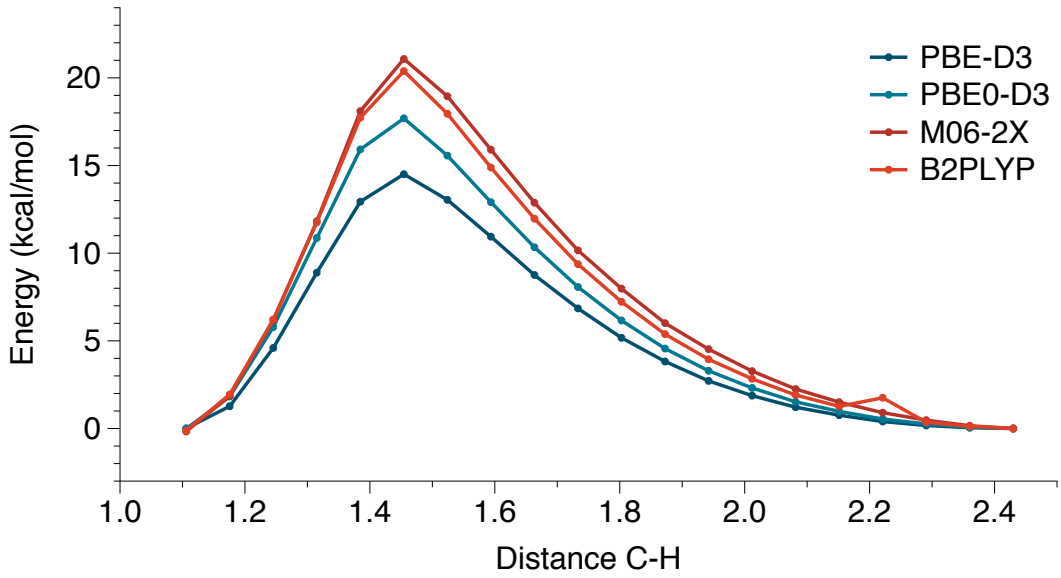

Figure 1.5: Energy depending on the distance $(CH_3)C-H(CH_4)$ in the complex $Cp^*_2Lu(CH_3)(CH_4)$; geometry optimisation was performed in the PBE-D3(BJ)/SVP and single point evaluations were performed using B2PLYP, M06-2X and PBE0-D3 functionals

The results are pretty similar in shape for the two complexes. The barrier is estimated between 14 and 21 kcal/mol depending on the density functional, which is similar to what was previously reported by Eisenstein *et al* for lutetium (20 kcal/mol). Using *ab initio*

calculations resulted in the same activation energy for both ytterbium and lutetium complexes (20 kcal/mol). Experimentally, the ytterbium complex does not undergo C-H activation while the lutetium compound does. This means that one effect is not taken into consideration during DFT or *ab initio* calculations. Cramer *et al* pointed out for lutetium that DFT could not evaluate properly the energy difference because of tunnelling effect[139,140]. However, considering the position in the periodic table of both ytterbium and lutetium, and the fact that in their trivalent state they have similar properties, the tunnelling effect difference between both compounds should not be significant.

1.4.2.2 Electronic structure of the methyl complex

Ytterbium ion is either $4f^{14}$ in its divalent state or $4f^{13}$ in its trivalent state. On the other hand, lutetium does not have a stable divalent state and is only stable in its trivalent state of electronic configuration $5d^{0}$. This difference could lead to mechanistic difference between $Cp^*_2Yb(CH_3)$ and $Cp^*_2Lu(CH_3)$, where the ytterbium ion might favour a radical pathway, while the lutetium one a proton transfer. DFT calculations are known to only favour the proton transfer type mechanism and methods based on the single-reference HF wave-function might not evaluate correctly the electronic structure of the ytterbium complex itself. The spin density of $Cp^*_2Yb(CH_3)$ was calculated using three different levels of theory (PBE-D3 and PBE0-D3 ZORA3 and HF DKH2) on the optimised geometry (PBE-D3). The results are presented in table 1.2.

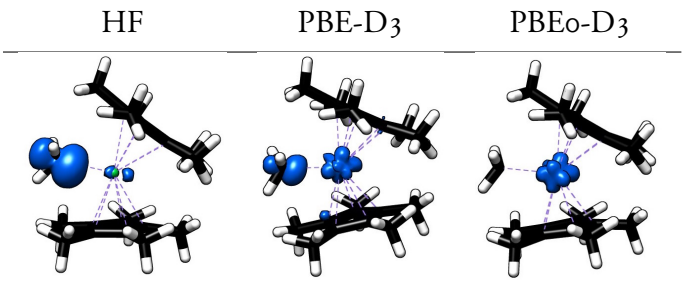

Table 1.2: Spin density of $Cp^*_2Yb(CH_3)$ at the PBE-D3 and PBE0-D3 ZORA3 and HF DKH2 level

Depending on the level of theory used, the spin density is passing from the lanthanide to the methyl group, which could be the result of a multi-configurational ground state. Indeed, Evans presented the decomposition of $Cp^*_2Yb(Me)(thf)$ at high temperature into

$Cp^*_2Yb(thf)_2$ and ethane[143]. Even if to the best of our knowledge the mechanism of the reaction is unknown, the methyl groups are acting as if they were radical moieties.

The electronic structure of this compound was explored using CASSCF. In order to select the orbitals to include in the active space, a decomposition of the interaction for this complex was done. The interaction between the 4f orbitals of the ytterbium and the p orbitals of the carbon atoms from the methyl groups is small, as the overlap between these orbitals is negligible. On the other hand, the 5d orbitals should have the right symmetry in order to get a favorable overlap with the p orbitals of the methyl group.

The CASSCF calculations were undertaken starting from the ROHF molecular orbital, or from the UHF natural orbital. Both starting orbitals led to the same results. The "perfect" active space for this system would include the lanthanide orbitals 4f, 5d, 6s and 6p, and the methyl orbitals σ, p_x and σ^*. This is indeed a too large active space that would include 23 orbitals and 19 electrons. As such, the choice of a proper active space is not easy. That is why different active space were used and summarised in table 1.3.

Electrons	Orbitals	Description of the orbitals	wave-function
15	8	p_x + 4f	Methyl radical
19	12	p_x + 4f + σ +σ^*	Methyl radical
15	13	p_x + 4f + 5d	Methyl radical
15	14	p_x + 4f + 5d + 6s	Methyl radical
21	16	p_x + 4f + 5p + 5d	Methyl radical

Table 1.3: Different active spaces used to calculate the electronic structure of Cp^*_2YbMe

The active space was varied from 8 to 16 orbitals without significant difference between the resulting electronic structure for the complex: $4f^{14}p^0_x$. The behaviour for ytterbium to prefer the $4f^{14}$ state while in a coordination mode with a methyl carbene was already observed theoretically in the more specific example of $Yb = CH_2$. While studying double bond for the whole series of rare earth, Pyykkö and Roos found[144] that it was not possible to get a double bond between ytterbium and CH_2 as ytterbium would prefer to keep the configuration $4f^{14}$ instead of creating a double bond with the carbon moiety.

Ytterbium is thus very particular in that matter, as it would prefer to have an entire 4f shell filled: this means that upon reduction of a ligand, *i.e.* the lanthanide being $4f^{13}$, the

possibility to come back to $4f^{14}$ is close in energy. This type of electronic structure will not be the same for lutetium, as lutetium +III electronic configuration is $4f^{14}6s^{0}5d^{0}$. Which means that the 4f shell is already filled, and there is no possibility to create a methyl radical.

Hence, there are two different pathways for the C-H activation between lutetium and ytterbium. Ytterbium C-H activation pattern should pass through a radical mechanism, while lutetium C-H activation pathway is passing through a proton transfer. Indeed, the presence of a radical on the methyl group could induce side reaction such as the formation of ethane, which could compete with the radical C-H activation mechanism. The activation energies for the two different mechanisms were calculated using DFT, and restraining the electronic configuration of ytterbium and lutetium using large core ECP, *i.e.* with the 14 4f electrons inside the core of the pseudopotential. The results are presented in table 1.4.

Activation energy (kcal/mol)	$Cp^*_2Yb(CH_3)$	$Cp^*_2Lu(CH_3)$
PBE-D3	21	16
PBE0-D3	24	19
M06-2X	24	21

Table 1.4: Activation energy (kcal/mol) using the PBE-D3, PBE0-D3, M06-2X density functionals

The activation energy is less important in the case of the lutetium complex than in the case of the ytterbium one, which could explain why ytterbium complexes do not activate C-H bonds of methane while lutetium ones do. For completeness, the tuck-in mechanism was also studied, but led to much higher activation energy for ytterbium, in agreement with previous results[139,140]. Experiments could be carried out in order to prove that the ytterbium complex is indeed involving a radical instead of a Yb^{III}. First of all, electrochemistry could give some insight into the electronic structure of the compound. Then, the starting material ($Cp^*_2Yb-Me-YbCp^*_2$) could be mixed with a free radical such as tempo to see if the radical attacks the methyl or the lanthanide itself.

1.4.3 Partial conclusion

In conclusion, the behaviour of samarium and ytterbium compounds is very complex. On one side, samarium molecules reduce easily organic molecules, and create strong interactions

with them. On the other side, ytterbium complexes can reduce molecules (such as phenanthroline[145], or bipyridine[85]) but the inner interaction between the lanthanide and the organic moiety is weak. Moreover, the presence of its divalent state very close in energy from its trivalent state, can trigger interesting reactivity at the ytterbium center, and further decrease the availability of the electron transferred for further reactivity (such as C-H activation). As a result ytterbium, because its Yb^{+II} form is stable, could be very useful as an electron donor. Depending on the reaction conditions, it could behave either as an Yb^{+III} with an electron transferred to the ligand or an Yb^{+II} and a neutral ligand. This behaviour could be useful in catalytic reactions where electrons are often needed on demand. Samarium could enable new radical processes. As the orbital interaction with the ligand is important, playing on the ligand orbital, *e.g.* enabling competitions between two radical species, could unleash specific reactivity that is not yet discovered. On the other side, it could be potentially useful to trigger the decoordination of the ligand itself in order to study its involvement in the bonding.

Finally, these two examples showed that there is a need for finding the right methodology for treating lanthanide complexes using quantum chemistry. In order to do that, phenanthroline complexes of samarium and ytterbium will be compared to computational quantum chemistry data, and the accuracy of different functionals will then be assessed. This will be useful to study lanthanide complexes reactivity.

References

[1] E. G. Lewars, *Computational Chemistry*, Springer, **2016**.

[2] M. Dolg, *Computational Methods in Lanthanide and Actinide Chemistry*, John Wiley & Sons, **2015**.

[3] M. Dolg, X. Cao, *Chem. Rev.* **2012**, *112*, 403–480.

[4] D. A. Pantazis, F. Neese, *J. Chem. Theory Comput.* **2009**, *5*, 2229–2238.

[5] F. Neese, *WIREs Comput. Mol. Sci.* **2011**, *2*, 73–78.

[6] F. Furche, R. Ahlrichs, C. Hättig, W. Klopper, M. Sierka, F. Weigend, *WIREs Comput. Mol. Sci.* **2013**, *4*, 91–100.

[7] F. Aquilante, J. Autschbach, R. K. Carlson, L. F. Chibotaru, M. G. Delcey, L. De Vico, I. F. Galván, N. Ferré, L. M. Frutos, L. Gagliardi, M. Garavelli, A. Giussani, C. E. Hoyer, G. L. Manni, H. Lischka, D. Ma, P. Å. Malmqvist, T. Müller, A. Nenov, M. Olivucci, T. B. Pedersen, D. Peng, F. Plasser, B. Pritchard, M. Reiher, I. Rivalta, I. Schapiro, J. Segarra-Martí, M. Stenrup, D. G. Truhlar, L. Ungur, A. Valentini, S. Vancoillie, V. Veryazov, V. P. Vysotskiy, O. Weingart, F. Zapata, R. Lindh, *J. Comput. Chem.* **2016**, *37*, 506–541.

[8] G. te Velde, F. M. Bickelhaupt, E. J. Baerends, C. Fonseca Guerra, S. J. A. Van Gisbergen, J. G. Snidjers, T. Ziegler, *J. Comput. Chem.* **2001**, *22*, 931–967.

[9] Y. Shao, Z. Gan, E. Epifanovsky, A. T. B. Gilbert, M. Wormit, J. Kussmann, A. W. Lange, A. Behn, J. Deng, X. Feng, D. Ghosh, M. Goldey, P. R. Horn, L. D. Jacobson, I. Kaliman, R. Z. Khaliullin, T. Kuś, A. Landau, J. Liu, E. I. Proynov, Y. M. Rhee, R. M. Richard, M. A. Rohrdanz, R. P. Steele, E. J. Sundstrom, H. L. Woodcock III, P. M. Zimmerman, D. Zuev, B. Albrecht, E. Alguire, B. Austin, G. J. O. Beran, Y. A. Bernard, E. Berquist, K. Brandhorst, K. B. Bravaya, S. T. Brown, D. Casanova, C.-M. Chang, Y. Chen, S. H. Chien, K. D. Closser, D. L. Crittenden, M. Diedenhofen, R. A. DiStasio Jr., H. Do, A. D. Dutoi, R. G. Edgar, S. Fatehi, L. Fusti-Molnar, A. Ghysels, A. Golubeva-Zadorozhnaya, J. Gomes, M. W. D. Hanson-Heine, P. H. P. Harbach, A. W. Hauser, E. G. Hohenstein, Z. C. Holden, T.-C. Jagau, H. Ji, B. Kaduk, K. Khistyaev, J. Kim, J. Kim, R. A. King, P. Klunzinger, D. Kosenkov, T. Kowalczyk, C. M. Krauter, K. U. Lao, A. D. Laurent, K. V. Lawler, S. V. Levchenko, C. Y. Lin, F. Liu, E. Livshits, R. C. Lochan, A. Luenser, P. Manohar, S. F. Manzer, S.-P. Mao, N. Mardirossian, A. V. Marenich, S. A. Maurer, N. J. Mayhall, E. Neuscamman, C. M. Oana, R. Olivares-Amaya, D. P. O'Neill, J. A. Parkhill, T. M. Perrine, R. Peverati, A. Prociuk, D. R. Rehn, E. Rosta, N. J. Russ, S. M. Sharada, S. Sharma, D. W. Small, A. Sodt, T. Stein, D. Stück, Y.-C. Su, A. J. W. Thom, T. Tsuchimochi, V. Vanovschi, L. Vogt, O. Vydrov, T. Wang, M. A. Watson, J. Wenzel, A. White, C. F. Williams, J. Yang, S. Yeganeh, S. R. Yost, Z.-Q. You, I. Y. Zhang, X. Zhang, Y. Zhao, B. R. Brooks, G. K. L. Chan, D. M. Chipman, C. J. Cramer, W. A. Goddard III, M. S. Gordon, W. J. Hehre, A. Klamt, H. F. Schaefer III, M. W. Schmidt, C. D. Sherrill, D. G. Truhlar, A. Warshel, X. Xu, A. Aspuru-Guzik, R. Baer, A. T. Bell, N. A. Besley, J.-D. Chai, A. Dreuw, B. D. Dunietz, T. R. Furlani, S. R. Gwaltney, C.-P. Hsu, Y. Jung, J. Kong, D. S. Lambrecht, W. Liang, C. Ochsenfeld, V. A. Rassolov, L. V. Slipchenko,

J. E. Subotnik, T. Van Voorhis, J. M. Herbert, A. I. Krylov, P. M. W. Gill, M. Head-Gordon, *Mol. Phys.* **2014**, *113*, 184–215.

[10] D. Peng, N. Middendorf, F. Weigend, M. Reiher, *J. Chem. Phys.* **2013**, *138*, 184105.

[11] E. Schrödinger, *Phys. Rev.* **1926**, *28*, 1049–1070.

[12] N. S. Ostlund, A. Szabo, *Modern Quantum Chemistry: Introduction to Advanced Electronic Structure Theory*, MacMillan Publishing, **1996**.

[13] S. Bubin, M. Pavanello, W.-C. Tung, K. L. Sharkey, L. Adamowicz, *Chem. Rev.* **2013**, *113*, 36–79.

[14] R. J. Bartlett, J. F. Stanton, *Rev. Comput. Chem.* **2007**, *5*, 65–169.

[15] C. Møller, M. S. Plesset, *Phys. Rev.* **1934**, *46*, 618–622.

[16] D. Cremer, *WIREs Comput. Mol. Sci.* **2011**, *1*, 509–530.

[17] J. Čížek, *J. Chem. Phys.* **1966**, *45*, 4256–4266.

[18] R. J. Bartlett, M. Musiał, *Rev. Mod. Phys.* **2007**, *79*, 291–352.

[19] J. F. Stanton, R. J. Bartlett, *J. Chem. Phys.* **1993**, *98*, 7029–7039.

[20] C. Hättig, F. Weigend, *J. Chem. Phys.* **2000**, *113*, 5154.

[21] B. O. Roos, P. R. Taylor, P. Si, *Chem. Phys.* **1980**, *48*, 157–173.

[22] B. r. O. Roos, R. Lindh, P. Å. Malmqvist, V. Veryazov, P.-O. Widmark, *Multiconfigurational Quantum Chemistry*, John Wiley & Sons, **2016**.

[23] P. G. Szalay, T. Müller, G. Gidofalvi, H. Lischka, R. Shepard, *Chem. Rev.* **2012**, *112*, 108–181.

[24] T. J. Lee, A. P. Rendell, P. R. Taylor, *J. Phys. Chem.* **1990**, *94*, 5477–5482.

[25] T. Fleig, J. Olsen, L. Visscher, *J. Chem. Phys.* **2003**, *119*, 2963–2971.

[26] D. Ma, G. Li Manni, L. Gagliardi, *J. Chem. Phys.* **2011**, *135*, 044128.

[27] E. Neuscamman, H. Wang, T. Yanai, *Frontiers in Quantum System in Chemistry and Physics* **2008**, *18*, 49–65.

[28] K. H. Marti, M. Reiher, *Phys. Chem. Chem. Phys.* **2011**, *13*, 6750–6759.

[29] K. Andersson, P. Å. Malmqvist, B. O. Roos, *J. Chem. Phys.* **1992**, *96*, 1218–1226.

[30] C. Angeli, R. Cimiraglia, S. Evangelisti, T. Leininger, J. P. Malrieu, *J. Chem. Phys.* **2001**, *114*, 10252–10264.

[31] I. Schapiro, K. Sivalingam, F. Neese, *J. Chem. Theory Comput.* **2013**, *9*, 3567–3580.

[32] P. Pulay, *Int. J. Quantum Chem.* **2011**, *111*, 3273–3279.

[33] P. Hohenberg, W. Kohn, *Phys. Rev.* **1964**, *136*, 864–871.

[34] W. Kohn, L. J. Sham, *Phys. Rev.* **1965**, *40*, 1133–1138.

[35] E. Engel, R. M. Dreizler, *Density Functional Theory*, Springer Science & Business Media, **2013**.

[36] W. Koch, M. C. Holthausen, *A Chemist's Guide to Density Functional Theory*, Wiley-VCH, **2001**.

[37] H. S. Yu, X. He, S. L. Li, D. G. Truhlar, *Chem. Sci.* **2016**, *7*, 5032–5051.

[38] Y. Zhao, D. G. Truhlar, *Acc. Chem. Res.* **2008**, *41*, 157–167.

[39] M. G. Medvedev, I. S. Bushmarinov, J. Sun, J. P. Perdew, K. A. Lyssenko, *Science* **2017**, *355*, 49–52.

[40] T. Tsuneda, K. Hirao, *WIREs Comput. Mol. Sci.* **2014**, *4*, 375–390.

[41] L. Goerigk, S. Grimme, *WIREs Comput. Mol. Sci.* **2014**, *4*, 576–600.

[42] S. Grimme, A. Hansen, J. G. Brandenburg, C. Bannwarth, *Chem. Rev.* **2016**, *116*, 5105–5154.

[43] S. Grimme, J. Antony, S. Ehrlich, H. Krieg, *J. Chem. Phys.* **2010**, *132*, 154104.

[44] N. Mardirossian, M. Head-Gordon, *J. Chem. Phys.* **2016**, *144*, 214110–214110.

[45] E. Runge, E. Gross, *Phys. Rev. Lett.* **1984**, *52*, 997–1000.

[46] S. Hirata, M. Head-Gordon, *Chem. Phys. Lett.* **1999**, *314*, 291–299.

[47] C. Bannwarth, S. Grimme, *Comput. Theo. Chem.* **2014**, *1040-1041*, 45–53.

[48] S. Grimme, *J. Chem. Phys.* **2013**, *138*, 244104.

[49] P. Pyykko, *Chem. Rev.* **1988**, *88*, 563–594.

[50] P. Pyykkö, *Chem. Rev.* **2012**, *112*, 371–384.

[51] M. Dolg, H. Stoll, H. Preuss, *J. Chem. Phys.* **1989**, *90*, 1730.

[52] K. Eichkorn, O. Treutler, H. Öhm, M. Häser, R. Ahlrichs, *Chem. Phys. Lett.* **1994**, *240*, 283–290.

[53] J. W. Mintmire, B. I. Dunlap, *Phys. Rev. A* **1982**, *25*, 88–95.

[54] M. Feyereisen, G. Fitzgerald, A. Komornicki, *Chem. Phys. Lett.* **1993**, *208*, 359–363.

[55] A. S. de Merás, T. B. Pedersen, *J. Chem. Phys.* **2003**, *118*, 9481.

[56] F. Aquilante, R. Lindh, T. Bondo Pedersen, *J. Chem. Phys.* **2007**, *127*, 114107.

[57] F. Aquilante, T. B. Pedersen, R. Lindh, B. O. Roos, A. Sánchez de Merás, H. Koch, *J. Chem. Phys.* **2008**, *129*, 024113.

[58] F. Neese, F. Wennmohs, A. Hansen, U. Becker, *Chem. Phys.* **2009**, *356*, 98–109.

[59] S. Manzer, P. R. Horn, N. Mardirossian, M. Head-Gordon, *J. Chem. Phys.* **2015**, *143*, 024113.

[60] S. F. Manzer, PhD thesis, UC Berkeley, **2016**.

[61] E. Rebolini, R. Izsák, S. S. Reine, T. Helgaker, T. B. Pedersen, *J. Chem. Theory Comput.* **2016**, *12*, 3514–3522.

[62] M. Reiher, A. Wolf, *Relativistic Quantum Chemistry*, John Wiley & Sons, **2014**.

[63] K. G. Dyall, K. Faegri Jr, *Introduction to Relativistic Quantum Chemistry*, Oxford University Press, **2007**.

[64] P. A. M. Dirac in Proceedings of the Royal Society A, **1928**, pp. 610–624.

[65] E. v. lenthe, PhD thesis, Vrije Universiteit, **1996**.

[66] E. van Lenthe, E. J. Baerends, J. G. Snijders, *J. Chem. Phys.* **1994**, *101*, 9783.

[67] E. van Lenthe, J. G. Snijders, E. J. Baerends, *Phys. Rev. B* **1997**, *56*, 13556–13562.

[68] C. van Wüllen, *J. Chem. Phys.* **1998**, *109*, 392.

[69] S. Faas, PhD thesis, Amsterdam, **2000**.

[70] S. Faas, J. G. Snijders, J. H. Van Lenthe, E. van Lenthe, *Chem. Phys.* **1995**, *246*, 632–640.

[71] M. Filatov, *Chem. Phys. Lett.* **2002**, *365*, 222–231.

[72] M. Filatov, D. Cremer, *J. Chem. Phys.* **2003**, *119*, 11526–11540.

[73] M. Filatov, D. Cremer, *J. Chem. Phys.* **2005**, *122*, 044104.

[74] A. Wolf, M. Reiher, B. A. Hess, *J. Chem. Phys.* **2002**, *117*, 9215–9226.

[75] M. Reiher, *Theor. Chem. Acc.* **2006**, *116*, 241–252.

[76] F. Aquilante, T. B. Pedersen, V. Veryazov, R. Lindh, *WIREs Comput. Mol. Sci.* **2012**, *3*, 143–149.

[77] D. Cremer, W. Zou, M. Filatov, *WIREs Comput. Mol. Sci.* **2014**, *4*, 436–467.

[78] D. Stück, T. A. Baker, P. Zimmerman, W. Kurlancheek, M. Head-Gordon, *J. Chem. Phys.* **2011**, *135*, 194306.

[79] G. Blanquart, *Int. J. Quantum Chem.* **2015**, *115*, 796–801.

[80] P. K. Nandi, T. Kar, A. B. Sannigrahi, *J. Mol. Struct.* **1996**, *362*, 69–75.

[81] J. Gräfenstein, D. Cremer, *Mol. Phys.* **2001**, *99*, 981–989.

[82] J. R. Schmidt, N. Shenvi, J. C. Tully, *J. Chem. Phys.* **2008**, *129*, 114110.

[83] J. M. Wittbrodt, H. B. Schlegel, *J. Chem. Phys.* **1996**, *105*, 6574–6577.

[84] B. Kaduk, T. Kowalczyk, T. Van Voorhis, *Chem. Rev.* **2012**, *112*, 321–370.

[85] C. H. Booth, M. D. Walter, D. Kazhdan, Y.-J. Hu, W. W. Lukens, E. D. Bauer, L. Maron, O. Eisenstein, R. A. Andersen, *J. Am. Chem. Soc.* **2009**, *131*, 6480–6491.

[86] J. Jung, PhD thesis, Université de Rennes, **2015**.

[87] L. Castro, PhD thesis, Université de Toulouse, Université Toulouse III-Paul Sabatier, **2012**.

[88] S. Essafi, PhD thesis, Ecole polytechnique, **2012**.

[89] N. Barros, O. Eisenstein, L. Maron, *Dalton Trans.* **2006**, 3052–3057.

[90] O. Eisenstein, L. Maron, *J. Organomet. Chem.* **2002**, *647*, 190–197.

[91] C. E. Kefalidis, L. Perrin, L. Maron, *Eur. J. Inorg. Chem.* **2013**, *2013*, 4042–4049.

[92] L. Maron, O. Eisenstein, *J. Phys. Chem. A* **2000**, *104*, 7140–7143.

[93] X. Zhao, L. Perrin, D. J. Procter, L. Maron, *Dalton Trans.* **2016**, *45*, 3706–3710.

[94] B. O. Roos, R. Lindh, P. A. Malmqvist, *J. Phys. Chem. A* **2004**, *108*, 2851–2858.

[95] B. O. Roos, R. Lindh, P. Å. Malmqvist, V. Veryazov, P.-O. Widmark, A. C. Borin, *J. Phys. Chem. A* **2008**, *112*, 11431–11435.

[96] D. A. Pantazis, F. Neese, *WIREs Comput. Mol. Sci.* **2014**, *4*, 363–374.

[97] M. Dolg, H. Stoll, H. Preuss, *J. Chem. Phys.* **1989**, *90*, 1730–1734.

[98] M. Dolg, H. Stoll, A. Savin, H. Preuss, *Theor. Chem. Acta* **1989**, *75*, 173–194.

[99] X. Cao, M. Dolg, *J. Mol. Struct.* **2002**, *581*, 139–147.

[100] D. Andrae, U. Haeussermann, M. Dolg, H. Stoll, *Theor. Chem. Acta* **1990**, *77*, 123–141.

[101] A. Bergner, M. Dolg, W. Küchle, H. Stoll, H. Preuss, *Mol. Phys.* **1993**, *80*, 1431–1441.

[102] A. Weigand, X. Cao, J. Yang, M. Dolg, *Theor. Chem. Acc.* **2009**, *126*, 117–127.

[103] F. Weigend, R. Ahlrichs, *Phys. Chem. Chem. Phys.* **2005**, *7*, 3297–3305.

[104] P. L. Arnold, A. Prescimone, J. H. Farnaby, S. M. Mansell, S. Parsons, N. Kaltsoyannis, *Angew. Chem. Int. Ed. Engl.* **2015**, *54*, 6735–6739.

[105] J. A. Hlina, J. R. Pankhurst, N. Kaltsoyannis, P. L. Arnold, *J. Am. Chem. Soc.* **2016**, *138*, 3333–3345.

[106] N. Kaltsoyannis, *Inorg. Chem.* **2013**, *52*, 3407–3413.

[107] M. Coreno, M. de Simone, J. C. Green, N. Kaltsoyannis, R. Coates, C. Hunston, N. Narband, A. Sella, *Dalton Trans.* **2014**, *43*, 5134–5141.

[108] R. F. W. Bader, *Chem. Rev.* **1991**, *91*, 893–928.

[109] F. Cortesguzman, R. Bader, *Coord. Chem. Rev.* **2005**, *249*, 633–662.

[110] C. F. Matta, R. J. Boyd, *The Quantum Theory of Atoms in Molecules*, John Wiley & Sons, **2007**.

[111] J. P. W. Wellington, A. Kerridge, N. Kaltsoyannis, *Polyhedron* **2016**, *116*, 57–63.

[112] J. S. M. Anderson, J. I. Rodríguez, P. W. Ayers, A. W. Götz, *J Comput Chem* **2016**, *38*, 81–86.

[113] A. D. Becke, K. E. Edgecombe, *J. Chem. Phys.* **1990**, *92*, 5397.

[114] B. Silvi, A. Savin, *Nature* **1994**, *371*, 683–686.

[115] M. Kohout, *Faraday Discuss.* **2007**, *135*, 43–54.

[116] C. Lepetit, P. Fau, K. Fajerwerg, M. L. Kahn, B. Silvi, *Coord. Chem. Rev.* **2017**, *345*, 150–181.

[117] J.-P. Dognon, *Coord. Chem. Rev.* **2017**, *344*, 150–162.

[118] J. Contreras-Garcia, E. R. Johnson, S. Keinan, R. Chaudret, J.-P. Piquemal, D. N. Beratan, W. Yang, *J. Chem. Theory Comput.* **2011**, *7*, 625–632.

[119] K. Morokuma, K. Kitaura in *Chemical Applications of Atomic and Molecular Electrostatic Potentials*, (Eds.: P. Politzer, D. G. Truhlar), Springer Science & Business Media, **1981**, pp. 215–242.

[120] K. Morokuma, *J. Chem. Phys.* **1971**, *55*, 1236.

[121] T. Ziegler, A. Rauk, *Theor. Chem. Acta* **1977**, *46*, 1–10.

[122] M. v. Hopffgarten, G. Frenking, *WIREs Comput. Mol. Sci.* **2011**, *2*, 43–62.

[123] A. C. Castro, M. P. Johansson, G. Merino, M. Swart, *Phys. Chem. Chem. Phys.* **2012**, *14*, 14905–14910.

[124] G. K. Schenter, E. D. Glendening, *J. Phys. Chem.* **1996**, *100*, 17152–17156.

[125] T. M. Parker, L. A. Burns, R. M. Parrish, A. G. Ryno, C. D. Sherrill, *J. Chem. Phys.* **2014**, *140*, 094106.

[126] K. Szalewicz, *WIREs Comput. Mol. Sci.* **2011**, *2*, 254–272.

[127] W. B. Schneider, G. Bistoni, M. Sparta, M. Saitow, C. Riplinger, A. A. Auer, F. Neese, *J. Chem. Theory Comput.* **2016**, *12*, 4778–4792.

[128] R. Z. Khaliullin, E. A. Cobar, R. C. Lochan, A. T. Bell, M. Head-Gordon, *J. Phys. Chem. A* **2007**, *111*, 8753–8765.

[129] D. S. Levine, P. R. Horn, Y. Mao, M. Head-Gordon, *J. Chem. Theory Comput.* **2016**, *12*, 4812–4820.

[130] D. S. Levine, M. Head-Gordon, *J. Phys. Chem. Lett.* **2017**, *8*, 1967–1972.

[131] A. Jaoul, C. Clavaguéra, G. Nocton, *New J. Chem.* **2016**, *40*, 6643–6649.

[132] P. L. Watson, *J. Am. Chem. Soc.* **1983**, *105*, 6491–6493.

[133] B. D. Santarsiero, W. P. Schaefer, J. E. Bercaw, *J. Am. Chem. Soc.* **1987**, *109*, 203–219.

[134] P. L. Watson, D. C. Roe, *J. Am. Chem. Soc.* **1982**, *104*, 6471–6473.

[135] P. L. Watson, *J. Chem. Soc. Chem. Commun.* **1983**, 276–277.

[136] H. Rabaa, J. Y. Saillard, R. Hoffmann, *J. Am. Chem. Soc.* **1986**, *108*, 4327–4333.

[137] P. L. Watson, *J. Am. Chem. Soc.* **1982**, *104*, 337–339.

[138] D. Balcells, E. Clot, O. Eisenstein, *Chem. Rev.* **2010**, *110*, 749–823.

[139] N. L. Woodrum, C. J. Cramer, *Organometallics* **2006**, *25*, 68–73.

[140] E. C. Sherer, C. J. Cramer, *Organometallics* **2003**, *22*, 1682–1689.

[141] E. L. Werkema, R. A. Andersen, A. Yahia, L. Maron, O. Eisenstein, *Organometallics* **2009**, *28*, 3173–3185.

[142] W. J. Evans, L. R. Chamberlain, T. A. Ulibarri, *J. Am. Chem. Soc.* **1988**, *110*, 6423–6432.

[143] W. J. Evans, R. Dominguez, T. P. Hanusa, *Organometallics* **1986**, *5*, 263–270.

[144] B. r. O. Roos, P. PyykkÃ, *Chem. Eur. J.* **2010**, *16*, 270–275.

[145] G. Nocton, W. W. Lukens, C. H. Booth, S. S. Rozenel, S. A. Medling, L. Maron, R. A. Andersen, *J. Am. Chem. Soc.* **2014**, *136*, 8626–8641.

I find it irrational to become attached to one theory. I prefer to let different ideas compete like horses in a race and watch which one wins.

— Sir Martin Rees *We are all stardust*

2 Organic molecules reduction

Selective reducing agents are scarce. Strong reducing agents, such as sodium or potassium, are not selective and often they are used in large excess, which might destroy some parts of the molecule of interest. Lanthanide molecules in their divalent state possess the ability of giving away one electron and to perform such an action selectively.

This process has been extensively used over the last couple of decades in order to induce radical reactions[1]. A large variety of moiety can be reduced and further used in organic reactions[2,3] with a well known reagent, SmI_2: ketones, aldehydes, halides, ... A wide range of new organic reactions have been performed with this reagent[4]. The solvent conditions were found to be very critical in the elaboration of a fast and efficient reaction: while the first reactions involved THF as a solvent, recently acetonitrile[5] and even water[6–8] have been used with good yield. Additives, such as HMPA[9], have been used in order to increase the yield of the reaction. The mechanism of the reaction, while known in a general sense since the 1980s[10], is still being investigated[11–13] as a way to improve the properties of the reducing agent and its selectivity.

One of the major problem of organic reduction lies in the non-catalytic aspect of the process. Indeed, the reaction is stœchiometric. This poses a problem as samarium is expensive and its molecular weight is high. Attempt to design a catalytic process with samarium has been done but, to the best of our knowledge, there is no such mechanism.

The design of the ligand surrounding samarium can be changed and many interesting reactions have been performed using $Sm(OTf)_2$, $SmBr_2$, $Sm(N(SiMe_3)_2)_2$[14] or even organometallic reagent such as Cp^*_2Sm[15]. With the same idea, the divalent lanthanide can be changed and thulium[16,17], dysprosium[18] or neodymium[19] complexes can be used. These metals have a lower redox potential, which means that more difficult reductions can be performed. This idea has been recently reviewed by the group of Procter[20].

The reduction potential of lanthanide can also be used in order to perform selective reduction of strong bonds such as in small molecules. For instance, the group of Evans have been designing molecules that were able to reduce dinitrogen[21], carbon dioxyde[22,23], as well as carbon monoxyde[24]. These processes could be used to create new molecules from carbon dioxyde. The high atmospheric concentration of carbon dioxyde requires novel ways of recycling carbon dioxyde and lanthanide molecules can be used in such a way.

Heteroarenes are often used in transition metal chemistry as redox non innocent ligand that enhance the catalytic properties of a system. The use of such ligands with lanthanide is somewhat recent[25,26]. Ytterbium complexes of bipyridine and phenanthroline have been particularly studied over the last decade[27,28]. These molecules possess a complicated electronic structure.

The interaction with one heteroarene can lead to three different electronic configurations: triplet $\pi^{*\uparrow}\,4f^{13\uparrow}$, or singlet $\pi^{*\downarrow}\,4f^{13\uparrow}$ or $\pi^{*0}\,f^{14}$ whether the molecule is reduced or not. The electronic structure of these molecules is a mixture of both configurations[29]: this is the typical case of multi-configuration between the open-shell and closed-shell singlet states. Modifying the structure of the ligand surrounding the lanthanide can change the proportion of the dominant configuration. As such, the bipyridine[30] complex is 83% open-shell singlet, while the dimethoxy-bipyridine[31] is 87% closed-shell singlet. The electronic structure difference in these molecules has been studied using a combination of physical measurement such as XANES, UV-visible spectroscopy, SQUID experiments, crystallographic data and CASSCF calculations.

Recently, phenanthroline complexes have been synthesised and were found to be in equilibrium between their monomeric radical state and their dimeric state[32,33]. Both the ligand and the lanthanide have been varied and differences were discovered. The study of this

equilibrium from a theoretical perspective can give insights into the electronic structure of the molecules at stake and also can enable a comparison between experimental and theoretical data.

This chapter will be devoted to the extensive comparison between experimental and theoretical data in the field of organic molecule reduction. Firstly, a benchmark study will be done on phenanthroline complexes of lanthanide with the help of experimental results and will lead to the definition of a protocol to treat lanthanide at the DFT level of theory. Then, reactions with two different ketones will be developed and explained and further assessed with the protocol developed for phenanthroline complexes.

2.1 Reduction of phenanthroline

Reduction of phenanthroline by complexes of ytterbium has been studied extensively by Andersen *et al*[27,32] over the last couple of years. These complexes present a simple electronic structure compared to the bipyridine complex of ytterbium[29] discussed previously: a mixture of $4f^{13}\ \pi^{*1}_{a_2}$ and $4f^{13}\ \pi^{*1}_{b_1}$, open-shell triplet ($\pi^*_{b_1}$ and $\pi^*_{a_2}$ are the lowest unoccupied orbitals of phenanthroline). In the text below and in future chapters, the electronic configuration will always be written with the orbitals of the neutral ligand, *i.e.* π^* orbitals, even if these orbitals are occupied.

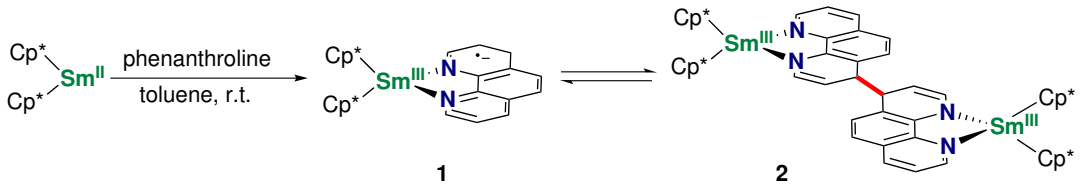

Figure 2.1: Equilibrium between radical phenanthroline complex of samarium (**1**) and dimer complex of samarium (**2**)

The study of phenanthroline as a ligand in lanthanide chemistry has been expanded by our group[33] to two other lanthanides, samarium and thulium. As in the case of dimethyl-phenanthroline complexes of ytterbium[32] an equilibrium is observed between the monomeric form of the complex and its dimeric one (Figure 2.1). Experimental studies on samarium complexes with modified Cp ligands with methyl or tert-butyl groups have enabled the extraction of thermodynamic constants for the equilibrium using variable temperature ^{1}H NMR (Table 2.1). The same extraction was attempted for thulium complexes, but the

Equilibrium	Cp^*	Cp^{tt}	Cp^{ttt}
$\Delta_r H(kcal/mol)$	-22	-19	-20
$\Delta_r S(cal/mol/K)$	-61	-51	-52
$\Delta_r G(kcal/mol)$	-3	-4	-5

Table 2.1: Experimental value for the equilibrium in Figure 2.1 with different ligands a: Cp^*; b: Cp^{tt}; c: Cp^{ttt}, data extracted from ref[33]

poor ^1H NMR, due to the high paramagnetism of the compound, disabled the extraction of such parameters.

The Cp ligand substitution by methyl, or tert-butyl groups seems to have a modest impact on the ΔG associated with the reaction. It is rather hard to interpret this difference as the error on the experimental dimerisation energy is around 5 kcal/mol.

Hence, quantum chemistry could give an interesting point of view on this equilibrium. First, it could evaluate the new C-C bond strength and compare it between different lanthanide complexes. Moreover, as experimental thermodynamic parameters are available, a comparison between these values and DFT energies could enable a better understanding of the C-C bond formation. This could also lead to an assessment of DFT functionals for this specific equilibrium as it is still rare to read an in depth comparison between density functionals and experimental energies for lanthanide complexes. Finally, experimental UV-visible spectrum for this equilibrium was also analysed and will be further studied using the quantum chemistry.

These three analyses will provide specific tools in order to study the C-C bond formation. Different hypotheses will be formulated for the intrinsic stabilisation of the dimer over the monomer in this specific case and the opposite for ytterbium complexes.

2.1.1 Electronic structure of the complexes

The electronic structure of phenanthroline has been known for decades. The point group of phenanthroline is C_{2v}. The C_{2v} character table is presented in Table 2.2.

The atomic orbitals (s, p, d) can be decomposed according to this character table. The s and p_z orbitals are of a_1 character while p_y is of b_2 and p_x of b_1.

Looking more closely into the phenanthroline molecule itself, there are three type of molecular orbitals: non-bonding orbital (n) such as the lone pair on the nitrogen atoms,

C_{2v}		
a_1	z	x^2, y^2, z^2
b_1	x, R_y	xz
a_2	R_z	xy
b_2	y, R_x	yz

Table 2.2: Character table of the C_{2v} symmetry

π-bonding orbitals that maintain the cohesion of the heterocycle and σ-orbitals (*i.e.* C-C or C-H or C-N bonds). These orbitals can be classified easily by their irreducible representations: σ and n orbitals are a_1 or b_2 orbitals, whereas π orbitals are classified as b_1 or a_2 orbitals.

Phenanthroline molecular orbitals have been calculated using the C_{2v} symmetry at the Hartree-Fock level of theory. The reduction of phenanthroline to form phenanthroline radical will take place in a π^* orbital. There is two low-lying π^* for phenanthroline, one in the irreducible representation a_2 and the other one in b_1. A few occupied and unoccupied molecular orbitals are shown in b_1 and a_2 representation whereas only occupied valence orbitals in a_1 or b_2 are pictured in Table 2.3.

As expected the LUMO in a_2 and b_1 are close in energy, only 0.0023 Hartree. Upon reduction, the electron could be distributed in these two orbitals with a multi-configuration wave-function ${\pi_1^*}^1$ and ${\pi_2^*}^1$. This type of behaviour was encountered for ytterbium complexes of phenanthroline[32]. Upon coordination with Cp_2^*Sm, the electronic structure of the radical monomer might also be multi-configurational. As a result, CASSCF calculations were performed in order to justify the use of DFT calculations.

2.1.1.1 The monomer

No crystal structure exists for $Cp *_2 Sm(phen)$, **1** (*the monomer*) and it is then really difficult to judge whether the geometry is accurate at our level of calculation. In order to assess its accuracy, a comparison between the calculated and the experimental structure of **2** was done (Table 2.4). In order to look at the influence of the ZORA model on the geometry, different approximations were used.

The geometries were calculated using either a relativistic pseudo-potential or a ZORA model and possess some differences. The largest one (± 0.04 Å) is found between the

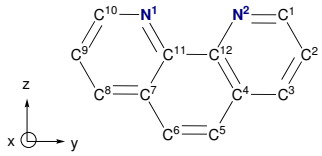

a_1	b_1	a_2	b_2
	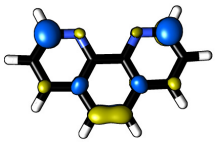 π_7^*	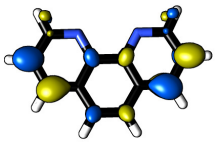 π_8^*	
	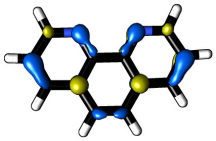 π_5^*	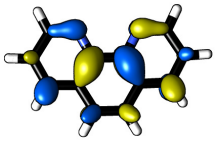 π_6^*	
	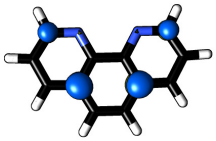 π_3^*	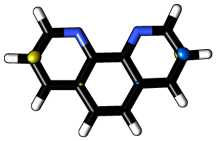 π_4^*	
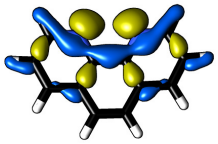 n_1	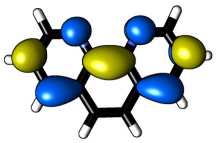 π_1^*	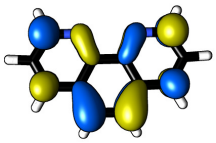 π_2^*	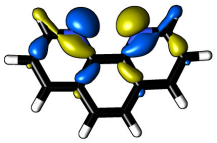 n_2
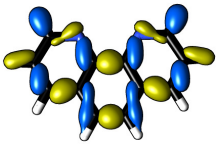 σ_1	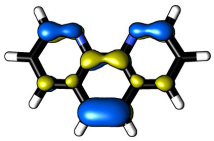 π_1	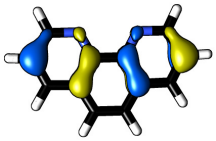 π_2	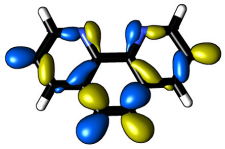 σ_2
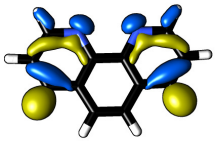 n_3	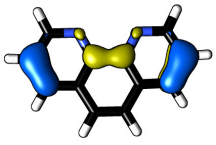 π_3	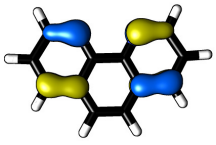 π_4	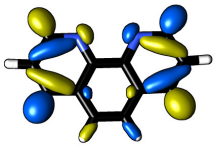 n_4

Table 2.3: Valence molecular orbitals of phenanthroline at HF/ANO-RCC DKH2 and their energies in Hartree

	X-Ray	PBE-D3 ZORA2	PBE-D3 ZORA1	PBE-D3 ECP-SC
Sm – N1 (avg)	2.38	2.50	2.49	2.53
Sm – N2 (avg)	2.48	2.50	2.50	2.53
Sm – Cp* (ctd avg)	2.43	2.45	2.43	2.47
Cp* – $\widehat{\text{Sm}}$ – Cp* (ctd avg)	138	140	142	141

Table 2.4: Geometry comparison between the crystallographic structure of **2** and the theoretically optimised structure of **1** using different approximations to treat the relativistic effects: ZORA1, ZORA2 and ECP-SC , where ctd stands for centroid and avg stands for average; distances are in angstroms and angles in degree

geometries optimised with a ZORA Hamiltonian and the small core ECP. There are also notable differences between the ZORA2 model and the ZORA-SAPA/ESA model; but these might be due to a change in the basis set, as the ZORA1 calculation is performed with Slater orbital and the ZORA2 with Gaussian orbitals. Overall the molecular geometries are close to the geometry of **2**. As the ZORA2 geometry was obtained faster than the two others, this level of theory is going to be used throughout this study to compute geometries.

The electronic structure of the monomer (**1**) was evaluated at the CASSCF level of theory, at the geometry optimised above. The active space was constituted of the 4f orbitals of the lanthanide and the two almost degenerate LUMOs of phenanthroline. The CASSCF calculation resulted in a $4f^5\ \pi_1^{*1}$ electronic configuration, without any involvement of the $4f^5\ \pi_2^{*\,1}$ state. Increasing the active space with the 5d orbital responsible for the bonding interaction with the a_2 orbital resulted in the same electronic structure.

The electronic ground state for trivalent lanthanide molecules can be of two different types: $4f^n$ or $4f^{n-1}\ 5d^1$[34]. The recent work by Nocton *et al.* showed that the π_1^* orbital of phenanthroline was involved mostly with 4f orbitals while 5d orbitals were involved with the π_2^* orbitals in C_{2v} symmetry. The present configuration contains the phenanthroline π_1^* orbital, which is significant from an involvement in the bonding of the 4f orbitals. On the contrary, the ytterbium molecule ground state was multi-configurational, with involvement of both the π_2^* and the π_1^* orbitals. It is known that ytterbium does not possess much orbital interaction with its ligand compared to samarium[35]. Hence, ytterbium will not favour any configuration and will possess a multi-configurational ground state, whereas samarium will favour one configuration over the other, *i.e.* the $4f^5\ \pi_1^{*1}$ electronic configuration.

LUMO	LUMO+1	LUMO+2
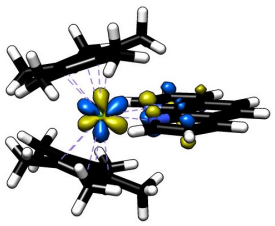	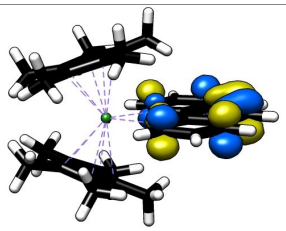	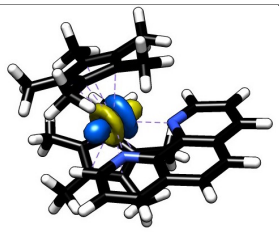
HOMO-5	**HOMO-1**	**HOMO**
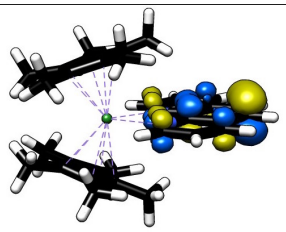	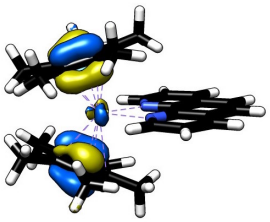	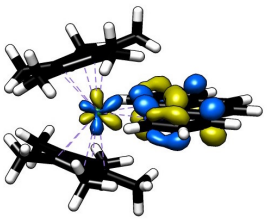

Table 2.5: Molecular orbitals of **1** using PBE0-D3 ZORA1

The Kohn-Sham molecular orbitals are similar to what was observed in the CASSCF calculation (*i.e.* $4f^5\pi_1^{*1}$). They are presented in Table 2.5. These orbitals present a delocalisation between the 4f and π orbitals of phenanthroline, which was also the case in the CASSCF calculation.

The LUMO of the system is the anti-bonding orbital between the π_1^* orbital of phenanthroline and a 4f orbital of the lanthanide complex. The LUMO+1 corresponds to the π_2^* orbital and the LUMO+2 is one pure 4f orbital from the samarium centre. On the other hand, the HOMO-1 represents the interaction between the π orbitals of the Cp^* ligands and one $5\mathrm{d}$ orbital of the lanthanide. The second occupied orbital with involvement from phenanthroline is the HOMO-5, one of the π orbital of phenanthroline without any involvement of the lanthanide orbitals.

The spin density of the molecule was analysed using Mulliken and Bader charges for two complexes $\mathrm{Cp}^*_2\mathrm{Yb(phen)}$ and $\mathrm{Cp}^*_2\mathrm{Sm(phen)}$. The results are presented in Table 2.6.

This evaluation for both complexes result in different repartition of the spin population. In the samarium case, there is a clear spin density excess on the C^3 or C^8 while for the ytterbium complex, the spin density is identical over the three positions of the phenanthroline C^2, C^3 and C^{11}. This might be a good indicator as to why samarium dimerise while ytterbium does not.

	Spin pop. (avg)	C^1,C^{10}	C^2, C^9	C^3, C^8	C^4, C^7	C^5,C^6	C^{11},C^{12}
$Cp^*_2Sm(phen)$	Mulliken	0.02	0.06	0.12	-0.03	-0.01	0.09
	Bader	0.02	0.06	0.10	-0.01	0.00	0.08
$Cp^*_2Yb(phen)$	Mulliken	-0.01	0.13	0.13	-0.01	0.00	0.11
	Bader	0.00	0.11	0.11	0.00	0.00	0.10

Table 2.6: Spin population of the carbon atoms in **1** using the numbers defined in Figure 2.3 with different population analysis at the PBE0-D3/ZORA1 level of theory for both $Cp^*_2Sm(phen)$ and $Cp^*_2Yb(phen)$

Moreover, the a_2 orbital (π^*_2) does not possess the right shape to favour a σ bonding with the C^3 atom, while the b_1 orbital (π^*_1) has the right shape to favour the dimerisation. The ytterbium complex electronic structure involves both the a_2 and the b_1 orbitals in the ground state of the system, while only the b_1 is present for the samarium complex. This might be the difference that explains why in one case the dimer is formed at room temperature while in the other the monomer is formed.

2.1.1.2 The σ dimer

The X-Ray structure of **2** (*i.e.* the σ dimer) was obtained experimentally. This structure has been used as a starting point for geometry optimisations. In order to assess the role of the density functional, different ones were used to optimise the geometry (Table 2.7).

PBE is one of the most popular GGA functional (*e.g.* DFT poll 2016[36]) and has been shown to reproduce accurately geometries and electronic structure of lanthanide molecules[37]. That is why, in order to test the effects of dispersion, Grimme's dispersion correction was added to this functional. Moreover, a COSMO solvation model was added on top of the calculation in order to study the influence of a solvent medium on the geometry of the complexes. TPSS, B97-D or M06L, three density functionals known to accurately reproduce geometries were also used.

Depending on the density functional, the geometries have several distances close to the experiment. M06L is able to reproduce accurately the C-C bond distance, whereas B97-D is far from being accurate. The C-N distances are well reproduced by PBE, but M06L seems to overestimate one C-N distance. Finally, TPSS and PBE give similar results.

Addition of dispersion corrections on top of the PBE functional improved the results. This has already been described in our group[38] and, more generally for transition metals[39,40]:

	X-Ray	PBE	PBE-D3	PBE-D3solv	TPSS	B97-D	M06L
C – C	1.61(1)	1.64	1.63	1.63	1.64	1.66	1.62
Sm – N1 (avg)	2.376(4)	2.417	2.403	2.412	2.414	2.425	2.392
Sm – N2 (avg)	2.482(4)	2.559	2.542	2.550	2.550	2.56	2.565
Sm – Cp*(ctd avg)	2.433(3)	2.481	2.448	2.460	2.482	2.497	2.467
Cp* – $\widehat{\text{Sm}}$ – Cp* (ctd avg)	139	136	139	138	138	139	137

Table 2.7: Geometry comparison between different density functionals optimised geometries (ZORA2) and the crystallographic structure of the dimer, where ctd stands for centroid and avg stands for average; distances are in angstroms and angles in degree

dispersion effects are to be taken into account in order to get a geometry closer to the X-Ray structure.

On the contrary, the addition of a solvation model does not improve the results significantly. The C-C bond created is 0.02 Å shorter, but other distances are elongated and worse than previously compared to the X-Ray structure.

CASSCF calculations were done on **2** using 10 electrons in 14 orbitals corresponding to the 14 4f orbitals. The obtained wave function was as expected $4f^5$ on each lanthanide, with multi-configuration for the 4f orbitals. Attempts to increase the active space in order to include the σ bonding and anti-bonding orbitals were done but, despite our best efforts, unwanted rotation of these orbitals – even after increasing the number of excitations – and the large size of the system (146 atoms $C_{64}H_{76}N_4Sm_2$) made this calculation undoable.

This electronic structure was compared to DFT calculations. The frontier Kohn-Sham orbitals of **2** are presented in Table 2.8. The orbital delocalisation on both samarium sites is still an artefact of DFT[41] as no magnetic coupling between the two samarium centres was observed experimentally and the CASSCF orbitals does not include this kind of delocalisation. The HOMO corresponds to the C-C σ bonding interaction, while the lowest LUMOs are localised on 4f orbitals. The HOMO-1 represent a π interaction in the dimeric phenanthroline and the HOMO-2 is the Cp* interaction with samarium. This is in agreement with what could be expected for this type of complex: the C-C σ bond is not thermodynamically stable and it makes sense that it would be the HOMO of this compound.

Moreover, it is possible theoretically to analyse the nature of this C-C bond formed in the dimer by combining different topological approaches (Table 2.9). Non-covalent interactions are represented in Figure 2.2. Coloured surfaces represent weak van der Waals interactions.

LUMO	LUMO+1
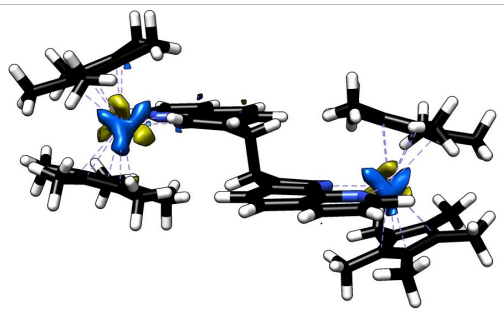	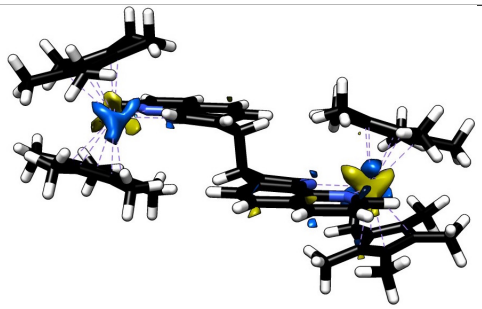
HOMO-1	HOMO
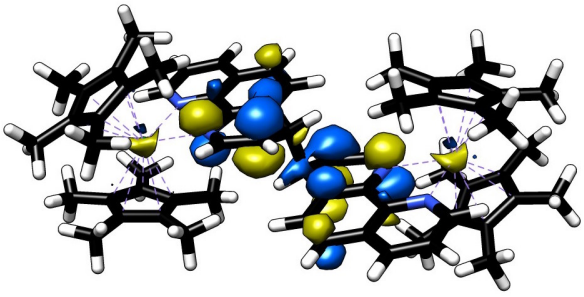	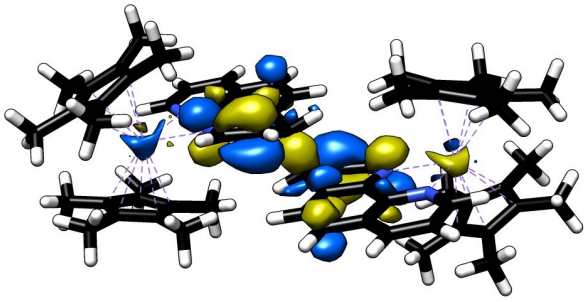

Table 2.8: Molecular Orbital of **2** at the PBE0-D3 ZORA1 level

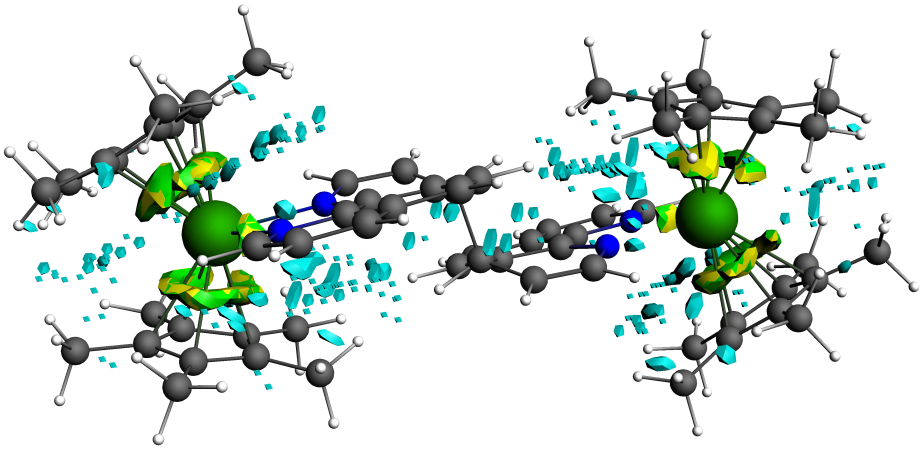

Figure 2.2: Non Covalent Interaction map on **2** at the PBE0-D3 ZORA1 level, the coloured surfaces are weak van der Waals forces

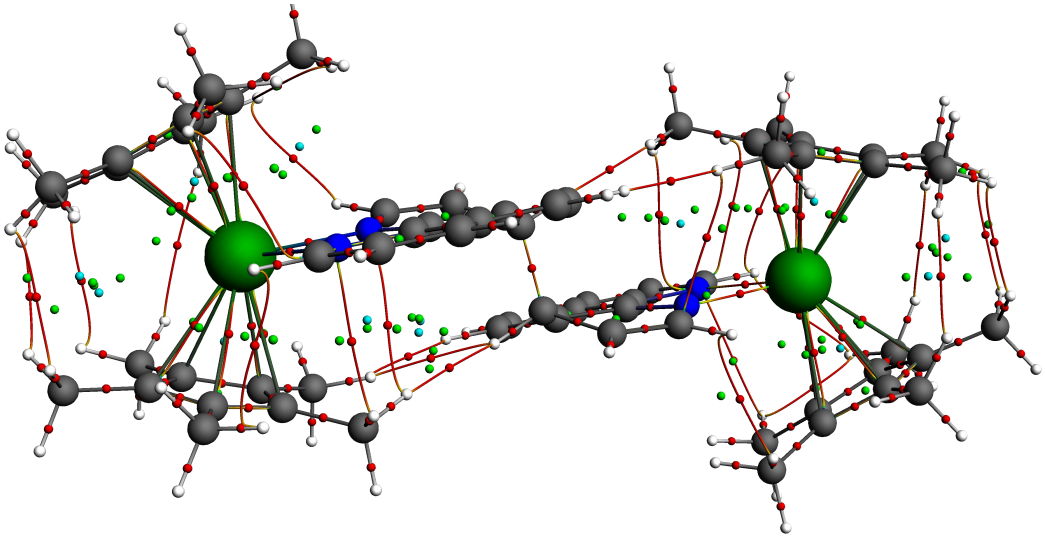

Figure 2.3: QTAIM molecular graph of **2** at the PBE0-D3 ZORA1 level of theory; red point corresponds to Bond Critical Point, green point to Ring Critical Point and blue to Cage Critical Point

The results show that no attractive dispersion interaction is found between the two carbon atoms corresponding to the dimer formation. In addition, QTAIM and ELF analyses have be used to understand the covalency of this bond. Figure 2.3 provides the bond paths and the critical points obtained from the QTAIM analysis. For the C-C bond especially, one bond path and one bond critical point have been found. The electron density and the Laplacian of the density at this critical point are 0.20 and -0.31, respectively and these values correspond to a shared interaction. Furthermore, a collection of cycle and cage critical points highlights a π-electron delocalisation in space which strengthens the interaction. ELF results point out one synaptic basin V(C,C) with a population of 1.71 electrons and a ELF value of 0.94 (Figure 2.4). The closer to 1 the ELF value, the more localised the electrons are. Globally, these analyses show that the two carbon atoms can be joined by a covalent chemical bond.

Finally, the C-C bond strength can be compared to other molecules: ethane that acts as a reference for a C-C σ bond and another lanthanide complex, $(\mathrm{Cp}^*_2\mathrm{Yb(phen)})_2$. Bond dissociation energies of the three systems have been estimated from ADF calculations by breaking the molecules in two entities on both sides of the C-C bond (Table 2.9). The energetic values show that the C-C bond in the lanthanide dimers is clearly weaker than in ethane. QTAIM, ELF and Mayer bond order results are also provided in Table 2.9. The C-C bond in ethane is strong with a short distance of 1.53 Åand a Mayer bond order of 0.91. The topological data support also this observation and the current values are very close to the

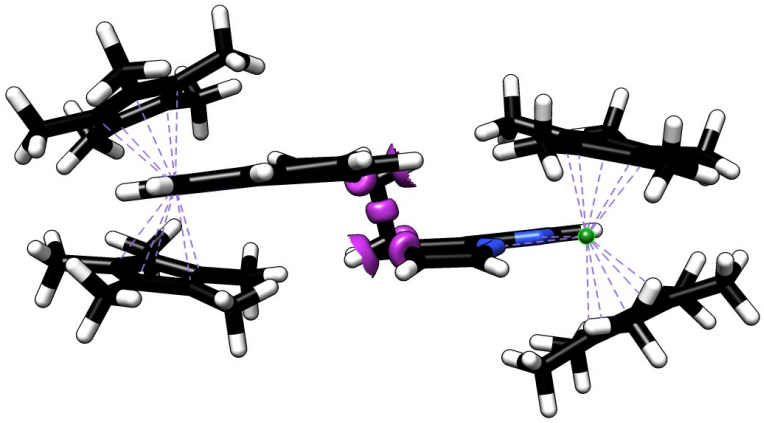

Figure 2.4: ELF representation of the V(C,C) synaptic basin (isosurface ELF = 0.03) in **2** in PBE0-D3 ZORA1

	Strength of the C-C bond	$(Cp^*_2Sm(phen))_2$	$(Cp^*_2Yb(phen))_2$	Ethane
	C — C distance	1.63	1.67	1.53
	Mayer Bond Order	0.78	0.76	0.91
	Bond dissociation energy	42	34	101
QTAIM	Laplacian of the density	-0.31	-0.23	-0.50
	Electron density	0.20	0.18	0.23
ELF	Electronic basin population	1.71	1.64	1.81
	ELF	0.94	0.93	0.95

Table 2.9: Computed data to compare the C-C bond strength for three different compounds starting from a PBE0-D3 ZORA1 density. Distances are in angstroms, bond dissociation energies in kcal/mol. Laplacian of the density and electron density are given for the C-C bond critical point. Electronic basin population corresponds to the V(C,C) basin.

ones available for ethane in the literature[42]. The samarium data are closer to the ethane ones than the ytterbium values and follow the experimental trend: the ytterbium complex exists mostly in its monomeric form at room temperature while the dimeric form of the samarium complex exists in solution, in equilibrium with the monomer.

In order to study more deeply the formation of this C-C σ bond, a comparison between DFT thermodynamic data and the experimental was performed using different type of density functionals: from GGA to double-hybrid density functionals.

2.1.2 Evaluation of the accuracy of different density functionals

Only few studies compare the accuracy of the functional with experimental data in lanthanide chemistry. In the 2000s, a communication from the group of Eisenstein[43], detailed an energy comparison between B3PW91, B3LYP and MP2, with SC-ECP. This early study showed that B3PW91 was the best density functional for specific reaction energies with lanthanide molecules. Recently, the group of Wilson[44] evaluated the performance of several density functionals over experimental energies of diatomic lanthanide molecules. They showed that TPSS was one of the best functional for these diatomic molecules. Yet, benchmark comparison of computed energies and experimental ones is still scarce.

As a result, the use of certain density functional could result in wrong energy evaluations or electronic structure. Moreover, for this σ bond creation, understanding the underlying reasons for specific density functionals to evaluate appropriately the energy could result in a better knowledge of the equilibrium at stake. This type of analysis was done for Cp^*_2Sm complexes of phenanthroline and the results are presented in Table 2.10.

This table contains a comparison between the signed error of ΔH and ΔG relative to the experimental value and the spin deviation observed for the energy evaluation of **2**. Different parameters were changed in order to look at their influence on the energy evaluation: the use of a solvation model, of dispersion corrected methods, of long range corrected methods as well as climbing the Jacob's ladder from GGA to double-hybrid.

Changing from the gas phase geometry to the one obtained with a COSMO solvation model induces small changes in the energy, only 0.5 kcal/mol at the PBE0-D3 level, leading even to slightly worse results. The dispersion effects were found to be important on the geometry of the compounds. The results shown in Table 2.10 indicate that the ΔH evaluation with hybrid functionals such as PBE0 or long range corrected functionals such as ωB97X benefits from the inclusion of dispersion effects. However, the use of dispersion corrections complementary to double hybrid functionals did not bring the same conclusions, as the results are worse than without the correction. The ΔH calculation is far from accurate as most functionals give an error of more than 15 kcal/mol. The general trend shows that the GGA functionals behave poorly compared to hybrid functionals and hybrid functionals behave poorly compared to double hybrid functionals. Different GGA functionals were used and a

Method	Geometry	Signed Error ΔH	Signed Error ΔG	Spin Deviation in **2**	% HF Exchange
PBE-D3	PBE-D3	16	22	0.47	0
OPBE		42	48	0.68	0
BP86		32	37	0.50	0
TPSS		31	37	0.40	0
M06L		29	35	0.52	0
PBE0-D3		4	10	0.06	25
PBE0-NL		4	10	0.06	25
PBE0		14	20	0.06	25
PBE0-D3 solv		7	14	0.06	25
PBE0-D3 solv	PBE-D3 solv	7	14	0.06	25
TPSSH		34	40	0.23	10
B3LYP-D3		15	21	0.11	20
B3PW91		28	34	0.13	20
M06		9	15	0.15	27
M06-2X		-1	5	0.03	54
ωB97X-D3	PBE-D3	0	6	0.05	SR:15.77 LR:100
ωB97X		7	13	0.05	SR:15.77 LR:100
ωB97		6	12	0.06	SR:0 LR:100
B97		31	37	0.14	19
LC-BLYP		13	19	0.10	SR:0 LR:100
CAM-B3LYP		20	26	0.05	SR:19 LR:60
B2PLYP		3	9	0.03	53
B2PLYP-D3		-5	1	0.03	53
B2PLYP-NL		-6	-1	0.03	53
PWPB95		1	7	0.02	50

Table 2.10: Signed error (kcal/mol) between experimental and theoretical ΔG and ΔH using different density functionals; SR: Short range, LR:Long Range; solv is an abbreviation for using the COSMO(Toluene) solvation model

few of them have already been proven to behave particularly well for problematic electronic structure calculations[45,46]. Nonetheless, neither OPBE, TPSS or BP86 provide accurate results and they are found to be worse than PBE-D3 in the evaluation of ΔH. The Minnesota suite of functionals performs well for this equilibrium, although this set of functionals has been developed using different molecular sets that do not include lanthanide data[47] and its use is controversial[48] . Compared to other functionals, M06 behaves well and M06-2X provides very good results with a ΔH evaluation close to the experimental data by -0.7 kcal/mol. B3LYP and B3PW91, that were used previously on similar cases[32,49], do not produce accurate data, with errors larger than 15 kcal/mol. Finally, PBE0-D3 provides also a good behaviour with an error of 3.9 kcal/mol.

Double hybrid functionals have not been extensively used to study lanthanide complexes, due to the rather long calculation time needed by these functionals in addition to the already time consuming calculations with large lanthanide complexes (ca. six times longer for a single-point energy calculation for **2**). The results obtained for this complex reinforce the already proven good agreement with experiments of this type of functionals[45,46]. Different forms of long range corrected functionals have been developed over the years[50] and used extensively on many systems. Here the comparison between five of these functionals LC-BLYP, CAM-B3LYP and the ωB97 suite showed fundamental differences. One of the first long range corrected functional developed, LC-BLYP, does reproduce well the equilibrium, with an error of 12 kcal/mol for the evaluation of the ΔH. Consequently, LC-BLYP is one of the best functional for this equilibrium. Other long-range corrected functionals, ωB97, ωB97X and ωB97X-D3, were used. The inclusion of short-range correlation was not found to be interesting in the case of this equilibrium. Passing from ωB97 to ωB97X, the enthalpy difference was higher in the latter case despite the inclusion of short-range exchange. The use of dispersion corrections with ωB97X-D3 led to a good evaluation of the energy compensating the problem observed for the inclusion of short-range effect. The Coulomb Attenuating Method (CAM) does include short-range HF exchange, but does not include 100% HF exchange at long distance. For CAM-B3LYP, at long distance the amount of exchange is 60% and the results are worse than for the four other functionals. This confirms that short-range HF exchange is not essential for the good evaluation of the

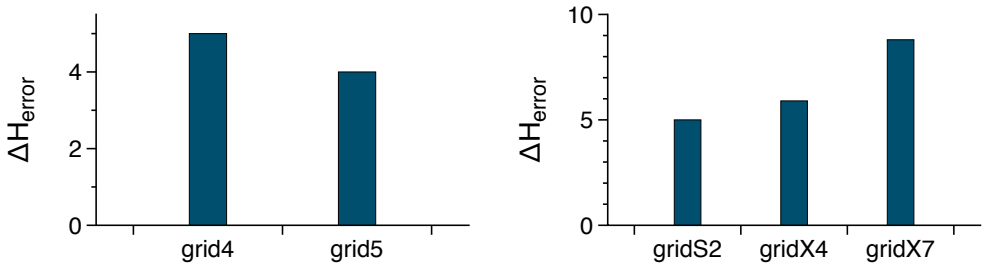

Figure 2.5: Signed Error (kcal/mol) between the experimental and theoretical ΔH value at the PBE0-D3 ZORA3 level of theory using different grid sizes (left) and gridX sizes(right)

energy and indicates the importance of long-range interactions regarding the exact evaluation of the enthalpy reaction of this equilibrium.

The quality of the integration grid is crucial to DFT and a change is sometimes required for specific functionals such as M06[51]. Moreover, the RIJCOSX approximation used to accelerate the calculations requires the use of a different grid parameter (gridX) that may influence the energy evaluation. Accordingly, the grid parameters were changed (Figure 2.5), but only led to a few kcal/mol difference. This could not account for error in the range of 20 to 30 kcal/mol observed in several cases in Table 2.10.

The enthalpy evaluations have been performed for two other complexes by changing the ligand and the results for the global set (Cp^*, Cp^{tt} and Cp^{ttt}) are presented in Figure 2.6. The results follow the same trend for the three complexes; a functional with a high percentage of HF exchange leads to the most accurate energetic results compared to experimental data. In this context, a few functionals outperform the others: M06-2X, PWPB95 and ωB97X-D3.

When looking at the free energy calculation, all the functionals give a positive value, which represents a bad evaluation of the experimental negative value. However, in the case of double hybrid functionals, the calculation of ΔG was found to be moderately accurate, as already shown previously in the literature[45,52]. The calculation of the entropic contribution is known to be difficult due to the harmonic approximation in the frequency calculations, which may explain these poor results. For the samarium complexes, the results do not agree with experiments as the entropy contribution is increasing passing from Cp^* to Cp^{ttt} (Table 2.11). Globally, the error on the enthalpy and free energy values is spread, from less than 5 to more than 20 kcal/mol, depending on the density functional. Techniques have been

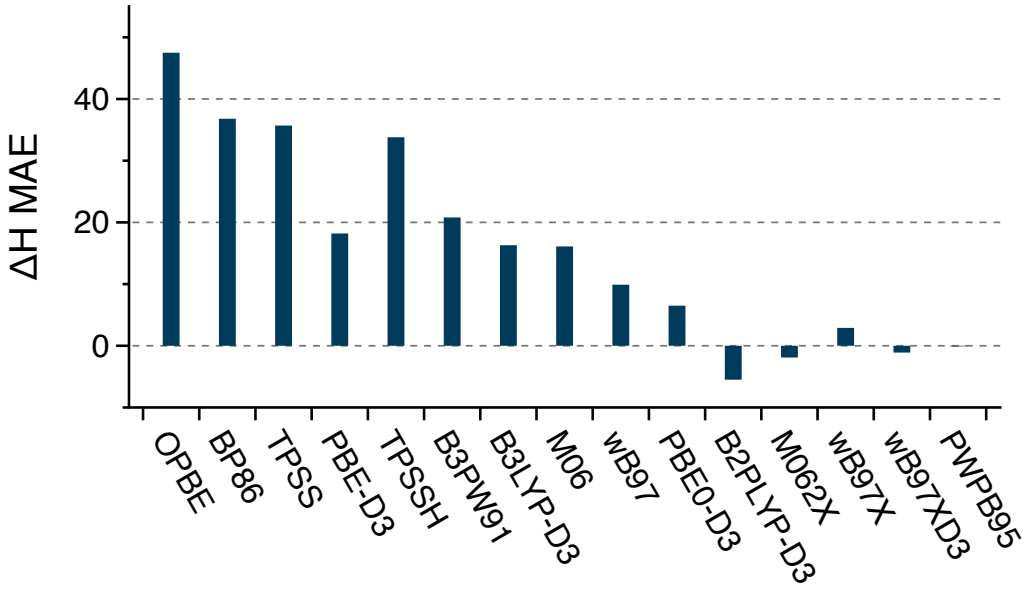

Figure 2.6: Mean Average Error (kcal/mol) between the theoretical and experimental ΔH for three different complexes bearing a Cp^*, Cp^{tt} and Cp^{ttt} ligand

ΔS	PBE-D3	Experimental
Cp^*	-71	-61
Cp^{ttt}	-78	-52
Cp^{tt}	-78	-51

Table 2.11: ΔS (cal/mol/K) values for the three different complexes at the PBE-D3 ZORA2 level

developed in order to remove this type of inconsistencies with the entropy evaluation using DFT[53–59]. But, no general technique can be used; as a result this type of approximation was not performed in this work.

Taking into account these results, calculations for ytterbium and thulium complexes, where no experimental data are available, were performed using four different functionals: M06-2X, PBE0-D3, B2PLYP and ωB97X-D3. The results are shown in Table 2.12.

Depending on the density functional, the ΔG or the ΔH ordering is changing. Experimentally, the ytterbium complex is more stable in its monomeric form at room temperature while in the two other cases the more stable form is the dimeric one. However, for these four density functionals it is difficult to conclude. Between samarium and ytterbium complexes, calculations at the PBE0-D3 level indicates that ΔG is lower for ytterbium than for samarium while for M06-2X the opposite is found.

	ytterbium		thulium		samarium	
	ΔH	ΔG	ΔH	ΔG	ΔH	ΔG
PBE0-D3	-17	3	-19	2	-13	8
M06-2X	-15	5	-16	5	-21	1
ωB97X-D3	-22	-2	-23	-2	-20	2
B2PLYP	-13	7	-15	7	-17	5

Table 2.12: Evaluation of ΔG and ΔH (kcal/mol) using three different density functionals for three different lanthanides bearing the same ligand Cp*

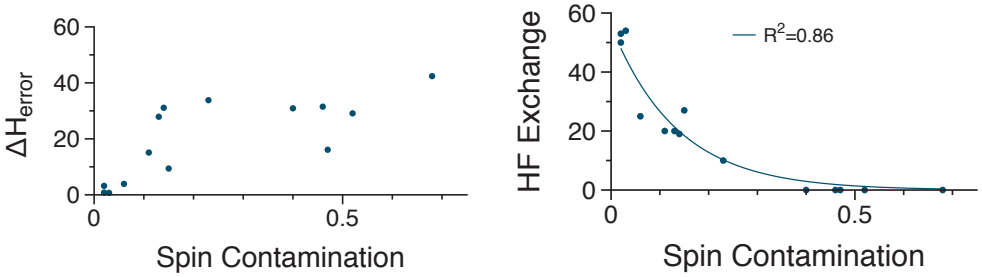

Figure 2.7: ΔH (kcal/mol) error (left) and the HF exchange % (right) depending on the spin contamination using the different methods presented in table 2.10, the different marks correspond to the computed data and the blue line corresponds to a quadratic fitting of the data

Savin recently explained that benchmark calculations are often used to extrapolate informations that can not be extrapolated without further investigations[60]. This is especially important in this case and in depth understanding of the behaviour of density functionals in one specific example could shed some new light to this benchmark calculation.

2.1.2.1 A spin contamination issue?

Looking back at the spin contamination evaluation in **2**, there is a general trend between this value and the energy error, as shown in Figure 2.7.

Spin contamination for **2** evolves as the energy error and is a function of the Hartree Fock exchange included in the functional (Figure 2.7). In addition, modifying the HF exchange in PBE0-D3 from 0 to 100% increases spin contamination for **1**, which leads to bad energy difference evaluation (Figure 2.8).

To further prove that spin contamination was related to the HF exchange % and linked to ΔH evaluation, the HF exchange % in PBE0-D3 and B3LYP-D3 was varied from 0 to 100 %. The results are presented in Figure 2.9. Both functionals follow the same trend for spin contamination (Figure 2.9): it decreases from 0 to 50%, then stays linear until

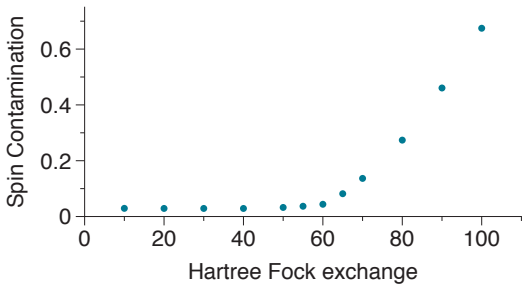

Figure 2.8: Spin contamination for the monomer at the PBE0-D3 ZORA3 level of theory, while changing the percentage of HF exchange % in PBE0-D3

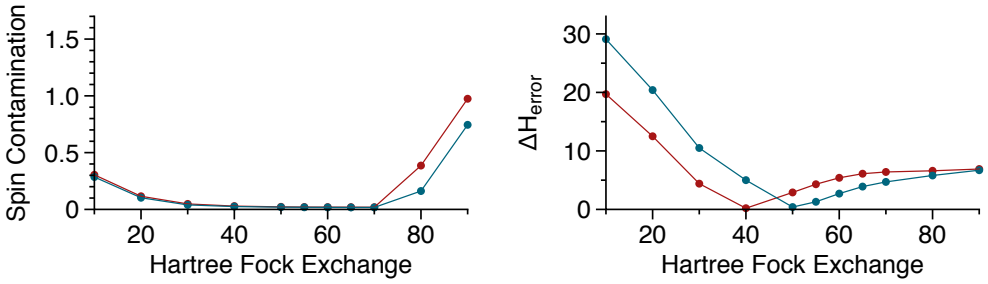

Figure 2.9: Evolution of the the spin contamination (left) and the error in the ΔH calculation (kcal/mol) (right) while changing the Hartree-Fock exchange percentage included in B3LYP-D3 (blue) and PBE0-D3 (red)

70% when it increases again. The plots for PBE0 and B3LYP are mixed up and cannot be distinguished from one another until 70% of HF exchange. On the other side of figure 2.9, the ΔH signed error does not follow the same trend (Figure 2.9). There is an optimum value for the HF-exchange % found at 40% for B3LYP-D3 and 50% for PBE0-D3 that enable a ΔH value close to the experiment.

This behaviour is slightly different than what has been reported in the literature. Radom *et al.* studied the influence of the density functional on spin contamination and energies[61]. They found an increase of spin contamination with the increase of the percentage of HF-exchange resulting to an inadequate energy evaluation. This result was validated by Baker *et al.*[62] and Herrman *et al.*[63] for other molecules with high spin contamination with DFT methods.

As discussed in chapter 1, spin contamination is a normal behaviour of unrestricted wavefunction[64]. For the dimer, the percent contamination varies from 0.5% to 2% depending on the density functional used. These values can be compared to usual spin-contaminated

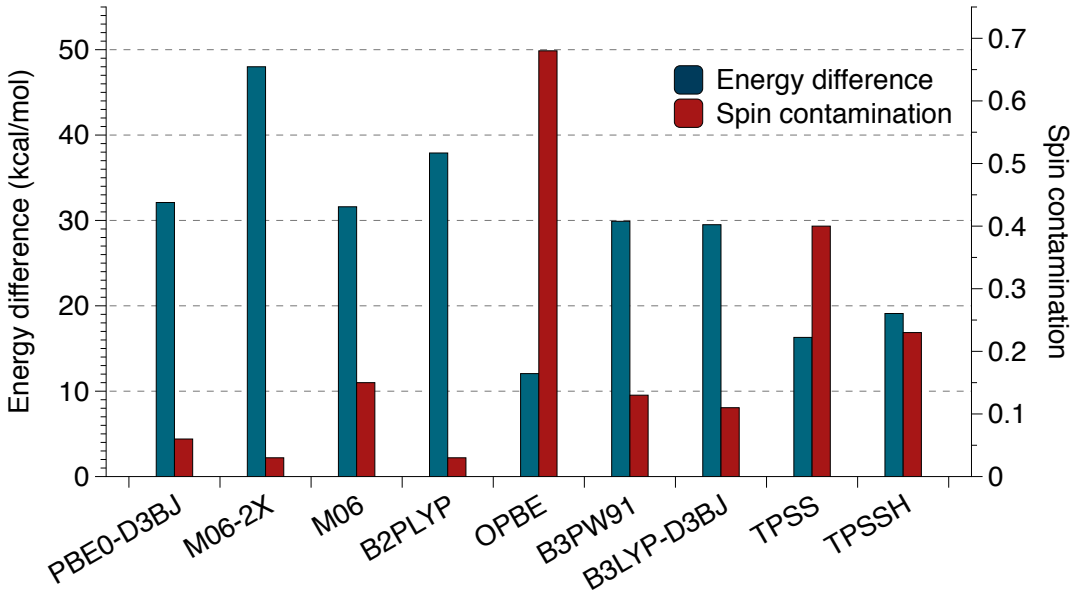

Figure 2.10: Energy difference between ms=11 and ms=13 and spin contamination in the energy evaluation at ms11 for **2** using different density functionals with ZORA3

HF calculation for doublet: in these cases spin contamination often ranges 0.25 and the percent contamination is then more important relative to the low spin multiplicity at stake. Here considering the large spin multiplicity at stake the error is small, but still represents a large error in the energy evaluation.

The spin contamination is related to the energy difference between the first excited state and the ground state. Although in the present case, there is no clear correlation between these two values (Figure 2.10). On one side, this explains why some functionals possess large spin contamination: OPBE, TPSS and TPSSH give small values for energy difference between the bi-radicaloid and the σ bond species, which result in a large spin contamination. Similarly, M06-2X gives a large energy, which leads to small spin contamination. But, in other cases it is difficult to discriminate between density functionals. PBE0-D3 gives an energy difference that is close to B3LYP-D3, M06, or B3PW91; these four density functionals provide a spin contamination value larger than PBE0-D3.

There is a difficulty to treat the 4f orbitals exactly using DFT. This treatment might lead to deficiency in the context of spin contamination.

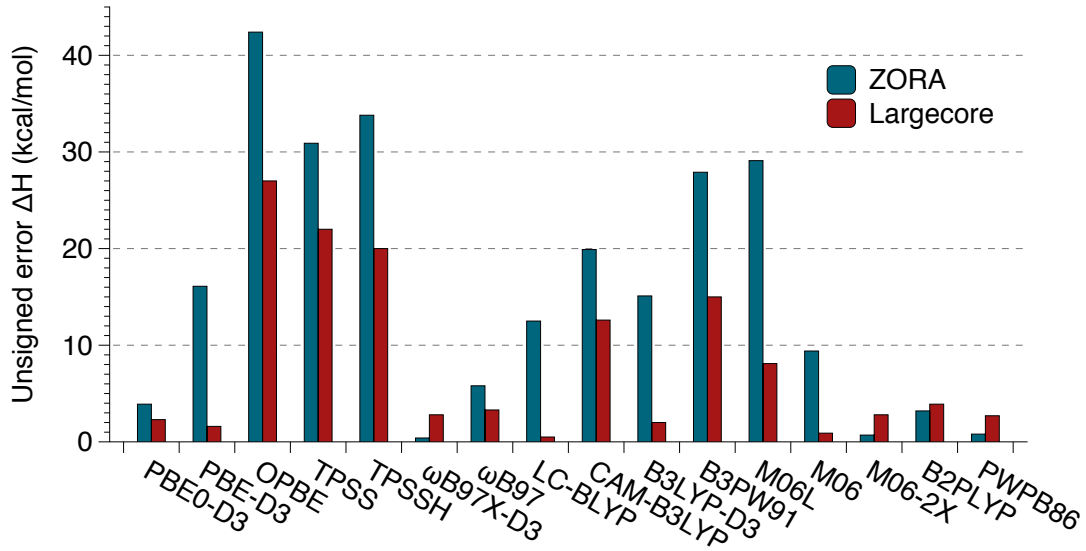

Figure 2.11: Unsigned error of ΔH using LC-ECP and ZORA3 calculations with different density functionals

2.1.2.2 Is the spin contamination related to the 4f orbitals?

In order to assess the importance of the 4f orbitals into the spin contamination issue, LC-ECP calculations were done on the Cp* complexes (Figure 2.11). The energies are closer to experimental values than previously.

An overall of 10 kcal/mol was observed for density functionals showing high spin contamination. On the other hand, density functionals such as PBE0-D3 or B2PLYP are worsened by the use of large core pseudo-potentials.

Thus, the 4f orbitals are responsible for the spin contamination issues and for the large difference between experimental results and theoretical ones. As detailed previously, the Kohn-Sham orbitals of **2** describe a particular error: there is a delocalisation between the two 4f orbitals of the lanthanide centres. This error could be responsible for the spin contamination and further lead to problems in the energy evaluation.

The evaluation of the delocalisation error as described previously in more simple cases[41] has been done on **2** as shown in Figure 2.11. The closer this value is from 0, the more correct the delocalisation is. Negative values correspond to a too localise density, while positive values correspond to a too delocalise density. Indeed, functionals with HF exchange lower

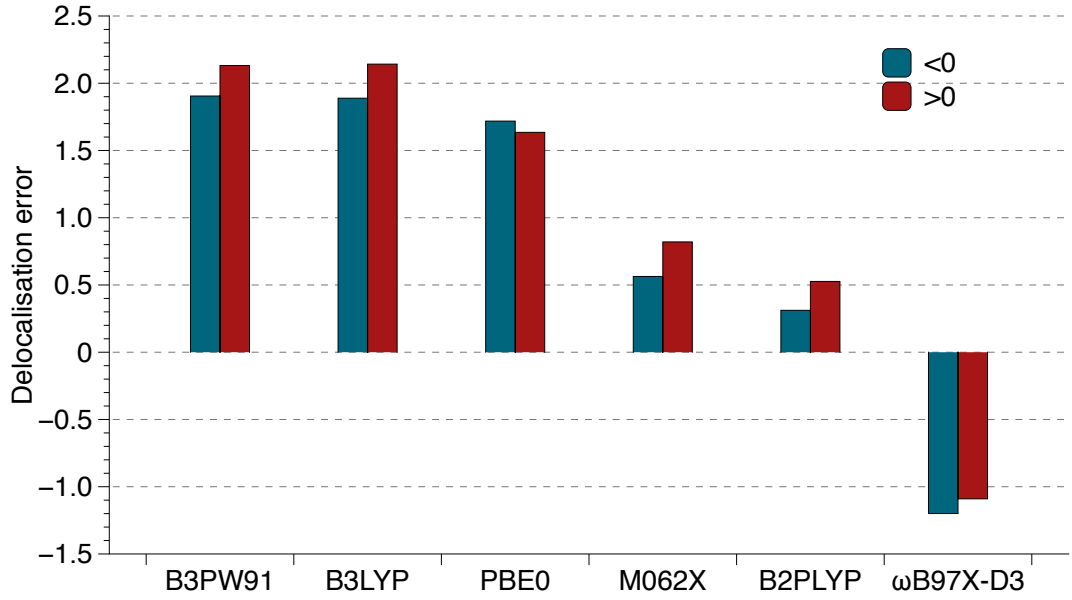

Figure 2.12: Delocalisation error for the dimer, the more positive the more delocalised, the more negative the more localised

than 25% possess an important delocalisation error, while functional with as much as 50 % HF exchange have a more correct behaviour. In this sense, M06-2X and B2PLYP have a correct behaviour, while PBE0, B3LYP and B3PW91 delocalisation error is similar. On the contrary, ωB97X-D3 behaviour is too localised.

There is no real correlation between the delocalisation error[65] and the spin contamination as PBE0, B3LYP and B3PW91 have the same delocalisation error, but do not give similar spin contamination. Hence, the spin contamination error could not be taken as an influence from the delocalisation error.

One question remains, where is the spin contamination located and what is the difference between high HF exchange percentage and low HF exchange percentage?

At high HF exchange percentage, the spin contamination is located on the phenanthroline moiety. In this fragment there is a correlation between the Mulliken and Loewdin spin population and the HF exchange. This behaviour was observed for both **1** and **2** after 70% of HF exchange: the spin charge of phenanthroline carbon atoms increased from a value nearing 0 to a value approaching 0.3. This is partly due to a spin contamination problem in the HF wave function itself.

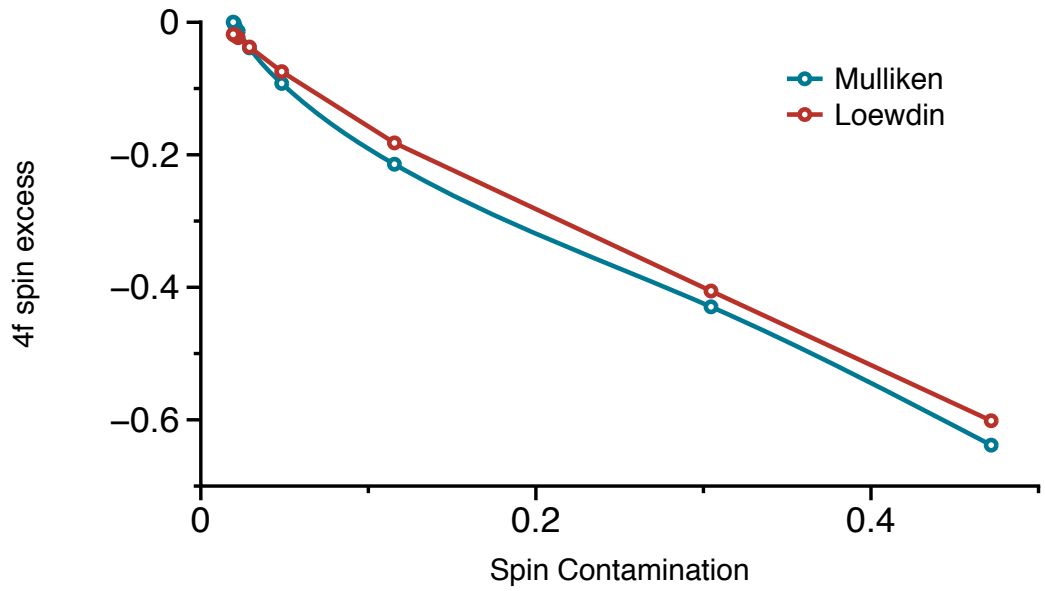

Figure 2.13: Evolution of the 4f spin excess compared to the spin contamination at the PBE0-D3 level of theory while varying the HF-exchange % for the dimer from 0% to 70%

For low HF exchange percentage, there is a clear correlation between the spin contamination and the spin population of the 4f orbitals (Figure 2.13). The spin excess can be defined as the spin population in the 4f orbitals x% HF exchange reduced over the spin population at 100% HF exchange. This value is decreasing as the spin contamination increases.

The Mulliken population of the lanthanide atom is also following a certain trend: the 4f population is decreasing as the HF exchange increases, while the 5d population follows the inverse trend (Figure 2.14). Previous work from the group of Autschbach[41] also showed that for lanthanum complexes, the 4f population decreased with the amount of HF exchange. This decrease in the 4f population was attributed to a ligand to metal donation and was also correlated with the delocalisation error of DFT. In the present case, the 5d population is increasing as the 4f decreases. This could be related to a charge transfer to 5d orbitals that is only possible at high HF exchange %.

The LaF_3 molecule, described in the study of Autschbach, should not present an important donation from the ligand into the metal orbitals. On the contrary, phenanthroline could induce an important charge transfer into the metal orbitals, but it is difficult to know theoretically in which orbital between the 4f or the 5d this donation will occur. Computationally, depending on the HF exchange %, it could be both. In the present

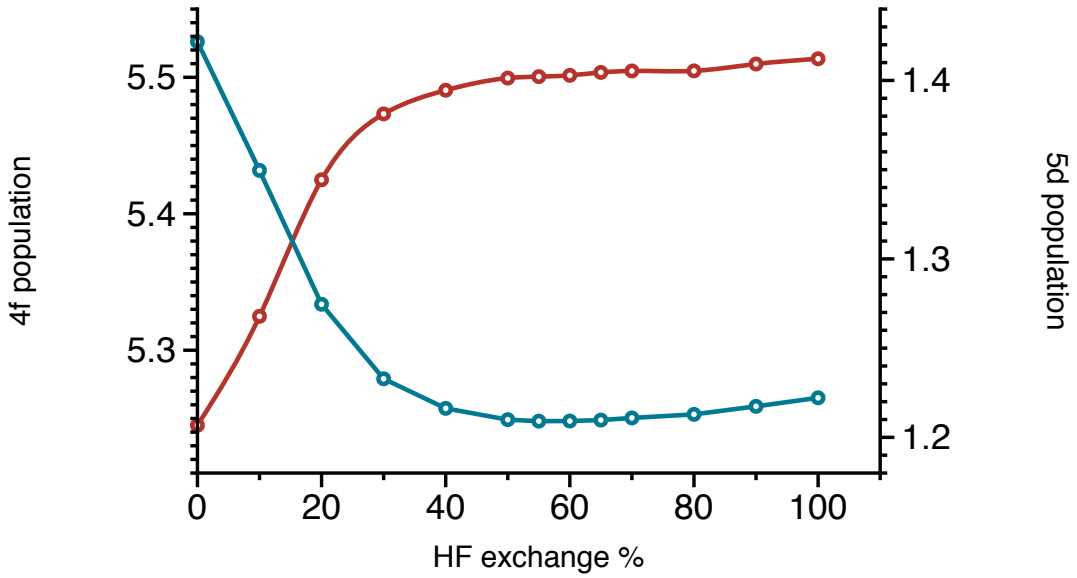

Figure 2.14: Evolution of the 5d (red) and 4f (blue) Mulliken population depending of the HF exchange % at the PBE0-D3 level of theory

case, higher HF exchange %, *i.e.* donation in the 5d orbitals, induces better energy differences. This is in agreement with the work from Grimmel *et al*[44] that detailed an energy comparison between several functionals and evaluated that GGA and meta GGA were very accurate for their set of tri-halide lanthanide complexes. In these molecules the ligand to metal charge transfer are not expected to be important contrary to phenanthroline complexes of lanthanide.

These results have to be extended using DFT tools such as Bader or Hirschfeld charges, as Mulliken charges are not a representation of the density.

More generally, the HOMO-LUMO gap is increasing a lot when increasing the HF exchange %. The more HF exchange %, the deeper in energy the 4f orbitals get. The 4f orbitals are the HOMO of the system at low HF exchange %, but when the HF exchange % increases, the 4f orbitals go deeper in energy. This behaviour was also observed on tri-halide complexes of lanthanides[41].

Atomic calculations on a Sm^{2+} ion also show this kind of behaviour. CASSCF calculations were done on the ion by including in the active space the 4f and the 5d orbitals. A state average calculation was done on the first 6^{th} states, as they were close in energy (SA-CASSCF(6,12)). The energy of the resulting canonical orbitals are compared to DFT results.

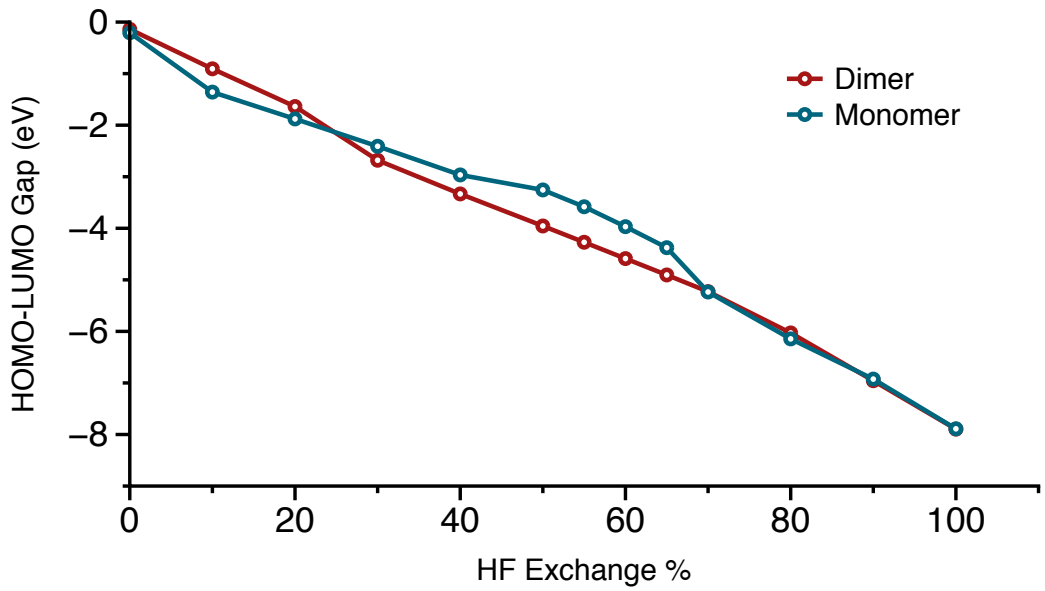

Figure 2.15: Evolution of the HOMO-LUMO gap depending on the HF exchange % for the monomer and the dimer at the PBE0-D3 level

DFT calculations were performed on the ion by using either the PBE functional, or the PBE0 functional with either 50% or 100% HF exchange. The results are presented in Figure 2.16.

An increase of HF exchange % results in a splitting of the 4f orbitals, that are grouped with the GGA functional. The PBE Kohn-Sham 4f orbitals have almost the same energy than the atomic orbital calculated at the SA-CASSCF level of theory. But, the 6s and 5d orbitals are poorly represented by the PBE functional. Increasing the HF exchange % lead to a better description of these orbitals compared to the CASSCF level of theory. However, increasing the HF exchange also splits the 4f orbitals and the occupied 4f orbitals are split by 0.4 Hartree from 0 to 100% HF exchange. Calculations done on the trivalent ion were able to reproduce the same trends.

While virtual orbitals evaluation is not done properly using standard DFT calculations, it is interesting to note that the trend for the 4f orbital is identical: the 4f is shifted from -0.6 Hartree to -0.1 Hartree from 0 to 100 % HF exchange. This could explain why at low HF exchange % in the dimer, the charge transfer is favoured into the 4f orbitals while at high HF exchange % the charge transfer is favoured in the 5d orbitals. The use of techniques that involve the virtual orbitals in the calculation such as SP-DFT[66] or MP-DFT[67]

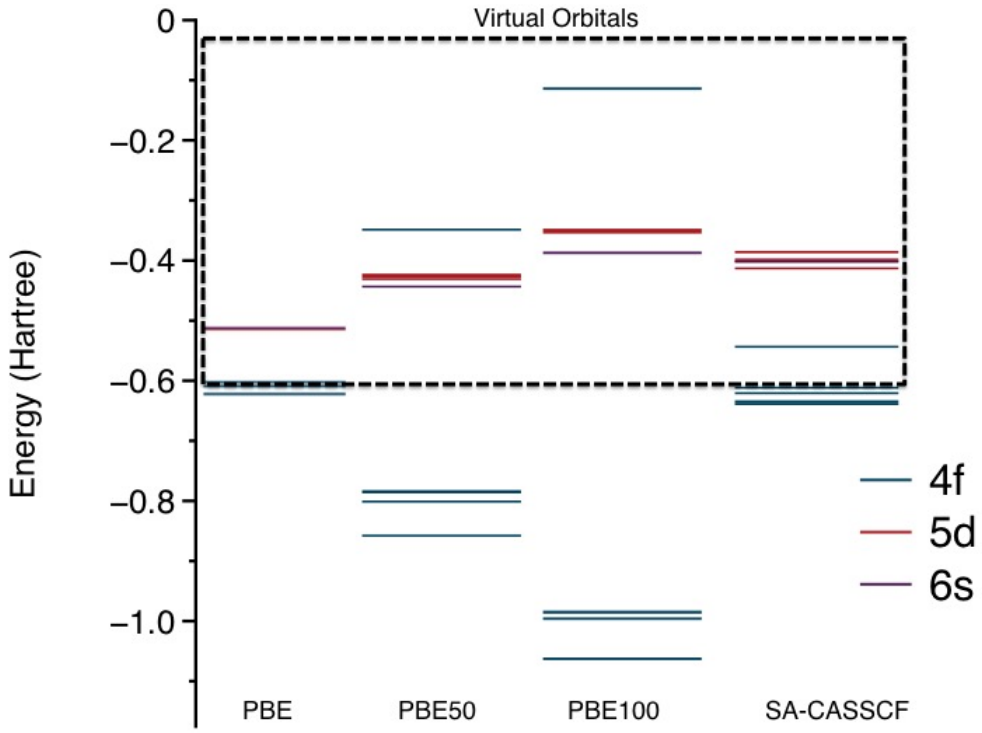

Figure 2.16: Atomic orbital energies of Sm^{2+} at the PBE ZORA3 level of theory while varying the amount of HF exchange % from 50 to 100% and compared to SA-CASSCF(6,12) calculation

that combines CASSCF and DFT calculations would be more suitable to compare this evolution of virtual orbitals.

Experimental results have shown that[34] the electronic structure of Ln^{2+} ions depends on the lanthanide and on the ligands themselves. In some cases, a lanthanide ion inside a complex can pass from a $4f^{n+1}$ configuration to a $4f^n5d^1$ one. In the present context our results have to be put in perspective: in extreme cases can DFT with higher exchange favour the 5d configuration over the 4f?

In conclusion, the choice of the density functional has a strong influence on the evaluation of the thermodynamic data for this equilibrium. The equilibrium itself is best described by functional with high HF exchange %, as at low HF exchange % spin contamination issues worsen the evaluation of ΔH. Spin contamination's origin lies in the ligand to metal charge transfer. The more HF exchange there is the more donation into the 5d there will be.

While for **2** the consequence is that at lower HF exchange % a donation from the ligand to the metal 4f orbitals lead to spin contamination, **1** is better evaluated at low HF exchange %.

Indeed, **1** is better described with phenanthroline donation into the 4f orbitals as described in I.1. As a result, the density functional needs to be appropriately chosen when doing calculations for lanthanide complexes.

The energy difference calculated previously for ytterbium and samarium complexes can be related to these findings (Table 2.12). This difference could directly be correlated with the donation from the ligand to the metal. The electronic structure of the ytterbium complex only showed an involvement of the 4f orbitals[32], which might be better described at low HF exchange %. On the other hand, the electronic structure of the samarium complex is better described with a ligand to metal charge transfer into the 5d orbitals of the metal. This means that a higher HF exchange % will give a better evaluation of the electronic structure.

As a result, the difference between the evaluated ΔG at the PBE0 and M06-2X level of theory is +2 kcal/mol for ytterbium complexes, while for the samarium one, the ΔG difference is -7 kcal/mol. On the other hand, while the inclusion of long range corrections has a modest impact on the samarium complex itself, the ytterbium complex is very different as ΔG evolves from 5 to -2 kcal/mol. This could be related to a lower than expected charge transfer in this complex. Moreover, one intriguing aspect of these result is the similarity between $\Delta G(\mathrm{Tm})$ and $\Delta G(\mathrm{Yb})$. This similarity is still very difficult to analyse.

The C-C σ bond strength is thus largely influenced by donation from the ligand to the metal, *i.e.* the more donation the ligand is giving to the 5d orbitals of the complex, the less spin contamination and the more accurate the results. This type of donation will have a significant influence in the UV-visible spectrum of the complexes. Thus, the theoretical study of UV-visible spectrum of $\mathrm{Cp}^*_2\mathrm{Sm(phen)}$ was done at the DFT and *ab initio* levels of theory.

2.1.3 UV-visible spectroscopy

The UV-visible spectra at various temperature have been measured and are shown in Figure 2.17 for the thulium complex. This spectrum was performed at different temperatures in order to prove that $\mathrm{TmCp}^{\mathrm{ttt}}_2\mathrm{phen}$ was also in equilibrium with its dimeric form. The evolution of the different spectra from 0 ^{0}C to 100^{o}C and the presence of an isosbestic point indicates that there is an equilibrium between two different forms of the molecule.

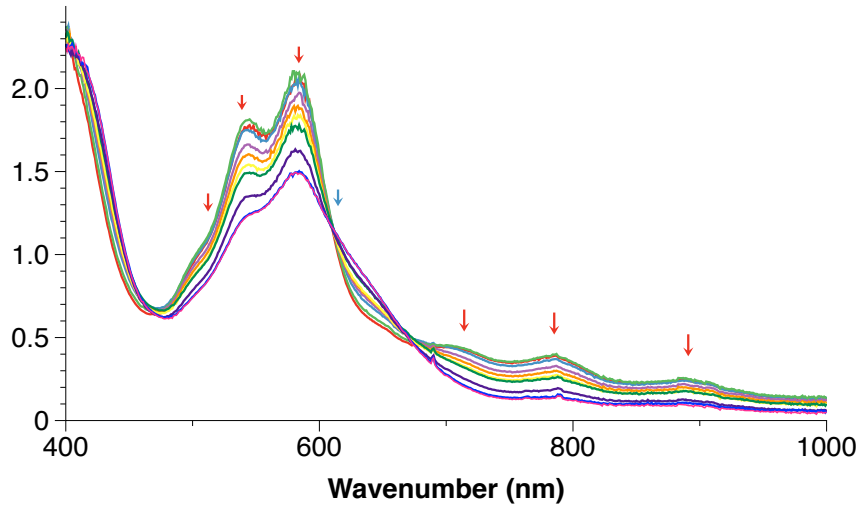

Figure 2.17: UV Visible spectrum of the equilibrium with $TmCp_2^{ttt}phen$ at different temperature, green being 100°C and purple being 0°C; excitations of the monomer are indicated with red arrows and excitations of the dimer are indicated with blue arrows

Monomer	502 nm	542 nm	586 nm	704 nm	780 nm	862 nm	925 nm
Dimer	639 nm						

Table 2.13: List of the different transitions for 1 and 2 between 500 and 1000 nm from the experiment

A deconvolution of the spectra at 100 °C and 0 °C was done using the MCDFit software[68]. The intensity were gathered in order to determine which peak corresponded to the monomer and which peak corresponded to the dimer. The results presented in Table 2.13 indicate that most of the peaks are due to the monomer and that only one peak could be consistent with the dimer. An in depth comparison between these results and already published electronic absorption for phenanthroline radical[69–71] revealed that the excitations in the spectrum corresponded mostly to phenanthroline radical. This is in agreement with already published UV-visible spectra of lanthanide complexes[72].

Moreover, this experiment was performed with other compounds such as $Cp_2^*Yb(phen)$ or $(Cp_2^*Sm(phen))_2$ and the same qualitative spectra are observed, indicating that the visible excitations comes mainly from phenanthroline radical.

The electronic structure of phenanthroline contains three types of molecular orbitals: n, lone pair of the nitrogens that will be in a_1 or b_2 symmetry, σ bond, that will also be in a_1 or b_2 and π, π^* orbitals that will be in a_2 or b_1 symmetry. The excitation mechanism of phenanthroline radical is mostly going to include $n \rightarrow \pi^*$ and $\pi \rightarrow \pi^*$ excitations.

Wavelength	Exp	PBE0-D3	CAM-B3LYP	B3LYP-D3	wB97X-D2	M06
	502					
	542					
$\pi \rightarrow \pi^*$	586	607 (1.5)	569 (3.7)	630 (1.0)	564 (3.9)	620 (1.3)
	704					
	780					
	862					
$\pi \rightarrow \pi^*$	925	948 (85.1)	992 (97.2)	951 (80.7)	989 (99.6)	970 (83.5)

Table 2.14: TDDFT excitation energies (nm) using different density functionals and compared to the experimental data for phenanthroline radical using a PCM solvation model with toluene as a solvent and a cc-pvtz basis set, oscillator strength in parenthesis in part per thousand; experimental corresponds to the experimental spectrum of $\mathrm{TmCp}_2^{\mathrm{ttt}}\mathrm{phen}$

As explained in a previous article[73], the absorption bands for the monomer correspond mainly to $\pi \rightarrow \pi^*$ transitions. In order to identify which transition exactly was creating these peaks and have a better understanding of the electronic structure of the lanthanide complexes, excited states calculations were performed.

2.1.3.1 TDDFT calculations

Previous studies have shown that only focussing on the excitation of the ligand could give reliable spectrum[72] in the case of lanthanide complexes. As such TDDFT calculations on phenanthroline radical were performed. The Table 2.14 regroups the different values for the excitation energy (in nm) and the strength of the oscillators for different functionals (as a part per thousand value).

Jacquemin recently proposed a benchmark review of the different DFT functionals and their application in excited states calculations[74]. His recommendations are to use hybrid or range separated density functionals in order to get close to experimental excited states values. He has also recently described the pitfall of TDDFT for $\pi \rightarrow \pi^*$ transitions[75], which could be related to the excitations of phenanthroline radical.

As a result TDDFT calculations were performed using three hybrids, B3LYP, M06-2X and PBE0 and two long range corrected density functionals ωB97X-D2 and CAM-B3LYP. The latter is known to behave well for excitation properties[74,76].

Only two peaks were obtained in these computations, which is a bad evaluation of the experimental spectrum. There is a small difference between density functionals, with a

Wavelength	Exp	PBE0-D3	CAM-B3LYP	B3LYP-D3	wB97X-D2	M06
$\pi \rightarrow \mathrm{Rydberg}$	502		549 (1.3)	508 (0.2)	531 (0.4)	
$\pi \rightarrow \mathrm{Rydberg}$	542	522 (0.5)	564 (16.2)			539 (1.8)
$\pi \rightarrow \pi^*$	586	566 (177.5)	583 (195.7)	572 (165.9)	584 (213.2)	587 (141.6)
$\pi \rightarrow \mathrm{Rydberg}$	704	617 (2.6)		688 (1.0)		651 (0.5)
$\pi \rightarrow \pi^*$	780	799 (4.3)	738 (6.7)	828 (3.7)	733 (6.5)	818 (5.0)
$\pi \rightarrow \mathrm{Rydberg}$	862		847 (0.4)			
$\pi \rightarrow \mathrm{Rydberg}$	925	911 (0.6)				924 (0.7)

Table 2.15: TDDFT excitation energies (nm) using different density functionals and compared to the experimental data for potassium phenanthroline radical using a PCM solvation model with toluene as a solvent, a cc-pvtz basis on C,N; and H and a 6-311++G(2d,2p) basis set on the potassium; oscillator strength in parenthesis in part per thousand; experimental corresponds to the experimental spectrum of $\mathrm{TmCp}_2^{\mathrm{ttt}}\mathrm{phen}$

maximum of 60 nm between PBE0-D3 and CAM-B3LYP. The oscillator strengths are not agreeing with experimental data, as the 900 nm peak has a higher oscillator strength than the second one, whereas in the experimental data, this is the opposite.

The inclusion of the metal itself might enable a better description of the system. Calculations with lanthanide molecules is rather complex due to the large size of the system and the poor description of the 4f orbitals by DFT. Therefore, a TDDFT spectrum was performed on a potassium phenanthroline radical and $(\mathrm{Cp}_2^*\mathrm{Yphen})_2$. Potassium phenanthroline radical will serve as a better representation of phenanthroline radical in solution and will be compared to the previous results found without the cation. The Table 2.15 contains the values for the excited spectrum of Kphen.

There are still two major $\pi \rightarrow \pi^*$ excitations. The oscillator strength repartition between them is coherent with the experimental spectrum. A lot of $\pi \rightarrow \mathrm{Rydberg}$ excitations are found which are not consistent with what is observed experimentally. The density functional is having a small influence on the $\pi \rightarrow \pi^*$ excitation energies (< 100 nm). However, these computed spectra are very different from those observed.

In order to get closer from the experimental system, yttrium complex of phenanthroline ($\mathrm{Cp}_2^*\mathrm{Yphen}$) spectrum was computed by TDDFT, as it was already done in the literature[72]. The results are presented in Table 2.16.

There is a good similarity between this calculated spectrum and the one calculated with potassium. Both contain only two $\pi \rightarrow \pi^*$ and the oscillator strengths are in the good

Wavelength	Exp	PBE0-D3	CAM-B3LYP	B3LYP-D3	wB97X-D2	M06
	502					
	542			530 (6.6)		
$\pi \rightarrow \pi^*$	586	538 (92.6)	538 (95.5)	546 (79.3)		559 (93.8)
$\pi \rightarrow \pi^*$	704	724 (12.2)	665 (16.5)	742 (10.8)		744 (12.7)
	780					
	862					
	925					

Table 2.16: TDDFT excitation energies (nm) using different density functionals and compared to the experimental data for $(Cp^*_2Yphen)_2$ using a PCM solvation model with toluene as a solvent and a cc-pvtz basis set for all C,N and H and a Stuttgart-Dresden ECP on the yttrium atom, oscillator strength in parenthesis in part per thousand; experimental corresponds to the experimental spectrum of $TmCp^{ttt}_2phen$

order compared to experiments. But, still the excitations do not clearly superpose with the experimental UV-visible spectrum.

Recently, TDDFT calculations have been performed on lanthanide complexes with some success[77]. Further TDDFT excitation calculations on the monomer and on the dimer of samarium ($Cp^*_2Sm(phen)$) were done and compared to previous results. The results in this case are similar to the yttrium case. Only two major $\pi \rightarrow \pi^*$ peaks were found in addition to a couple of $4f \rightarrow 4f$ transitions that were not supposed to appear.

In conclusion, the excitation spectrum of phenanthroline radical seems to be poorly described by DFT. Over four different compounds only two $\pi \rightarrow \pi^*$ transitions were found, which could not explain the experimental UV-visible spectrum. Even though TDDFT has been performed successfully on open-shell[78] and closed-shell system[79] alike over the last decades, many challenges have not been yet defeated as shown recently by Li[80,81] for open-shell molecules and by Corminboeuf[75] for low-lying $\pi \rightarrow \pi^*$ transitions in heteroaromatic molecules. The use of *ab initio* calculations in the context of a radical will bring back the problem of spin contamination, as in the case of phenanthroline radical a simple UHF calculation gives a spin contamination of 33% of the $S(S+1)$. As such, further CC2 or EOM-CCSD that are known to be particularly useful in excited states calculations only gave poor results (Table 2.17).

Wavelength	**Experimental**	RI-CC2	EOM-CCSD
	502		
	542		
$\pi \rightarrow \pi^*$	586	612 (168.0)	539 (2.2)
	704		
	780		
	862		
$\pi \rightarrow \pi^*$	925	948 (1.4)	884 (76.1)

Table 2.17: RI-CC2 and EOM-CCSD excitation energies (nm) compared to the experimental data for radical phenanthroline using a PCM solvation model with toluene as a solvent for **1** with a def2-TZVP basis, oscillator strength in parenthesis in part per thousand; experimental corresponds to the experimental spectrum of $\mathrm{TmCp}_2^{\mathrm{ttt}}\mathrm{phen}$

2.1.3.2 CASSCF calculations

Both *ab initio* and TDDFT calculations showed an excited state close in energy to the ground state of the molecule at less than 1 eV, whatever the method used. This could be the result of a multi-reference ground state wave function. CASSCF calculations on phenanthroline radical could give an insight into the electronic structure of phenanthroline in $\mathrm{Cp}_2^*\mathrm{Sm(phen)}$.

The HF molecular orbitals of phenanthroline have been detailed in Table 2.3. These molecular orbitals will be used as a starting point in order to choose the active space. The resulting absorption spectrum will be compared to the UV-visible spectrum.

- **Active space determination**

Two types of excitations might be of interest in the study of phenanthroline radical: $\mathrm{n} \rightarrow \pi^*$ and $\pi \rightarrow \pi^*$.

In order to support these excitations, the active space should contain lone pair orbitals (n), the π orbitals and several π^* orbitals. The active space was varied and the natural occupation of the different molecular orbitals was evaluated. The results are presented in Table 2.18.

The different active spaces gave similar results consistent with a donation from the lone pair of the nitrogen into the π^* system of the heterocycle. Overall, the ground state electronic structure does not require a large active space to be able to evaluate it correctly, but as excitations are going to be calculated into the π^* system, there is a need to include multiple π^* orbitals in b_1 and a_2 symmetries. Inclusion of more occupied molecular orbitals in

	[9, (1,5,5,1)]	[13, (2,4,4,2)]	[9, (2,3,3,2)]
n_1	1.51	1.51	1.53
n_2	1.48	1.48	1.46
n_3	2.00	2.00	2.00
n_4	2.00	2.00	2.00
π_1	1.96	1.96	2.00
π_2	1.94	1.94	2.00
π_3	2.00	2.00	2.00
π_4	2.00	2.00	2.00
π_1^*	1.42	1.42	1.28
π_2^*	0.57	0.57	0.66
π_3^*	0.01	0.01	0.00
π_4^*	0.00	0.00	0.00
π_5^*	0.04	0.04	0.04
π_6^*	0.05	0.05	0.03
π_7^*	0.00	0.00	0.00
π_8^*	0.00	0.00	0.00

Table 2.18: Natural occupation of the molecular orbitals for phenanthroline radical, the number in parenthesis represent the number of orbital in each symmetry to include in the active space; the orbital names are defined in Table 2.3

the a_1 or b_2 symmetry were not found to be useful. The ground state electronic structure is a multi-reference wave-function involving 41Â % of the configuration $n_1^{\uparrow}\pi_1^{*2}\pi_2^{*0}n_2^2$ and 45 % of $n_1^2\pi_1^{*\uparrow}\pi_2^{*\downarrow}n_2^{\uparrow}$.

The active space was chosen to be [9, (1,5,5,1)] and was used to further calculate the excitation spectrum of phenanthroline radical.

- **Absorption spectrum**

The absorption spectrum can be calculated using different multi-reference methods: CASSCF, CASPT2, MS-CASPT2 and MS-CASPT2-SO. The dipole moments were calculated at each wave function for every excitation. The spectra issued from the calculation of 13 excitations of the [9,(1,5,5,1)] CASSCF and MS-CASPT2-SO calculations are shown in Figure 2.18 and in Table 2.19. The MS-CASPT2-SO involved the spin orbit coupling between the doublet (13 excitations) and the quartet (8 excitations). The quartet was close in energy from the doublet, which validates this approach.

Wavelength	**Experimental**	CASSCF	CASPT2	MS-CASPT2	MS-CASPT2-SO
$\pi \rightarrow \pi^*$	502	445 (8.4)	445 (0.5)	453 (1.29)	481 (2.1)
$\pi \rightarrow \pi^*$	542	539 (6.9)	512 (2.0)	506 (2.45)	559 (5.0)
$\pi \rightarrow \pi^*$	586	575 (1.0)	639 (6.0)	613 (5.4)	586 (2.7)
$\pi \rightarrow \pi^*$	704	667 (1.4)	716 (0.5)	668 (0.8)	666 (0.4)
$\pi \rightarrow \pi^*$	780		740 (5.5)	725 (5.6)	781 (0.3)
$\pi \rightarrow \pi^*$	862		855 (1.2)	948 (0.1)	
$\pi \rightarrow \pi^*$	925	910 (0.6)	993 (0.5)	985 (0.8)	

Table 2.19: Excitation energy (nm) using different multi-reference methods with a PCM(toluene) solvation model and experimental data for $Cp^{ttt}_2Tm(phen)$, oscillator strength in parenthesis in part per thousand; experimental corresponds to the experimental spectrum of $TmCp^{ttt}_2phen$

As expected, the first excited state was close in energy from the ground state (only 0.04 eV). As such the ground state is defined as the combination of both this first excited state and the actual ground state of the system.

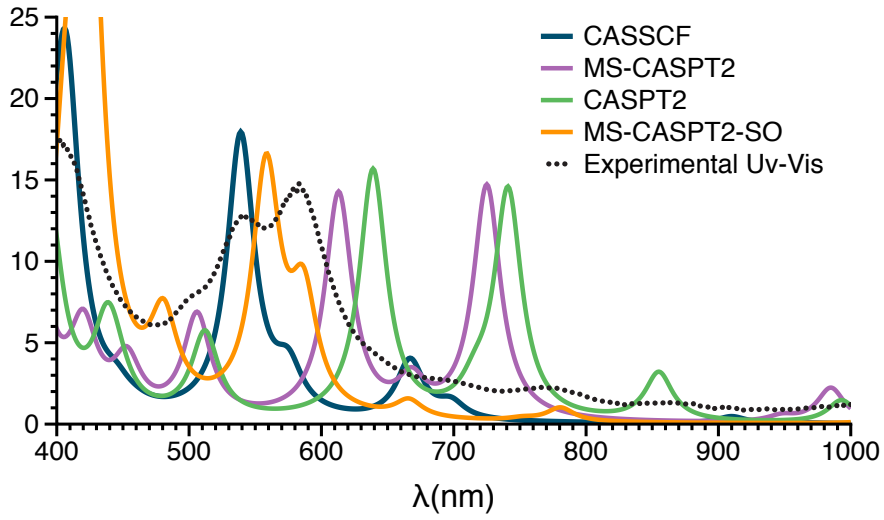

Figure 2.18: Multireference spectra of phenanthroline radical and experimental UV-visible of the equilibrium using a PCM(toluene) solvation model; convolution with a Lorentzian function with FWHM = 25 nm

Contrary to what was previously found with either TDDFT or CC2, the three major peaks of the spectrum are well represented using multi-reference methods. The different excitations are all $\pi \rightarrow \pi^*$ excitations. Compared to the CASSCF calculation, the MS-CASPT2 or CASPT2 calculations do not reproduce well the experimental absorption spectra. The MS-CASPT2-SO excitation energies are close to the three mains experimental excitation energies. This might result from an involvement of the quartet in the excitation spectrum

Wavelength nm	**Experimental**	PBE0-D3	ωB97X-D3	B3LYP-D3	M06-2X
$\pi \rightarrow \pi^*$	639	709	547	752	575

Table 2.20: TDDFT excitation energy (nm) of the di-anion phen-phen using different functional and a PCM solvation model and experimental data of $Cp^{ttt}_2Tm(phen)$

of phenanthroline radical, which was not expected. This is related to the small difference in energy between the two states.

Globally, these multi-reference calculations are in good agreement with the experimental spectrum. Similar CASSCF calculations were performed on phenanthroline radical without taking into account the symmetry. The resulting CASPT2, MS-CASPT2-SO or CASSCF excitation energies were in worse agreement with the experimental spectrum which validates the use of the symmetry to study the electronic structure and the excitations of radical N-heterocycles. One question that remains to be solved is about the excitations of the dimer **2**.

- **Absorption spectrum of the σ dimer**

The σ dimer can be described easily. It may not involve a multi-reference state as all the electrons are already paired up. As a result, contrary to previous calculations, simple TDDFT should give meaningful results.

Excitations of the di-anion dimer phen-phen are presented in Table 2.20.

Using TDDFT, one excitation corresponding to the transition from the HOMO (σ bond and π interaction) to a π^* of the system is found whatever the density functional. The excitation energy varies between the density functionals, but overall the excitation is identical.

2.1.3.3 Partial conclusion

The experimental UV-visible spectrum has been compared to theoretical excitation spectra. The computational study has shown that excitation of phenanthroline radical can not be analysed only by TDDFT, RI-CC2 or EOM-CCSD calculations. Indeed, phenanthroline possesses a multi-reference ground state, that can only be investigated using mulitreference methods. On the other hand, the dimer does not possess such a multi-reference wave function and simple TDDFT calculations are able to reproduce experimental data with errors of less than 100 nm.

Experimentally, $Cp^*_2Ln(phen)$ complexes (with Ln being Yb, Sm, or Tm) have the same electronic absorption than phenanthroline radical. This is indicative of the electronic structure of the lanthanide complex itself. The ground state of phenanthroline radical is a multi-reference one which involves the lone pair of the nitrogen and the two π^* of phenanthroline of b_1 and a_2 symmetry. As a result, the bonding interaction between the lanthanide and the phenanthroline moiety is weak. If it was not weak, the lone pair could not be involved in a delocalisation into the π^* system.

Initially, CASSCF calculations on $Cp^*_2Sm(phen)$ did not show a multi-reference wave function on the π^* of phenanthroline. Experimentally the ground state of this complex possesses the same electronic structure than phenanathroline radical, *i.e.* a multi-reference one. Hence, the initial CASSCF calculation did not produce the correct results concerning the complex.

A new active space was designed with the seven 4f orbitals and one 5d orbital of samarium and three π^* and the two lone pair of phenanthroline (CASSCF(10,13) with 60 excitations). At this level of theory, the excitation energy from $4f^5\pi^{*\uparrow}_{b_1}$ to $4f^5\pi^{*\uparrow}_{a_2}$ is 0.85 eV. While no multi-configuration was observed on the ground state of the complex, this low excitation energy might be a sign that both states are combined at room temperature. Expanding the active space above the 13 orbital space was not possible despite our best efforts. The restrictions of the CASSCF level of theory pose the limit of the electronic structure calculation of $Cp^*_2Sm(phen)$.

The dimerisation process of heterocycles has been know for a long time[82–84]. The first example for the dimerisation of pyridine using sodium dates from the 1960s. The understanding of the inner mechanisms of this type of dimerisation is unknown.

2.1.4 Is it a π dimer or a σ dimer?

Bond formation between aromatic compounds has been a subject of investigation in the last decades. The phenalenyl compound has been studied both theoretically and experimentally in this matter, as it can perform two distinctive types of dimerisation: σ and π[85,86]. These two types of dimerisation occur when different substituants are encountered on the moiety

Distance C-C (Å)	Cp^*	Cp^{tt}
Experimental	1.61(1)	1.58(1)
PBE ZORA2	1.64	1.65
PBE-D3 ZORA2	1.63	1.64
PBE-D3 ZORA2 solv	1.62	1.64
PBE-D3 ZORA3	1.63	1.64
PBE-D3 LC-ECP	1.61	1.60
M06L ZORA2	1.62	1.63

Table 2.21: C-C distance using different levels of theory for $(Cp^{tt}_2Sm(phen))_2$ and $(Cp^*_2Sm(phen))_2$

itself[87]. However, understanding the reasons why π or σ bonding is preferred is still unknown, to the best of our knowledge.

Such type of bi-radical was observed by the group of Abe[88] experimentally. They developed experimental techniques to follow the ultrafast transition between the triplet and the open-shell singlet bi-radical, with a π bonding interaction and the closed-shell singlet[89]. This type of study indicates that σ bonds can exist as multiple resonance structures which involve π and σ compounds. In this sense, the phenanthroline dimer synthesised previously could be an interesting case of study. In the ytterbium case, dimethyl-phenanthroline dimer was observed in the crystal structure as both a π and a σ dimer[32]. This raises the question of the π dimer energy compared to the σ dimer for samarium in solution.

Experimentally, $(Cp^*_2Yb(phen))_2$ showed a $C-C$ bond distance of 1.618 Å. Using calculations, this distance was difficult to reproduce and was longer than the experimental one (1.67 Å using PBE-D3).

The same distance observation was found for Cp^{tt}_2Sm complexes of phenanthroline. Changing the density functional in the optimisation did not solve this problem, as the difference between the experimental and computed value was large (almost 0.05Å) (Table 2.21).

This difference could be related to packing interactions that are not treated accurately when optimising the geometry. But, if the packing interaction is strong, could it mean that in solution, the σ dimer breaks to form a π dimer (Figure 2.19)?

This hypothesis is somewhat validated by calculations presented previously. Spin contamination indicates that the σ dimer is contaminated by the bi-radical π dimer or two mono radicals. Could this mean that the experimental ΔG is evaluated between the monomer

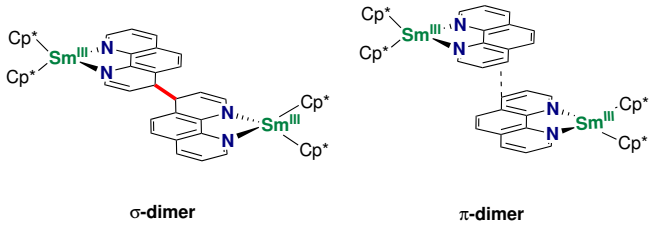

Figure 2.19: π-dimer vs σ-dimer structure

and the π dimer? Finally, the UV-visible spectrum only showed one excitation in the visible area for what is considered as the σ dimer. But, could it be possible that instead of having excitation for a σ dimer, the π dimer was the only one involved?

It is still difficult to answer these questions. EPR analyses are in progress in order to study the presence in solution of a bi-radicaloid species or a mono-radical species. These kind of data would enable a better understanding of this dimerisation process, which could give information on the differences observed between ytterbium and samarium complexes of phenanthroline.

Pyridine dimerisation process was investigated in the early 70s with sodium[82–84]. While sodium reduces pyridine, ytterbium does not. Hence, the redox potential of the reducing agent has to play a role in the C-C σ coupling of pyridine and as an extension, in the C-C σ coupling of phenanthroline. We could then formulate an hypothesis on why ytterbium complexes favours radical monomer while samarium complexes favours σ dimer: the redox potential plays a role in the formation of the C-C bond.

2.2 Ketone reduction

Contrary to heteroarene reduction, ketone reduction by lanthanide complexes has been extensively studied experimentally[1] by changing the reaction conditions such as the solvent, additives, etc. Kinetic studies have been performed[7,8] and have been used to improve the reaction yields, by the addition of a protic source during the reaction. However, few studies only were focussed in the isolation of the organometallic intermediates and their further study.

Phenanthroline complexes are in equilibrium between their monomeric and dimeric form. As such, it would be interesting to understand if ketone complexes are following the

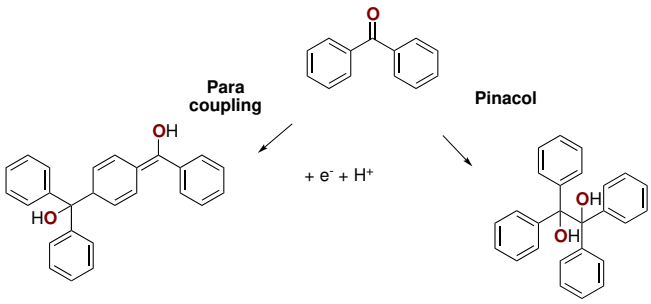

Figure 2.20: Different types of coupling for benzophenone

same rule and if not, what triggers the equilibrium itself. The techniques described above will be a good starting point to study the reduction of both benzophenone and chalcone.

2.2.1 Benzophenone: is there an equilibrium?

2.2.1.1 Thf and acetonitrile

Benzophenone (bph) is one of the most easily reducible ketone, due to the presence of two phenyl rings. The ketyl radical synthesised can further react and create a C-C bond and a dimeric structure as exposed earlier for phenanthroline. Other types of rearrangement can also occur as shown in Figure 2.20[90].

Over the years, multiple groups have been interested in the reduction of benzophenone by lanthanide complexes. The ligand surrounding the lanthanide ion is of particular importance as much as the solvent itself. Wakatsuki *et al.* were able to show that there was an equilibrium between the monomer and dimeric form of fluorenone complexes of lanthanide[91] and that the solvent had an influence onto the formation of the ketyl radical and the dimeric structure. The ligand[92] has also been used to produce different coupling products.

In the case of benzophenone, studies using very reductive reagents such as DyI_2 or $SmTMS_2$ have been able to characterise the ketyl radical complex, while studies with bulky ligands have been able to show the coupling on the phenyl moieties[93]. Only rare papers try to focus on the isolation of organometallic derivatives for SmI_2 reagents and to the best of our knowledge no crystal structure of the benzophenone reduced compound with SmI_2 exists in the CCDC database. Moreover, the addition of proton donors influences the formation of either the the benzhydrol (protonated monomer) or the pinacol (protonated

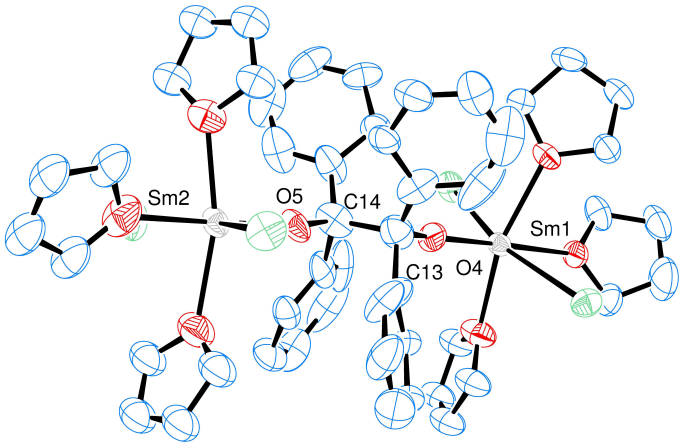

Figure 2.21: X-Ray crystallographic structure of the dimer of benzophenone; significant bond distances: C — C 1.58(3) Å, Sm — O (ketone - avg) 2.08(1) Å, Sm — O (thf - avg) 2.45(2) Å, Sm — I (avg) 3.100(1) Å

dimer) depending on its concentration[94]. As a result, the study of the benzophenone reduction by SmI_2 could be of interest in understanding the C-C σ bond strength and the importance of additives on its stability.

Reaction of one equivalent of SmI_2 and benzophenone was done in thf. Upon addition of a solution of benzophenone in thf, the solution changes from deep blue to clear yellow. After a few days at -40 ^{o}C, small crystals were grown and were suitable for X-Ray diffraction studies (Figure 2.21).

Three thf molecules surround the lanthanide center in order to complete its coordination sphere. The C-C bond distance is only 1.58 Å as expected from previous results with phenanthroline. The somehow long distance of the C-C bond could mean that an equilibrium exists between the ketyl radical and the σ dimer.

This dimeric compound is not soluble in many solvents. As a result, following the reaction by ^{1}H NMR is difficult in thf as the compound precipitates during the reaction. While in acetonitrile the compound is more soluble, precipitation of the dimeric structure occurs very rapidly after the beginning of the reaction. At the end of the reaction, the acetonitrile solution is yellow, which is the characteristic color of the pinacol compound. Increasing the

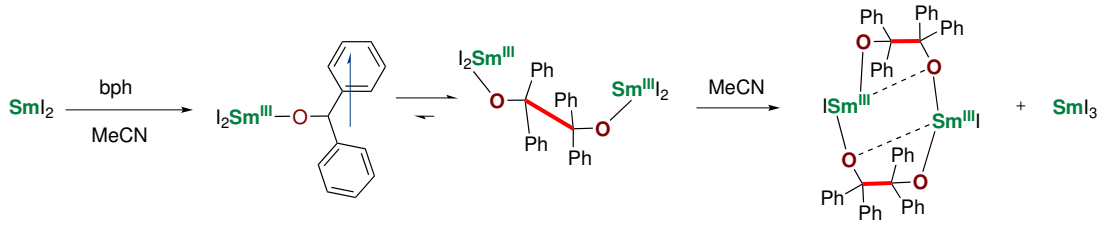

Figure 2.22: Final products obtained in acetonitrile, as observed using X-Ray diffraction analysis; acetonitrile molecules were removed for clarity

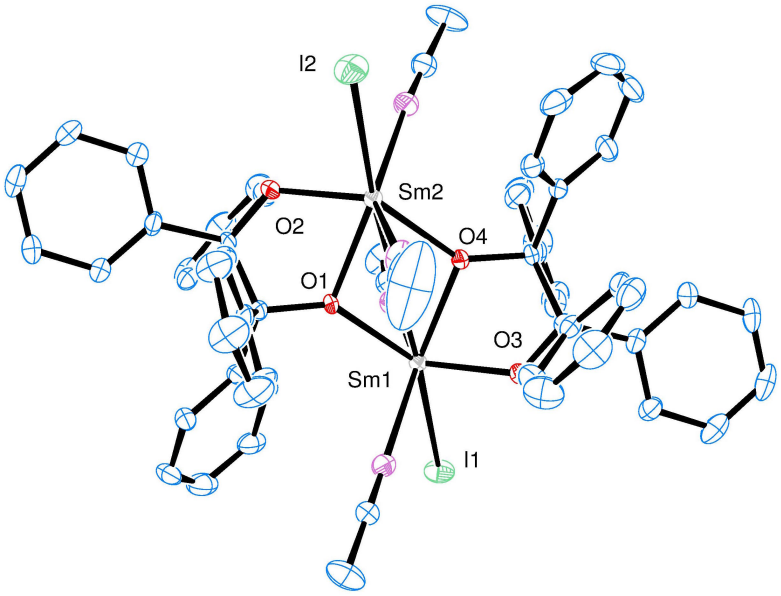

Figure 2.23: X-Ray Crystallographic structure of the dimer of benzophenone; significant bond distances: C-C (avg) 1.619(6) Å, Sm1-O3 2.132(3) Å, Sm1-O4 , Sm1-01 2.317(3) Å, Sm1-O4 2.348(3) Å, Sm2-O2 2.132(3) Å, Sm2-O4 2.306(3)Å, Sm2-O1 2.338(3) Å, Sm-N (MeCN - avg) 2.557(3) Å, Sm-I (avg) 3.1475(3) Å

temperature of the solution to 80 °C changed the color of the solution to dark/green, which might indicate the presence at high temperature of the ketyl radical.

In acetonitrile, contrary to what happened in thf, two different crystal structures were obtained which is consistent with the reaction mechanism detailed in Figure 2.22. The X-Ray crystallographic structure of both SmI_3 and a bis-pinacol dimeric samarium complex, $(ISm(bph-bph))_2$, were obtained in acetonitrile at -40 °C (Figure 2.23). The final products of the reaction are different from what was obtained in thf. Acetonitrile favours the formation of the ionic species SmI_3 whereas thf does not. This was already observed for actinide complexes[95].

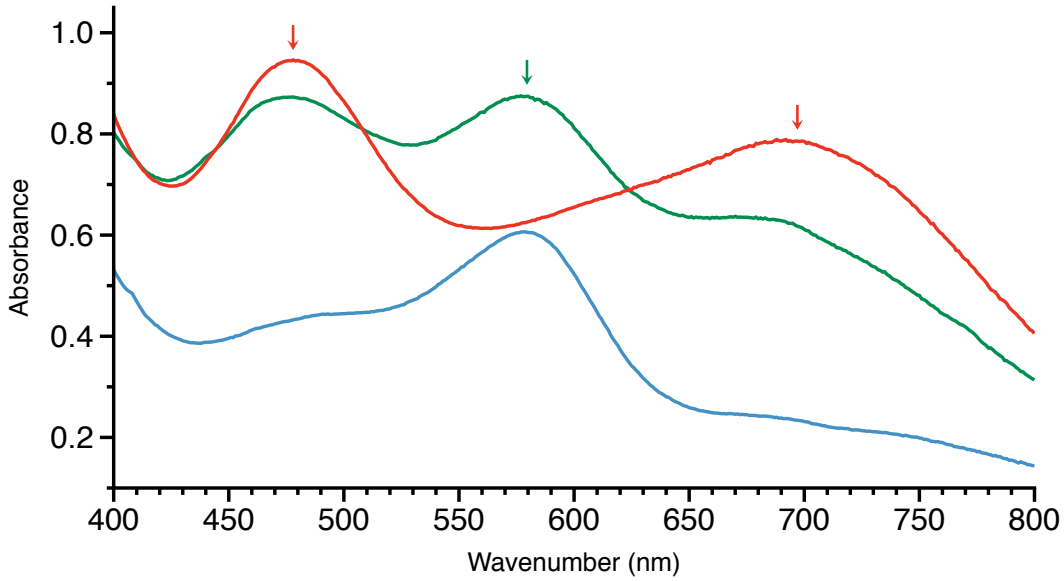

Figure 2.24: UV-visible spectrum in pyridine of $I_2Sm(pyr)$ (red) at room temperature and of $I_2Sm(bph)$ at room temperature (blue) and at 100 °C (green); green arrow indicates the peak of benzophenone ketyl radical and red arrows indicate the peak of pyridine radical

Evaporation of thf, resulted in a yellow powder. While changing the solvent from thf to acetonitrile gave the same yellow solution, putting the yellow solid into pyridine led to a deep black/purple solution, characteristic of the ketyl radical.

2.2.1.2 Pyridine

At room temperature, SmI_2 is capable of reducing pyridine[96]. As a result pyridine is a "non-innocent" solvent that could trigger interesting reactivity for lanthanide complexes.

Crystals of $(I_2Sm(bph)(thf)_3)_2$ were dissolved in pyridine. After a few minutes stirring at room temperature, the solution turned black purple. The resulting compound (named $I_2Sm(bph)$) was analysed by UV-visible spectrum at two temperatures (room temperature and 100 °C) and compared to the spectrum of $I_2Sm(pyr)$ obtained at room temperature (Figure 2.24).

The spectrum at room temperature for $I_2Sm(bph)$ is characteristic of a benzophenone ketyl radical, with an absorption at 550 nm corresponding to a $\pi^* \rightarrow \pi^*$ transitions tabulated in the literature[97]. The spectrum at high temperature contains two peaks characteristic from the $I_2Sm(pyr)$ radical complex, which might be in equilibrium with the ketyl radical.

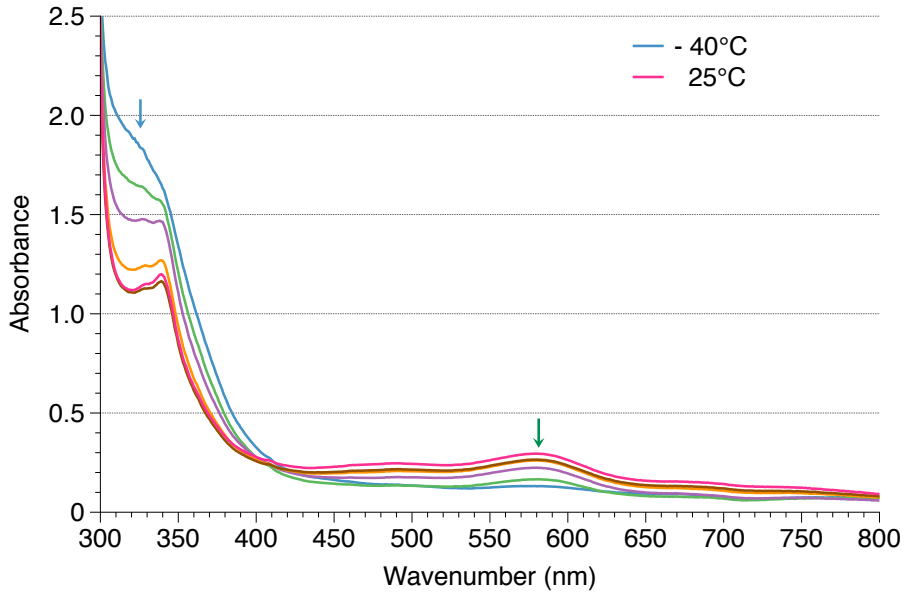

Figure 2.25: Variable temperature UV-visible spectrum between -40°C (blue) and 25°C (red); blue arrow indicates the peak of the σ dimer benzophenone compound and green arrow indicates the peak of benzophenone radical

At low temperature (-40,°C), the color of the solution changes from deep blue to yellow. This colour evolution was followed by UV-visible. The variable temperature UV-visible spectrum showed the presence of an isosbestic point at 400 nm (Figure 2.25). This isosbestic point indicates the presence of an equilibrium between two forms of the molecule. The apparition of a peak at 330 nm could be due to the formation of a dimeric species of benzophenone.

A ^{1}H NMR of the reaction was performed from -35°C to 50°C and showed the disappearance of peaks that could be related to the dimer and apparitions of other peaks that might correspond to the ketyl radical (Figure 2.26). The spectrum was too paramagnetic to enable a complete integration of the different peaks and disabled the evaluation of ΔG via an Eyring plot.

There is an equilibrium in solution between three forms of the molecule: the radical monomeric form of benzophenone, the σ dimer and the pyridine radical. This means that at low temperature, the formation of the dimer is favoured (*i.e.* $\Delta G < 0$) and that at room temperature the monomer formation is favoured thermodynamically (*i.e.* $\Delta G > 0$). Finally, at high temperature, there is formation of a pyridine radical intermediate. This could have

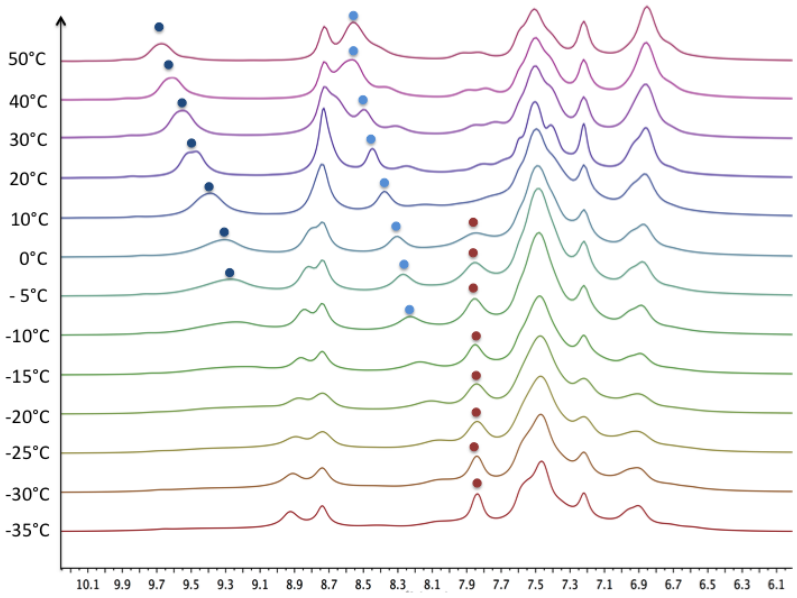

Figure 2.26: Variable temperature ^{1}H NMR in pyridine-d5; red dots indicate the disappearance of peaks and blue dots indicate the appearance of peaks

significant impact in organic chemistry: the σ bond in the pinacol compound can be broken easily. The radical on the benzophenone can also be transferred to the pyridine adduct.

However, it is still unclear what the role of the solvent medium is. Is it only acting as a ligand and by doing that acting as a donor? Could it give electron density to 5d or 4f orbitals of the samarium depending on the ligand surrounding it? Is the radical stabilised because some of its excited states involves pyridine radical? Is the ketone itself important? Changing the ketone, by enabling a larger delocalisation and thus an easier reduction, could trigger an evolution in the stability of the ketyl radical. The performance of the ketone in the radical/dimer equilibrium is of crucial interest in order to better understand its behaviour.

2.2.1.3 What happens when the ketone is changed?

The redox-potential of the ketone has an importance in the reversible mechanisms. Chalcone has the advantage of having an even more delocalised radical, which should stabilise it and further stabilise the ketyl radical complex. The reaction of one equivalent of SmI_2 and one equivalent of chalcone led to a yellow solution (Figure 2.27). The structure was determined by X-Ray crystallographic experiments but the data was not good enough to enable a comparison between the distances for benzophenone and chalcone. The X-Ray crystallographic structure

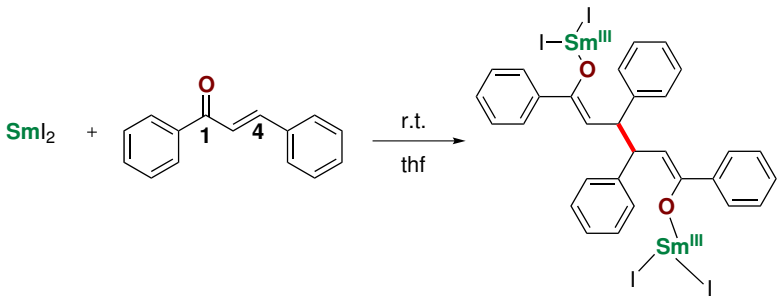

Figure 2.27: Chalcone reduction with SmI_2

showed that the coupling happened in the 4^{th} position, which leads to more coordinations of thf molecules around the lanthanide center.

This coupling in the 4^{th} position leads to a stabilisation of the dimeric structure, as no experimental differences were observed while changing the solvent from thf to pyridine or while heating the solution. This behaviour might be the result of the redox potential of both compounds[98,99]: chalcone is easier to reduce than benzophenone. As a result, the C-C σ bond is stabilised for chalcone and reduction of pyridine is not favoured which decreases the stability of the radical itself.

The dimerisation of benzophenone presents an interesting behaviour, with an equilibrium between three states of the molecule. In order to understand this equilibrium, thermodynamic constants were computed at the DFT level of theory using two solvent media: thf and pyridine. The knowledge acquired on the phenanthroline example could be of huge interest in this case in order to differentiate both solvent.

2.2.2 Quantum chemistry details for the dimerisation process

2.2.2.1 Evaluation of thermodynamic constants

Describing accurately the solvent medium for SmI_2 reaction is of high importance because depending on the solvent its reactivity is different. In the present case, thf and pyridine induce two different behaviours for the reduction of benzophenone.

Firstly, the solvent medium was treated explicitly by adding coordinated solvent molecules to the samarium ion. Based on the crystal structure, three molecules of thf or three molecules of pyridine were coordinated to samarium before the geometry optimisation. In addition to

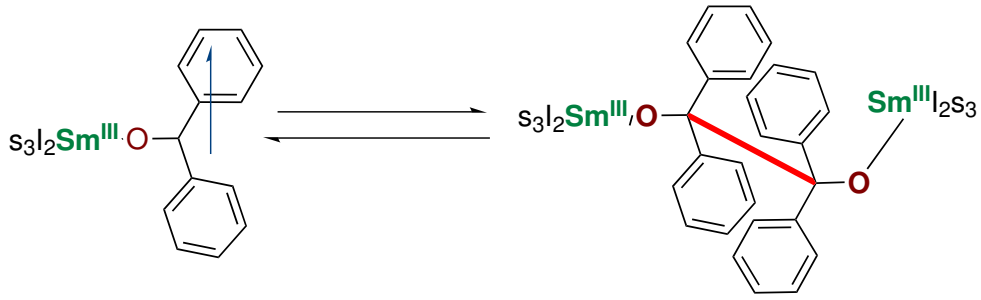

Figure 2.28: Reaction studied using DFT; s is a solvent molecule, either thf or pyridine

Distance (Å)	Experimental (thf)	Thf	Pyridine	
		Gaz	Gaz	Solvant
C — C bond created	1.58(3)	1.63	1.63	1.64
Sm — O (ketone - avg)	2.08(1)	2.11	2.10	2.12
Sm — I(avg)	3.100(1)	3.09	3.11	3.13
Sm — N (avg)			2.64	2.59
Sm — O (thf - avg)	2.45(2)	2.49		

Table 2.22: Distances in angstroms for the PBE-D3 and the crystallographic structures of the dimer in different solvent (thf and pyridine), where avg stands for average, Solvant indicates that in addition to explicit solvent molecules, implicit solvent model COSMO was also used

this procedure, a COSMO solvation model was also used for the pyridine adduct. Table 2.22 gathers all the structural informations and compares them to the thf crystallographic structure.

As said previously, the inclusion of a COSMO solvation model to optimise the geometry only gave minimum difference with the gaz phase optimisation. The C-C σ bond distance is still different between the optimised structure and the experimental one. The effect of packing in this kind of bond is very important in order to describe them accurately. The energy differences between the monomer and the dimer were calculated using different density functionals. The results are presented in Table 2.23.

The energy values are strongly functional dependent. They vary from 11 to -35 kcal/mol for thf and from -40 to 7 kcal/mol for pyridine complexes. This difference follows the same trend than for phenanthroline complexes of samarium: GGA favours monomeric structures while hybrid functionals such as PBE0 or M062X favours dimeric structures. For both complexes, the addition of an implicit solvation model destabilises the formation of the dimer as ΔG is larger with the solvation model than without it (14 kcal/mol and 5 kcal/mol

Method	thf		Pyridine	
	ΔH	ΔG	ΔH	ΔG
PBE-D3	-9	11	-12	7
PBE0-D3	-55	-35	-30	-8
PBE0-D3 + COSMO	-41	-21	-25	-3
M06-2X	-47	-27	-62	-40

Table 2.23: ΔG and ΔH computed energies (kcal/mol) with different density functionals for the equilibrium with benzophenone complexes of samarium, in two different solvents: thf and pyridine

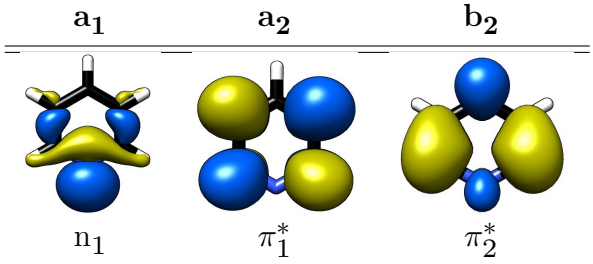

Table 2.24: Natural molecular orbitals of pyridine at the CASSCF(7,[1,0,4,4]) level

difference respectively for thf and pyridine). Overall, for the different density functionals, the thf complexes are more easily transformed into the dimer compared to the pyridine complex. This is in agreement with the experiment as pyridine favours the presence of the monomer radical while thf favours the presence of the σ dimer.

Depending on the density functional used, the energy difference is varying significantly. The treatment of the solvent effects in the quantum chemistry calculation might be related to this difference. During the transformation from the monomer to the dimer, the solvent will have a strong influence.

2.2.2.2 Excited states calculations

The presence of an equilibrium between the ketyl radical and the pyridine one at high temperature was also investigated at the CASSCF level of theory. As the phenanthroline ligand, pyridine is a molecule of C_{2v} symmetry. Its valence molecular orbitals are gathered in Table 2.24.

The pyridine radical anion ground state electronic structure is similar to the one from phenanthroline radical : the lone pair of the nitrogen is involved in a donnation into the π_2^* orbital of the pyridine molecule. If there is an equilibrium with the pyridine radical moiety

for $I_2Sm(bph)(pyr)_3$, the π_2^* orbital will be occupied depending on the temperature. In order to study the position of this excited state, the ground state for $I_2Sm(bph)(pyr)_3$ was investigated at the CASSCF level of theory, using the data gathered from the CASSCF of pyridine; further excited states calculations were then performed in order to get the energy distance between the benzophenone and the pyridine radical inside the molecule.

In order to perform such a calculation, the active space was chosen as the seven 4f orbitals of samarium, the lowest π_{bph}^* of benzophenone, the lowest π_2^* of one pyridine moiety accompanied by its corresponding nitrogen lone pair and one 5d orbital of the lanthanide with the right symmetry to have an overlap with the π_2^* of this pyridine moiety (Table 2.25). Using this active space, the ground state of the complex is $4f^5\pi_{bph}^*$. The first excited state involving the π_2^* of pyridine was at a relatively high energy from the ground state, *i.e.* 40 kcal/mol. But the overall close vicinity of the states with the π_{bph}^* occupied and the π_2^* occupied might trigger an equilibrium between the two states of the molecules. The electronic structure may also be influenced by the implicit treatment of the solvent, the augmentation of the active space size and the increase in the number of solvent molecules surrounding the lanthanide.

Then, the difference between thf and pyridine could be of two different orders. On one side, the difference in electronic structure, with the relative closeness of the excited states of pyridine, might stabilise the radical species over the dimeric species at room temperature using pyridine as a solvent. Moreover, the donation from the pyridine moieties to the lanthanide center is more important than the one from acetonitrile which might result in a stabilisation of the radical. On the other hand, it is still unclear whether in solution the iodide atoms are uncoordinated to the lanthanide centre, which might change the overall behaviour of the compound. Crystallographic structures of SmI_3 in either acetonitrile or pyridine present this kind of difference as in acetonitrile the iodide atoms are uncoordinated while in pyridine they are (structures not shown here). This difference could explain the poor results obtained at the DFT level.

2.3 Conclusion and perspective

In conclusion, the quantum chemistry tools bring a better understanding of both the electronic structure of electron transfer to organic moieties and the relative stabilisation of monomeric

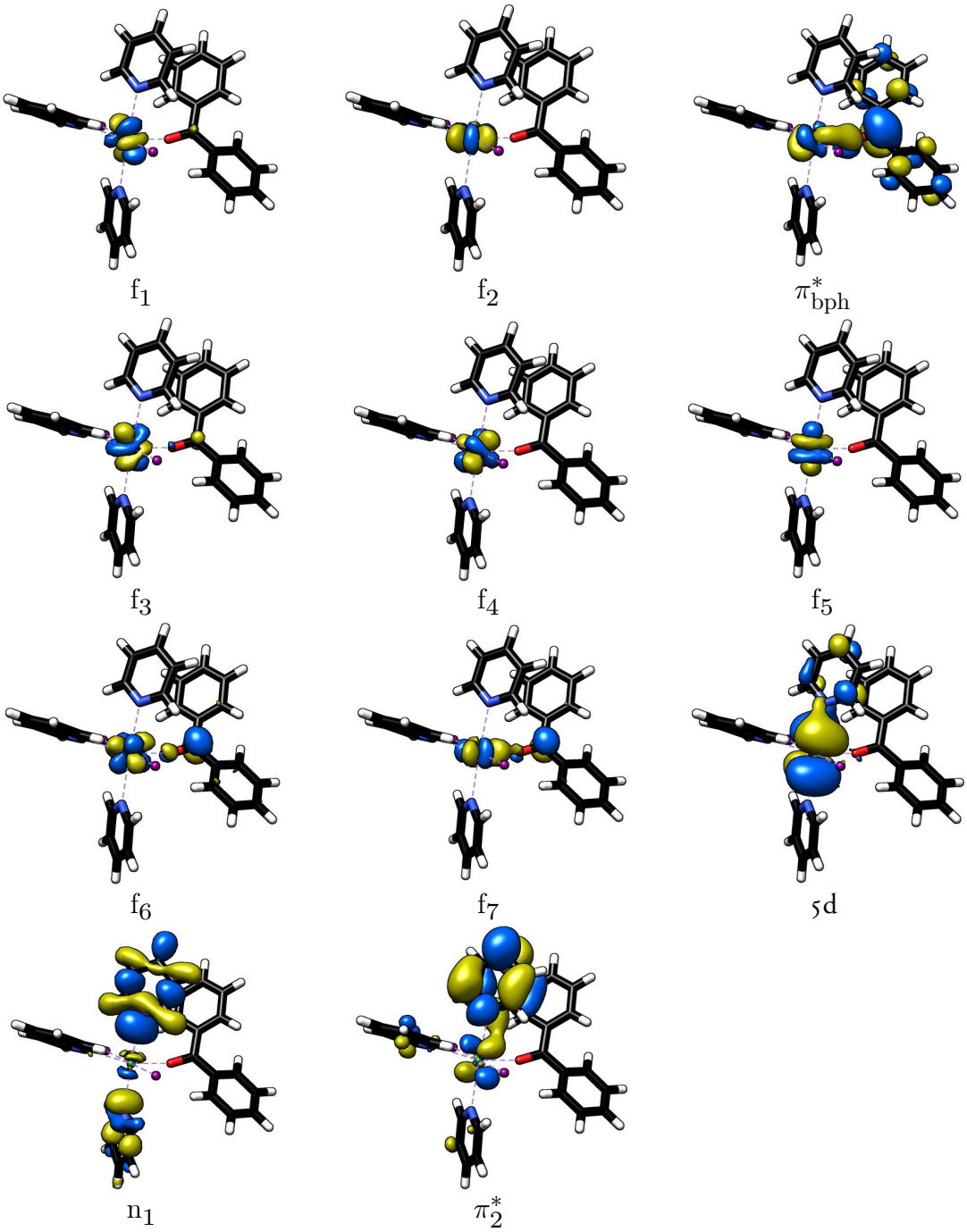

Table 2.25: Molecular orbitals of $I_2Sm(bph)(pyr)_3$ at the CASSCF(8,11) level

versus dimeric structures in these reactions.

Firstly, for phenanthroline electron transfer, the electronic structure of the monomeric samarium complex of phenanthroline radical was analysed using both DFT and CASSCF calculations. The DFT energy results were compared to the experimental ones and a relationship between the HF exchange percentage and the precision of the DFT result was demonstrated. The spin contamination, related to the presence of a bi-radicaloid species close in energy from the σ dimer, prevented the correct evaluation of the energy. This spin contamination was related to the charge transfer in the 4f or the 5d orbitals of the complex. The electronic structure of $\mathrm{Cp}^*_2\mathrm{Sm(phen)}$ was further assessed using experimental UV-visible experiments compared to TDDFT/CASSCF results. The multi-configuration found in the ground state for phenanthroline radical involves one lone pair of phenanthroline. As a result, for $\mathrm{Cp}^*_2\mathrm{Sm(phen)}$, the lone pair is not involved strongly in the interaction between the lanthanide and the phenanthroline ligand.

Investigating further reduction of benzophenone by $\mathrm{I_2Sm}$ complexes led to large differences between solvents, as experimentally in pyridine an equilibrium between the monomeric, dimeric and pyridine radical complex was found, whereas in thf, the dimeric structure did not evolve to the monomeric form and in acetonitrile the molecule is dissociated into $\mathrm{SmI_3}$ and $(\mathrm{ISm(bph_2)})_2$. These results have been related to the charge transfer from the ligand to the lanthanide and the proximity from the radical delocalisation on the pyridine moieties.

It is still difficult to understand exactly in which cases there is a stabilisation of the radical over the dimeric structure. Quantum chemistry points out towards a better donation to the lanthanide centre. Experimental understanding could pass through the use of $\mathrm{Cp}^*_2\mathrm{Sm(phen)}$ and $\mathrm{I_2Sm(bph)}$ in reactions where the radical is involved. The use of a persistent radical such as tempo or the use of a better donor than pyridine such as phenanthroline could also shed light into the electronic structure of both compounds.

References

[1] H. B. Kagan, *Tetrahedron* **2003**, *59*, 10351–10372.

[2] D. J. Procter, R. A. Flowers, T. Skrydstrup, *Organic Synthesis Using Samarium Diiodide*, Royal Society of Chemistry, **2010**.

[3] X. Just-Baringo, I. Yalavac, D. Procter, *Organometallic Chemistry* **2016**, *40*, 1–32.

[4] M. Szostak, M. Spain, D. J. Procter, *Chem. Soc. Rev.* **2013**, *42*, 9155–9183.

[5] T. Maisano, K. E. Tempest, D. V. Sadasivam, R. A. Flowers II, *Org. Biomol. Chem.* **2011**, *9*, 1714–1716.

[6] E. Prasad, R. A. Flowers, *J. Am. Chem. Soc.* **2005**, *127*, 18093–18099.

[7] T. V. Chciuk, W. R. Anderson, R. A. Flowers, *J. Am. Chem. Soc.* **2016**, *138*, 8738–8741.

[8] T. V. Chciuk, R. A. Flowers II, *J. Am. Chem. Soc.* **2015**, *137*, 11526–11531.

[9] M. Shabangi, R. A. Flowers, *Tetrahedron Lett.* **1997**, *38*, 1137–1140.

[10] H. B. Kagan, J. L. Namy, P. Girard, *Tetrahedron* **1981**, *37*, 175–180.

[11] R. S. Miller, J. M. Sealy, M. Shabangi, M. L. Kuhlman, J. R. Fuchs, R. A. Flowers, *J. Am. Chem. Soc.* **2000**, *122*, 7718–7722.

[12] T. V. Chciuk, W. R. Anderson, R. A. Flowers, *Angew. Chem. Int. Ed. Engl.* **2016**, *55*, 6033–6036.

[13] M. Szostak, M. Spain, A. J. Eberhart, D. J. Procter, *J. Org. Chem.* **2014**, *79*, 11988–12003.

[14] E. Prasad, B. W. Knettle, R. A. Flowers, *J. Am. Chem. Soc.* **2002**, *124*, 14663–14667.

[15] M. Plesniak, X. Just-Baringo, F. Ortu, D. P. Mills, D. J. Procter, *Chem. Commun.* **2016**, *52*, 13503–13506.

[16] M. Szostak, M. Spain, D. J. Procter, *Angew. Chem. Int. Ed. Engl.* **2013**, *52*, 7237–7241.

[17] W. J. Evans, N. T. Allen, *J. Am. Chem. Soc.* **2000**, *122*, 2118–2119.

[18] W. J. Evans, N. T. Allen, J. W. Ziller, *J. Am. Chem. Soc.* **2000**, *122*, 11749–11750.

[19] A. A. Fagin, T. V. Balashova, D. M. Kusyaev, T. I. Kulikova, T. A. Glukhova, N. P. Makarenko, Y. A. Kurskii, W. J. Evans, M. N. Bochkarev, *Polyhedron* **2006**, *25*, 1105–1110.

[20] M. Szostak, D. J. Procter, *Angew. Chem. Int. Ed. Engl.* **2012**, *51*, 9238–9256.

[21] W. J. Evans, T. A. Ulibarri, J. W. Ziller, *J. Am. Chem. Soc.* **1988**, *110*, 6877–6879.

[22] W. J. Evans, C. A. Seibel, J. W. Ziller, *Inorg. Chem.* **1998**, *37*, 770–776.

[23] L. Castro, S. Labouille, D. R. Kindra, J. W. Ziller, F. Nief, W. J. Evans, L. Maron, *Chem. Eur. J.* **2012**, *18*, 7886–7895.

[24] W. J. Evans, D. K. Drummond, L. R. Chamberlain, R. J. Doedens, S. G. Bott, H. Zhang, J. L. Atwood, *J. Am. Chem. Soc.* **1988**, *110*, 4983–4994.

[25] M. Schultz, PhD thesis, University of California, Berkeley, **2000**.

[26] D. J. Berg, J. M. Boncella, R. A. Andersen, *Organometallics* **2002**, *21*, 4622–4631.

[27] M. Schultz, J. M. Boncella, D. J. Berg, T. D. Tilley, R. A. Andersen, *Organometallics* **2002**, *21*, 460–472.

[28] M. D. Walter, D. J. Berg, R. A. Andersen, *Organometallics* **2006**, *25*, 3228–3237.

[29] C. H. Booth, M. D. Walter, D. Kazhdan, Y.-J. Hu, W. W. Lukens, E. D. Bauer, L. Maron, O. Eisenstein, R. A. Andersen, *J. Am. Chem. Soc.* **2009**, *131*, 6480–6491.

[30] C. H. Booth, D. Kazhdan, E. L. Werkema, M. D. Walter, W. W. Lukens, E. D. Bauer, Y.-J. Hu, L. Maron, O. Eisenstein, M. Head-Gordon, R. A. Andersen, *J. Am. Chem. Soc.* **2010**, *132*, 17537–17549.

[31] G. Nocton, C. H. Booth, L. Maron, R. A. Andersen, *Organometallics* **2013**, *32*, 5305–5312.

[32] G. Nocton, W. W. Lukens, C. H. Booth, S. S. Rozenel, S. A. Medling, L. Maron, R. A. Andersen, *J. Am. Chem. Soc.* **2014**, *136*, 8626–8641.

[33] G. Nocton, L. Ricard, *Chem. Commun.* **2015**, *51*, 3578–3581.

[34] M. E. Fieser, M. R. MacDonald, B. T. Krull, J. E. Bates, J. W. Ziller, F. Furche, W. J. Evans, *J. Am. Chem. Soc.* **2015**, *137*, 369–382.

[35] A. Jaoul, C. Clavaguéra, G. Nocton, *New J. Chem.* **2016**, *40*, 6643–6649.

[36] M. Swart, F. M. Bickelhaupt, M. Duran, DFT2016 poll, http://www.marcelswart.eu/dft-poll/newsitem.pdf, **2016**.

[37] M. B. Jones, A. J. Gaunt, J. C. Gordon, N. Kaltsoyannis, M. P. Neu, B. L. Scott, *Chem. Sci.* **2013**, *4*, 1189–1203.

[38] S. Labouille, C. Clavaguéra, F. Nief, *Organometallics* **2013**, *32*, 1265–1271.

[39] H. Jacobsen, L. Cavallo, *ChemPhysChem* **2011**, *13*, 562–569.

[40] A. Hansen, C. Bannwarth, S. Grimme, P. Petrović, C. Werlé, J.-P. Djukic, *Chemistry-Open* **2014**, *3*, 177–189.

[41] T. J. Duignan, J. Autschbach, *J. Chem. Theory Comput.* **2016**, *12*, 3109–3121.

[42] S. Shaik, D. Danovich, B. Silvi, D. L. Lauvergnat, P. C. Hiberty, *Chem. Eur. J.* **2005**, *11*, 6358–6371.

[43] L. Maron, O. Eisenstein, *J. Phys. Chem. A* **2000**, *104*, 7140–7143.

[44] S. Grimmel, G. Schoendorff, A. K. Wilson, *J. Chem. Theory Comput.* **2016**, *12*, 1259–1266.

[45] D. Bousquet, E. Brémond, J. C. Sancho-García, I. Ciofini, C. Adamo, *Theor. Chem. Acc.* **2014**, *134*, 1602.

[46] L. Goerigk, S. Grimme, *WIREs Comput. Mol. Sci.* **2014**, *4*, 576–600.

[47] Y. Zhao, D. G. Truhlar, *Acc. Chem. Res.* **2008**, *41*, 157–167.

[48] M. G. Medvedev, I. S. Bushmarinov, J. Sun, J. P. Perdew, K. A. Lyssenko, *Science* **2017**, *355*, 49–52.

[49] E. C. Sherer, C. J. Cramer, *Organometallics* **2003**, *22*, 1682–1689.

[50] T. Tsuneda, K. Hirao, *WIREs Comput. Mol. Sci.* **2014**, *4*, 375–390.

[51] S. E. Wheeler, K. N. Houk, *J. Chem. Theory Comput.* **2010**, *6*, 395–404.

[52] T. Schwabe, S. Grimme, *Phys. Chem. Chem. Phys.* **2007**, *9*, 3397–3406.

[53] J. Cooper, T. Ziegler, *Inorg. Chem.* **2002**, *41*, 6614–6622.

[54] J. M. Deutch, G. M. Whitesides, *J. Org. Chem.* **1998**, *63*, 3821–3830.

[55] A. Ishikawa, Y. Nakao, H. Sato, S. Sakaki, *Inorg. Chem.* **2009**, *48*, 8154–8163.

[56] Y. Okuno, *Chem. Eur. J.* **1997**, *3*, 212–218.

[57] S. Tobisch, *Chem. Eur. J.* **2005**, *11*, 3113–3126.

[58] S. Di Tommaso, V. Tognetti, E. Sicilia, C. Adamo, N. Russo, *Inorg. Chem.* **2010**, *49*, 9875–9883.

[59] D. H. Wertz, *J. Am. Chem. Soc.* **1980**, *102*, 5316–5322.

[60] B. Civalleri, R. Dovesi, P. Pernot, D. Presti, A. Savin, *Computation* **2016**, *4*, 20.

[61] A. S. Menon, L. Radom, *J. Phys. Chem. A* **2008**, *112*, 13225–13230.

[62] J. Baker, A. Scheiner, J. Andzelm, *Chem. Phys. Lett.* **1993**, *216*, 380–388.

[63] C. Herrmann, PhD thesis, ETH Zurich, **2006**.

[64] N. S. Ostlund, A. Szabo, *Modern Quantum Chemistry: Introduction to Advanced Electronic Structure Theory*, MacMillan Publishing, **1996**.

[65] J. Autschbach, M. Srebro, *Acc. Chem. Res.* **2014**, *47*, 2592–2602.

[66] G. L. Manni, R. K. Carlson, D. G. Truhlar, L. Gagliardi, *Chem. Sci.* **2016**, *7*, 2399–2413.

[67] G. Li Manni, R. K. Carlson, S. Luo, D. Ma, J. Olsen, D. G. Truhlar, L. Gagliardi, *J. Chem. Theory Comput.* **2014**, *10*, 3669–3680.

[68] MCDFit, https://sourceforge.net/projects/mcdfit/, **2013**.

[69] T. Kato, T. Shida, *J. Am. Chem. Soc.* **1979**, *101*, 6869–6876.

[70] S. Zališ, C. Consani, A. El Nahhas, A. Cannizzo, M. Chergui, F. Hartl, A. Vlček Jr, *Inorganica Chimica Acta* **2011**, *374*, 578–585.

[71] C. Turró, Y. C. Chung, N. Leventis, M. E. Kuchenmeister, P. J. Wagner, G. E. Leroi, *Inorg. Chem.* **1996**, *35*, 5104–5106.

[72] F. Pointillart, B. L. Guennic, S. Golhen, O. Cador, O. Maury, L. Ouahab, *Chem. Commun.* **2013**, *49*, 615.

[73] R. E. Da Re, C. J. Kuehl, M. G. Brown, R. C. Rocha, E. D. Bauer, K. D. John, D. E. Morris, A. P. Shreve, J. L. Sarrao, *Inorg. Chem.* **2003**, *42*, 5551–5559.

[74] A. D. Laurent, D. Jacquemin, *Int. J. Quantum Chem.* **2013**, *113*, 2019–2039.

[75] A. Prlj, M. E. Sandoval-Salinas, D. Casanova, D. Jacquemin, C. Corminboeuf, *J. Chem. Theory Comput.* **2016**, *12*, 2652–2660.

[76] C. Latouche, D. Skouteris, F. Palazzetti, V. Barone, *J. Chem. Theory Comput.* **2015**, *11*, 3281–3289.

[77] M. R. MacDonald, J. E. Bates, J. W. Ziller, F. Furche, W. J. Evans, *J. Am. Chem. Soc.* **2013**, *135*, 9857–9868.

[78] F. Wang, T. Ziegler, *Mol. Phys.* **2004**, *102*, 2585–2595.

[79] N. Ferré, M. Filatov, M. Huix-Rotllant, *Density-Functional Methods for Excited States*, Springer, **2015**.

[80] Z. Li, W. Liu, *J. Chem. Theory Comput.* **2016**, *12*, 238–260.

[81] Z. Li, W. Liu, *J. Chem. Theory Comput.* **2016**, *12*, 2517–2527.

[82] A. Rainis, M. Szwarc, *J. Phys. Chem.* **1975**, *79*, 106–109.

[83] V. Kalyanaraman, C. N. R. Rao, M. V. George, *J. Chem. Soc. B:* **1971**, 2406.

[84] C. D. Schmulbach, C. C. Hinckley, D. Wasmund, *J. Am. Chem. Soc.* **1968**, *90*, 6600–6602.

[85] Z. Mou, K. Uchida, T. Kubo, M. Kertesz, *J. Am. Chem. Soc.* **2014**, *136*, 18009–18022.

[86] D. Small, S. V. Rosokha, J. K. Kochi, M. Head-Gordon, *J. Phys. Chem. A* **2005**, *109*, 11261–11267.

[87] V. Zaitsev, S. V. Rosokha, M. Head-Gordon, J. K. Kochi, *J. Org. Chem.* **2006**, *71*, 520–526.

[88] M. Abe, *Chem. Rev.* **2013**, *113*, 7011–7088.

[89] Y. Kobayashi, H. Okajima, H. Sotome, *J. Am. Chem. Soc.* **2017**, *139*, 6382–6389.

[90] O. Maury, PhD thesis, Université Pierre Et Marie Curie, **1997**.

[91] Z. Hou, T.-a. Koizumi, M. Nishiura, Y. Wakatsuki, *Organometallics* **2001**, *20*, 3323–3328.

[92] Z. Hou, A. Fujita, Y. Zhang, T. Miyano, H. Yamazaki, Y. Wakatsuki, *J. Am. Chem. Soc.* **1998**, *120*, 754–766.

[93] G. B. Deacon, P. C. Junk, J. Wang, D. Werner, *Inorg. Chem.* **2014**, *53*, 12553–12563.

[94] G. Kleiner, A. Tarnopolsky, S. Hoz, *Org. Lett.* **2005**, *7*, 4197–4200.

[95] G. Nocton, PhD thesis, CEA Grenoble, **2010**.

[96] Y. Kamochi, T. Kudo, *Heterocycles* **1993**, *36*, 2383–2395.

[97] T. Shida, *Electronic absorption spectra of radical ions*, Elsevier Science Ltd, **1988**.

[98] J. Y. Alston, A. J. Fry, *Electrochimica Acta* **2004**, *49*, 455–459.

[99] J. Grimshaw, R. Hamilton, *J. Electroanal. Chem.* **1980**, *106*, 339–346.

Thus it becomes obvious that one must be wary in attributing scientific discovery wholly to anyone person. Almost every discovery has a long and precarious history. Someone finds a bit here, another a bit there. A third step succeeds later and thus onward till a genius pieces the bits together and makes the decisive contribution. Science, like the Mississippi, begins in a tiny rivulet in the distant forest. Gradually other streams swell its volume. And the roaring river that bursts the dikes is formed from countless sources.

— Abraham Flexner *The usefulness of useless knowledge*

3 Radical reactions

Once the electron has been transferred to an organic moiety, the radical intermediate can be used in further radical reactions. The diversity of radical reactions available with samarium complexes has been recently reviewed[1,2]. Different functional groups can be reduced by SmI_2: ketones, aldehydes, alkyl halides, carboxylic acids, carbonyls groups, etc. SmI_2 can also be used to create $C-C$ bonds in pinacol couplings, or Barbier reaction for example.

The molecules synthesised in the previous chapter could be reacted in such ways, with radical reagents or with other molecules of interest in order to understand their reactivity. This chapter will be devoted to the study of radical reactions with samarium complexes. It will focus on two examples involving a permanent radical, tempo, and a coupling reaction between phenanthroline and benzophenone.

3.1 Reaction with tempo

Radical reactions with samarium cyclopentadienyl complexes of samarium have been intensely studied by the group of Evans[3] in the last decades. One of the principles he developed, sterically induced reductions, is at the base of his chemistry. It is of immense interest in the field of radical reactions involving tempo and Cp^*_2Sm complexes.

3.1.1 Sterically induced reductions

In the 1990s, the trivalent Cp^*_3Sm was synthesised by the group of Evans[4]. The steric crowding around the samarium center led to long $Sm - Cp^*$ distances, which destabilised the lanthanide ion. As a result, this lanthanide molecule has a very specific type of reactivity where one of the Cp^* ligand can easily be eliminated via the formation of a Cp^* radical intermediate, and the whole complex could react as a Sm^{2+} equivalent. Removal of Cp^* radical intermediate was also observed with zirconium complexes as shown by the group of Roesky[5]. These "sterically induced reductions" have been used for two decades by the group of Evans and have triggered the characterisation of new compounds that cannot be synthesised using standard Cp^*_2Sm complexes[3]. This principle has been extended to Cp^*_3Ln (where Ln is Nd, La, Ce, Pr, and Gd), and the reduction power of these compounds was further related to the size of the lanthanide ion, which is in agreement with an involvement of sterics in this type of reduction[6].

Recently, our group has been studying Dtp_2Tm reactions with bipyridine[7]. Addition of one equivalent of bipyridine led to its coordination on the thulium ion and its subsequent reduction. Addition of more than one equivalent has the same kind of reactivity: coordination of a bipyridine and its subsequent reduction with removal of one Dtp radical (Figure 3.1). The postulated mechanism involves the formation of a η^1-Dtp complex that leads to the separation of a Dtp radical. Indeed, the presence of a phosphorous in the Dtp moiety facilitates the formation of this η^1 compound, that was also postulated for Cp^*_3Sm complexes[3]. However, it is noteworthy that the crowding around the lanthanide center is not as strong as in the case of $Dtp_2Tm(bipy)$ compared to Cp^*_3Sm. Could the sterics not be the only factor in sterically induced reduction?

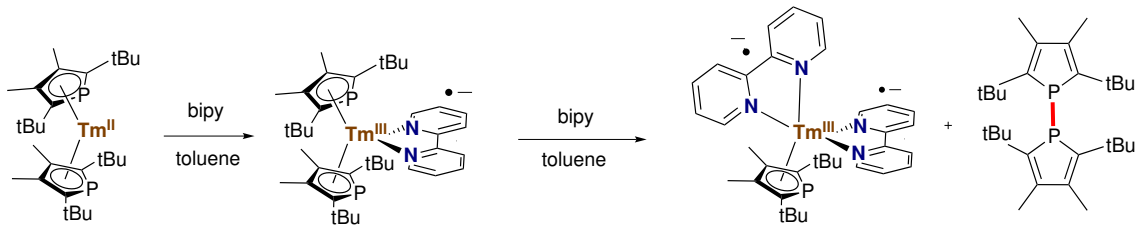

Figure 3.1: Reactivity of bipyridine with Dtp_2Tm as reported by Nocton *et al*[7]

In the context of sterically induced reduction, tempo is one of the first reagents that have been used over Cp^*_3Sm. The very easy replacement by tempo of the three Cp^* molecules, forming the bimetallic $(Sm(tempo)_3)_2$, was studied by Evans[8] (Figure 3.2 top). In this complex, two types of binding for the tempo ligand were found consistent with earlier studies describing tempo as a "chameleonic" ligand[9]. Tempo could be involved as both a Lewis base and a reducible material[9]. The reactivity of tempo on f-block compounds was recently expanded with thorium complexes, and the same kind of reactivity was observed with removal of Cp^* radical derivatives[10] (Figure 3.2 bottom).

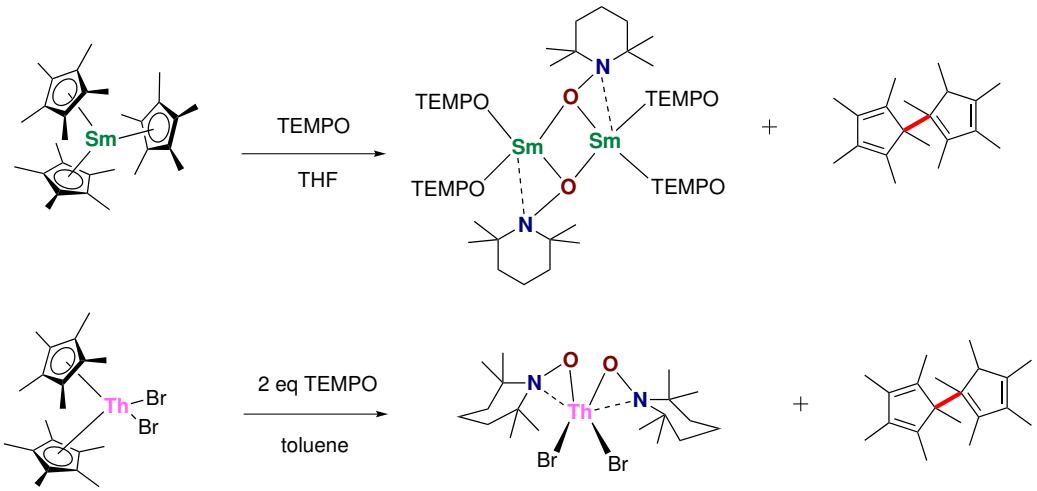

Figure 3.2: Reactivity of Cp^*_3Sm (top) and $Cp^*_2ThBr_2$ (bottom) with tempo as reported by Evans *et al.*[8,10]

The reaction of radical intermediates such as $Cp^*_2Sm(phen)$ with tempo could present two advantages. Firstly, two types of additions are possible with tempo and $Cp^*_2Sm(phen)$: addition on the samarium itself, or addition on the phenanthroline moiety via formation of a $C-O$ bond. Then, addition of multiple molecules of tempo could trigger further decoordination of the Cp^* ligand, and could be compared to previous results from Evans. A conclusion might be drawn from these two experiences into the importance of sterics in this kind of reactions.

Firstly, divalent Cp^*_2Sm and Cp^{ttt}_2Sm will be reacted with tempo. The comparison between their two different types of reactivity will lead to better understanding of reactions involving $Cp^*_2Sm(phen)$ and $Cp^{ttt}_2Sm(phen)$. Overall, the reaction mechanism will be studied using quantum chemistry calculations.

3.1.2 Reactions between tempo and complexes of samarium

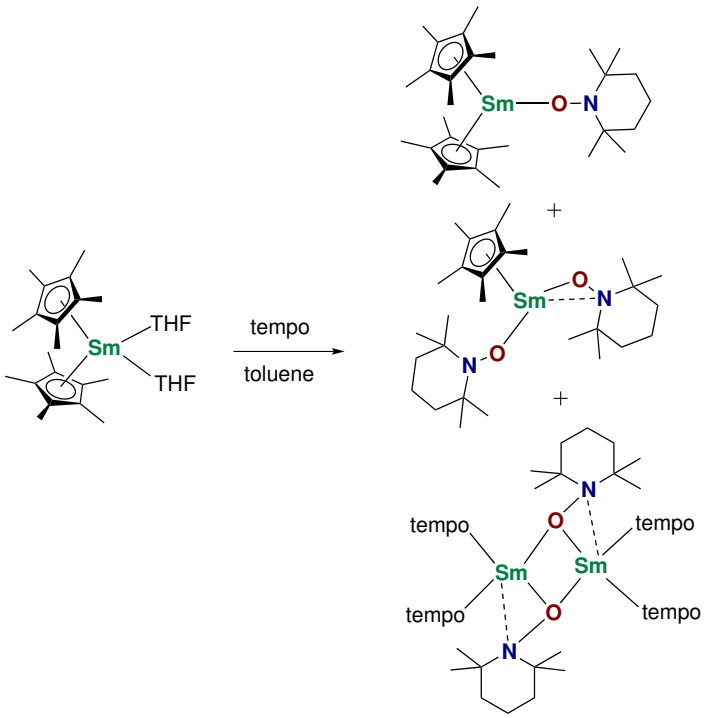

Figure 3.3: Reaction of $Cp^*_2Sm(thf)_2$ with tempo, all the compounds seemed to be present in solution

One equivalent of tempo was added to a solution of $Cp^*_2Sm(Et_2O)$ in toluene (Figure 3.3). The solution coloured rapidly to dark/yellow, and the ^1H NMR analysis indicated multiple products and the presence of the $Cp^* - Cp^*$ dimeric compound (which ^1H NMR can be found in the original paper from Jutzi[11]) typical of the formation of an intermediate Cp^* radical[12,13]. Putting the solution in the freezer at -40^oC led to crystallisation of yellow block crystals that were suitable for X-Ray diffraction study and showed the presence of the bimetallic compound already observed by Evans, $(Sm(tempo)_3)_2$. Following the addition of an increasing amount of tempo from 0.5 to 3 equivalents in toluene-d_8 enabled the identification of the peaks as adducts of one, two and three equivalents of tempo on the samarium centre (Figure 3.4).

While Cp^*_2Sm reacted identically to Cp^*_3Sm, Cp^{ttt}_2Sm had a different reactivity. After addition of one equivalent of tempo in toluene, a red colouration was observed. The compound was analysed by ^1H NMR (Figure 3.5). The molecule synthesised is consistent with a $Cp^{ttt}_2Sm(tempo)$ structure, with three peaks corresponding to the tert-butyl groups at

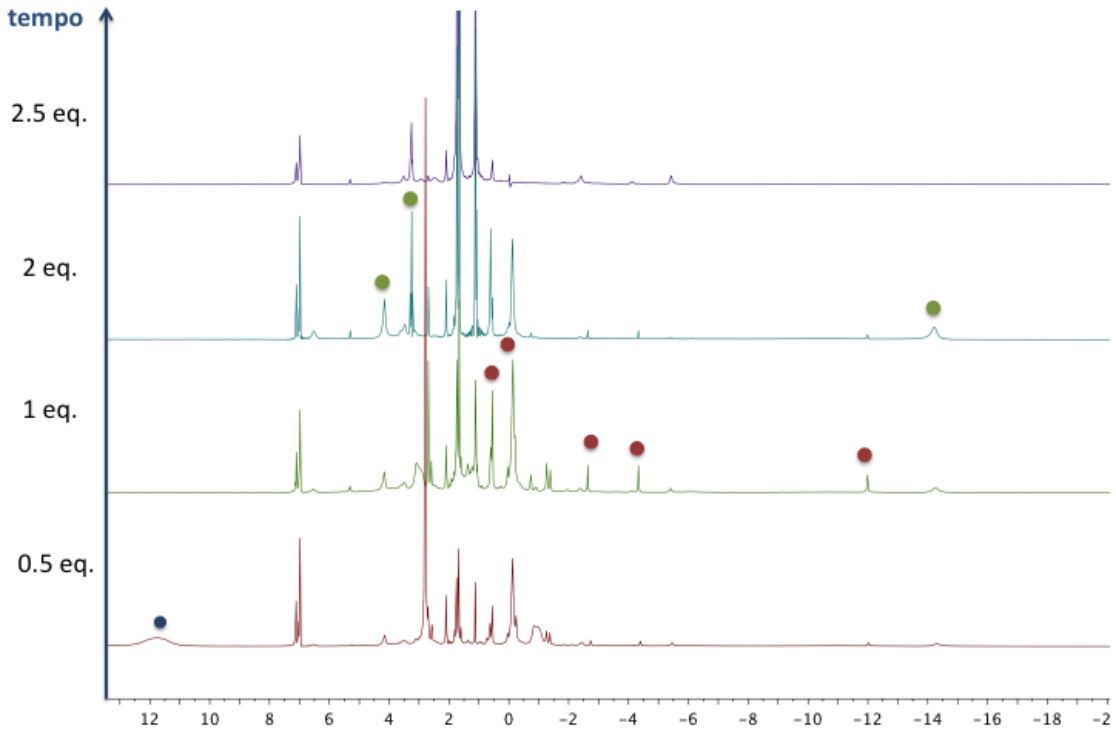

Figure 3.4: ^{1}H NMR of $Cp^{*}_{2}Sm$ in toluene-d_8 after addition of one equivalent of tempo; the different peaks were attributed following their disappearances after addition of an increasing amount of tempo; blue dot indicates the starting material and red and green dots the possible adducts with one equivalent of tempo and two equivalents of tempo, respectively

respectively 2.33, 0.25 and -8.42 ppm, two peaks corresponding to the hydrogens of the Cp^{ttt} ligand at 23.70 and 21.08 ppm and peaks corresponding to tempo at 4.92, 3.35, 3.08, 2.92 and 0.61 ppm. Addition of more than one equivalent of tempo did not change the ^{1}H NMR data. In the present case, the formation of Cp^{ttt}—Cp^{ttt} is not observed. However, this intermediate was already observed in several occasions with bismuth[14] or lanthanide compounds[15].

After a few days at -40^{o}C, small red plates were isolated and were in agreement with a $Cp^{ttt}_{2}Sm(tempo)$ structure (Figure 3.6). The distances between the samarium center and the centroid of the Cp^{ttt} ligands are 2.534 Å which is consistent with a Sm^{+III} as already reported in the litterature[16]. The distance with the tempo ligand is 2.112(3) Å corresponding to a strong interaction between the lanthanide and the oxygen atom.

This is the first example of a single tempo coordinated on a samarium centre. The crowding around the lanthanide ion might be responsible for such a structure. It can forbid

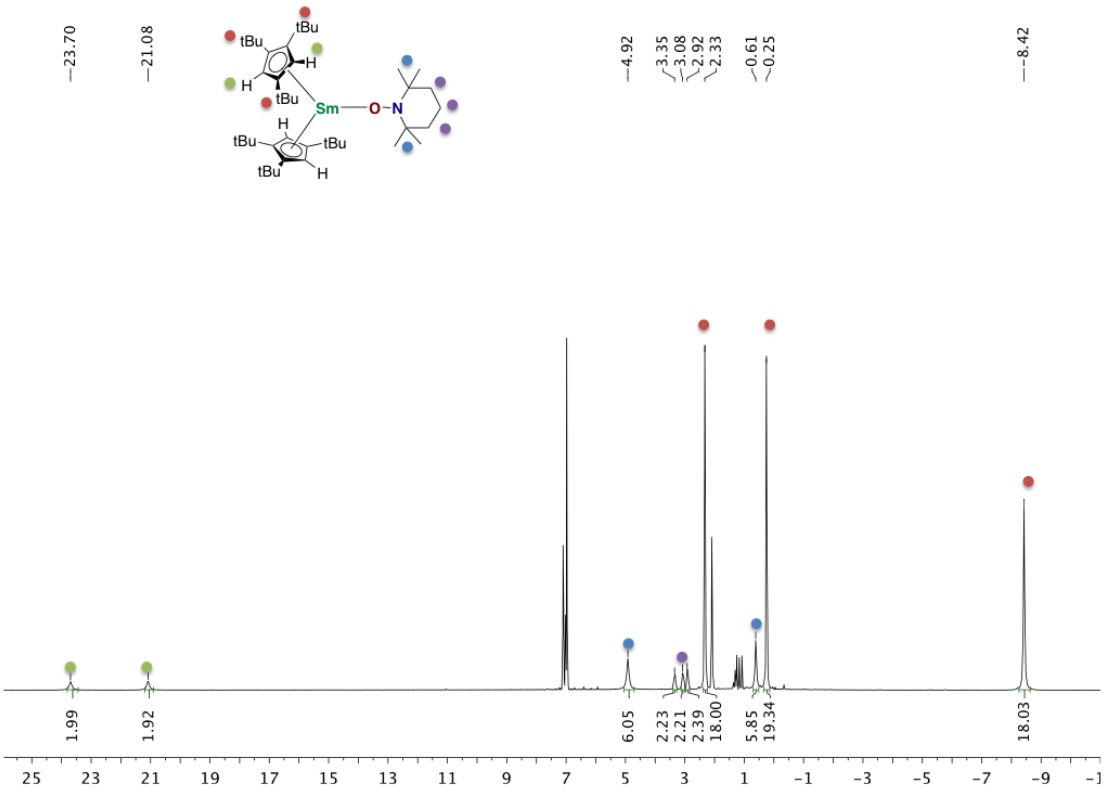

Figure 3.5: ^{1}H NMR of $Cp^{ttt}_{2}Sm(tempo)$ in toluene-d_8

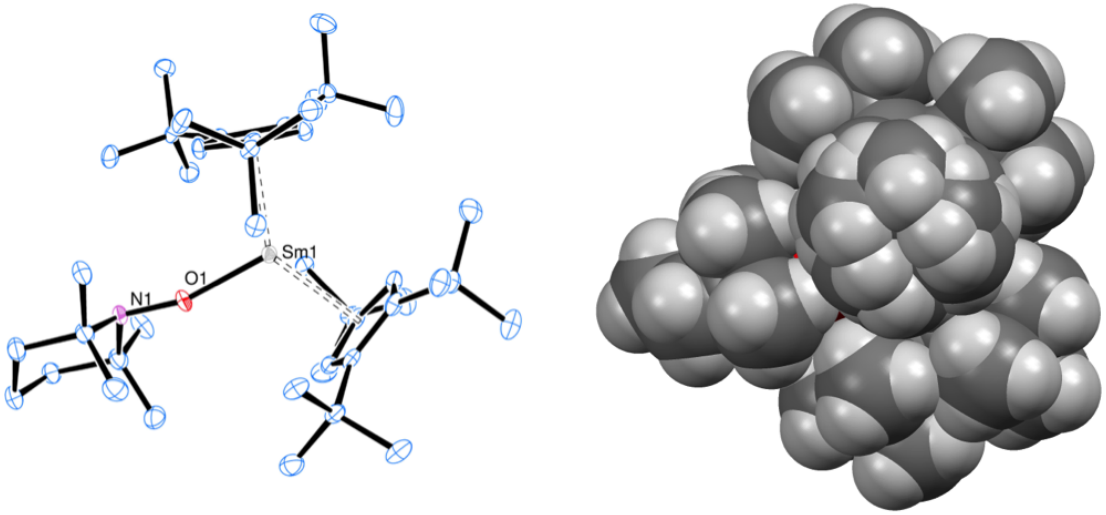

Figure 3.6: ORTEP of the X-Ray structure of $Cp^{ttt}_{2}Sm(tempo)$ (left) and its space-fill representation (right)

the approach of another tempo molecule, which prohibits the separation of the Cp^{ttt} radical derivatives. In Figure 3.6, the space-fill representation of $Cp^{ttt}_2Sm(tempo)$ shows that the lanthanide ion is difficult to reach, as the sterical crowding makes it disappear. However, contrary to molecules such as Cp^*_3Sm, this molecule has normal $Sm - Cp^{ttt}$ distances and cannot behave as a Sm^{+II} molecule.

These examples show that depending on the ligand surrounding the lanthanide, different reactivity with tempo can be expected. The presence of phenanthroline radical in the vicinity of the lanthanide centre could as well present differences with these two reactions and show that the radical has an influence on further reactivity with tempo.

Addition of one equivalent of tempo to a solution of the dimer $(Cp^*_2Sm(phen))_2$ led to the slight decoloration of the solution from purple/black to red/black. ^1H NMR analysis showed that multiple products were found similarly to its Cp^*_2Sm parent. The presence of several peaks in the aromatic region are in agreement with a decoordination of the phenanthroline neutral molecule. Other peaks can be related to the presence of either one, two or three molecules coordinated to the lanthanide centre. Attempts to crystallise the different products were conducted, and led to the isolation of two products corresponding to two and three tempo coordinated on the samarium ion (Figure 3.7).

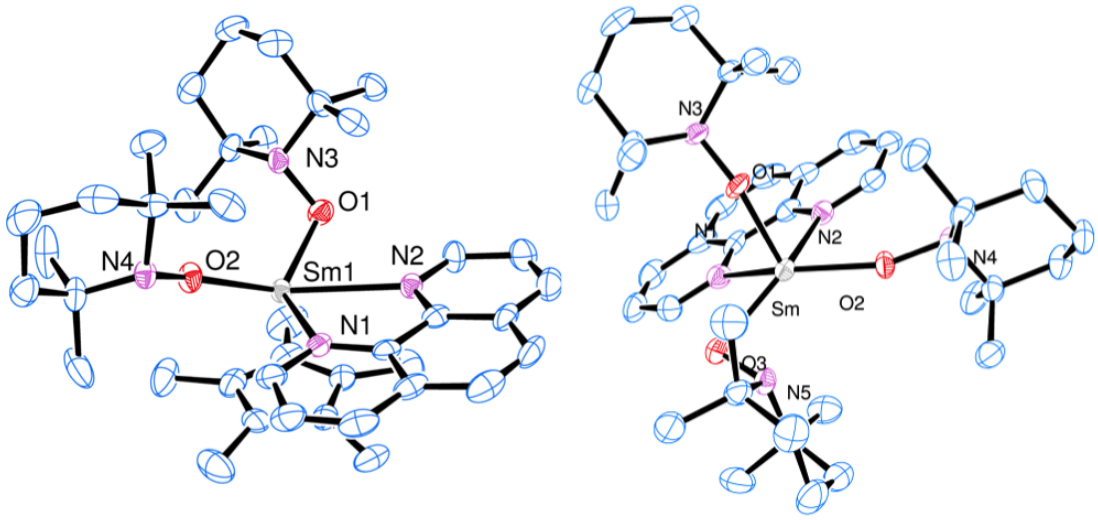

Figure 3.7: ORTEP of the X-Ray structures of $Cp^*Sm(tempo)_2(phen)$ (left) and $Sm(tempo)_3(phen)$ (right)

The distances in both complexes are compared in Table 3.1. As detailed in previous papers[9,17], tempo can form two types of bonding interactions: a η^1 coordination with the

lone pair of the oxygen atom and a η^2 coordination with both the lone pair of the oxygen and the lone pair of the nitrogen. Depending on the sterics around the lanthanide, the η^1 or the η^2 coordination is favoured: in $Cp^*Sm(tempo)_2(phen)$, the large number of atoms prohibits a strong interaction between the lanthanide and the nitrogen and constrains the $Sm - N$ distance to be long (2.787(5) Å) whereas in $Sm(tempo)_3(phen)$ the steric hindrance are more favourable for an η^2 interaction which strengthens the interaction between the Sm and the N atom (2.558(5) Å). In both complexes, the phenanthroline molecule is coordinated in a disymmetric way to the samarium atom, with one nitrogen atom closer than the other from the samarium centre, countering the interaction in the trans position of the $Sm - (\eta^2\,tempo)$ bond.

	$Cp^*Sm(tempo)_2(phen)$	$Sm(tempo)_3(phen)$
Sm-O (tempo-η^1, avg)	2.165(4)	2.136(5)
Sm-O (tempo-η^2)	2.214(4)	2.233(5)
Sm-N (tempo-η^2)	2.787(5)	2.558(5)
Sm-N1 (phen)	2.611(5)	2.655(5)
Sm-N2 (phen)	2.686(4)	2.592(5)

Table 3.1: Distances in angstroms for the two X-Ray crystallographic structures of $Cp^*Sm(tempo)_2(phen)$ and $Sm(tempo)_3(phen)$

The ^1H NMR spectrum of $Cp^*Sm(tempo)_2(phen)$ crystals was recorded in thf-d_8, and is shown in Figure 3.8. The proton peaks of the tempo molecules coordinated to the samarium ion are broadened by proximity of this paramagnetic centre. Peaks corresponding to the six protons on the cycle in the tempo molecule were not found in this spectrum, and might have been too broad to be seen. Two sets of peaks were found in the aromatic region. These peaks correspond the coordinated and uncoordinated phenanthroline molecule, which indicate that the interaction between this species and the samarium ion is weak. This is validated by the $Sm - N$ distances found in the X-Ray crystallographic structure that are longer than in the case of dimeric $(Cp^*_2Sm(phen))_2$ (Chapter 2).

While the ^1H NMR follow-up of the reaction of tempo with $(Cp^*_2Sm(phen))_2$ was difficult, treating $(Cp^{ttt}_2Sm(phen))_2$ with one equivalent of tempo led to a mixture of two compounds: the previous $Cp^{ttt}_2Sm(tempo)$ and another compound that involve a multitude

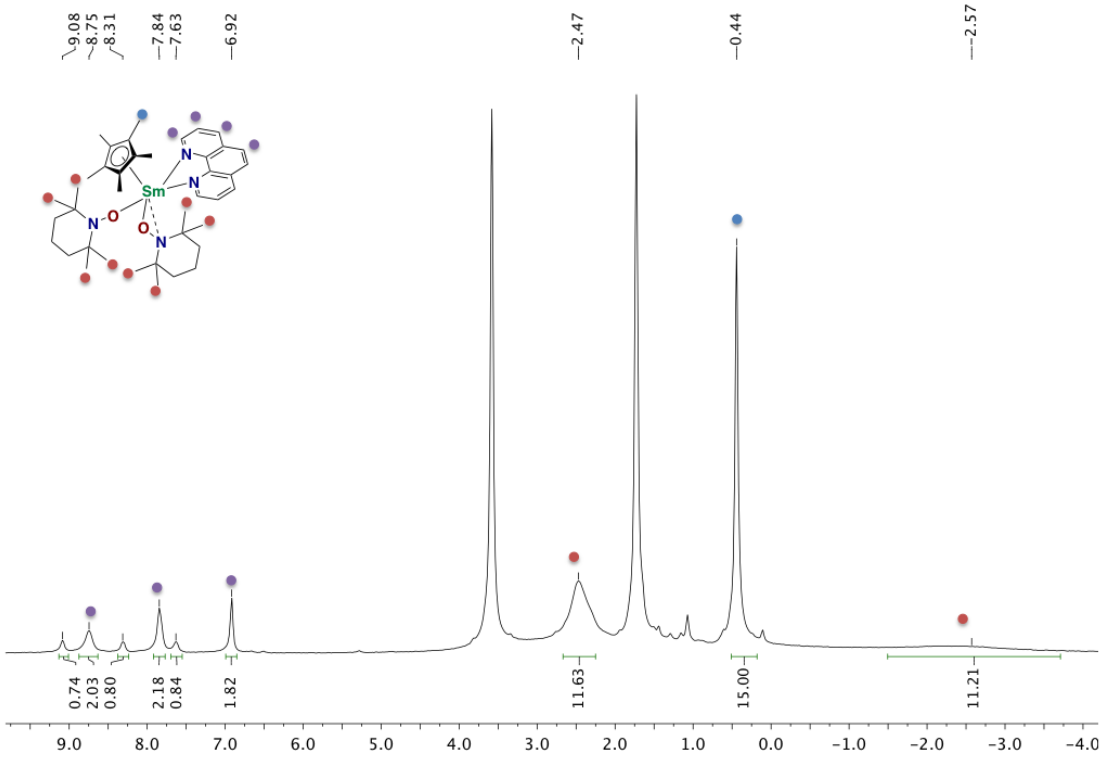

Figure 3.8: ^{1}H NMR of $Cp^*Sm(tempo)_2(phen)$ in thf-d_8

of small peaks and could correspond to a dimeric $(Cp^{ttt}_2Sm(phen)(tempo))_2$ (Figure 3.9). As with $Cp^{ttt}_2Sm(tempo)$, addition of more than one equivalent of tempo did not change the ^{1}H NMR, in agreement with a crowded environment for the samarium ion. Traces of neutral phenanthroline can be seen in the aromatic region, and are consistent with the formation of a $Cp^{ttt}_2Sm(tempo)$ molecule. Red crystals of this molecule can be extracted at -40^oC, but the isolation of the other molecule was not possible despite our best efforts.

In summary, the addition of tempo over divalent complexes of samarium leads to the decoordination of small ligands such as Cp^* but did not permit the decoordination of bigger ligands such as Cp^{ttt}. This difference can be related to the presence of a reaction intermediate that involves the coordination of a tempo molecule on the $Cp_2Sm(tempo)$ molecule. Moreover, phenanthroline radical complexes of samarium followed the same type of reactivity. This means that the electron stored on the N-heterocycle ligand can be transferred to other molecules of interest such as tempo.

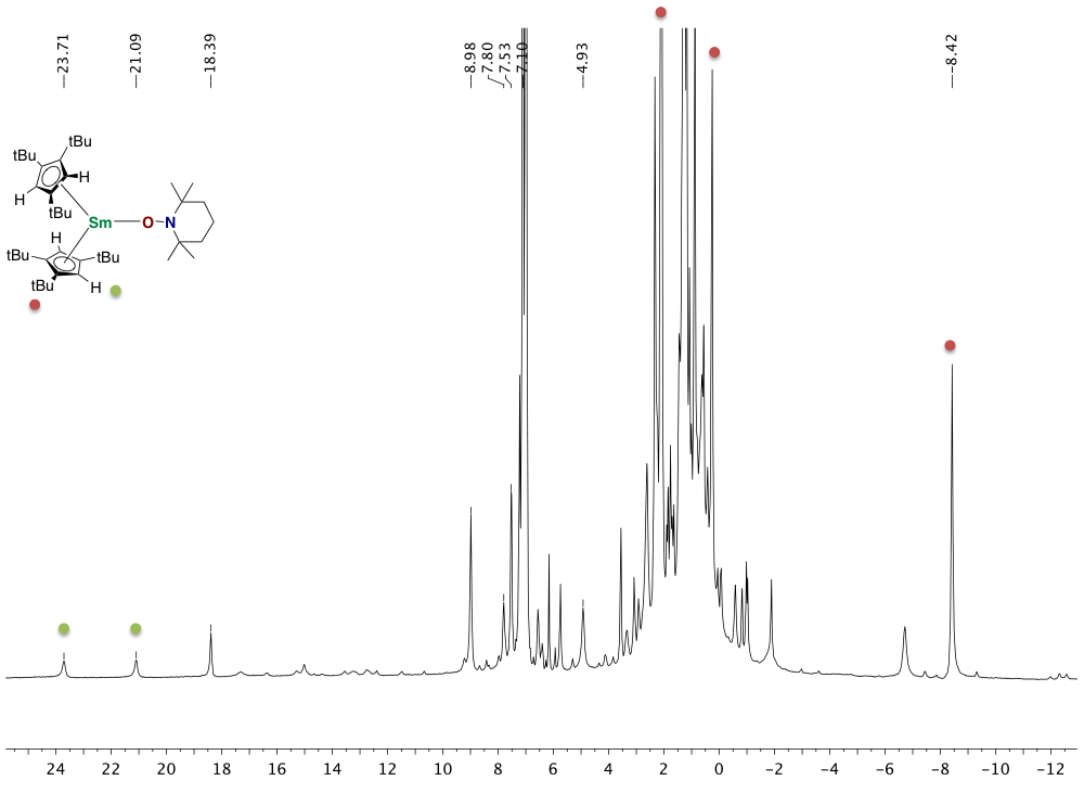

Figure 3.9: ^{1}H NMR of $(Cp^{ttt}_2Sm(phen))_2$ after addition of one equivalent of tempo in toluene-d_8

This behaviour was also observed with SmI_2 complexes of benzophenone presented in Chapter 2. Upon addition of tempo on $(I_2Sm(bph)(thf)_3)_2$ in dme, the solution passed from yellow to red, and after several days at -40^oC, red crystals of $I_2Sm(tempo)(dme)_2$ were isolated (Figure 3.10). This could have significant impact in further reactivity as the ligand, bph or phen are behaving as electron reservoir which the lanthanide uses to stabilise itself and perform the same kind of reactivity than Sm^{2+} complexes.

Therefore, these reactions can be divided in two distinct parts: the formation of $Cp^*_2Sm(tempo)$ from $Cp^*_2Sm(phen)$, and the difference in reactivity between $Cp^*_2Sm(tempo)$ and $Cp^{ttt}_2Sm(tempo)$ over additions of more than one equivalent of tempo. The first mechanism could involve the formation of a $Cp^*_2Sm(tempo)(phen)$ as the ^{1}H NMR of the reaction between $Cp^{ttt}_2Sm(phen)$ and tempo is suggesting, or it could pass through a second sphere electron transfer that would involve the formation of $tempo^-$ and $Cp^*_2Sm(phen)^+$ molecules. The difference between $Cp^{ttt}_2Sm(tempo)$ and

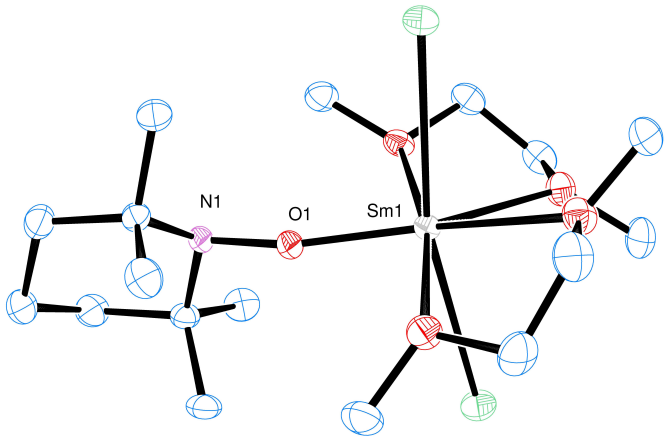

Figure 3.10: ORTEP of the X-Ray structures of $I_2Sm(tempo)(dme)_2$; selected distances in angstroms: $Sm-O$ (tempo) 2.064(2) Å, $Sm-O$ (dme, avg) 2.550(2) Å, $Sm-I$ (avg) 3.1400(2) Å

$Cp^*_2Sm(tempo)$ has been related to the sterics around the lanthanide centre that prohibits the coordination of the tempo molecule, and thus the liberation of a Cp^{ttt} radical molecule.

In order to investigate these two different behaviours, quantum chemistry calculations were performed for both molecules.

3.1.3 Mechanism of the reaction

3.1.3.1 Phenanthroline radical: an electron reservoir

The addition of tempo on $Cp^*_2Sm(phen)$ was studied at both the DFT and CASSCF levels of theory.

The mechanism involves an electron transfer from the phenanthroline radical to the tempo radical in order to form the neutral phenanthroline and the anionic tempo (SOMO of tempo presented in Figure 3.11). This type of electron transfer involves a modification of the system's spin multiplicity, that is going to pass from the octet to the sextet. This spin-forbidden transition will pass through a Minimum Energy Crossing Point (MECP) between the two Potential Energy Surface (PES)[18] at which the electron transfer will occur. Usually, for reactions involving both bond formation and change in spin-state, the preferred mechanism occurs in more than one step[19]. In the present case, the mechanism could involve the formation of the $Sm-O$ (tempo) bond followed by the electron transfer, or the electron transfer followed by the formation of the $Sm-O$ bond.

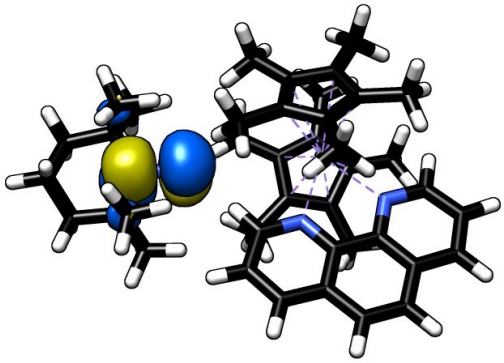

Figure 3.11: SOMO of tempo (n_{tempo}) in the complex $Cp^*_2Sm(phen)(tempo)$

At the PBE0-D3 level of theory, the 2nd sphere electron transfer is rather unlikely: the ΔG is greater than 100 kcal/mol. This is coherent with the high stability of phenanthroline radical and tempo radical which should not interact with each other because of their respective redox potential.

- **The octet: electronic structure of long and short distance complexes**

In a first step, the quantum chemical calculations focussed on looking for the optimum octet structure for $Cp^*_2Sm(phen)(tempo)$, *i.e.* phenanthroline and tempo radicals coordinated to the lanthanide. The geometry optimisation was started from different conformations, and two optimum structures were found with positive frequencies. These two geometries correspond to two positions of the tempo molecule: one at a long distance from the lanthanide ion (4.517 Å) and another at a short distance (2.615 Å) (Figure 3.12 right and left side, respectively).

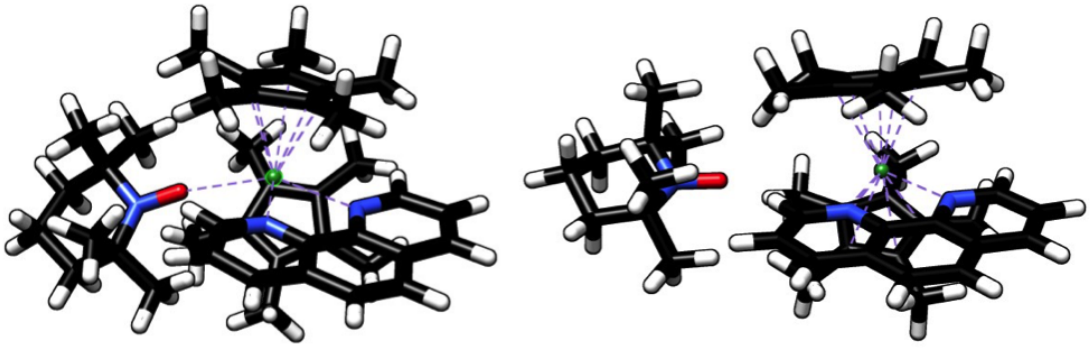

Figure 3.12: Optimised structures at the PBE-D3/ZORA2 level showing two different distances between the tempo molecule and the lanthanide ion

The presence of these two different structures for the octet was further investigated by performing a relaxed surface scan for the Sm—O (tempo) distance between 2.0 and 5.0 Å. The results are presented in Figure 3.13. The geometry were optimised using PBE-D3/ZORA2, and single point on each geometry were done at either the PBE0-D3, M062X or PBE-D3 ZORA3 levels. The different density functional results are in agreement with the presence of two local minima: one where tempo is at a close vicinity from the lanthanide ion and another at a long distance. In all the different cases, the adduct is more stable at long distances than at short distance, with an energy difference of 12, 3 and 6 kcal/mol respectively for PBE0-D3, M062X and PBE-D3. To have a better estimate of the energy difference between the two complexes, CASSCF - CASPT2 calculations were performed on the two optimised structures to compare their respective energies.

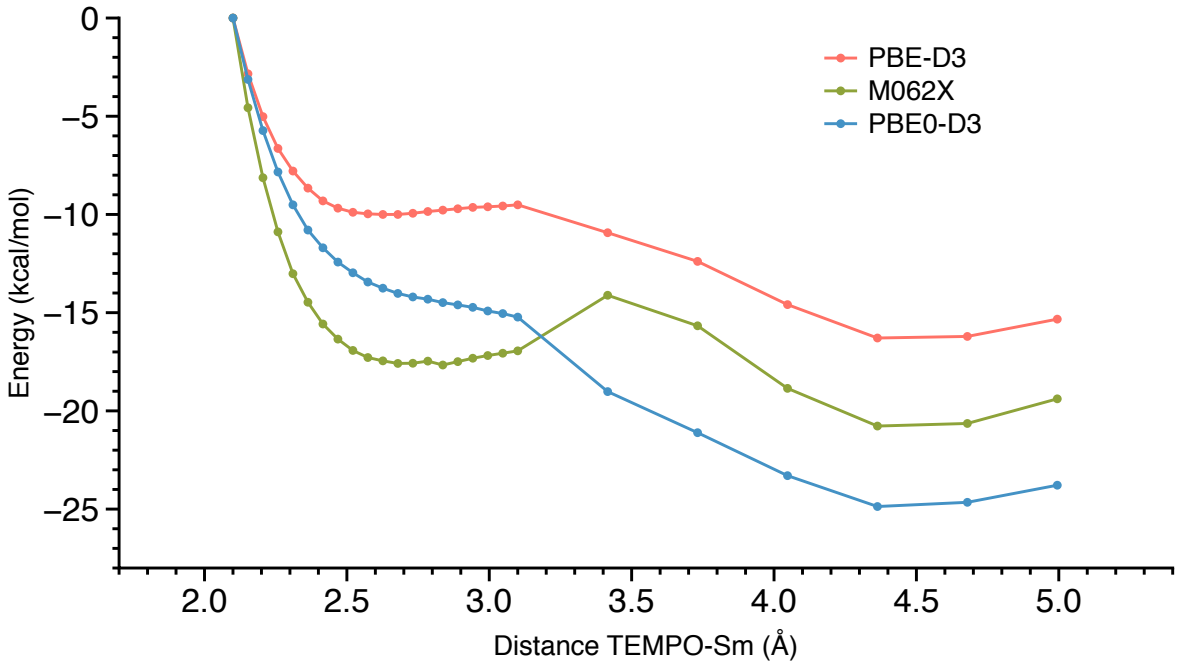

Figure 3.13: Potential energy surface of the reaction between tempo and $Cp^*_2Sm(phen)$, when changing the distance between the oxygen of tempo and the samarium ion from 2.0 and 5.0 Å using different density functionals

For this specific example, the active space was chosen as the seven 4f orbitals, the π^*_1 of phenanthroline and the SOMO of tempo (n_{tpo}). As with phenanthroline complexes of samarium, the multi-reference character observed for phenanthroline radical cannot be observed in these two complexes. The electronic structure of both compounds at the

CASSCF(7,9) level is $4f^5\pi_1^{*\uparrow}n_{tpo}^{\uparrow}$. Increasing the active space by including the π_2^* and the lone pairs of phenanthroline, the 5d orbitals of samarium or other orbitals of tempo resulted in the same electronic configuration with small or no involvement of these orbitals. The energy difference between the two molecules at the CASPT2 and CASSCF level of theory is 8.5 kcal/mol and -25 kcal/mol, respectively, in favour of the small-distance complex.

There is a notable difference between the CASSCF and DFT results, and the CASPT2 ones. Both CASSCF and DFT methods predict a positive energy difference when approaching the tempo molecule, while the CASPT2 method predicts the opposite. For DFT methods, the SIE might be responsible for an over-expression of the delocalisation, which might stabilise the long-distance complex. At the CASSCF level, dynamic correlation is not taken into account which might favour as well the long distance complex. Overall, apart from the CASSCF results, the difference between these two geometries is weak, which is in agreement with a rapid coordination of tempo on the samarium ion.

- **The sextet: electronic structure and energy difference with the octet**

Passing from the octet to the sextet leads to an evolution in the electronic structure of the complex (Figure 3.14). Compared to the octet only one optimised geometry was found at short distances, with a $Sm - O$ (tempo) distance of 2.325 Å. This shortened distance might indicate a stronger interaction in the case of the sextet compared to the octet. Another geometry optimisation was done for the MECP between the sextet and the octet. In this complex, the distance is longer, and is coherent with the second optimised structure found for the octet, with a $Sm - O$ (tempo) distance of 4.545 Å.

The PES of the sextet from 2.0 to 5.0 Å was calculated similarly to the PES of the octet. Both PES were combined in Figure 3.15. There is an important stabilisation for the octet over the sextet when the tempo molecule is coordinated to the samarium ion using PBE0, M062X or PBE. The energy difference that accounts for this surface crossover is 22.5, 13.7, and 9.9 kcal/mol respectively in favour for the sextet. This indicates that using DFT the electron transfer first happens and then the tempo molecule coordinates to the lanthanide ion.

The electronic structure of the sextet was also investigated at the CASSCF level of theory. The orbitals included aside from the seven 4f orbitals are described in Table 3.2 for the MECP

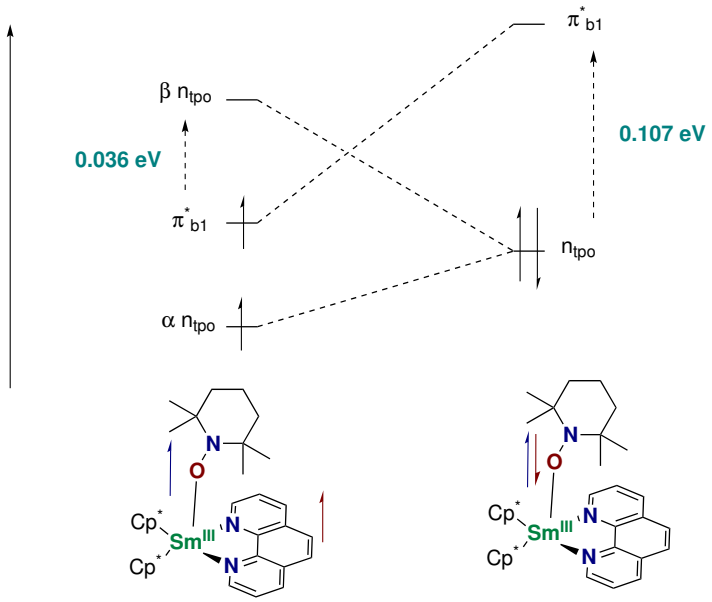

Figure 3.14: Evolution of the orbitals from the sextet to the octet; energies are calculated at the PBE0-D3 ZORA1 level of theory

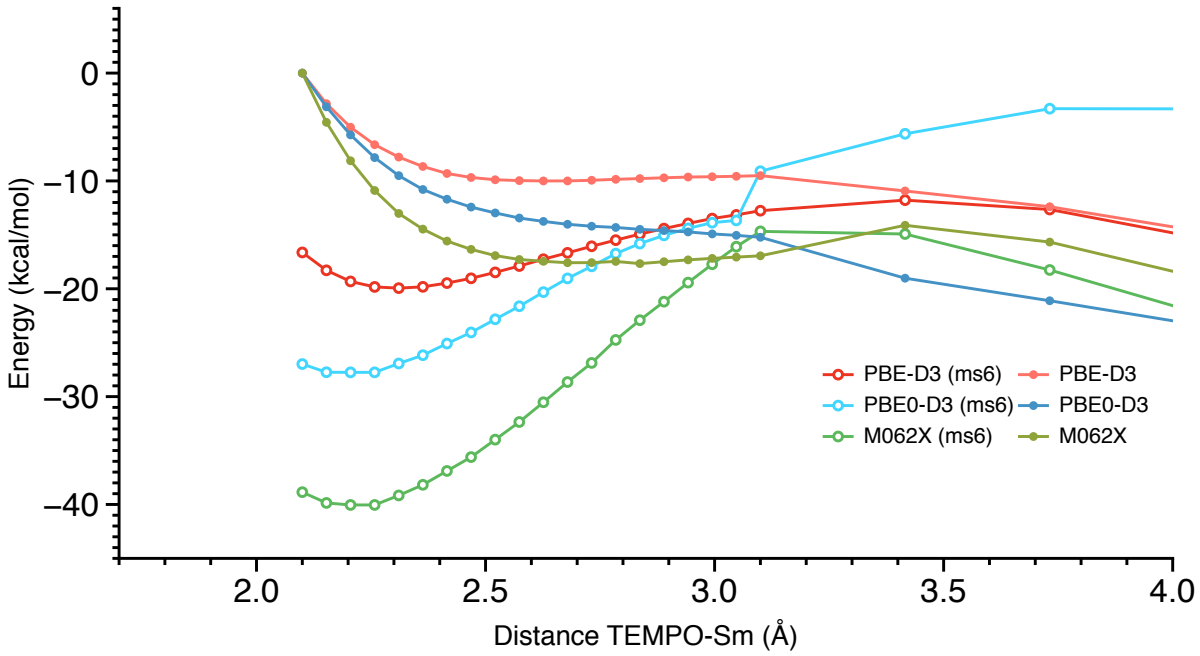

Figure 3.15: Potential energy surface of the reaction between tempo and $Cp^*_2Sm(phen)$ for the sextet (ms6) and the octet, when changing the distance between the oxygen of tempo and the samarium ion from 2.0 and 5.0 Å using different density functionals

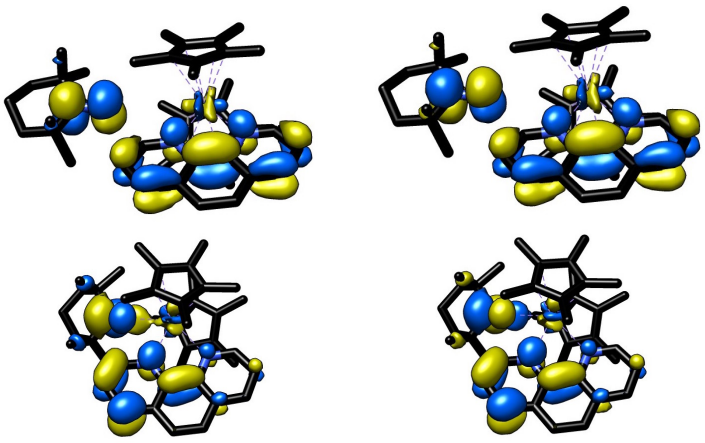

Table 3.2: Molecular orbitals of $Cp^*_2Sm(phen)(tempo)$ sextet at the CASSCF(7,9) level of theory at two different geometries, $Sm-O$ (tempo) distance of 2.325 Å (bottom) and 4.545 Å (top)

(top) and the optimised geometry (bottom). The π orbital of the complex is a mixture between the π^*_1 phenanthroline orbital and the SOMO of tempo n_{tpo}. Upon coordination of tempo, *i.e.* passing from the MECP to the optimised structure, the π and π^* orbital shape changes. In the MECP, the shape of these orbitals is localised on both phenanthroline π^*_1 and tempo n_{tpo}. On the contrary, in the optimised structure, their shape is localised mainly on the tempo n_{tpo} orbital with contribution from an asymmetric version of the phenanthroline π^*_1 orbital. The electronic structure for both complexes at the CASSCF(7,9) level is $4f^5\pi^{*\uparrow}\pi^{\downarrow}$.

Although DFT methods found a difference in energy between the sextet and the octet at their optimised structures where the tempo molecule is close to the samarium ion, at both the CASSCF and CASPT2 level of theory ΔE is close to 0 kcal/mol. This might be the result of the electronic structure of $Cp^*_2Sm(phen)(tempo)$ sextet that differs from what is found using standard DFT methods.

The activation energy for this electron transfer step needs to be evaluated at the CASSCF level of theory, but due to the high computational expenses of CASSCF calculations with this type of complex, a full MECP search was not performed. The results presented above show that there is a difference between the CASSCF and DFT electronic structure for these samarium complexes, which triggers an interesting pathway for the electron to be transferred from phenanthroline to tempo. The density on the phenanthroline π^*_1 is decreasing with a $Sm-O$ (tempo) distance decrease. This can be translated as : when the tempo

Energy (kcal/mol)	$Cp^*_2Sm(tempo)$	$Cp^*_2Sm(phen)$
Pauli	96	91
Electrostatic Interaction	-165	-169
Orbital interaction	-141	-130
Dispersion	-12	-13

Table 3.3: EDA at the PBE0-D3 ZORA1 level of theory for different complexes decomposing the Cp^*_2Sm-L bond into a fragment Cp^*_2Sm and a fragment L

molecule approaches the samarium ion, the electron transfer occurs and finishes when the phenanthroline neutral molecule is decoordinated.

3.1.3.2 Sterically induced reduction?

The electronic structure of $Cp^*_2Sm(tempo)$ corresponds to a $4f^5 n^2_{tpo}$. Using DFT technique could give insights into the bond strength of the created $Sm-O$ (tempo) bond. The geometry structure of the compound was optimised at the PBE-D3 ZORA2 level of theory. An energy decomposition analysis of the interaction between Cp^*_2Sm and tempo was then performed at the PBE0-D3 ZORA1 level of theory. The results are presented in Table 3.3 for both $Cp^*_2Sm(tempo)$ and $Cp^*_2Sm(phen)$. Both interactions involve almost equal level of electrostatic and orbital interaction. For tempo, the orbital interaction is higher which is expected as oxygen atoms are more donors than nitrogen ones.

Once the tempo complex, $Cp^*_2Sm(tempo)$, is formed, addition of other equivalents of tempo is leading to $Cp^*Sm(tempo)_3$. The mechanism from the former to the latter can pass through the formation of intermediate species such as $Cp^*Sm(tempo)_2$ or $Cp^*_2Sm(tempo)_2$. The mechanism was investigated at the DFT level of theory, as no multi-configuration character is expected in the ground state for this reaction. The PBE0-D3 results are presented in Figure 3.16. The first step is the coordination of another molecule of tempo on the $Cp^*_2Sm(tempo)$ molecule. Then, this intermediate can easily lose a Cp^* radical that will directly dimerise. The $Cp^*Sm(tempo)_2$ then formed is not stable and can easily coordinate another molecule of tempo or of phenanthroline which might lead to the subsequent removal of another Cp^* radical. The dimerisation energy for the $Sm(tempo)_3$ is favourable and pushed the reaction towards the formation of a dimeric $(Sm(tempo)_3)_2$.

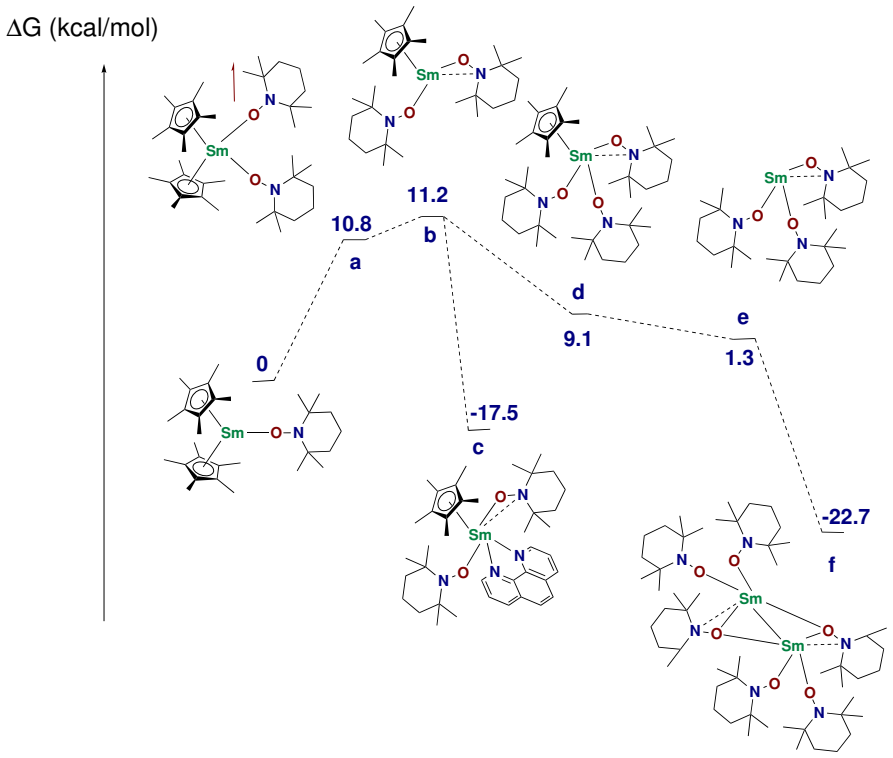

Figure 3.16: DFT reaction mechanism for the formation of $Cp^*Sm(tempo)_2$ at the PBE0-D3 ZORA3 level of theory

The mechanism was simulated using other density functionals such as PBE-D3, M06-2X and ω B97X-D3 and the results are shown in Table 3.4. Even if some differences between the different functionals exist, the general mechanism presented in Figure 3.16 and detailed earlier is validated using all the functionals.

ΔG (kcal/mol)	PBE-D3	PBE0-D3	M06-2X	ωB97X-D3
a	6.9	10.8	5.4	13.6
b	9.2	11.2	8.9	11.5
c	-22.8	-17.5	-27.7	-17.7
d	-11.0	9.1	1.5	6.0
e	-0.7	1.3	-2.1	2.1
f	-27.4	-22.7	-31.2	-30.4

Table 3.4: Gibbs free enthalpy of the different intermediates defined in Figure 3.16 using different density functional compared to the initial reagent $Cp^*_2Sm(tempo)$

These results indicate that $Cp^*_2Sm(tempo)$ is rather easily transformed into $(Sm(tempo)_3)_2$, as the formation of $Cp^*Sm(tempo)_3$ is thermodynamically favoured, which aids the deco-ordination of a Cp^* radical and further coordination of a tempo molecule.

These calculations have also been investigated with the bulkier Cp^{ttt} ligand. The activation energy for the first addition of a tempo molecule (**a**) has been calculated at the PBE0-D3 and PBE-D3 level of theory. Compared to the activation energy for the Cp^* molecules, the Cp^{ttt} activation energy is twice as high: 18.0, 25.7 and 23.1 kcal/mol at the PBE-D3, PBE0-D3 and M06-2X level of theory. The steric hindrance around the lanthanide ion prohibits the coordination of another tempo molecule. This is in agreement with experiments as no experimental degradation of $Cp^{ttt}_2Sm(tempo)$ was found in either thf or toluene.

3.1.4 Partial conclusion

The reaction of tempo with derivatives of samarium (Cp^*_2Sm and Cp^{ttt}_2Sm) led to the formation of new complexes bearing tempo molecule. The addition of tempo on Cp^*_2Sm led to the direct formation of multiple products ($Cp^*_2Sm(tempo)$, $Cp^*Sm(tempo)_2$ and $(Sm(tempo)_3)_2$). This was rationalised using DFT methods, as the formation of the intermediate $Cp^*Sm(tempo)_2$ starting from $Cp^*_2Sm(tempo)$ is easy and leads to $(Sm(tempo)_3)_2$. For Cp^{ttt}_2Sm complexes, the addition is stopped at the $Cp^{ttt}_2Sm(tempo)$ step because the sterics around the lanthanide centre is prohibiting the formation of an intermediate $Cp^{ttt}_2Sm(tempo)_2$, which increases the activation energy necessary for this reaction to happen. The propensity of Cp^* ligands to form their radical counterpart have led to the successful characterisation of these different complexes. However, in the present case, the sterics did not play a facilitator role as for Cp^*_3Sm but rather inhibited the formation of $Cp^{ttt}_2Sm(tempo)_2$.

The use of phenanthroline radical as an electron reservoir was proven, as both complexes of phenanthroline, $Cp^*_2Sm(phen)$ and $Cp^{ttt}_2Sm(phen)$ exhibit the same type of reactivity than their parents molecule with no phenanthroline. The electron transfer from phenanthroline to tempo is passing through an intermediate $Cp^*_2Sm(phen)(tempo)$. In this molecule, the electron transfer is occurring, and leads to the easy decoordination of phenanthroline. Electron reservoir can be used in order to store one electron and this electron can be used in order to selectively perform the same type of reaction than with a Sm^{2+} ion.

It could be interesting to study the influence of the radical electron on the phenanthroline moiety, by using other molecules that can easily react with this type of radical instead of

reacting on the lanthanide itself. In this context reactions with CO_2, and benzoquinone have been performed but did not lead to the characterisation of any material, due to the large number of side-products for these reactions.

The redox potential of benzophenone is lower than phenanthroline. As a result, upon addition of SmI_2 on a mixture of phenanthroline and benzophenone, the latter is reduced while the former is present in solution. This could trigger a reactivity from the ketyl radical to the phenanthroline molecule.

3.2 Coupling reaction between benzophenone and N-heterocycle molecules

3.2.1 Minisci reaction

In medicinal chemistry, heterocycle fragments are often used for the design of new drugs[20] (for a review on recent development in heterocycle chemistry related to drug discovery read the review from Fadeyi[21]). Specifically, aromatic heterocycles have been vastly explored for everything related to drug discovery. By doing so, medicinal chemists are attempting to copy nature that uses aromatic heterocycles in molecules such as hemoglobin or Vitamin B1[22]. N-heterocycles have been among the most prominent fragments in drug discovery[23] and their design is constantly under study in order to promote novel molecules[24].

Functionalisation of N-heteroaromatic molecules can be performed using different processes: electrophilic addition at the nitrogen atom, electrophilic and nucleophilic substitution at the carbon atoms, and radical substitution of hydrogen atoms[25]. While coupling reactions using palladium[26] or cobalt complexes[27,28] have been deeply investigated in recent years, the radical substitution reactions are rather under-used[29].

Radical substitution reactions on N-heterocycles have been known since the 1890s[30], but only after the seminal work of Minisci and coworkers in the 1970s[31] did these reactions found an interest in organic chemistry[32]. The early attempts faced a challenge linked to the selectivity of the reaction as the ortho, meta and para substitution of the hydrogen atoms were possible[33] (Figure 3.17). Minisci and coworkers were able to show that in an acid media, the reaction was selective and favoured one position over the others depending on

the N-heteroaromatic compound. One of the other drawbacks is the small yields ($< 50\%$) associated with a consumption of less than one equivalent of the starting materials[29]. Even though these limitations exist, Minisci reactions have been able to perform novel C-H functionalisation on N-heteroarenes that cannot be done using other methodologies[34]. In the last decade, Minisci reactions have been taken back in front of the scene with the substantial work of Baran *et al.*[35]. They were capable of producing borono-Minisci couplings[36], electro-chemically induced Minsci coupling[37] and recently iron-mediated Minisci reactions with moderate to high yields[38].

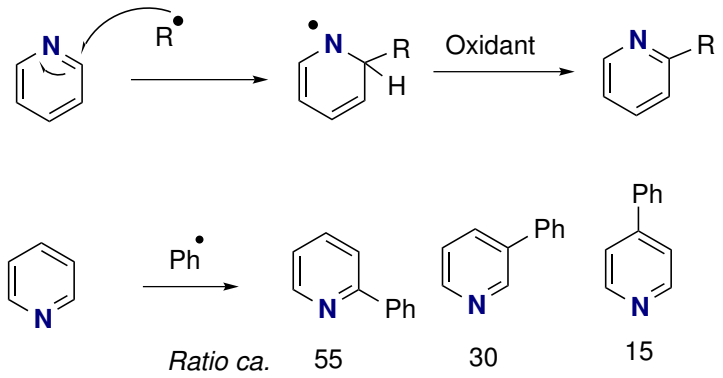

Figure 3.17: Mechanism of the Minisci reaction (top), and early problems with radical substitution (bottom)

The coupling between heteroarene and ketone such as benzophenone has been recently studied with thorium[39–41] and uranium complexes[42] (Figure 3.18). In the thorium complexes, an anionic bipyridine is coordinated to the metal centre and, upon addition of benzophenone, the latter is reduced and a coupling is observed between benzophenone and bipyridine. The same type of mechanism was observed with uranium complexes bearing a radical bipyridine moiety: uranium reduces benzophenone and both radical couple to form the C-C bond. Contrary to the Minisci reaction, in both cases the hydrogen is not removed from the bipyridine and the resulting product has lost its aromaticity.

In this sense, could samarium complexes be able to perform selectively Minisci type reaction in ortho of the N-heterocycle? In order to study this type of coupling samarium complexes bearing a benzophenone ketyl radical moiety were reacted with phenanthroline (Figure 3.19). In the hypothetical system that bears both phenanthroline and benzophenone, the radical transfer will process selectively to the benzophenone ketyl radical, as benzophenone

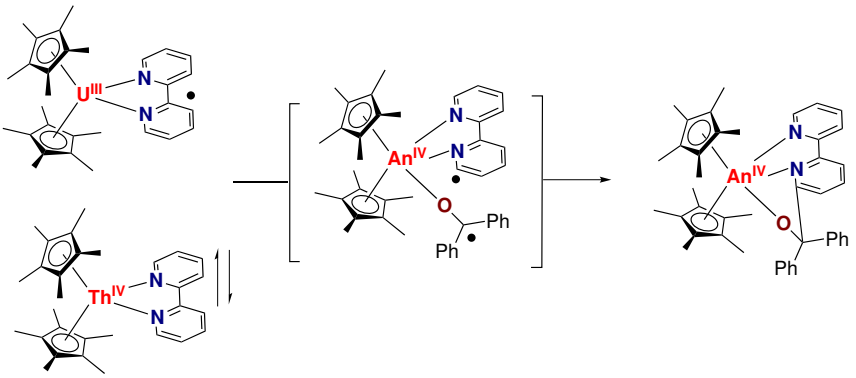

Figure 3.18: Coupling reaction between a bipyridine and a benzophenone moiety for different actinide complexes[39,42]; An = Th, U, the starting material for uranium contains a radical bipyridine, and the thorium complex contains a bipyridine anion

redox potential is higher than phenanthroline. In a first time, the coupling between phenanthroline and benzophenone will be presented in two different solvants. Investigation into its mechanism will be developed next and analysed with both DFT and CASSCF methods.

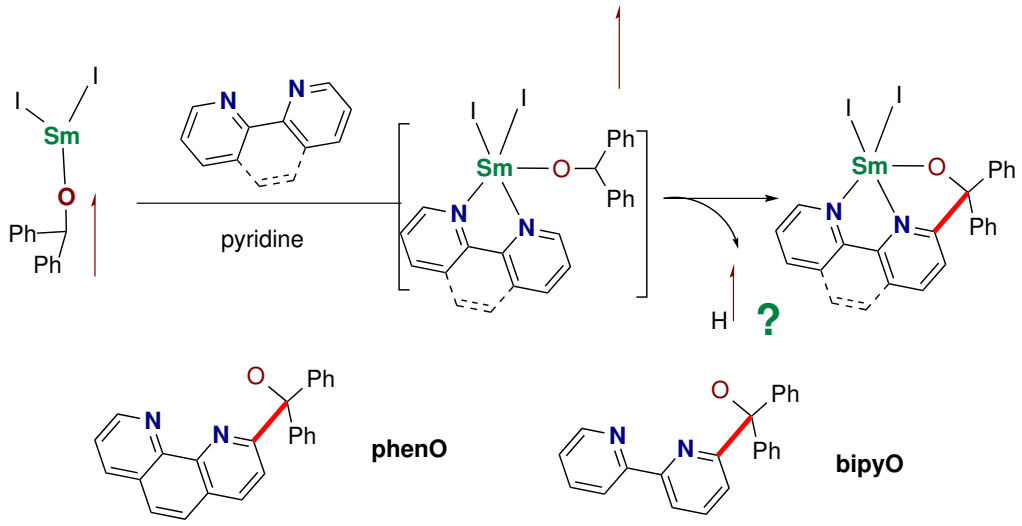

Figure 3.19: Coupling reaction between benzophenone and phenanthroline with SmI_2 derivatives

3.2.2 Coupling reaction

A solution of $I_2Sm(bph)$ in pyridine (detailed in Chapter 2) is reacted with one equivalent of phenanthroline. Upon addition, the solution passes from black-purple to deep-yellow. Crystallisation of the complex in pyridine only resulted in crystals that were not suitable for X-Ray diffraction analysis. On the contrary in acetonitrile, the crystals were suitable for X-Ray diffraction analysis, and the resulting X-Ray is presented in Figure 3.20. In addition

to the *phenO* ligand, the structure presents one acetonitrile and one neutral phenanthroline molecule coordinated to the lanthanide centre in order to complete its coordination sphere. There is a disymmetry of the two nitrogens of the phenanthroline arm of *phenO*, which is related to the close $\mathrm{Sm-O}$ distance and the related angle $\widehat{\mathrm{OCC}}(\mathrm{phen})$.

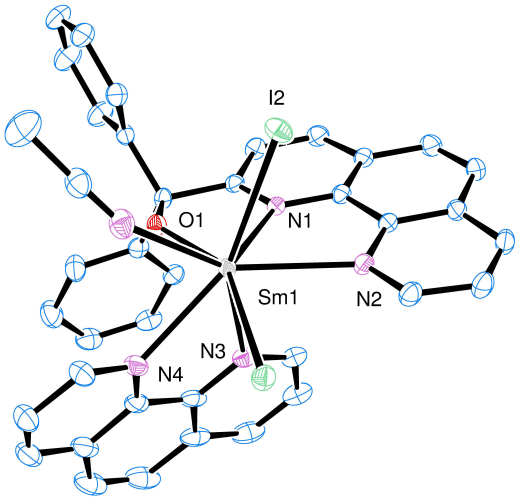

Figure 3.20: ORTEP of the X-Ray structure of $\mathrm{I_2Sm(phenO)(MeCN)(phen)}$; selected distances in angstroms: $\mathrm{Sm-O}$ 2.129(1), $\mathrm{Sm-N1}$ 2.544(2), $\mathrm{Sm-N2}$ 2.681(2), $\mathrm{Sm-N3}$ 2.606(2), $\mathrm{Sm-N4}$ 2.622(2), $\mathrm{Sm-I1}$ 3.2828(2), $\mathrm{Sm-I2}$ 3.1819(2)

Changing the N-heterocycle from phenanthroline to bipyridine resulted in the same type of coupling. Instead of a change in color that happens directly after addition of phenanthroline, the solution turned yellow with bipyridine at a slower rate. This can be due to a slow exchange between pyridine and bipyridine in solution. Yellow block crystals were then gathered but were unsuitable for further X-Ray diffraction analysis. Other N-aromatic molecules such as phenylpyridine, quinoline, quinaldine and neocuproine produced a color change from black purple to deep yellow, and the resulting compounds are currently under study.

In order to study the mechanism and the influence of the ketone on this coupling, chalcone complexes of samarium (Chapter 2) were reacted with phenanthroline in pyridine. The solution did not change colour, even after heating for several hours at $110^{\circ}\mathrm{C}$. Yellow crystals were nonetheless gathered and were suitable for X-Ray diffraction analysis (Figure 3.21). The coupling did not occur and phenanthroline and chalcone are both present in the new complex. As discussed in Chapter 2, with chalcone, it was not possible to see an equilibrium between the monomer radical and the dimer in solution using different solvents.

This might be related to the absence of coupling, as the C-C σ bond is thermodynamically more stable than the one in benzophenone dimers.

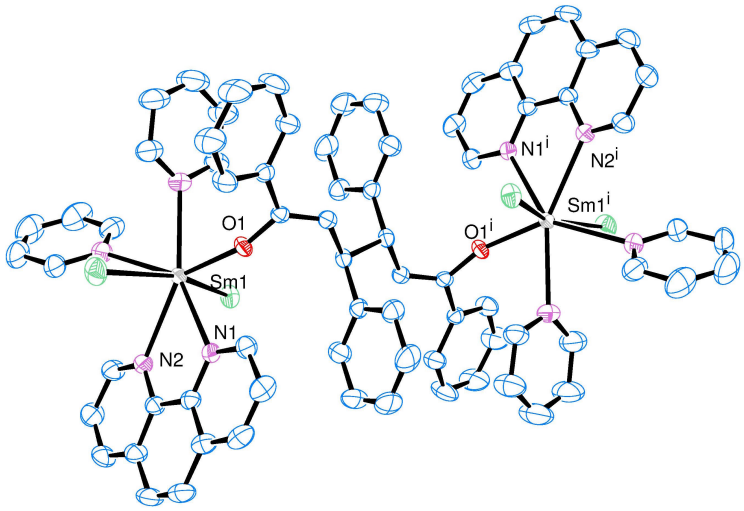

Figure 3.21: ORTEP of the X-Ray structure of $(I_2Sm(phen)(pyr)(chalcone))_2$; selected distances in angstroms: Sm — O 2.125(3), Sm — N1 2.594(3), Sm — N2 2.625(4), Sm — I1 3.1089(4), Sm — I2 3.1228(4)

The hydrolysis of $I_2Sm(phenO)(MeCN)(phen)$ was conducted under acidic conditions. After extraction in dichloromethane, the compound was recrystallised in ethanol and yielded 30 % of *phenOH*. $I_2Sm(bph)$ was also stirred in pyridine at 110°C for 12 hours, and the color of the solution turned from dark purple to deep yellow. After the extraction, the reaction yielded 20 % of colourless crystals of *pyrOH* (Figure 3.22 for crystal structures of *phenOH* and *pyrOH*). This means that pyridine might be in competition with other N-heteroarenes.

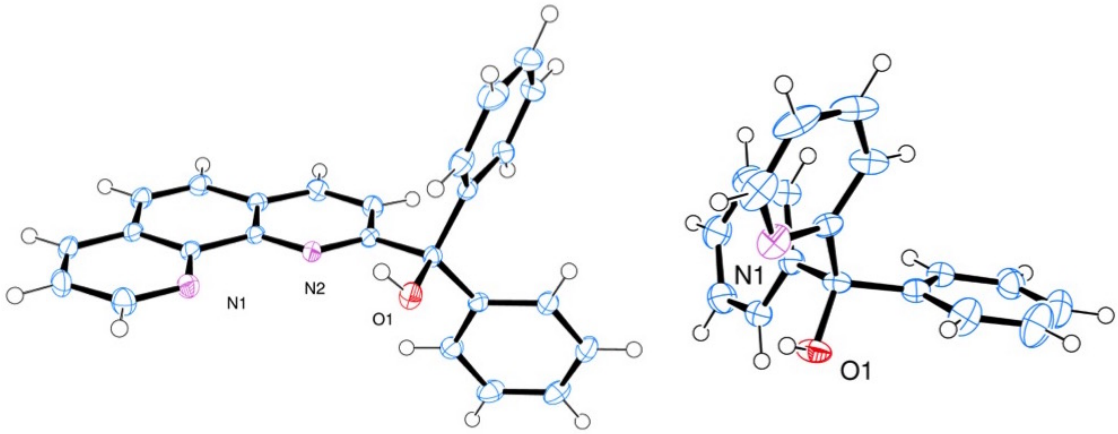

Figure 3.22: ORTEP of the X-Ray structure of *phenO* and *pyrO*

Therefore, the reaction was also performed in acetonitrile. In acetonitrile, upon addition of phenanthroline on $I_2Sm(bph)$, the solution turns from yellow to deep red. This colour does not evolve for a few hours and then turns to yellow, the characteristic colour from the coupling product. Crystals of the final product were obtained and were similar to what was previously found (Figure 3.20).

Despite our best efforts, the crystallisation attempts of the red intermediate were not possible, and pale blocks were crystallised instead. They corresponded to a polymetallic structure containing two lanthanides, two *phenO* ligands, one benzhydrol anionic ligand, and two iodide atoms coordinated to the lanthanide and an out-of-coordination iodide ion (Figure 3.23). Compared to the previous structure, the distance $Sm - O$ is longer (2.1 and 2.3 Å respectively). This is probably due to the large number of oxygen atoms surrounding both samarium ions, that decreases the propensity of samarium to create strong bonds with oxygen atoms. This structure points out towards a bimetallic reaction where one benzophenone ketyl radical attacks the phenanthroline ligand and another one is performing a $C - H$ abstraction on phenanthroline.

3.2.3 Mechanism

Minisci reactions are known to happen in a specific pathway: first the radical is attacking the π system and then, an oxidant triggers the aromatisation of the π system (Figure 3.17). For this specific example, only $I_2Sm(bph)$, phenanthroline and benzophenone are present in solution. None of these molecules can act as an oxidant, as their redox potential is too small to promote such an reaction[43].

At this stage two different mechanisms can be expected. Upon addition of phenanthroline on $I_2Sm(bph)$, an equilibrium will be formed between the dimeric benzophenone complex and the monomeric ketyl radical complexes. Then, when the molecule is in its monomeric state, the coupling between the benzophenone ketyl radical and phenanthroline is possible either in a mono-molecular way (Figure 3.24), or in a bi-molecular way (Figure 3.25). The mono-molecular pathway involves the attack of the radical on the phenanthroline moiety and subsequent formation of a hydrogen radical that can either react with itself to form

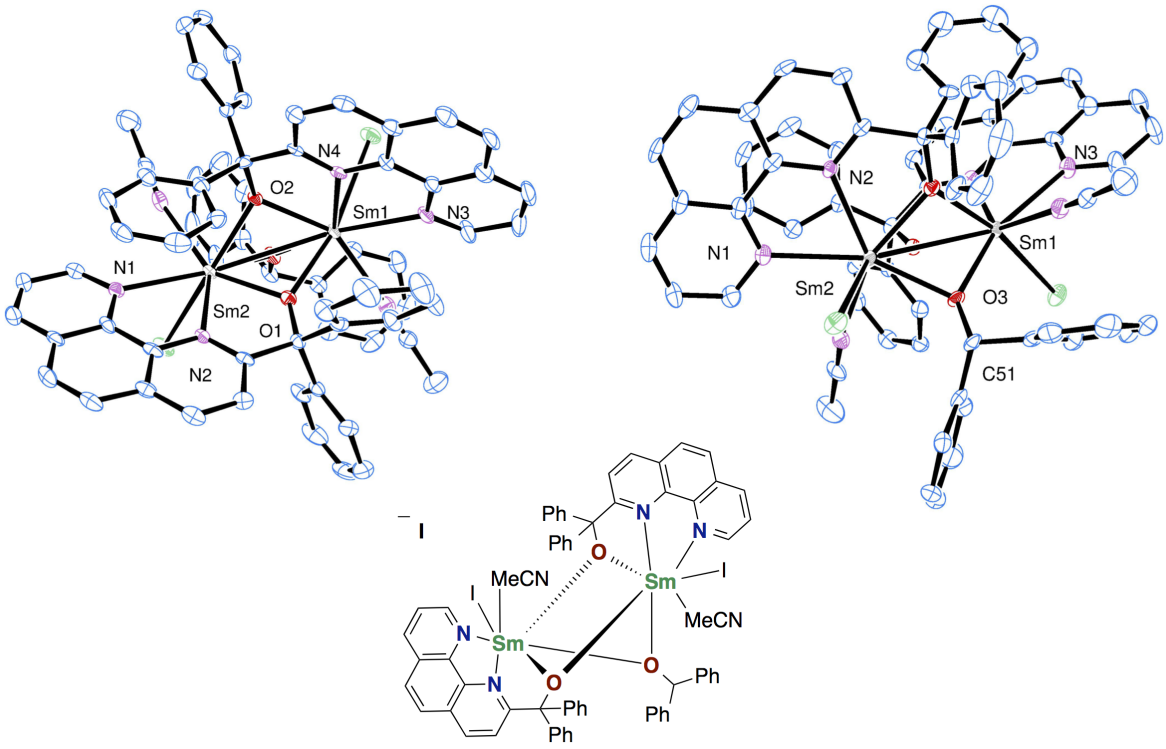

Figure 3.23: ORTEPs of the X-Ray structure of the intermediate compound, acetonitrile solvants and the uncoordinated iodide were removed from the plots for clarity; selected distances in angstroms: Sm1 — O1 2.357(3), Sm1 — O2 2.340(3), Sm1 — O3 2.316(3), Sm1 — N3 2.599(4), Sm1 — N4 2.527(4), Sm2 — O1 2.335(3), Sm2 — O2 2.324(3), Sm2 — O3 2.377(3), Sm2 — N1 2.601(4), Sm2 — N2 2.515(4), Sm1 — Sm2 3.4410(4), 03 — C51 1.431(5)

H_2 or with one ketyl radical (M). The bi-molecular pathway is processing through a H-abstraction of one hydrogen of the phenanthroline moiety by the ketyl radical and then coupling between the two radicals.

Both pathways seem difficult to evaluate. The removal of a radical hydrogen atom is difficult, and should not happen without a strong abstractor. The bimolecular mechanism seems rather unlikely as the removal of a hydrogen from a phenanthroline molecule is difficult. Experimentally, the reaction was performed in pyridine with less than one equivalent of either dihydroanthacene or 1,4-cyclohexadiene, known to behave as hydrogen radical donor[44]. Following the reaction by ^{1}H NMR did not show any disappearance that could be related to a consumption of these compounds. This seems to indicate that there is no hydrogen radical present in the solution.

In order to differentiate both pathways, quantum chemistry analyses were undertaken.

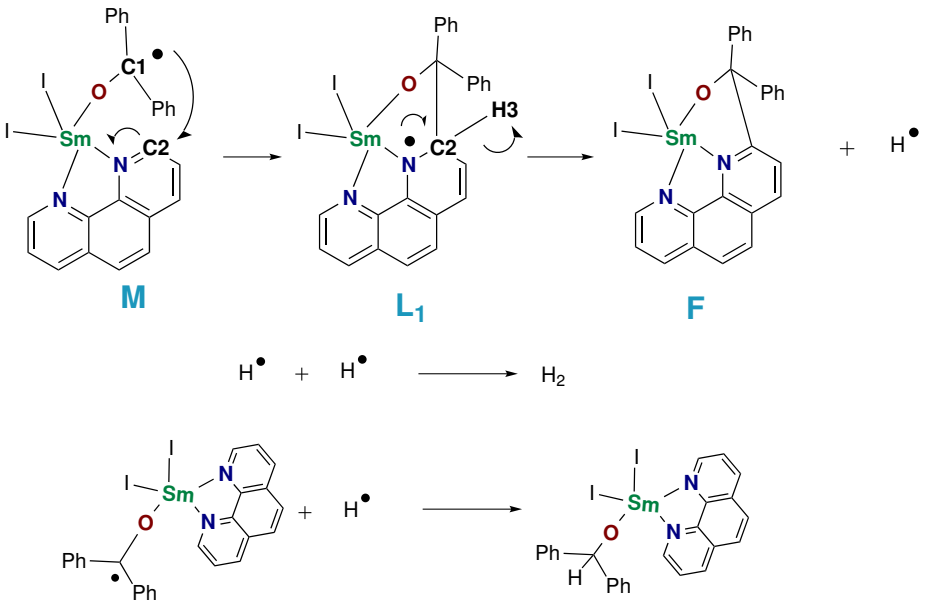

Figure 3.24: Mono-molecular mechanism

3.2.3.1 Understanding the mechanism of the reaction

It is interesting to understand the electronic structure of M. The redox potential of benzophenone and phenanthroline are in agreement with a reduced benzophenone instead of a reduced phenanthroline. But the proximity of these two states could also be the starting element for the coupling between benzophenone and phenanthroline to occur. The calculations were performed on pyridine solvated complexes with two pyridines on each samarium centre in addition to the iodide atoms, bph and phen.

- **Electronic structure of M**

The electronic structure of M was investigated at the CASSCF level of theory, CASSCF(10,12). The active space consists in the seven 4f orbitals, the π^*_{bph} orbital of benzophenone, π^*_2 and π^*_1 of phenanthroline and the corresponding two lone pairs of the nitrogen (Chapter 2 for a view of these orbitals). The ground state electronic structure of the molecule is $4f^5\pi^{*\uparrow}_{\text{bph}}$. The first excited state that promotes one electron into the π^*_1 is distant of 52.4 (63.8) kcal/mol at the CASPT2 (CASSCF) level of theory. It seems highly unlikely that such a distant excited state has an influence in the reaction mechanism. Considering this data, the mechanism from M to F will be investigated using DFT methods as no multi-reference character is expected in the ground state.

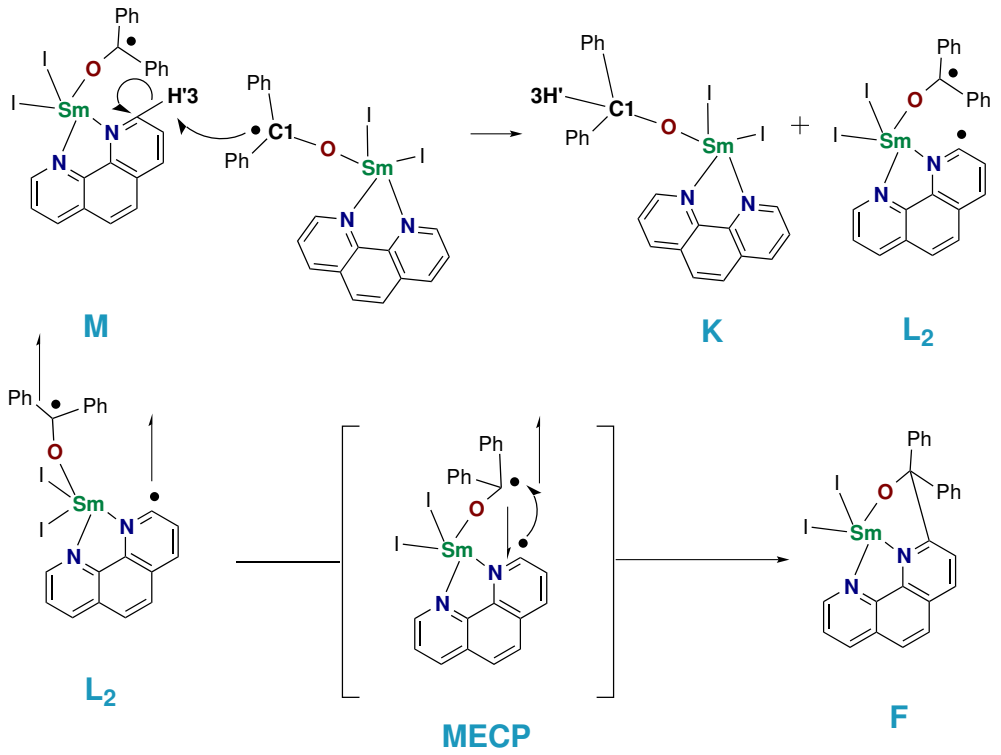

Figure 3.25: Bi-molecular mechanism

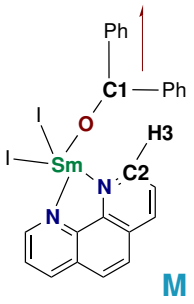

Figure 3.26: Label for the different atoms in M

- **Bi-molecular mechanism**

The bi-molecular pathway (Figure 3.25) was investigated at the DFT level. A Potential Energy Surface (PES) plot of the C1 — H′3 distance between two different M molecules was performed at the PBE-D3 level of theory.

The PES shows that at a C1 — H′3 distance of 1.17 Å an abrupt change in the energy occurs: the hydrogen radical is transferred to the ketyl radical, inducing a geometry evolution of the two molecules in interaction. Starting from the highest point of the PES, a transition state calculation was able to converge towards the transition state of this reaction. For this

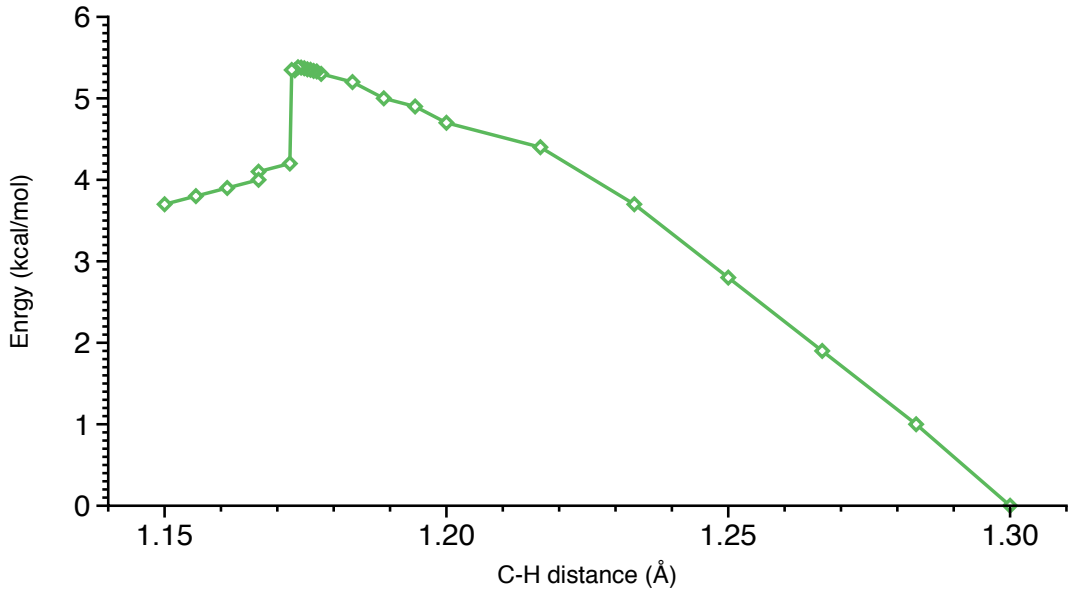

Figure 3.27: Potential energy surface depending on the C1 — H′3 distance at the PBE-D3 level of theory

compound C1 — H3 is 1.174 Å, and C2 — H3 is 1.693 Å.

The mechanism detailed in Figure 3.25 was then calculated at the PBE-D3 level of theory. The results are summarised in Figure 3.28. As detailed previously the rate determining step is the C-H bond abstraction. The activation energy for this step is 51.1 kcal at the PBE-D3 level. Then, the mechanism passes through the MECP which is almost degenerate with the geometry of L_2. After crossing the MECP, the final compound is created by C — C coupling.

From these results, two conclusions can be drawn: the bimolecular mechanism is highly unlikely and the thermodynamics are not favourable for the formation of this C — C bond. While the former can be understood as the monomolecular pathway might be preferable, the latter means that the mechanism lack the driving force of the reaction. In a first step, the monomolecular pathway will be investigated by DFT calculations.

- **Mono-molecular mechanism**

The mono-molecular mechanism passes through the formation of the C1 — C2 bond, and by subsequent removal of a hydrogen radical (Figure 3.24). Starting from the optimised structure of $I_2Sm(phen)(bph)(pyr)_2$ (M), the C1—C2 distance was varied from its original value (3.14 Å) to 1.50 Å at the PBE-D3 level. The energy was then calculated for each point using PBE0-D3 and M06-2X. The activation energies at the M06-2X and PBE0-D3 levels

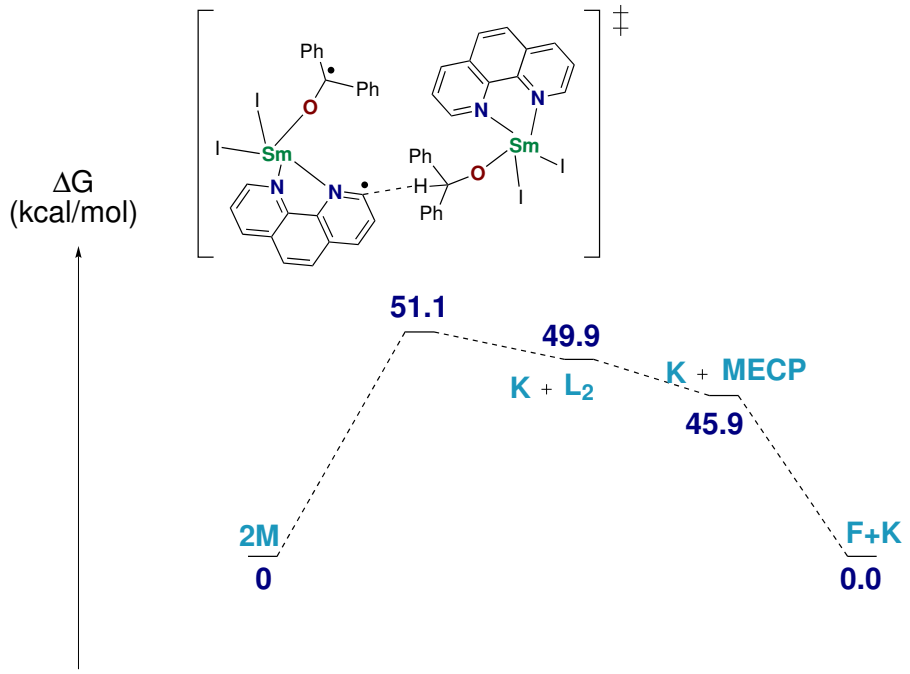

Figure 3.28: Reaction mechanism for the formation of *phenO* and relative energies at the PBE-D3 level of theory; pyridine solvent molecules coordinated to the samarium centre were removed for clarity

are 15.2 kcal/mol and 13.7 kcal/mol respectively. Contrary to what could have been expected, this activation energy is not high and could mean that in solution there is an equilibrium between the coupled product and the non-coupled one. The transition state orbitals were analysed at the PBE0-D3 ZORA1 level of theory (Table 3.5).

The spin density of this molecule indicates that the radical is localised on the π cycle of phenanthroline, with a delocalisation into the σ bond created. This is in agreement with a thermodynamically not stable C — C bond. The SOMO is localised on one side of the phenanthroline ligand with little involvement from the iodide atoms. The first LUMO is one 4f orbital, and the LUMO+1 and LUMO+5 corresponds to the π_1^* and π_2^* orbitals of phenanthroline.

The ejection of a H radical was then studied. The C2 — H3 distance was varied from 1.1 Å to 1.8 Å at the PBE-D3 level of theory. The potential energy surface depending on the C2 — H3 bond distance is shown in Figure 3.29 for three different density functionals. The activation energy for this C — H dissociation is high, and has a similar value using PBE0-D3, PBE-D3 or M06-2X. It is therefore expected for this C — H abstraction to occur that it should be helped by a base capable of performing the abstraction. One of such base is the

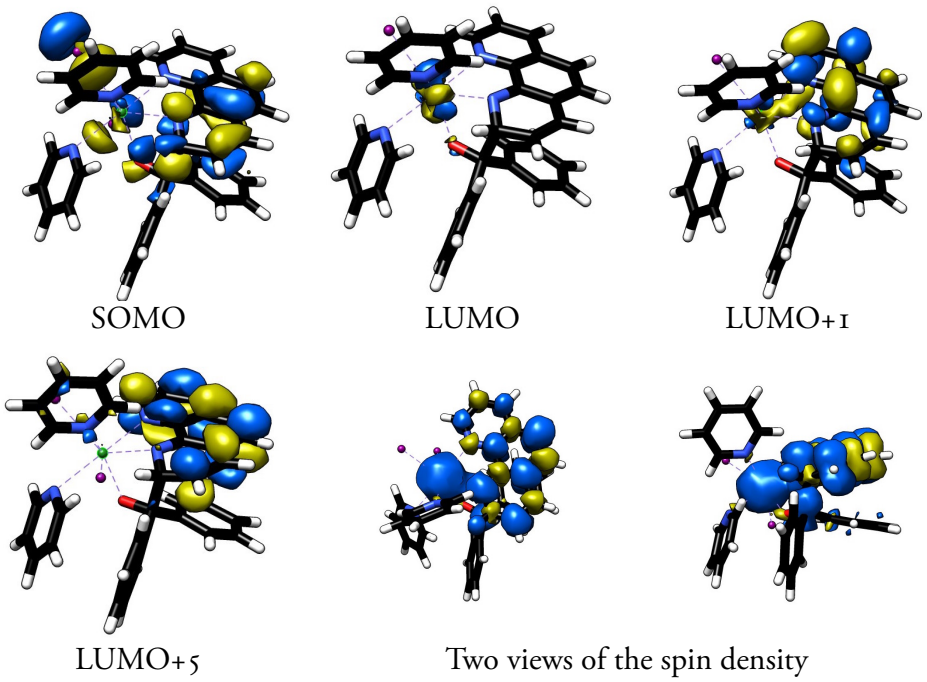

Table 3.5: Molecular orbitals and spin density of L_1 at the PBE0-D3 level

initial ketyl radical, but despite our best efforts optimising the geometry for the bimolecular C2 — H3 abstraction starting from the intermediate L_1 only resulted in the breaking of the C1 — C2 bond in L_1 leading back to M.

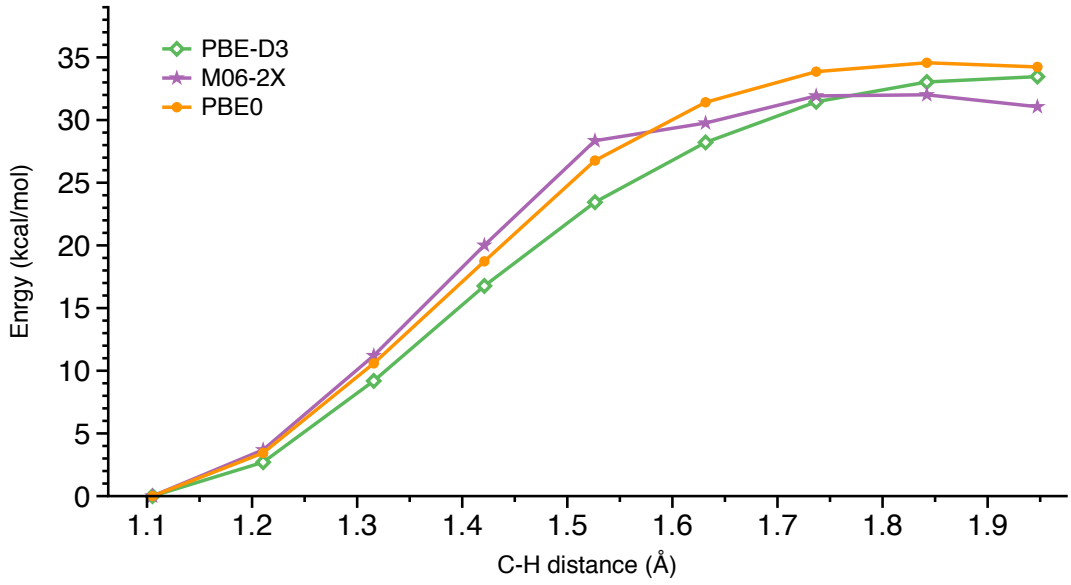

Figure 3.29: Potential energy surface depending on the C2 — H3 distance using different density functionals

Overall, there is no big difference in the activation energy for both pathways: around 50

kcal/mol. Based on the DFT results, both pathways are rather unlikely at room temperature. Other experimental mechanistic evidences have to be gained in order to understand better the reaction mechanism.

3.2.3.2 Following the reaction by UV-vis

Contrary to pyridine in which the reaction happened too fast to be followed by any spectroscopy at our disposal, in acetonitrile an intermediate species was observed experimentally. The UV-visible spectrum of $I_2Sm(bph)$, the intermediate species, the final product and $I_2Sm(phen)$ are presented in Figure 3.30.

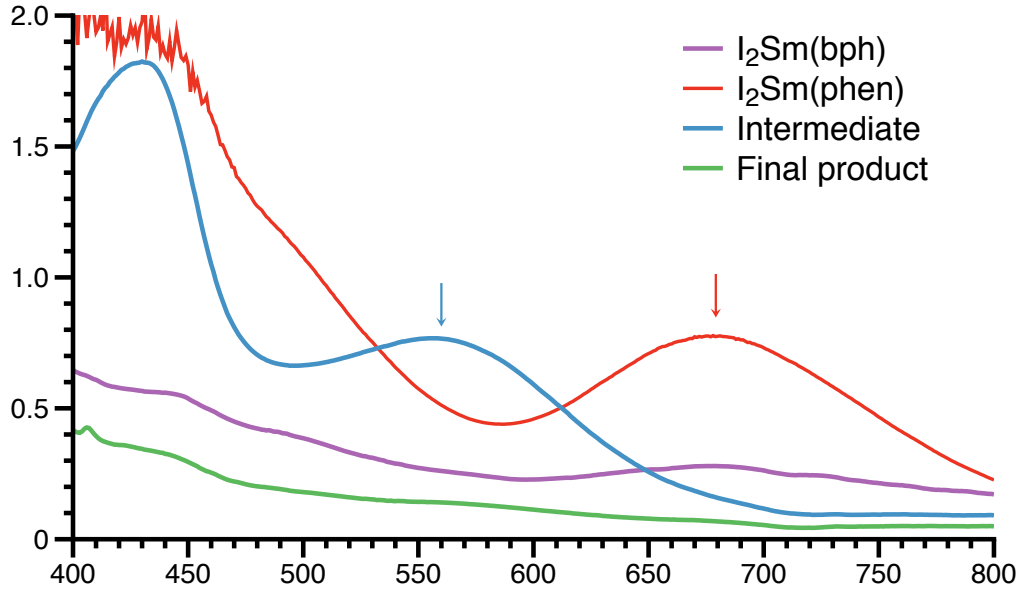

Figure 3.30: UV-visible spectrum of different compounds, $I_2Sm(bph)$, $I_2Sm(phen)$, the intermediate and the final product of the coupling reaction; arrows indicate significant peaks corresponding to $I_2Sm(phen)$ or to the intermediate

Both $I_2Sm(bph)$ and the final compound of the reaction do not present significant absorption in the visible range of the spectrum. $I_2Sm(phen)$ and the intermediate compound do possess absorption bands in the visible range of the spectrum. As a result the decomposition of the intermediate species can be followed by UV-visible spectrum, as it will correspond to the disappearance of the peak at 560 nm. This peak does not correspond to phenanthroline radical (Figure 3.30) or to benzophenone ketyl radical (Chapter 2) as both molecules absorb at different wavelength.

Therefore, degradation kinetics depending on different experimental parameters such as the concentration of each reactant can be performed. Such analysis was able to give indications about the influence of the concentration of each molecule, SmI_2, bph and phen on the half-life time of the reaction. In a first step the concentration of all the molecules was decreased from 7.4 to 2.5 mmol/L (Figure 3.31). The half-life depends on the inverse of the concentration, which indicates that the global order of the reaction is -1. Increasing the concentration of either phenanthroline or benzophenone resulted in a faster degradation, *i.e.* lower half-life. On the contrary, increasing the concentration of SmI_2 led to slower degradation, *i.e.* higher half-time.

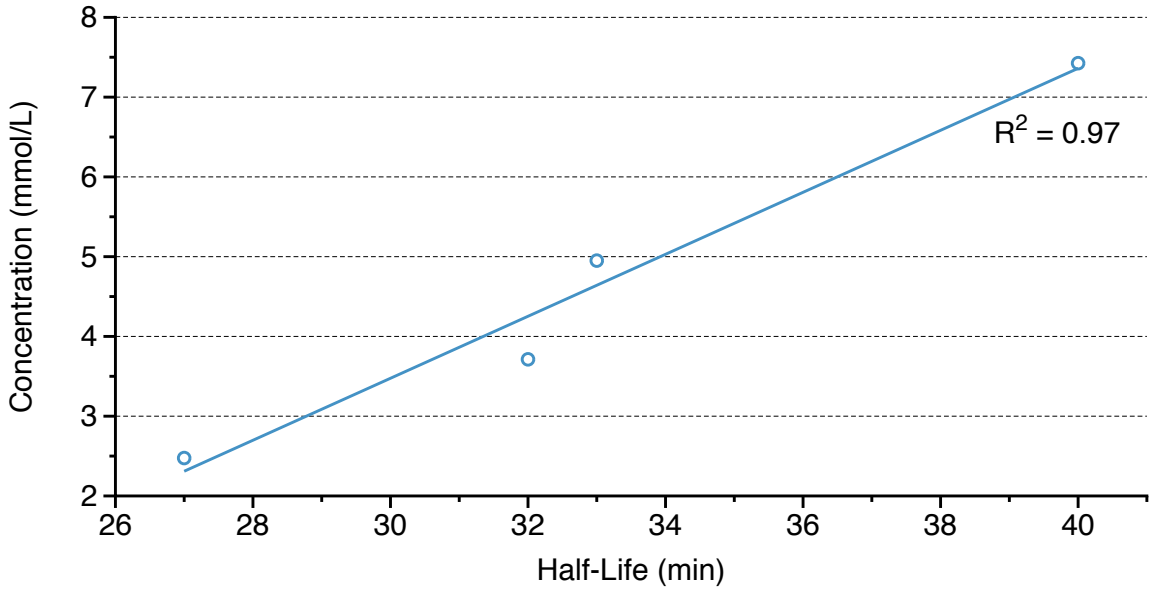

Figure 3.31: Evolution of the half-life for the intermediate species depending on the concentration of all the reactants

On one hand, the kinetics of this degradation has a linear dependance in the concentration of bph and phen. This is indicative of an order 1 for both compounds. On the other hand there is an inverse dependancy on the concentration of SmI_2, which is in agreement with an inverse order for this compound.

In the Minisci reaction, an oxidant is needed and triggers the aromatisation of the intermediate L_1 via departure of a proton. In this situation, we previously said that no oxidant were present in solution to trigger this type of reactivity. However, considering the kinetic inverse dependancy for SmI_2 and the high activation energy for the radical

mechanisms, could this reaction use samarium as an oxidant? In this context, the presence in excess of SmI_2 would decrease the rate of the samarium ion oxidation in L_1. This inverse rate could also be explained by the formation of poly-metallic species in presence of SmI_2, which are stable enough not to trigger the $C-C$ coupling. These hypotheses are currently being studied using an excess of SmI_3, the tempo radical, or oxidants such as I_2 to study the influence of these parameters on the half-life of the intermediate.

3.2.4 Conclusion and perspectives

In conclusion, SmI_2 can be used to couple N-heteroarenes and benzophenone. This type of reaction happens in a fast and clean way in pyridine leading to the subsequent formation of a new molecule *phenOH*, that can be isolated in a 30% yield. Other N-heteroarenes have been found to possess the same behaviour such as bipyridine, phenylpyridine, quinaldine, quinoline, neocuproine and pyridine. The formation of a coupling product with pyridine only happens at high temperature which might be related to the difficulty to abstract an hydrogen radical for pyridine compared to phenanthroline. The mechanism of this reaction can process either through a mono-molecular process or a bi-molecular process. Both processes have been investigated using quantum chemistry calculations and found that the bi-molecular pathway was the most favourable one. The identification of different species involved in this mechanism has been done using PBE-D3.

While in pyridine the reaction between benzophenone and phenanthroline happened in a fast and clean way, in acetonitrile, the coupling reaction is slow and passes through an intermediate that possesses a characteristic UV-vis spectrum with an absorption peak at 550 nm. Despite many attempts, the characterisation of this intermediate by means of standard X-Ray diffraction analysis only revealed the presence of the final product bearing two samarium centres. This intermediate specie can be the ketyl radical complex or the coupled L_1 compound that is close in energy from the ketyl radical. Further addition on this intermediate of oxydants and SmI_3 is being investigated in order to understand the nature of this intermediate. Another way to get information around this mechanism can pass through the scope of this reaction with different substrates and analysis of the different half-time of the intermediate species. This is also being investigated.

PhenO can also be used as a ligand in lanthanide chemistry. Bearing one oxygen and two nitrogen makes it particularly suitable for the design of new organolanthanide complexes. Moreover, its size is large enough to be coordinated on the lanthanide. The phenanthroline part of *phenO* can be used as an electron reservoir, or can also be decoordinated from the lanthanide centre (the molecule would still be coordinated through its oxygen). This type of ligand is needed in lanthanide chemistry in order to diversify the number of ligands available in this chemistry. Preliminary results with this ligand showed the formation of a symmetric $Sm(phenO)_3$ that was suitable for X-Ray diffraction analysis (Figure 3.32).

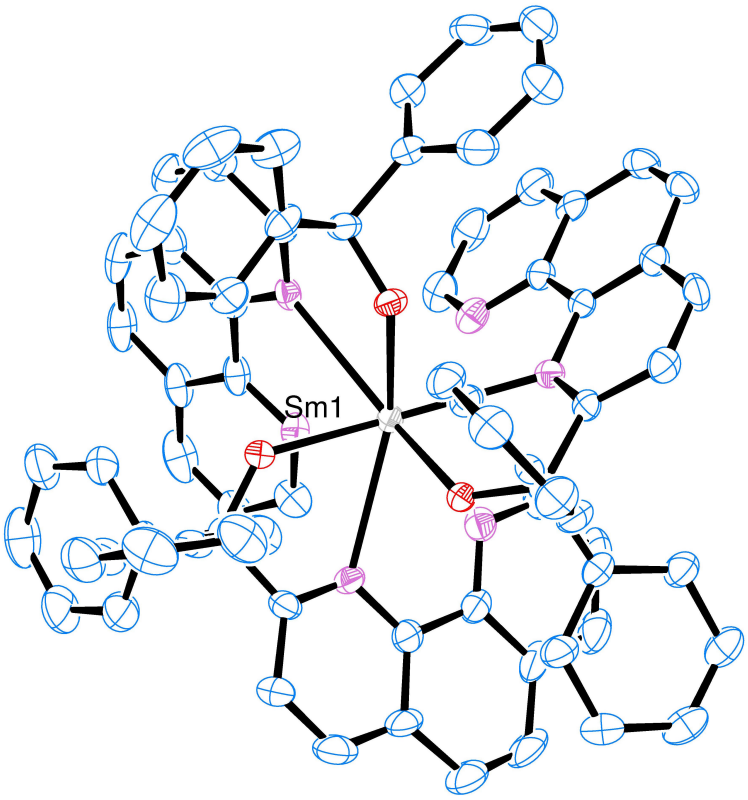

Figure 3.32: ORTEPs of the X-Ray structure of the intermediate structure, toluene molecules and the uncoordinated iodide were removed from the plots for clarity

References

[1] D. J. Procter, R. A. Flowers, T. Skrydstrup, *Organic Synthesis Using Samarium Diiodide*, Royal Society of Chemistry, **2010**.

[2] S. Kobayashi, R. Anwander, *Lanthanides: Chemistry and Use in Organic Synthesis*, Springer Science & Business Media, **1999**.

[3] W. J. Evans, *J. Alloys Compd.* **2009**, *488*, 493–510.

[4] W. J. Evans, S. L. Gonzales, J. W. Ziller, *J. Am. Chem. Soc.* **1991**, *113*, 7423–7424.

[5] R. P. Kelly, N. Kazeminejad, C. A. Lamsfus, L. Maron, P. W. Roesky, *Chem. Commun.* **2016**, *52*, 13090–13093.

[6] W. J. Evans, J. M. Perotti, S. A. Kozimor, T. M. Champagne, B. L. Davis, G. W. Nyce, C. H. Fujimoto, R. D. Clark, M. A. Johnston, J. W. Ziller, *Organometallics* **2005**, *24*, 3916–3931.

[7] L. Jacquot, M. Xémard, C. Clavaguéra, G. Nocton, *Organometallics* **2014**, *33*, 4100–4106.

[8] W. J. Evans, J. M. Perotti, R. J. Doedens, J. W. Ziller, *Chem. Commun.* **2001**, 2326–2327.

[9] G. C. Forbes, A. R. Kennedy, R. E. Mulvey, P. J. A. Rodger, *Chem. Commun.* **2001**, 1400–1401.

[10] R. R. Langeslay, J. R. Walensky, J. W. Ziller, W. J. Evans, *Inorg. Chem.* **2014**, *53*, 8455–8463.

[11] P. Jutzi, F. Kohl, *J. Organomet. Chem.* **1979**, *164*, 141–152.

[12] A. G. Davies, J. Lusztyk, *J. Chem. Soc. Chem. Commun.* **1980**, 554–555.

[13] A. G. Davies, J. Lusztyk, *J. Chem. Soc. Perkin Trans. 2* **1981**, 692–696.

[14] H. Sitzmann, G. Wolmershäuser, *Chem. Ber.* **1994**, *127*, 1335–1342.

[15] H. Sitzmann, T. Dezember, O. Schmitt, *Z. Anorg. Allf. Chem.* **2000**, *626*, 2241–2244.

[16] G. Nocton, L. Ricard, *Chem. Commun.* **2015**, *51*, 3578–3581.

[17] L. Balloch, A. M. Drummond, P. García-Álvarez, D. V. Graham, A. R. Kennedy, J. Klett, R. E. Mulvey, C. T. O'Hara, P. J. A. Rodger, I. D. Rushworth, *Inorg. Chem.* **2009**, *48*, 6934–6944.

[18] J. N. Harvey, *WIREs Comput. Mol. Sci.* **2013**, *4*, 1–14.

[19] M. Besora, J.-L. Carreón-Macedo, Á. Cimas, J. N. Harvey, *Adv. Inorg. Chem.* **2009**, *61*, 573–623.

[20] A. Gomtsyan, *Chemistry of heterocyclic compounds* **2012**, *48*, 7–10.

[21] A. P. Taylor, R. P. Robinson, Y. M. Fobian, D. C. Blakemore, L. H. Jones, O. Fadeyi, *Org. Biomol. Chem.* **2016**, *14*, 6611–6637.

[22] J. J. Li, *Heterocyclic chemistry in drug discovery*, (Ed.: J. J. Li), John Wiley & Sons, **2013**.

[23] E. Vitaku, D. T. Smith, J. T. Njardarson, *J. Med. Chem.* **2014**, *57*, 10257–10274.

[24] W. R. Pitt, D. M. Parry, B. G. Perry, C. R. Groom, *J. Med. Chem.* **2009**, *52*, 2952–2963.

[25] J. A. J. Mills, Keith, *Heterocyclic Chemistry, Fifth Edition*, Wiley & Sons, **2010**.

[26] J. J. Li, G. W. Gribble, *Palladium in heterocyclic chemistry: a guide for the synthetic chemist*, Pergamon Press Ltd., **2006**.

[27] Y. Cai, PhD thesis, Ecole polytechnique, **2016**.

[28] A. Rerat, PhD thesis, Ecole polytechnique, **2016**.

[29] M. A. J. Duncton, *Med. Chem. Commun.* **2011**, *2*, 1135–1161.

[30] R. Möhlau, R. Berger, *Ber. Dtsch. Chem. Ges.* **1893**, *26*, 1196–1200.

[31] F. Minisci, R. Bernardi, F. Bertini, R. Galli, *Tetrahedron* **1971**, 1–6.

[32] F. Minisci, E. Vismara, F. Fontana, *Heterocycles* **1989**, *28*, 489–519.

[33] M. Gomberg, W. E. Bachmann, *J. Am. Chem. Soc.* **1924**, *46*, 2339–2343.

[34] D. C. Harrowven, B. J. Sutton, *Progress in Heterocyclic Chemistry* **2005**.

[35] Q. Michaudel, Y. Ishihara, P. S. Baran, *Acc. Chem. Res.* **2015**, *48*, 712–721.

[36] Y. Fujiwara, J. A. Dixon, F. O'Hara, E. D. Funder, D. D. Dixon, R. A. Rodriguez, R. D. Baxter, B. Herlé, N. Sach, M. R. Collins, Y. Ishihara, P. S. Baran, *Nature* **2012**, *492*, 95–99.

[37] E. J. Horn, B. R. Rosen, P. S. Baran, *ACS Cent. Sci.* **2016**, *2*, 302–308.

[38] J. C. Lo, D. Kim, C.-M. Pan, J. T. Edwards, Y. Yabe, J. Gui, T. Qin, S. Guti rrez, J. Giacoboni, M. W. Smith, P. L. Holland, P. S. Baran, *J. Am. Chem. Soc.* **2017**, *139*, 2484–2503.

[39] P. Yang, E. Zhou, B. Fang, G. Hou, G. Zi, M. D. Walter, *Organometallics* **2016**, *35*, 2129–2139.

[40] M. E. Garner, S. Hohloch, L. Maron, J. Arnold, *Organometallics* **2016**, *35*, 2915–2922.

[41] W. Ren, W. W. Lukens, G. Zi, L. Maron, M. D. Walter, *Chem. Sci.* **2013**, *4*, 1168–1174.

[42] L. Zhang, C. Zhang, G. Hou, G. Zi, M. D. Walter, *Organometallics* **2017**, *36*, 1179–1187.

[43] N. G. Connelly, W. E. Geiger, *Chem. Rev.* **1996**, *96*, 877–910.

[44] G. Nocton, C. H. Booth, L. Maron, L. Ricard, *Organometallics* **2014**, *33*, 6819–6829.

It is not easy to be a pioneer - but oh, it is fascinating! I would not trade one moment, even the worst moment, for all the riches in the world.

Elizabeth Blackwell

4

Transferring electrons to a transition metal

Divalent lanthanides are powerful reducing agents. They can act both selectively and fast which is of very high interest in the field of chemistry.

In chapter 2, we described the reduction mechanisms of phenanthroline by complexes of divalent lanthanide. This reduction was selective and modulated depending on the lanthanide itself: the samarium was able to promote a dimerisation of phenanthroline while the ytterbium was not. This specificity of electron transfer to act differently for specific lanthanides is of use in reactivity. That is why, we investigated in chapter 3 radical reactions that can be initiated by lanthanide molecules. The effect of the ligand on this kind of reactivity was described and a new type of C-H activation was discovered. As such, the interest in divalent lanthanide fragment as electron transfer reagent is not to prove[1].

Electron transfer is a key component of catalytic reactions. Understanding these reactions and their mechanisms is of crucial interest. In order to investigate these mechanisms occurring at the Transition Metal (TM) centre, the stabilisation of intermediate species such as Pd^{III} or Pd^{IV}[2] or even Ni^{IV}[3] is needed. Stabilising these intermediates often requires electron donating and redox non-innocent ligands[4–6]. These ligands are enhancing the catalytic activity of the TM complexes but only a few intermediates have been isolated.

In recent years, the use of bimetallic complexes to perform such a task has encountered some success[7]: palladium (+III) intermediates have been stabilised by the group of Ritter. Moreover, there is a growing interest in the field of photocatalytic bimetallic complexes[8]: one

species is photo-activated and transfers one electron to a transition metal during catalysis. This scheme can be extended using lanthanides. Lanthanides could transfer electrons selectively to the transition metal without a photo-activation step. The potential applications of these molecules could either be to study reaction mechanisms, or to give interesting magnetic or luminescent properties.

To this end, the development of new hetero-bimetallic complexes was investigated. The aim of this chapter is to provide a first look into designing and characterising hetero-bimetallic complexes with divalent lanthanides. We will focus on finding which tool can be used to analyse these molecules, or to develop more effective ones. Firstly, the design of the molecules will be discussed, taking into account what was explained in the previous chapters. Then, the deep characterisation and reactivity of two molecules will be detailed. And finally, experimental and theoretical calculations will get combined in order to design a more effective ligand.

4.1 Bimetallic complexes

4.1.1 Heterobimetallic complexes

Redox non-innocent ligands have the main advantage of being able to get reduced or oxidised instead of the metal itself. This type of behaviour could unlock specific type of reactivity. For example, van der Vlugt was able to create a new palladium (+II) species capable of selectively performing a one electron process. This is very uncommon for palladium complexes that are usually behaving with two electron processes[9].

Moreover, multi-metallic reactions present several advantages for catalytic applications. The combination of multiple active sites can be of interest in catalytic cycles, where one site can perform a specific task and another can be performed on the second site[10,11]. This has been described during the 2010 Nobel Prize in chemistry: in Sonogashira cross-couplings, the combination of a copper and a palladium complex enabled a new kind of reactivity. The same idea can be used to combine photoactive species and a TM catalysts[12,13] to reproduce, in a way, biological systems.

In order to perform a selective catalysis, the multi-metallic compounds need to communicate. Different strategies exist to trigger this communication.

The different metal centres can be connected through bonding or interactions. Complexes of this type have been developed by the group of van der Vlugt in the last couple of years[14]. The proximity of two transition metals can generate new intermediates through charge transfer or electron repulsion between the two metals.

Another strategy involve the use of redox-non innocent ligand to connect the two metals together. Two methodologies have been developed in this context. The first one is to combine a Lewis acid with a TM. In this field, the group of Tilley developed compounds that combine a platinum complex with Lewis acid, such as boron[15] or zinc derivatives[16], which accelerate reductive elimination. The second one is to combine photoactive species with TM catalysts. Upon excitation, the photoactive switch will transfer one electron to the redox-active ligand which, during the catalysis, will help to create new reactions. The recent implementation of such a scheme has for example unlocked cross coupling reactions with a nickel catalyst[17], which has been the centre of interest for the last couple of years of inorganic chemists[8,18–24]. However, the understanding of the mechanisms involved is still in its infancy as the fast processes and the lack of theoretical and experimental relevant tools make the analysis of these systems difficult.

Divalent lanthanide use in hetero-metallic complexes is rather limited. In the 1980s, Andersen's group showed that upon addition of $Cp^*_2Yb(OEt_2)$ to a solution of a platinum complex, the ytterbium compound was able to bond slightly over the Pt-Me or Pt-H bonds[25]. This interaction was mainly due to a Lewis base over a Lewis acid interaction. In recent years, the combination of lanthanides and TM compounds has been studied for either their inherent magnetic properties[26] or for their Lewis acidity[16]. Yet, the use of divalent lanthanide for electron transfer in these kind of complex is limited.

4.1.2 Using lanthanide to promote single electron transfer

Lanthanide could be used instead of a photocatalyst in order to transfer electrons during the catalytic reaction. In order to be used in reactions involving TM, the lanthanide centre needs to be stable enough not to react during the catalysis and the ligand itself should be

considered very carefully as to transfer selectively electrons to the TM centre. The design of such a molecule is described in Figure 4.1.

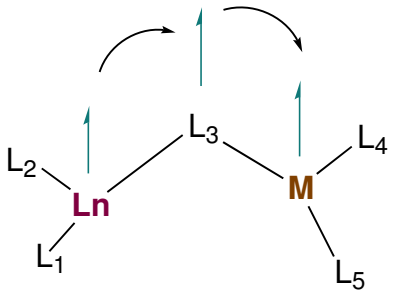

Figure 4.1: General scheme of the bimetallic complexes investigated and the electron path (arrow) involved in these complexes

In this context, the three different blocks of this molecule (the lanthanide [Ln], the bridging ligand [ligand] and the TM [TM]) need to be chosen carefully.

4.1.2.1 Choosing the right lanthanide

As detailed previously, the lanthanide has to be chosen so that it transfers its electron but is not highly reactive and would not interfere during the catalysis. Different lanthanides have the appropriate redox potentials (+II/+III) that fit these criteria: europium, samarium and ytterbium.

We have seen that samarium is reactive and that side reactions such as tempo addition can decompose the complex itself (Chapter 3). Europium on the other hand, has a too high redox potential, so that its redox activity is not adequate for the reduction of an organic moiety.

Ytterbium is a better fit, as its redox potential is low enough to perform reduction of organic molecules, but not as low as it would be reactive in catalytic cycles. In molecular complexes involving radical ligands, this behaviour is responsible for the multi-reference character of ytterbium ions between three different states[27] involving the π^* molecular orbital of the bipyridine neutral ligand: singlet $4f^{14}\pi^{*0}$, Open-Shell Singlet (OSS) $4f^{13\uparrow}\pi^{*\downarrow}$ and triplet $4f^{13\uparrow}\pi^{*\uparrow}$. This behaviour could trigger new development in the field of catalysis as the electron can be shared between the ligand and the lanthanide centre. Finally, ytterbium in its divalent state is diamagnetic, which will lead to easier NMR studies and easy-to-understand magnetic behaviour.

4.1.2.2 Choosing the right ligand

The phenanthroline and bipyridine molecules have been studied extensively with lanthanide ions as we have shown in Chapter 2. When combined with ytterbium, in addition to the multi-reference character of the lanthanide ion, the π^* molecular orbitals of the neutral ligand are also occupied in a multi-reference fashion. This behaviour has been developed in detail in Chapter 2. It has been shown that for phenanthroline complexes of ytterbium and samarium, while the electron transfer was not as important in the case of ytterbium, the electronic structure of these complexes was very similar[28,29]. As a result, using an aromatic ligands could present advantages, as the electron is transferred selectively to its π^* orbitals in a multi-reference fashion. This can lead to innovative molecules.

Based on these findings, a phenanthroline-like ligand was chosen, the taphen (4,5,9,10-tetraazaphenanthrene). This molecule has the same symmetry than phenanthroline (C_{2v}). This ligand has been poorly used in TM chemistry, even if several early papers are discussing the difference between phenanthroline and taphen in ruthenium complexes[30]. Nonetheless, some methods are available to chlorinate or fluorinate the C-H bonds of the ligands[31]. Hence, it could be modulated in order to tune the electronic structure of the complex itself.

As with phenanthroline ligand, the valence molecular orbitals of taphen are π, π^* and lone pairs on the nitrogens. For the radical molecule, the natural occupation of these orbitals have been evaluated at the CASSCF(13,[2,2,3,3]) including two π, four π^* and four lone pairs orbitals of taphen (Table 4.1). Contrary to phenanthroline, only one of these π^* orbital is mainly occupied for radical taphen (π_1^*). The absence of strong multi-reference validates the use of DFT for further analysis of bimetallic complexes using this specific ligand.

4.1.2.3 Catalytic cycle

Group 10 elements are widely used in catalysis, especially palladium and platinum. Their application spectrum is huge from cross coupling to C-H activation[32] so that the stabilisation of key intermediate has always been important for understanding the mechanism of these processes[33].

Platinum has been known in three main oxidation states 0, +II and +IV and has been widely used in catalysis especially with the Shilov reaction and other C-H activation types

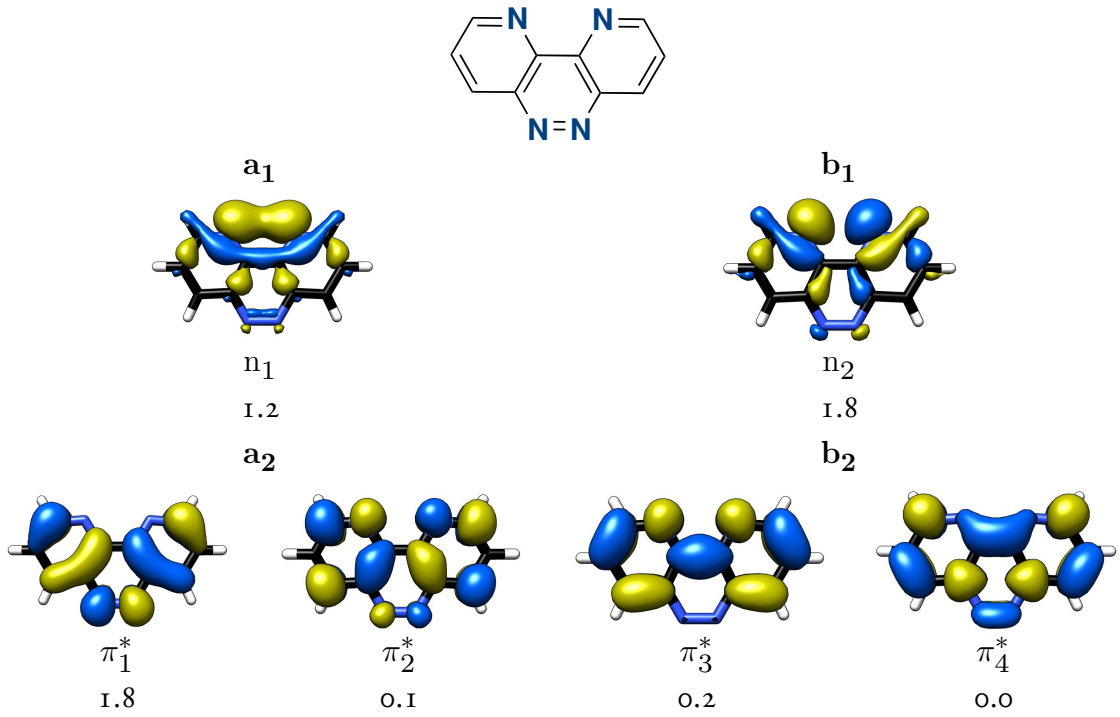

Table 4.1: Valence molecular orbitals and natural occupation of radical taphen at the CASSCF(13,[2,2,3,3]) level; the π orbitals that are not represented in this table are doubly occupied

of catalysis[34]. The chemistry of platinum (+III) and platinum (+I) is scarce and has been developed slowly during the last decade[35], certainly due to the high price of platinum itself.

Palladium can exist in five oxidation states (0,+I,+II,+III,+IV). While the most common examples of palladium complexes described for the past decades involves Pd^{0} or Pd^{II}, Pd^{III}, Pd^{I} and Pd^{IV} are still not well known. Two electrons oxidation and reduction are involved in the usual mechanisms and as such important studies need to be done on Pd^{IV}. Even if it was discovered a decade ago[36], Pd^{IV} is intriguing and remains a matter of discovery especially in the recent years[2,37–40]. The groups of Sanford and Ritter have particularly exploited this type of chemistry using new complexes of Pd^{III}[7,38,41–43]. Usually, Pd^{III} involves a Pd-Pd bond but some Pd^{III} complexes without Pd-Pd bond were also isolated[44]. Advancements on Pd^{III} also triggered advancement on radical processes involving palladium[45]. The group of Sanford has been able to characterise multiple palladium III and IV derivatives and has led the way to new nickel +IV chemistry[3].

As his counterpart, nickel has been characterised in the usual 0 and +II oxidation states. But contrary to palladium or even platinum, nickel cross coupling reaction involves generally

the Ni^{I}/Ni^{III} couple[46–48]. But more recently several studies submitted the idea that such mechanism could actually involve some nickel +IV intermediates[49]. Following this paper, multiple articles started appearing on nickel +IV and its potential power in catalysis[50,51].

Investigating these unusual oxidation states could give a better understanding of the mechanism associated with oxidative addition and reductive elimination. In a first step, palladium will be used as the catalytic system, but other group 10 elements will be investigated as well, to provide a point of comparison.

4.2 Novel bimetallic complexes

4.2.1 Taphen, a new type of bridging ligand

4.2.1.1 Preliminary studies

Different strategies can be used to form a [Yb][taphen][Pd] compound. The first scheme involves the synthesis of the [Yb][taphen] part and then addition of the [Pd] part to form the final [Yb][taphen][Pd] (mentioned as *Yb(taphen)Pd*, the italics font refers to this notation and will be used in the text below).

Taphen can be synthesised according to existing procedures[52] (Figure 4.2).

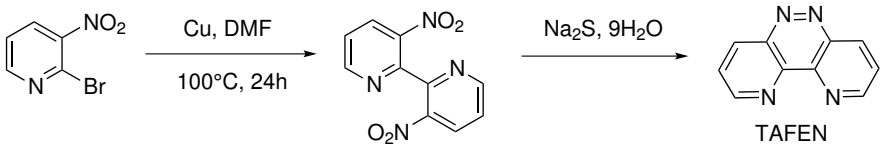

Figure 4.2: Scheme for the synthesis of taphen[52]

The [Yb][taphen] block synthesis was done by addition of toluene on $Cp^{*}_{2}Yb(OEt_2)$ and taphen (Figure 4.3). The resulting purple solution was crystallised at -40°C and the dark blue needle crystals were suitable for X-Ray diffraction analysis.

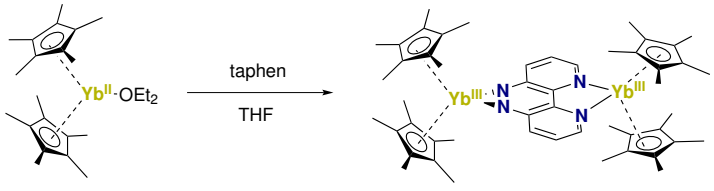

Figure 4.3: Scheme for the synthesis of *Yb(taphen)Yb*

The crystallographic structure presents only a doubly bridging compound: $Cp^*_2Yb(taphen)YbCp^*_2$, mentioned as *Yb(taphen)Yb* (Figure 4.4).

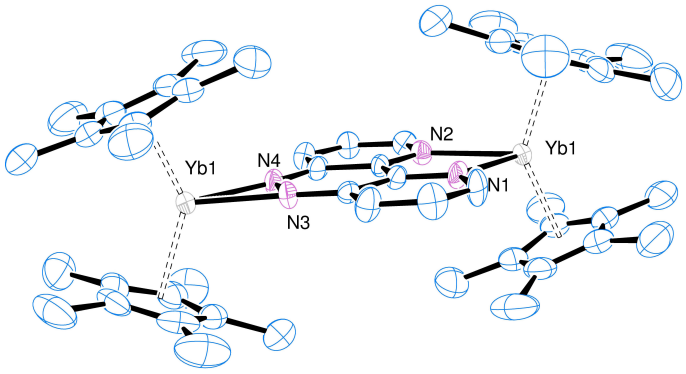

Figure 4.4: ORTEP of the X-Ray diffraction structure of *Yb(taphen)Yb*; selected distances in angstroms: Yb1 – N1, N2 (avg) 2.363, Yb1 – N3, N4 (avg) 2.215, Yb – Yb 7.617, Yb – Cp* (ctd avg) 2.282, Cp* – $\widehat{Yb}$ – Cp* (ctd) 139.25

The structure is symmetric, which leads to the same distances between the two ytterbium centres and the Cp* ligands. This distance is characteristic of the lanthanide oxidation state. For ytterbium (+III), it is around 2.30 Å[28] while for ytterbium (+II) it is around 2.40 Å[53]. Here the distance is 2.28 Å for both ytterbium which is in favour of two reductions of the taphen ligand.

The magnetism is also in accordance with two ytterbium (+III), as χT for the complex is approaching $5.2\,cm^3.K.mol^{-1}$ at room temperature. Further low temperature magnetisms were conducted but did not find any single molecule magnet behaviour contrary to what was previously observed for $(Cp^*_2Dy(bpm)DyCp^*_2)^+$[54]. This conclusion is in agreement with previous results by Andersen *et al.* where they studied dimeric complexes of bipyrimidine (bpm) with ytterbium[55].

In conclusion, the synthesis of the *Yb(taphen)Pd* complex should pass first by the synthesis of a [taphen][Pd] block and by subsequent addition of the [Yb] block.

4.2.1.2 Synthesis and characterisation of $(taphen)PdMe_2$

Many starting materials of palladium can be used to form bimetallic complexes. One of the most simple, $(taphen)PdCl_2$, was used following existing procedures[56]. The coordination of the taphen ligand was done, but the poor solubility of the complex did not enable further

characterisation of a bimetallic species. A more soluble complex such as $(\mathrm{tmeda})\mathrm{PdMe}_2$ could be more suitable.

Addition of one equivalent of taphen on $(\mathrm{tmeda})\mathrm{PdMe}_2$ in thf gave after one night stirring at room temperature under an argon atmosphere red needle crystals. These crystals were washed with pentane (yield 85%)and were suitable for X-Ray diffraction studies (Figure 4.6). The resulting palladium taphen compound was isolated as a square planar complex and was further characterised by $^1\mathrm{H}$ NMR.

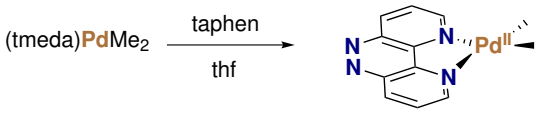

Figure 4.5: Scheme for the synthesis of $(\mathrm{taphen})\mathrm{PdMe}_2$

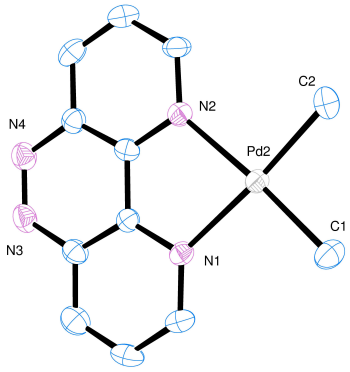

Figure 4.6: ORTEP of the X-Ray diffraction structure of $(\mathrm{taphen})\mathrm{PdMe}_2$

The molecular orbital diagram of a square planar complex of palladium is presented in Figure 4.7 and the shape of the frontier molecular orbitals are presented in Table 4.2.

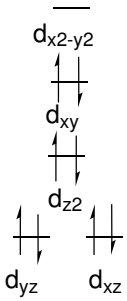

Figure 4.7: Square planar orbital diagram for $\mathrm{Pd}^{+\mathrm{II}}$ complexes with four distinctive ligands

HOMO	LUMO	LUMO+1
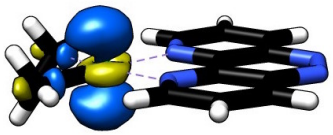	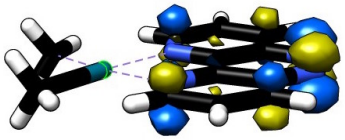	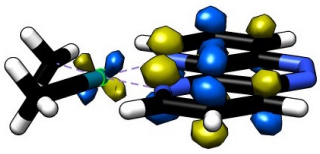

Table 4.2: Frontier molecular orbitals of $(\mathrm{taphen})\mathrm{PdMe_2}$

Contrary to the square planar orbital diagram with four different ligands, the HOMO is the $4d_{z2}$. Because the ligand is bi-dentate, the $4d_{xy}$ orbital is lower in energy than the $4d_{z2}$. As it can be expected, the first two LUMOs of the complex do not correspond to the $4d_{x2-y2}$, but to the LUMOs of taphen (π_1^* and π_3^*). These orbitals are weakly delocalised on the palladium centre, which might be of importance for further reactivity.

4.2.1.3 Synthesis and characterisation of *Yb(taphen)Pd*

- **Synthesis and experimental characterisation**

The isolated red crystals of $(\mathrm{taphen})\mathrm{PdMe_2}$ were used in the synthesis of the hetero-bimetallic complexes. One equivalent of $\mathrm{Cp^*_2Yb(OEt_2)}$ was added to a mixture of the red crystals in toluene. The solution passed from green-black with a red precipitate to dark purple. After stirring for over 10 minutes, the mixture was put at $-40\,^{\circ}\mathrm{C}$ overnight. Small dark crystals were then isolated (50% yield) and were suitable for X-Ray diffraction studies (Figure 4.9). Further comparison between this structure and the initial palladium complex one are presented in Table 4.3.

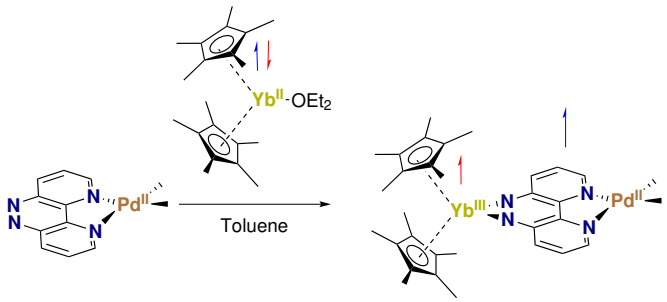

Figure 4.8: Scheme for the synthesis of *Yb(taphen)Pd*

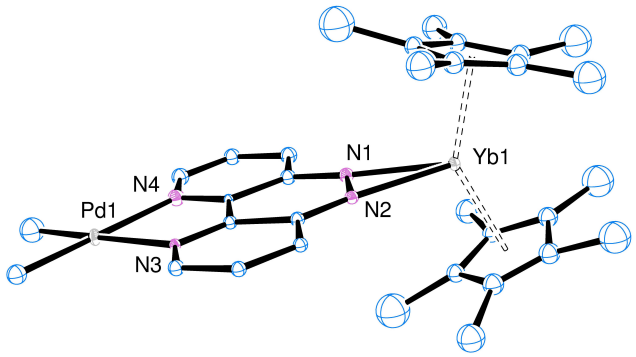

Figure 4.9: ORTEP of the X-Ray diffraction structure of *Yb(taphen)Pd*

	Yb(taphen)Pd	$(\text{taphen})\text{PdMe}_2$	PBE-D3 ZORA2
Yb-N (avg)	2.290(6)		2.312
Yb-Pd	7.45		7.507
Pd-C (Me) (avg)	1.990(3)	2.028(8)	2.034
Pd-N (avg)	2.174(4)	2.152(5)	2.179

Table 4.3: Distances for $(\text{taphen})\text{PdMe}_2$ and *Yb(taphen)Pd* in their X-Ray structures and in the DFT optimised structure of *Yb(taphen)Pd*, bond length are in angstroms, avg stands for average

The geometries of the palladium centre are practically identical in both compounds, with a very slight contraction around the methyl and expansion around the taphen for *Yb(taphen)Pd*. The distances range from 2.03 Å to 1.99 Å for the Pd-C bond and from 2.15 to 2.17 Å for Pd-N. That is indicative of a taphen reduction by the ytterbium centre. Similarly to what was found for *Yb(taphen)Yb*, the distance between ytterbium and the Cp* moieties, *i.e.* 2.285 Å, is typical from other Yb^{III}.

The ^{1}H NMR was recorded in thf-d_8 and showed three highly shifted peaks corresponding to the taphen ligand, one peak corresponding to the methyl groups and one peak corresponding to the Cp* ligand (Figure 4.10). This paramagnetism can only be induced if the ytterbium is oxidised to Yb^{III}.

The magnetism of the complex is also in agreement with an oxidised ytterbium centre. The χT value is around 2.5 $\text{cm}^3.\text{K}.\text{mol}^{-1}$ at room temperature, which is typical of an ytterbium III complex (Figure 4.11). This indicates that the electron is localised on the fragment $(\text{taphen})\text{PdMe}_2$ without any coupling to the ytterbium centre itself. This is

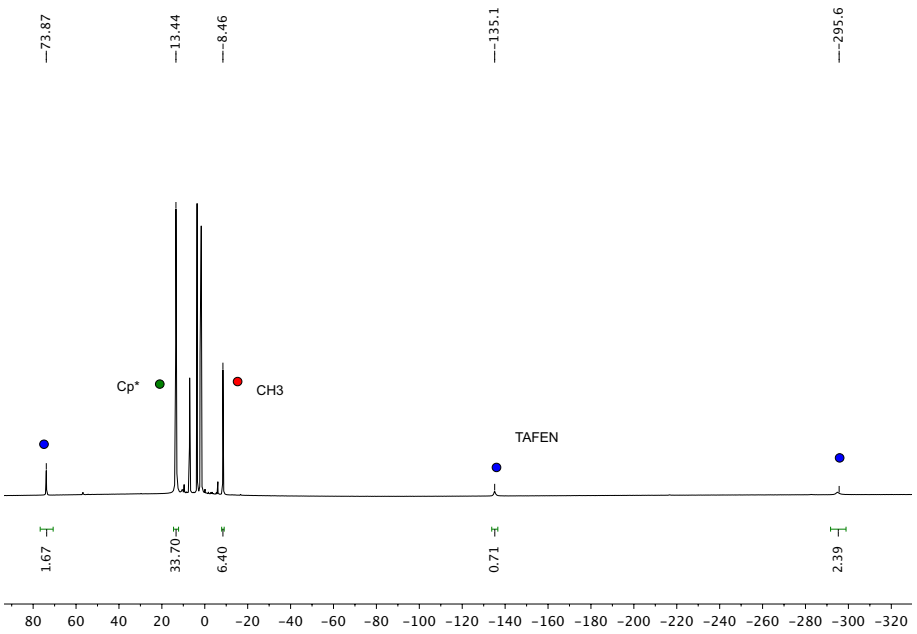

Figure 4.10: ^{1}H NMR of *Yb(taphen)Pd* in thf-d8

different from what was observed for phenanthroline complexes of ytterbium, where two triplets were close in energy[28].

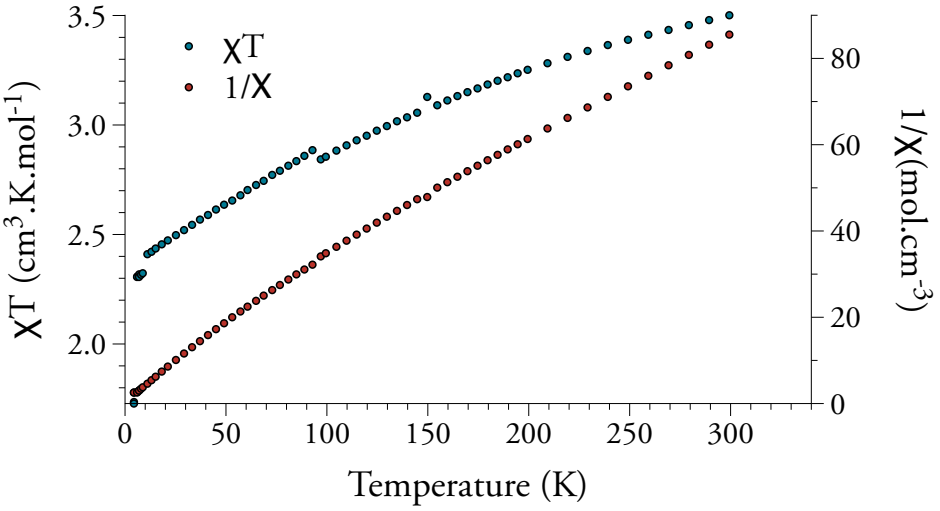

Figure 4.11: Temperature dependent magnetic data for *Yb(taphen)Pd* from 5 K to 300 K at 0.5 T $1/\chi$ vs T is given as filled red dots, χT vs. T as filled blue dots

The localisation of the electron was further assessed using EPR analysis at room temperature. The data presented in Figure 4.12, show a narrow peak at 3540 Gauss. It corresponds to an organic radical. The slight broadening of the signal is due to the presence of the ytterbium centre in the neighbourhood of the radical. This result further indicates that

the electron is localised on the taphen ligand.

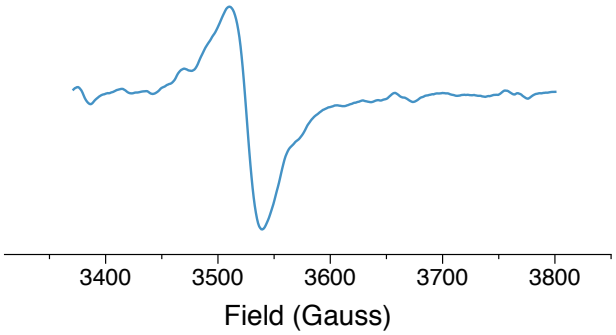

Figure 4.12: EPR spectrum at room temperature and in the solid state of *Yb(taphen)Pd*

- **Theoretical characterisation and bonding interactions**

In order to better understand the electronic structure of the complex, theoretical investigations were performed. The geometry optimisation, using the triplet spin multiplicity (*i.e.* one single electron transferred to the taphen and one single electron on the ytterbium itself), gave a geometry in agreement with the crystallographic one (Table 4.3). The singlet spin state (*i.e.* Yb^{+II} and no electron located on the taphen) is close in energy from the triplet spin state. After a geometry optimisation for the singlet, Gibbs free energies of both spin states were compared at the PBE0 ZORA3 level of theory. The triplet is located 20 kcal/mol below the singlet, which indicates further the preference for the triplet over the singlet. These results could be improved using CASSCF techniques, as hybrid density functionals favour high spin multiplicity[57,58].

The frontier molecular orbitals of *Yb(taphen)Pd* are presented in Figure 4.4.

SOMO	HOMO	LUMO
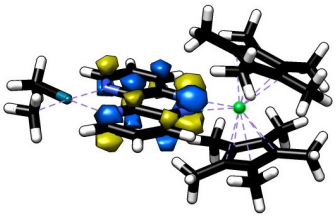	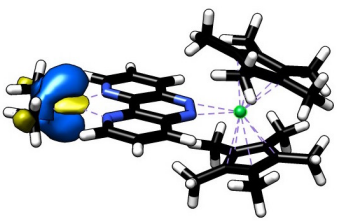	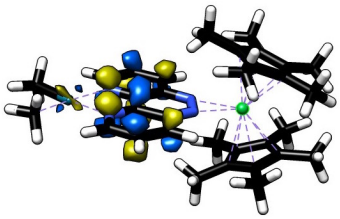

Table 4.4: Valence molecular orbitals of *Yb(taphen)Pd*

There are two low-lying occupied orbitals, the SOMO and the HOMO of the system. The SOMO corresponds to the π_1^* orbital of neutral taphen with less than 1% influence from the orbitals of the palladium centre and the HOMO to the Pd $4d_{z}2$ orbital. The two orbitals are close in energy, as the SOMO-HOMO gap is 0.10, 0.13 and -0.4 eV respectively at the PBE0-D3, B3LYP-D3 and ωB97X-D3 level of theory. The first LUMO orbital corresponds to an interaction between the $4d_{xz}$ and the π_4^* orbital of the taphen molecule. The LUMO+1 represents the $5dz^2$ orbital from the ytterbium centre. These two orbitals are not close in energy from the HOMO and small or no involvement in further reactivity on the palladium centre are expected. From this, two conclusions can be drawn: the electron is transferred from the ytterbium to the taphen ligand but the density is not found on the palladium centre and the very close position of the SOMO and the HOMO of the system can trigger interesting reactivity on the palladium complex itself.

The bonding energy inside the complex was decomposed using the EDA scheme between a Cp_2^*Yb fragment and a $(taphen)PdMe_2$ one. For a similar example, BSSE[59] calculations were performed using the same basis set and functional and led to small corrections (1.5 kcal/mol). As a result, the BSSE was neglected in the present calculations. The values are presented in Figure 4.13 and compared to the ones from $Cp_2^*Yb(phen)$.

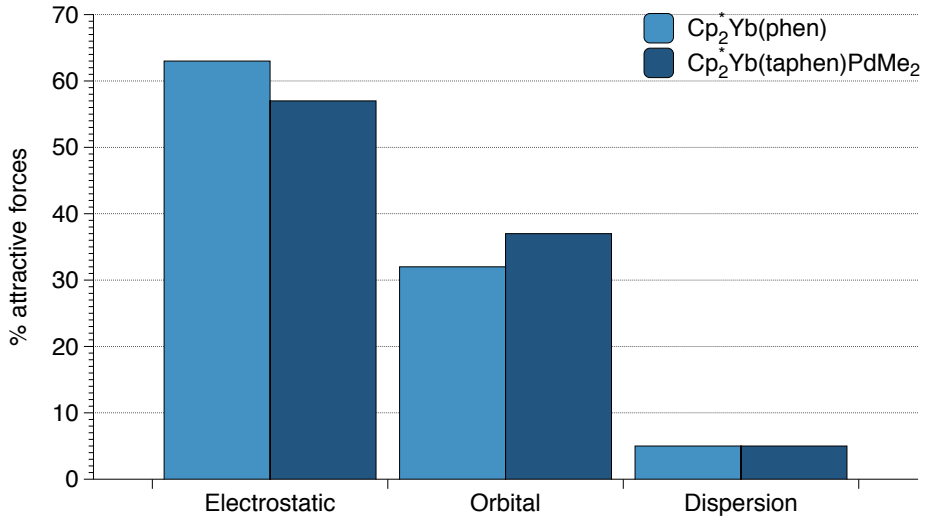

Figure 4.13: Repartition of the attractive forces in % for *Yb(taphen)Pd* and $Cp_2^*Ybphen$ while cutting the Ln-N bonds, at the PBE0-D3 ZORA3 level of theory

The $Cp_2^*Yb(phen)$ complex possesses a stronger electrostatic interaction with its ligand than *Yb(taphen)Pd*. This is due to a preference for bidentate ligand in a coordination allowing

a 5-member cycle. In the taphen case, only a 3-member cycle between the ytterbium and the two nitrogen is possible whereas in the phenanthroline case a 5 member cycle is created between the Yb, the two nitrogens and the two carbons. Moreover, in the phenanthroline case, the ytterbium centre is surrounded by the phenanthroline ligand, which increases the electrostatic interaction. On the contrary, the orbital interaction is higher for *Yb(taphen)Pd*. The presence of a π system between the two nitrogens might favour an interaction of these orbitals with the orbitals of the lanthanide. The presence of the palladium on the ligand can as well favour the presence of a stronger orbital interaction between the two fragments.

Overall, the bonding is weak in both complexes (60 and 53 kcal/mol for *Yb(taphen)Pd* and $Cp^*_2Yb(phen)$ respectively). Most of the bond strength, 66%, come from the lanthanide itself while only 33% comes from the two Cp^* moieties that stabilise the complex. A detailed comparison between different density functionals could be interesting at this point in order to assess the type of functional to use in order to evaluate the bonding interaction properly. The use of the recent ALMO-EDA scheme[60,61], which is supposed to be functional independent[62], could reduce this problem of functional dependency while giving appropriate values for the energy. Only a comparison of different EDA with the same couple density functional/ basis set is reliable. In this sense, this PBE0-D3 ZORA3 calculation will act as a reference for the rest of the study.

As described in Chapter 2, the bond strength can also be evaluated using QTAIM techniques[63]. The evaluation of different parameters issued from QTAIM calculation are presented in Table 4.5. In all these cases, the interaction can be characterised as electrostatic interaction: at the critical point the density is small and the laplacian is positive. This is a common prediction for TM complexes and a comparison between the different values for the density and the laplacian for the complexes *Yb(taphen)Pd*, $Cp^*_2Yb(phen)$, $(taphen)PdMe_2$ and Cp^*_2Yb will enable a better understanding of the bonding in each system.

Yb(taphen)Pd	$\nabla^2\rho$	ρ	BCP	RCP	CCP
$Yb-N$ (avg)	0.236	0.057	2	1	0
$Yb-Cp^*$ (avg)	0.116	0.039	9	9	2
$Pd-N$ (avg)	0.344	0.075	2	1	0
$Pd-C$ (avg)	0.144	0.126	2	0	0
$Cp^*_2Yb(phen)$					
$Yb-N$ (avg)	0.198	0.060	2	1	0
$Yb-Cp^*$ (avg)	0.111	0.037	6	6	2
$(taphen)PdMe_2$					
$Pd-N$ (avg)	0.364	0.077	2	1	0
$Pd-C$ (avg)	0.140	0.125	2	0	0
Cp^*_2Yb					
$Yb-Cp^*$ (avg)	0.129	0.038	10	10	2

Table 4.5: QTAIM values for ρ and $\nabla^2\rho$ at the BCP; BCP, RCP and CCP indicate the number of Bond Critical Point, of Ring Critical Point and of Cage Critical Point present in the interaction for different complexes Cp^*_2Yb, $(taphen)PdMe_2$, $Cp^*_2Yb(phen)$ and *Yb(taphen)Pd*

Upon coordination with the $(taphen)PdMe_2$, Cp^*_2Yb is observing a slight decrease in coordination strength with the Cp^* ligands, as the number of critical points (BCP and RCP) is decreasing from 10/10 to 9/9. The evolution of the density related to the BCP between in the $Yb-N$ bond is not significant passing from (taphen)$PdMe_2$ to *Yb(taphen)Pd*.

The $\nabla^2\rho$ value for the Pd-C and the Pd-N bonds are different for $(taphen)PdMe_2$. This is due to the type of ligand bonding to the palladium: the methyl groups are X type and the taphen is L type according to Green classification[64] . As a result, the interaction is less important with taphen than with the methyl groups. As such the decrease in $\nabla^2\rho$ for the Pd-N bond when passing from $Me_2Pdtaphen$ to *Yb(taphen)Pd* is normal, corresponding to a stronger interaction between the palladium and the nitrogen due to the charge on the taphen. Similarly, the bond between the ytterbium center and the taphen is less strong than the bond between the ytterbium and phenanthroline. This is probably due to the less common three-center interaction in the case of *Yb(taphen)Pd* compared to five-center interaction in the case of $Cp^*_2Ybphen$.

4.2.1.4 Reactivity on *Yb(taphen)Pd*

The bimetallic complex of palladium possesses an electron delocalised on the π system of the taphen ligand that is located near the palladium centre. Upon reactivity this electron might be of use in accelerating catalytic processes, creating new ones or stabilising Pd^{+IV} species. The development of this kind of reactivity was investigated.

- **Catalysis**

The use of fluorine in pharmaceutical compounds[65], or in novel materials has increased the need for new fluorination protocols. Nonetheless, fluorination remains a difficult topic that is still investigated by numerous groups[66–74]. The development of one electron processes for this kind of transformation has enable the use of metals such as cobalt[69].

Such one electron process cannot, in theory, happen for palladium complexes. Nonetheless, the use of *Yb(taphen)Pd*, containing an electron stored on the ligand near the palladium, could help promote such reactivity. That is why the same type of catalysis as proposed by Hiroya *et al.*[69] was attempted with *Yb(taphen)Pd*. The initial mechanism postulated for their reaction with cobalt involved an intermediate Co^{III} species, which in the case of palladium could be easily stabilised by the electron stored on the taphen ligand.

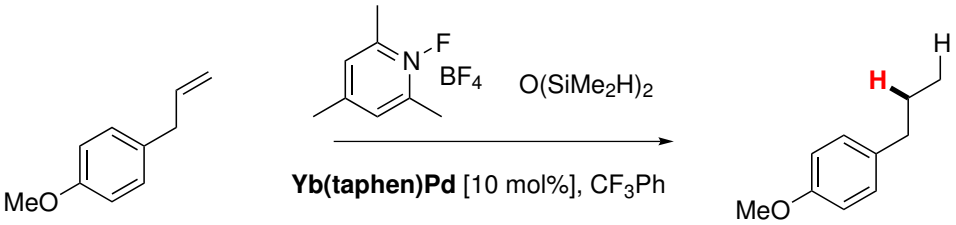

Figure 4.14: Scheme of the catalysis using *Yb(taphen)Pd*

Two sets of experiments were done with two different starting materials: allylbenzene and allylmethoxybenzene. The hydrogen source was chosen as $(Me_2SiH)_2O$ and the fluorine source as Selectfluor and their respective quantity used during the catalysis were 1 and 2 equivalents. The catalyst, *Yb(taphen)Pd*, was used at a mol 1% quantity. The reaction was performed in CF_3Ph, as detailed in Hiroya's paper[69].

However, after analyses of both reactions using ^{19}F NMR and GCMS, the presence of a single peak at -135 ppm indicated the presence of a Si-F bond only[75,76] and no fluorination

was performed. Instead, the alkene hydrogenation was possible. Changing the fluor source from Selectfluor to trimethylpyridinium tetrafluoroborate as well as changing the siloxide agent did not change this result. The fact that no other fluorine compound was found in solution suggests that the siloxide is too reactive upon the fluorine source and that the palladium in this situation did not favour one electron process.

In order to get more insight into the mechanism of the reaction and the possible side reactions that could occur, different stoichiometric reactions were performed. A reaction was attempted between the fluorine source and *Yb(taphen)Pd*. The resulting solution turned black red and crystals from (taphen)$PdMe_2$ were gathered on the edge of the flask, indicating a possible side reaction between the ytterbium complex and the fluorine source. Analysis of the resulting compound was not possible due to a ^{1}H NMR with multiple side products and no crystal structure.

Another reaction was done between the alkene and *Yb(taphen)Pd*. Upon addition of the alkene, new peaks were found in the ^{1}H NMR corresponding to the coordinated alkene in solution. When putting the solution under *vacuum* the peaks disappeared, as the alkene evaporates. Attempts of hydrogenation by addition of H_2 on the coordinated complex did not lead to further hydrogenation of the alkene. Attempts of doing an iodation of the alkene were done in toluene with MeI but led to unsuccessful results.

Lanthanides are known to activate C-F bonds, as reported for ytterbium[77], lanthanum[78] or even samarium[79] and some fluorine atoms are even used to create 3d-4f clusters[80]. The presence of lanthanide in the vicinity of palladium during fluorination catalysis could in that sense induce side reactions, with for instance coordination of the fluor atom on the lanthanide itself instead of on the palladium.

Sonogashira coupling involving alkene and alkynes could be performed with *Yb(taphen)Pd* in order to study the influence of the electron presence near the palladium centre. The problem with this type of catalysis is that it often involves acids and acids could easily break the Cp* bond with ytterbium. Here lies the limitation of the *Yb(taphen)Pd* system: ytterbium species are reactive, even in their trivalent state and multiple side reactions could occur during catalysis.

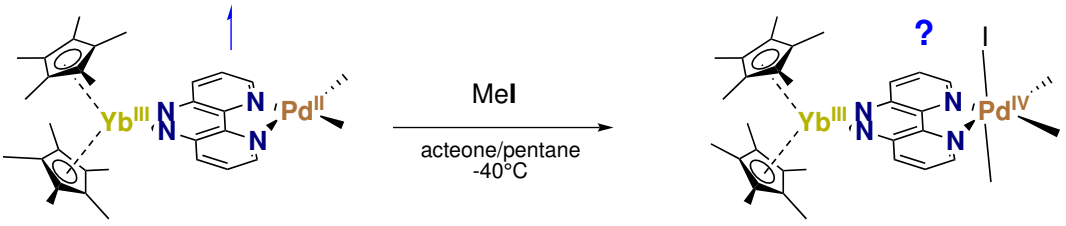

Figure 4.15: Scheme of the addition of MeI on *Yb(taphen)Pd* forming *Yb(taphen)PdMeI*

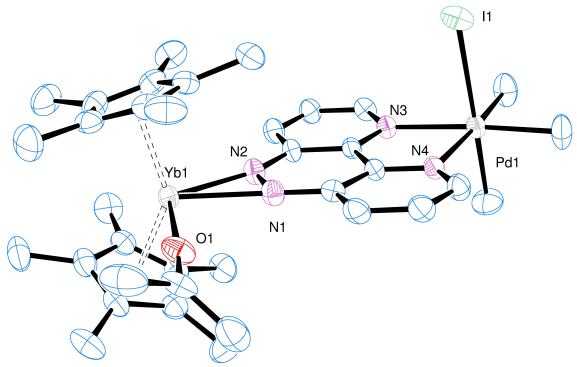

Figure 4.16: ORTEP of the X-Ray diffraction structure of *Yb(taphen)PdMeI*

- **Stabilisation of Pd^{+IV} compounds**

In order to prove the efficiency of the designed hetero-bimetallic complex, reactivity was attempted with alkyl-halogen. These compounds are known to react with palladium (+II) complexes and form metastable (+IV) palladium complexes[36,37]. The newly synthesised complex might enable the stabilisation of such intermediates and might even make possible the characterisation of such compounds.

First attempts were done with iodo-methane, because it has been known for decades to form metastable (bipy)$PdMe_3I$[36,37] (Figure 4.15). The reaction attempted in toluene gave unsatisfactory results. Even when low temperature reactions were done, ^1H NMR signals for ethane were found as well as two different environments for the methyl groups bonded to the palladium. This is in agreement with a rapid reductive elimination for this complex and a meta-stable Pd^{IV} intermediate.

When doing the reaction in a mixture of acetone and pentane at room temperature for a few minutes and letting the solution at $-40\,^{o}C$ overnight, black crystals were isolated and were suitable for X-Ray diffraction analysis. The crystal structure corresponded to a palladium +IV compound, with one acetone coordinated on the ytterbium centre (Figure 4.16).

	Yb(taphen)Pd	(taphen)$PdMe_2$	*Yb(taphen)PdMeI*	(bipy)$PdMe_3I$	PBE-D3
Yb-N (avg)	2.290(6)		2.334(6)		2.353
Yb-Pd	7.45		7.53		7.529
Pd-C (Me) (avg)	1.990(3)	2.028(8)	2.045(6)	2.037(8)	2.048
Pd-N (avg)	2.174(4)	2.152(5)	2.194(4)	2.181(5)	2.211

Table 4.6: Distances (angstroms) in the X-Ray structures of *Yb(taphen)Pd*, (taphen)$PdMe_2$, *Yb(taphen)Pd* and $PdMe_3$Ibipy[37] and the DFT structure of *Yb(taphen)PdMeI*, avg stands for average

The distances in *Yb(taphen)PdMeI* around the palladium centre are similar to the one of (bipy)$PdMe_3I$ already published[37] (Table 4.6). There is an expansion of the bonds surrounding the palladium, which is expected as two anti-bonding orbitals of the palladium are populated. The same effect was encountered on the ytterbium centre, as there is a coordination of an acetone molecule, which indicates that even if ytterbium (+II) is reactive towards acetone, the stabilisation of its electron by the presence of taphen prevents this reactivity. The reactivity with acetone is not fast enough to prevent the formation of *Yb(taphen)PdMeI*.

The characterisation of *Yb(taphen)PdMeI* was completed by EPR and magnetic studies. The magnetic data is coherent with an ytterbium (+III) centre and the EPR showed a broad radical spectrum, indicating that the electron did not move from the taphen ligand. In addition to the experimental investigations related to this complex, DFT calculations were performed. The optimised structure was found to have only little difference with the crystal structure (Table 4.6).

The SOMO of the system is still localised on the taphen π_1^* with no contribution of the palladium centre. The first orbital centred on the palladium is the LUMO + 6 and is the anti-bonding orbital of the newly formed I-Pd-Me bond. The LUMO+1 of the system is the LUMO of the acetone molecule, which is expected as acetone is very easily reducible.

The ^{1}H NMR of the complex in acetone-d_6 or toluene-d_8 either at room or at low temperature ($-80\,^{o}$C) showed traces of ethane. The decomposition of the Pd^{IV} complex is, therefore, happening very quickly. Upon liberation of ethane, the newly formed bimetallic complex can react with acetone on the ytterbium centre, which could accelerate the decomposition of the intermediate Pd^{+IV} specie.

This has been proven to happen easily, as upon letting a solution of *Yb(taphen)PdMeI* in acetone-d_6 over a period of 8 hours, red needle crystals of $(taphen)PdMeI$ grew and

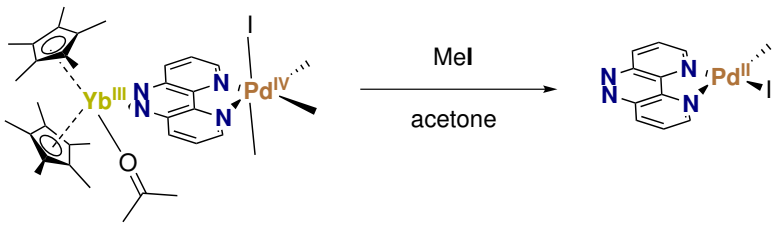

Figure 4.17: Decomposition scheme of *Yb(taphen)PdMeI*

were suitable for X-Ray diffraction analysis (Figure 4.17). This is well linked with the above details about the orbitals, *i.e.* the LUMO+1 is localised on the acetone and might interact with Cp^*_2Yb.

Other types of reactivity were attempted using either other alkaline-halogen compounds, or radical reagent. The use of PhI led to similar results to the one detailed previously, with the formation of toluene upon addition of *Yb(taphen)Pd*. Reactivity with TEMPO led to the release of $(taphen)PdMe_2$, which could account for the reaction of Cp^*_2Yb with TEMPO. Addition of small molecules, such as CO_2, or CO only resulted in unsoluble nano-material unsuitable for further analysis.

- **Newly formed trimetallic complex**

- Experimental characterisation

The reactivity of the bimetallic complex could also be investigated towards another electron transfer to the taphen ligand. In order to perform such electron transfer (Figure 4.18), one equivalent of $Cp^*_2Yb(OEt_2)$ was added to one equivalent of *Yb(taphen)Pd*. The resulting purple black solution gave upon cooling at $-40\,^{o}C$ fine dark crystals that were suitable for X-Ray diffraction analysis (Figure 4.19).

This molecule is reminiscent of the Cp^*_2Yb bonded to platinum complexes in a Lewis acid - Lewis base fashion observed by the group of Andersen[25] (Table 4.9 for a closer look). When looking at the unit [Yb][taphen][Pd] inside *Yb(taphen)PdYb* the distances are different from *Yb(taphen)Pd* (Table 4.7). The distances between each metal and the taphen moiety decreased strongly and the distance between the two metals is shorter of more than 0.20 Å. This overall contraction might be due to a second electron transfer from the Lewis adduct to the whole taphen moiety.

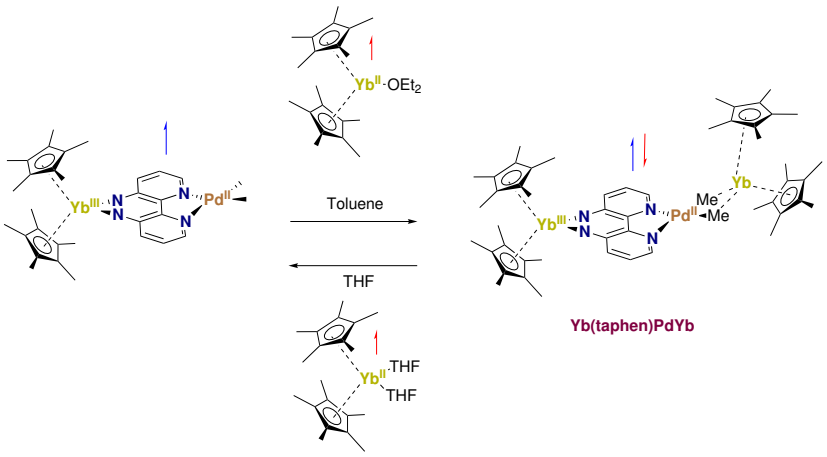

Figure 4.18: Scheme for the synthesis of *Yb(taphen)PdYb*

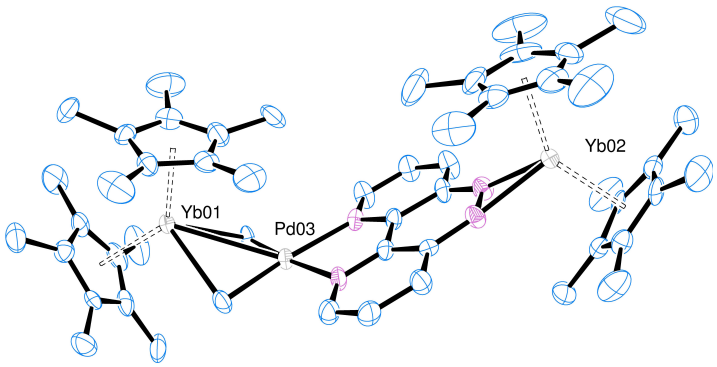

Figure 4.19: ORTEP of the X-Ray diffraction structure of *Yb(taphen)PdYb*

	Yb(taphen)Pd	*Yb(taphen)PdYb*	PBE-D3 ZORA2
Yb2-N (avg)	2.290(6)	2.214(8)	2.306
Yb2-Pd	7.45	7.24	7.403
Pd-C (Me) (avg)	1.990(3)	2.05(1)	2.050
Pd-N (avg)	2.174(4)	2.120(7)	2.144
Yb1-C (Me) (avg)		2.56(1)	2.66
Yb1-Pd		3.0815(7)	3.215

Table 4.7: Distances in the X-Ray structures of *Yb(taphen)Pd* and *Yb(taphen)PdYb* and in the computationally predicted one of *Yb(taphen)PdYb*, distances are in angstroms, avg stands for average

The geometry for the interaction between Yb1 and the methyl groups is not linear as in Andersen paper but is bent and the distance is 0.34 Å shorter than the one previously reported by Andersen (Table 4.9). This indicates a stronger interaction between the two compounds than simply a Lewis acid-Lewis base adduct. Moreover, the equilibrium is reversible: in thf, the Cp^*_2Yb moiety coordinated to the methyl groups is uncoordinated and further coordinates to thf, to form $Cp^*_2Yb(thf)_2$, while in toluene *Yb(taphen)PdYb* is formed.

The magnetic studies of *Yb(taphen)PdYb* were done and showed that two ytterbium (+III) atoms were present in the molecule (Figure 4.20). Finally, the silent EPR at room temperature showed that the pair of electrons was located on the taphen ligand.

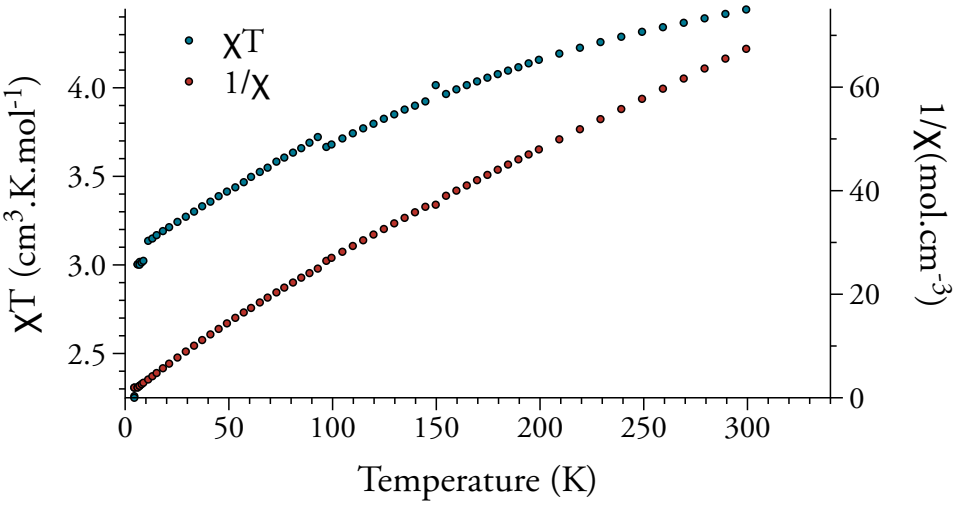

Figure 4.20: Temperature dependent magnetic data for *Yb(taphen)PdYb* from 5 K to 300 K at 0.5 T $1/\chi$ vs T is given as filled red dots, χT vs. T as filled blue dots

- Theoretical characterisation

The electronic structure of the singlet dianion taphen ligand has been computed at the CASSCF(8,7) level of theory. This molecule presents a ground state electronic structure : π_1^{*2} (Table 4.1), which validates the use of usual DFT methods to study the tri-metallic complex *Yb(taphen)PdYb*. A differentiation was firstly done between three hypothetical spin states at the DFT level: singlet, triplet and quintet. At the PBE0-D3 level, the triplet was lower in energy than both the singlet and the quintet. This result is in agreement with both the EPR and Squid measurements.

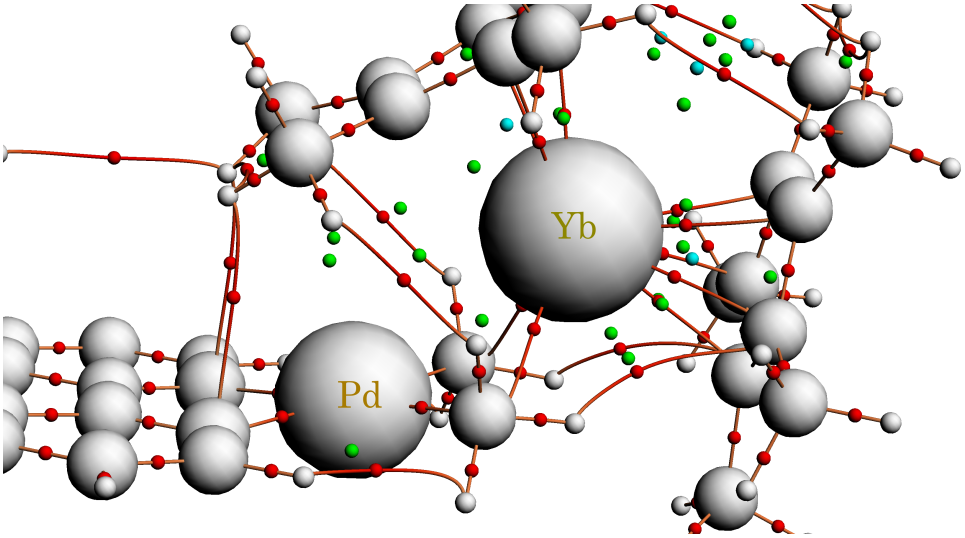

Figure 4.21: QTAIM molecular graph of *Yb(taphen)PdYb* focussed on the Me-Yb interaction at the PBE0-D3 ZORA1 level of theory, BCP are given in red, RCP in green and CCP in blue

- QTAIM and ELF analyses

A closer look at the molecular orbitals of the complex did not show any sign of a bonding interaction between the methyl groups and the lanthanide ion. Instead, QTAIM and ELF analyses were performed to get an overview of the bonding structure of both complexes.

The QTAIM calculation locates two BCP between the ytterbium ion and the two methyl groups (Figure 4.21). The interaction between the palladium and its ligands changed in this complex compared to *Yb(taphen)Pd*. The Pd-N and Pd-C bonding are slightly more ionic, with laplacian values larger than without the presence of the second ytterbium (from 0.34 to 0.36 for Pd-N and from 0.14 to 0.17 for Pd-C). The BCP located between the methyl groups and the ytterbium ion has a positive laplacian (0.111) and a small density (0.028): this bonding is weak and electrostatic.

Contrary to the QTAIM calculation, no basin was found between the C and the lanthanide in the ELF calculation. Instead, valence basins $\mathrm{V(Yb, H)}$ located close to the lanthanide (at 1.45 Å) and shared with the four closest hydrogen atoms were found (see Figure 4.22). The total density for these basins is 7.6 electrons, which means 3.8 electrons per methyl group. We can compare this value with the one found for the basins between the lanthanide and the carbon atoms of the Cp* rings, $\mathrm{V(Yb, C_{Cp^*})}$. These basins are located at 1.44 Å from the lanthanide and the total density for the two Cp* rings of Yb1 is 5.8 electrons. Hence,

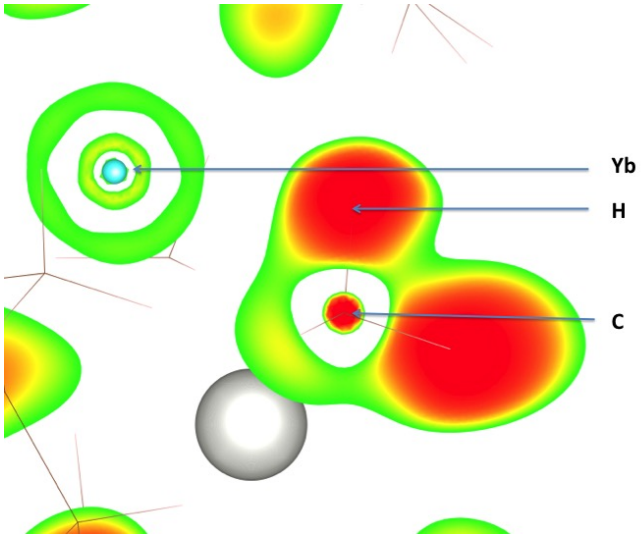

Figure 4.22: ELF basins of *Yb(taphen)PdYb* while cutting the isodensity in the plane Yb-C-H with an isosurface of 0.48

there is more electron shared with the two methyl groups than with the two Cp^*. However, compared with samarium complexes basins[81], the deformation of the valence basins is small, corresponding to an electrostatic interaction between the lanthanide and the methyl groups.

As a result, the interaction with the two methyl groups can be associated with the presence of valence basins between the lanthanide and the hydrogen atoms and the presence of a BCP between the lanthanide and the carbon atoms. While there are differences between these two analyses, they both indicates an interaction between the ytterbium center and the methyl groups.

An EDA was also performed to get a better idea of the interaction strength between the ytterbium centre and the methyl groups. The molecule was divided in two fragments: one Cp^*_2Yb fragment and one $Cp^*_2Yb(taphen)PdMe_2$ fragment and the EDA results are presented in Table 4.8.

The total bond strength between the lanthanide and the methyl groups is weaker than between the lanthanide and the taphen moiety : in the present case the bond strength is 35 kcal/mol while it was 60 kcal/mol between Cp^*_2Yb and (taphen)$PdMe_2$. The bonding interaction is spread over electrostatic (51%) and orbital interactions (39%) with a small influence of the dispersion effects (5 %) like for *Yb(taphen)Pd*.

Compared to $Cp^*_2Yb(thf)_2$, the bond strength is almost similar (35 vs 31 kcal/mol). But the repartition of the bonding interaction is different. For $Cp^*_2Yb(thf)_2$, the dispersion

Energy (kcal/mol)	*Yb(taphen)PdYb*	$Cp^*_2Yb(thf)_2$	$(tmeda)PdMe_2YbCp^*_2$
Pauli	67	54.3	60.3
Electrostatic Interaction	-107	-53	-47
Orbital interaction	-79	-25	-28
Dispersion	-18	-18	-15
ΔE_{prep}	102	9	6
Bond Strength	35	31	24

Table 4.8: Bond Strength and EDA (kcal/mol) in *Yb(taphen)PdYb* and $(tmeda)PdMe_2YbCp^*_2$ when cutting the Yb-C-Pd bond formed and in $Cp^*_2Yb(thf)_2$ when cutting the Yb-thf bonds

forces accounts for 20 % of the bonding, the orbital interaction for 26 % and the electrostatic interaction for 55%. While this percentage for electrostatic interaction is similar between the two complexes, the dispersion forces play a more important role in the interaction of $Cp^*_2Yb(thf)_2$. The similar value for the bond strength makes it easy to understand why experimentally at room temperature in thf, the ytterbium molecule coordinated to the methyl groups prefers to coordinate to thf.

These three analyses points out towards a bonding interaction between the lanthanide and the methyl groups. While this interaction is weak, 35 kcal/mol, ELF and QTAIM analyses found basins and critical points between the methyl groups and the lanthanide ions. Another important characteristics of the structure was the bent angle between Yb1 and the methyl groups linked to the palladium. This interaction was specific to this compound, as it was not observed previously by Andersen *et al.*[25]. Two different hypotheses surrounding this bent structure have been analysed using theoretical tools.

- A bent complex?

Taking a closer look at the molecular orbitals, one interaction was found to possibly explain this structure: there is a small interaction between the π orbitals of one Cp^* ring and the $4d_{z2}$ of the palladium centre (Figure 4.23). This type of orbital overlap is not supposed to be favourable as it is a four electrons in two orbitals interaction. However, the Pd $4d_{z2}$ orbital energy decreases compared to *Yb(taphen)Pd*, passing from the HOMO to a deeper orbital. Hence, this is enhancing the stability of the compound.

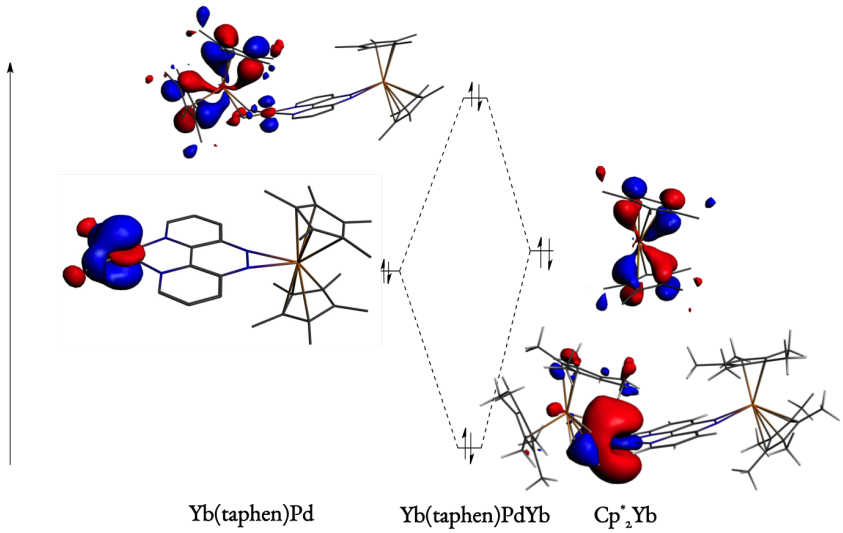

Figure 4.23: Orbital interaction diagram that could explain the bent structure of *Yb(taphen)PdYb*

Moreover, dispersion effects are keeping the cohesion of this structure. The molecule optimisation without the Grimme's dispersion corrections (D3) leads to a linear structure. The plot of the non-covalent interaction (NCI) identified an important amount of van der Waals forces between the palladium and the ytterbium complex (Figure 4.24). These two properties show that dispersion forces are in part responsible for the bending[81].

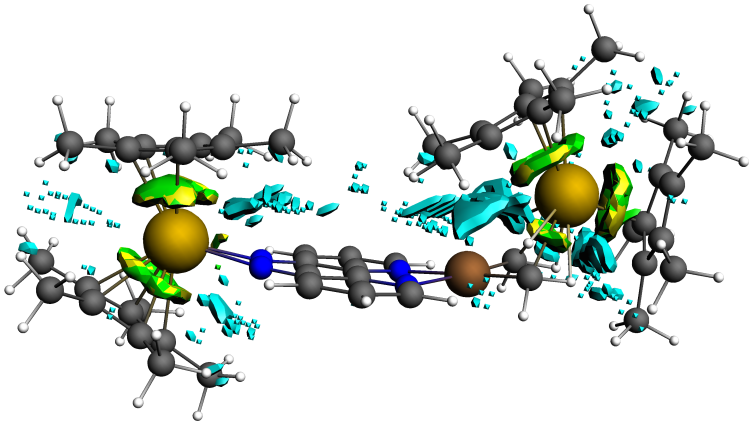

Figure 4.24: NCI plot of *Yb(taphen)PdYb* at the PBE0-D3 ZORA1 level of theory, blue, yellow and green surface represent weak van der Waals interactions, isosurface = 0.03

The orbital interaction is strong between the lanthanide and the methyl group and accounts for 39% of the bonding interaction. In this sense the bent angle observed experimentally with this complex is strongly related to the bonding interactions that occurs between the lanthanide and the methyl groups. However, the dispersion effects also play a role in the

bent conformation as a relatively high amount of van der Waals forces were found between the lanthanide molecule and the palladium centre.

The bent angle was not observed for other Lewis acid-Lewis base complexes. The reaction of one equivalent of $Cp^*_2Yb(OEt_2)$ and one equivalent of $(tmeda)PdMe_2$ led to the formation of a $(tmeda)PdMe_2YbCp^*_2$ complex. This adduct was analysed by X-Ray diffraction studies (Figure 4.25 for the structure and Table 4.9 for a comparison of the geometries). This compound contains a diamagnetic, $4f^{14}$, Yb^{II} ion that does not transfer its electron to the palladium complex (silent magnetism analysis).

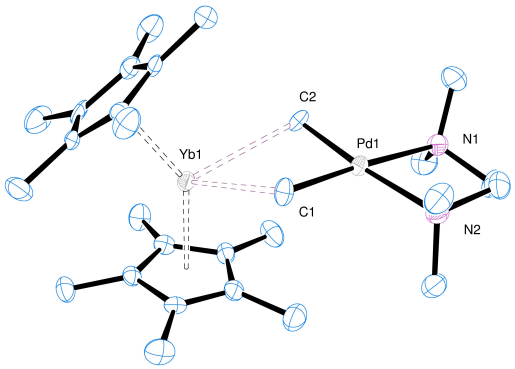

Figure 4.25: ORTEP of the X-Ray diffraction structure of $(tmeda)PdMe_2YbCp^*_2$

	Yb(taphen)PdYb	$(tmeda)PdMe_2YbCp^*_2$	$Cp^*_2YbMe_2Ptdippe$[25]
Yb-M	3.0815(7)	3.73	4.04
Yb-C (Me) (avg)	2.56(1)	2.799(5)	2.90(1)
M-C (Me) (avg)	2.05(1)	2.033(5)	2.09(1)

Table 4.9: X-Ray structures distances (angstroms) for *Yb(taphen)PdYb* , $(tmeda)PdMe_2YbCp^*_2$, with the already published $Cp^*_2YbMe_2Ptdippe$[25], where avg stands for average

The distances between the palladium centre and the carbon atoms of the methyl groups are longer for *Yb(taphen)PdYb* (2.05 Åand 2.03 Å for $(tmeda)PdMe_2YbCp^*_2$). This could result from the interaction between the lanthanide ion and the palladium centre that is stronger for *Yb(taphen)PdYb*: the distance between the lanthanide and the methyl groups for the tri-metallic complex and between the lanthanide ion and the palladium centre is 0.24 Å and 0.65 Å shorter, respectively. Comparing these distances to the already published structure $Cp^*_2YbMe_2Ptdippe$[25] gives shorter distances in the case of $(tmeda)PdMe_2YbCp^*_2$. The

distance between the lanthanide ion and the the carbon atoms is 0.1 Å shorter for this molecule. This could result from a stronger interaction for $(\mathrm{tmeda})\mathrm{PdMe_2YbCp^*_2}$.

The EDA of $(\mathrm{tmeda})\mathrm{PdMe_2YbCp^*_2}$ is presented in Table 4.8. It shows that the amount of dispersion forces in the attractive interactions is more important than in the case of *Yb(taphen)PdYb* (17% compared to 8%). Moreover, the total bond strength between the $\mathrm{Cp^*_2Yb}$ fragment and the $(\mathrm{tmeda})\mathrm{PdMe_2}$ is weak, 24 kcal/mol. Therefore, the presence of a taphen moiety in the vicinity of the palladium centre is creating the bent structure and the presence of an electron transferred to the ligand strengthens this interaction. Other types of Lewis adducts have been synthesised recently[82] and further analysis of their bonding interaction could result in better understanding of lanthanide bonding interactions.

4.2.2 Bipyrimidine as a ligand

The taphen ligand has enabled the synthesis and characterisation of several compounds. Nonetheless, the propensity of this ligand to keep its electron was demonstrated during reactivity with MeI. Changing the orbital of the bridging ligand could lead to a change in reactivity.

Bipyrimidine (bpm) is one of the most common ligands used for the synthesis of polymetallic complexes. Compared to taphen, phenanthroline, or bipyridine the point group of bipyrimidine is $\mathrm{D_{2h}}$. Its valence orbitals includes four lone pairs on each nitrogens and several π and π^* orbitals (see Table 4.10 for pictures of the π^* orbitals). The electronic structure of the radical anion of bpm has been calculated at the CASSCF(17,[1,1,1,1,2,2,2,2]) and CASPT2 level of theory. As for bipyridine and phenanthroline, the ground and the first excited states are more distanced than for taphen (0.76 and 0.66 eV at the CASPT2 and CASSCF level respectively). The ground state has an important multi-reference character with occupation of three π^* orbitals of bipyrimidine: 32 % $\mathrm{n_3^{\uparrow}\pi_1^{*\downarrow}\pi_3^{*\uparrow}}$, 45 % $\mathrm{n_4^{\uparrow}\pi_1^{*\downarrow}\pi_4^{*\uparrow}}$ and 5 % % $\mathrm{n_1^{\uparrow}\pi_1^{*2}}$. These orbitals can be involved with the lanthanide into a multi-reference ground state, like in the case of phenanthroline complexes of samarium described in Chapter 2 or for bipyridine complexes of ytterbium[83]. The occupation of these three LUMOs could induce interesting reactivity and could enable further stabilisation of $\mathrm{Pd^{IV}}$ intermediates.

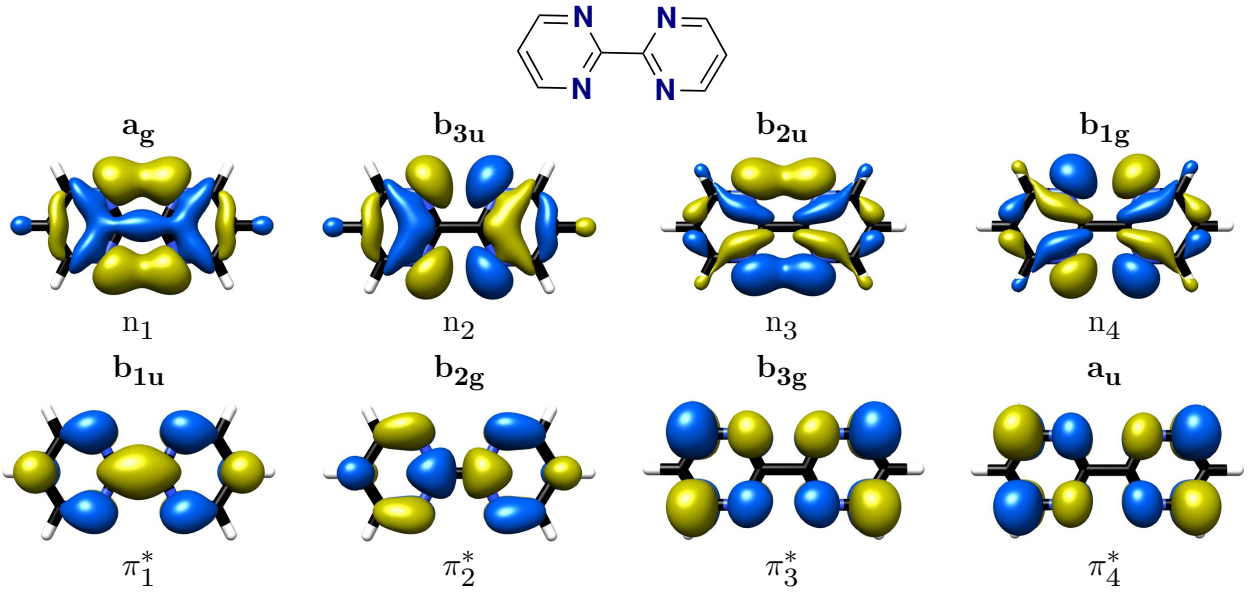

Table 4.10: Valence molecular orbitals of bpm in the ground state at the CASSCF(17,[1,1,1,1,2,2,2,2]); orbitals not represented have a natural occupation close to 2.0

4.2.2.1 *Yb(bpm)Pd* synthesis and characterisation

The same experimental procedure described for taphen was capable of producing crystals of $Cp^*_2Yb(bpm)PdMe_2$ (*Yb(bpm)Pd*). This compound was characterised using NMR and solid state magnetic measurement. The X-Ray crystallographic structure of *Yb(bpm)Pd* is shown in Figure 4.26 and relevant distances are shown in Table 4.11.

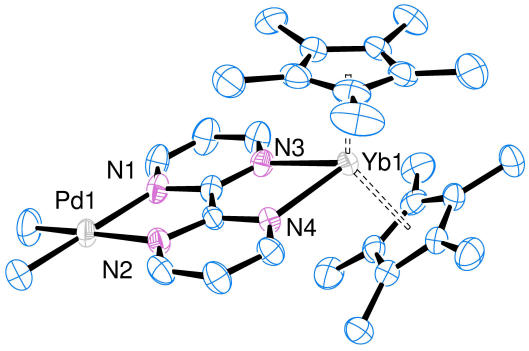

Figure 4.26: ORTEP of the X-Ray diffraction structure of *Yb(bpm)Pd*,

	Yb(taphen)Pd	*Yb(bpm)Pd*	Triplet	Singlet	$(\mathrm{bpm})\mathrm{PdMe_2}$
Yb-N (avg)	2.290(6)	2.36(2)	2.39	2.38	
Yb-Pd	7.24	5.99	6.09	5.98	
Pd-C (Me) (avg)	1.990(3)	2.028(2)	2.03	2.04	2.028(5)
Pd-N (avg)	2.174(4)	2.16	2.14	2.14	2.139(4)

Table 4.11: Geometric parameters (distances in angstroms) of the X-Ray structures of *Yb(taphen)Pd*, *Yb(bpm)Pd* and $(\mathrm{bpm})\mathrm{PdMe_2}$, and the DFT optimised structure of *Yb(bpm)Pd* for the singlet and the triplet spin multiplicities at the PBE-D3 level, where avg stands for average

The distances around the lanthanide center are indicative of a $\mathrm{Yb}^{+\mathrm{III}}$ complex, as the $\mathrm{Yb} - \mathrm{Cp}^*$ distance is 2.305(8) Å, close from the expected distance for $\mathrm{Yb}^{+\mathrm{III}}$ molecules (around 2.30 Å). Around the palladium, compared to the monometallic $(\mathrm{bpm})\mathrm{PdMe_2}$, the distances are similar for Pd-C, but elongated for Pd-N, which is consistent with an electron transfer from the lanthanide to the organic moiety. Compared to *Yb(taphen)Pd*, the distances are shorter for Pd-C, which is indicative of a stronger interaction between the palladium and the methyl groups.

The magnetic data is different from the one of *Yb(taphen)Pd*. There are two inflexion points: one at 15 K and another at 50 K. These characteristics are typical of a multi-configurational singlet state that populates with temperature the triplet state. The two inflexion points indicate two different singlet wave-functions. At low temperature, the electronic structure should be an open-shell singlet with one electron on the π system of bipyridine. The first inflexion point indicates the presence of another open-shell singlet state close in energy from the first open-shell singlet. Finally, the second inflexion point indicates the temperature at which the triplet state is starting to be populated. As a result, three configurations (two open-shell singlets and one triplet) are close in energy[84].

This behaviour was already observed for substituted bipyridine complexes of ytterbium[83,85]. However, in this situation, the close vicinity of the palladium centre could enable stabilisation of palladium IV intermediate for example.

4.2.2.2 Theoretical characterisation

Even if there is an experimental proof for the different low-lying configurations for *Yb(bpm)Pd*, geometry optimisations were performed at the DFT level of theory. This was validated by

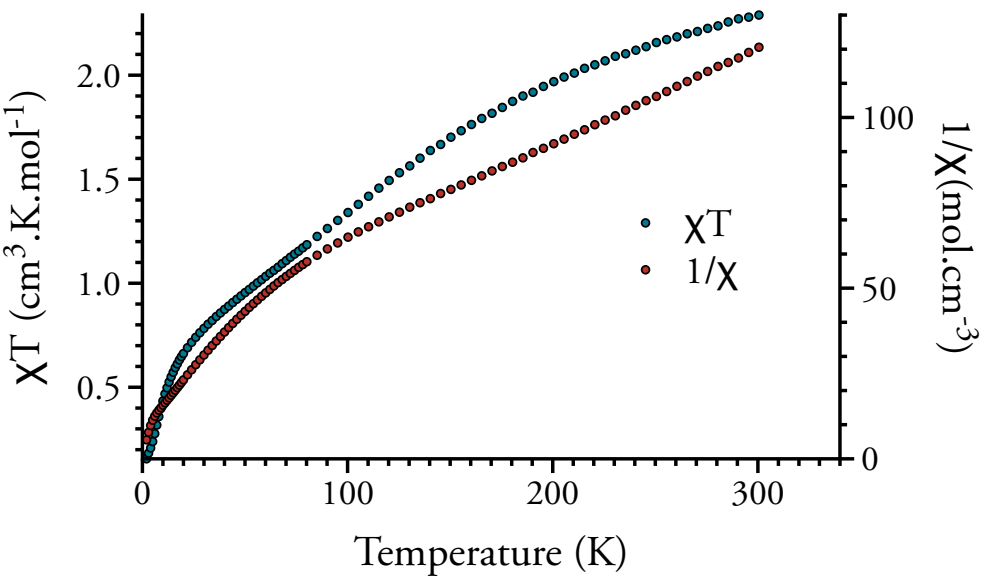

Figure 4.27: Temperature dependent magnetic data for *Yb(bpm)Pd* from 5 K to 300 K at 0.5 T $1/\chi$ vs T is given as filled red dots, χT vs. T as filled blue dots

previous studies on bipyridine complexes of ytterbium that did not find significant differences between the CASSCF optimised geometry and the DFT one[83,85]. Different distances are presented in Table 4.11 with different spin multiplicities for the complex.

The optimised geometry of *Yb(taphen)Pd* both in its triplet or singlet spin states differs from the experimental X-Ray diffraction analysis. The geometry closest to the experimental value is the one optimised for the singlet spin state *i.e.* without any electron transfer to the palladium. This is different to what was observed previously by Maron *et al.* for bipyridine complexes of ytterbium[83,85].

The presence of low-lying states can be responsible for multireference character of the ground state. As a result, CASSCF calculations need to be performed in order to have an idea of the electronic structure of the complex. However, the definition of the active space is not easy with this compound as it could include the orbitals of ytterbium (4f + 5d), the orbitals of the bpm ligand (four lone pairs, four π and four $\pi*$) and the orbitals of the palladium compound (4d). Including all these orbitals result in a too large active space that cannot be suitable for CASSCF calculation. Therefore, two approximated active spaces have been used for *Yb(bpm)Pd* and the results are presented in Table 4.12.

Electrons	Orbitals	Description of the orbitals	Ground State
14	10	3 π^* + 3 4f + 4 π	$4f^{13\uparrow}\pi_1^{*\downarrow}$
8	10	4 π^* bpm + 3 4f + 2 4d + 1 5d	$4f^{13\uparrow}(\pi_1\pi_4)^{*\downarrow}$

Table 4.12: The two active spaces used to calculate the electronic structure of *Yb(bpm)Pd*; a spin average calculation was performed on the first 10 states

The two active spaces are consistent with the formation of a radical bpm, and an oxidised ytterbium. Both active space do not show sign of a multi-configuration on the lanthanide ion with involvement of $4f^{14}$ and $4f^{13}$ wave-functions. However, the two active space does not result in the same wave-function on the bpm core itself: while the first active space results in a donation of one electron to π_1^* of bpm, the second result in a multi-configuration between π_1^* and π_4^* (Figure 4.10 for a view of the orbitals). The multi-reference character of the wave-function for the second active space might result from the inclusion of 5d orbitals, which have the right symmetry to interact with π_4^*.

The second active space, [8,10], was used to compare the energies of the triplet and the Open-Shell Singlet (OSS) wave-function and the excited states of the OSS at the CASPT2 level of theory (Table 4.13).

Configuration	CASSCF Energy	CASPT2 Energy	Wave-function
Triplet-1	0	0	$4f^{13}\pi_1^{*0.60}\pi_4^{*0.30}\pi_3^{*0.10}$
OSS-1	0.01	0.00	$4f^{13}\pi_1^{*0.60}\pi_4^{*0.30}\pi_3^{*0.10}$
OSS-2	1.94	1.95	$4f^{13}\pi_1^{*0.15}\pi_4^{*0.65}\pi_3^{*0.15}$
OSS-3	2.38	2.39	$4f^{13}\pi_1^{*0.20}\pi_4^{*0.05}\pi_3^{*0.70}$
OSS-4	3.80	3.51	$4f^{13}5d^1$

Table 4.13: Energies (eV) of the triplet ground state, the OSS ground and excited states and the different natural occupation numbers of the 4f and π^* orbitals; the names π_1^*, $\pi_4^*$and π_3^* refers to the orbitals of neutral bpm described in Table 4.10

The energy difference between the OSS and the triplet is low at the CASPT2 level of theory. This is different from what was previously observed for $Cp*_2Yb(bipy)$ complexes[85]. The energy difference between the first OSS excited state and the ground state is as well high and could not account for the formation of the two low-lying OSS observed experimentally. Changing the active space for [14,10] did not change the qualitative evaluation of the energy.

Increasing the active space past the [14,10] threshold did not result in successful calculations or only led to similar electronic structure. However, addition of other orbitals (5d of ytterbium, 4d of palladium, π and n orbitals of bpm) can decrease the energy difference between the OSS ground state and the first excited states.

As detailed in previous publications[27,83], the configuration of ytterbium complexes is dependant on the redox potential of the ligand. Depending on the redox potential of the ligand, the configuration will be $4f^{13\uparrow}(\text{ligand})^{\downarrow}$ or $4f^{14}(\text{ligand})^{0}$, if the ytterbium +II ion is capable of reducing the ligand or not. For intermediate redox potentials, the configuration of the resulting complex is a mixed-valent one combining the two configurations. Therefore, the orbitals of bipyrimidine radical can be looked at in a first approximation. In the bpm's CASSCF calculation described earlier, the ground state was multi-configurational with involvement of π_1^*, π_3^* and π_4^*. Moreover, at both the CASSCF and CASPT2 level, this ground state possessed a low-lying excited state (0.19 and 0.12 eV respectively). The closeness of these two states are probably triggering the two OSS observed on the magnetic data of *Yb(bpm)Pd*. This cannot be reproduced using CASSCF on the full molecule, as the active space for such a calculation is important and cannot fit a normal CASSCF calculation.

The molecule will be approximated in the next paragraphs in order to hide the problems related to the triplet and singlet closeness in energy. The 4f electrons will be approximated using a LC-ECP. It will mask the electronic ground state problem (triplet or singlet) –which is validated considering that this is probably not responsible for the reactivity of these compounds–, but it will not mask the one of the relative closeness of the two OSS states observed experimentally and due to the electronic structure of bpm.

4.2.2.3 Reactivity with MeI and comparison with *Yb(taphen)Pd*

The reactivity of *Yb(bpm)Pd* was performed with MeI in toluene[84]. The intermediate Pd^{IV} was crystallised in toluene at -40 °C (X-Ray structure not shown). Compared to previous results with *Yb(taphen)Pd*, the stability of the Pd^{IV} species is more important and has enabled variable temperature ^1H NMR (Figure 4.28) between -80 °C and -20 °C, without significant decomposition of the compound. However, after a couple of hours at room temperature, the compound decomposes and liberates ethane. This degradation was

slow enough to be followed by ^{1}H NMRand a kinetic study was performed at different temperature. An Eyring plot was able to evaluate the enthalpy and entropy for this reaction ($\Delta H^{\neq} = 24(1)$ kcal/mol and $\Delta S^{\neq} = 6(6)$ cal/mol/K).

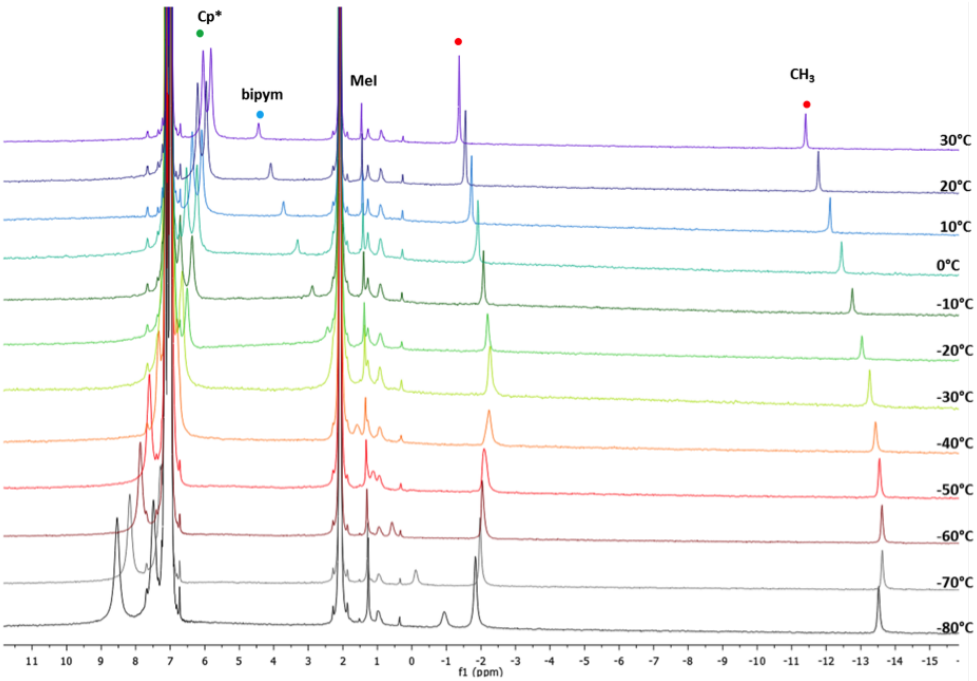

Figure 4.28: Variable temperature ^{1}H NMR of *Yb(bpm)PdMeI*

Different pathways have been discussed for reductive elimination over the years[2,86] (Figure 4.29). Mechanisms involve generally a reaction intermediate with a 5-coordinate palladium[87,88], that has then more space in order to proceed towards the reductive elimination. Two decoordinations can be hypothesised: one decoordination of the iodide as describe by Canty *et al.*[88] and the decoordination of one arm of the bipyrimidine/taphen moieties, which has been described recently by Sanford's group[86] and by Goldberg's group for platinum complexes[87] (Figure 4.29).

Previous values for the enthalpy and entropy of reaction for $(\mathrm{bipy})\mathrm{PdMe}_2$[89] were ranging for $\Delta H^{\neq}$ from 8 to 18.6 kcal/mol and for $\Delta S^{\neq}$ from -11 to -34 cal/mol/K. The $\Delta S^{\neq}$ value is negative which is in agreement with a cation formation, inducing a high order in the first solvation sphere and is inconsistent with the decoordination of one arm of the bipyridine moiety. For *Yb(bpm)PdMeI*, while $\Delta H^{\neq}$ is almost identical, $\Delta S^{\neq}$ does not have the same sign. This difference for $\Delta S^{\neq}$ can indicate a mechanistic difference between $(\mathrm{bipy})\mathrm{PdMe}_2$

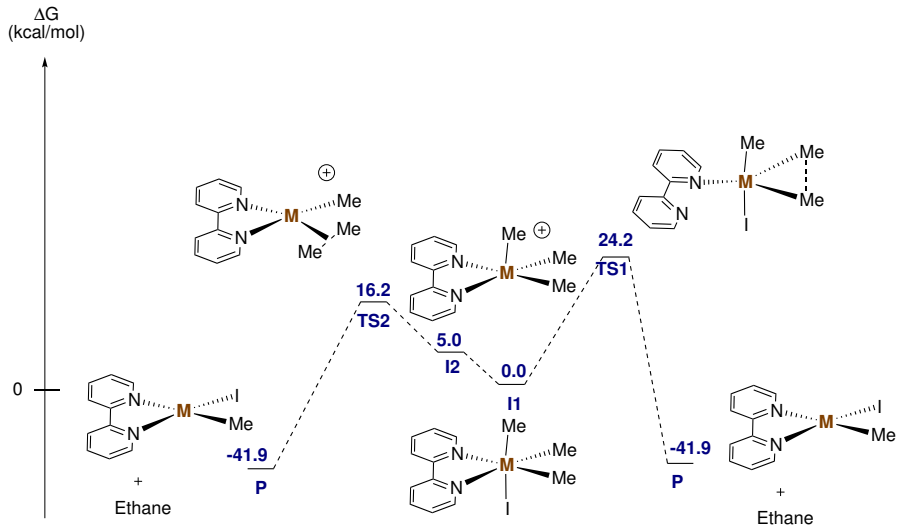

Figure 4.29: Mechanism for the reductive elimination of ethane upon oxidative addition of MeI on bipyridine palladium complexes in acetone

and *Yb(bpm)PdMeI*. *Yb(bpm)PdMeI* reductive elimination is one of the rare example[90] of a Pd^{IV} with a positive $\Delta S^{\neq}$, in agreement with the absence of cation formation in the transition state. Its small value ($\Delta S^{\neq} = 6(6)$ cal/mol/K) could be in agreement with a mechanism where one arm of the bipyrimidine is decoordinated from the palladium complex.

The mechanism was studied at the DFT level of theory. On palladium complexes, the group of Sanford has been interested in simulation of the mechanisms at the DFT level[86]. At their level of theory they were able to reproduce accurately palladium reaction mechanisms. As a result, their methodology will be used below to treat our new molecular complexes. The geometry optimisation was done at the PBE-D3/BS2and a single point was performed at the ωB97X-D2/BS3 with addition of an implicit solvation model (SMD) (BS2 and BS3 were defined in Chapter 1). The results are presented in Table 4.14 for $(bipy)PdMe_2$ using two different solvent media: acetone and toluene.

ΔG	Acetone	Toluene
I1	0	0
TS1	24.2	24.0
I2	5.0	37.1
TS2	16.2	47.1
P	-41.9	-43.1

Table 4.14: ΔG (kcal/mol) calculated at the ωB97X-D2/BS2 for different intermediate of $(bipy)PdMe_3I$ in acetone and toluene, the names are defined in Figure 4.29

The two mechanisms are favoured depending on the solvent: the mechanism involving a decoordination of the iodide ion is occurring in acetone while the mechanism involving a decoordination of one arm of the bipyridine moiety is favoured in toluene. This is not surprising as the stability of the cationic form $(\mathrm{taphen})\mathrm{PdMe}_3^+$ in non polar solvent such as toluene is reduced. Previous studies in acetone already showed that the mechanism passed by a decoordination of one iodide atom[89]. But, the reaction mechanism in toluene is yet to be studied extensively as only few degradation kinetic studies of the reductive elimination for the $\mathrm{Pd}^{\mathrm{IV}}$ intermediate were done in toluene. According to these results, changing the solvent could change the relative energies of TS1 and TS2 which might explain the formation of the crystal structure of *Yb(taphen)Pd* in acetone while in toluene the decomposition is too fast to be followed.

The reaction mechanism was performed for the four complexes *(taphen)PdMeI*, *(bpm)PdMeI*, *Yb(taphen)PdMeI* and *Yb(bpm)PdMeI*. For the four complexes, the TS1 geometry present a very asymmetric coordination to the palladium centre. The asymmetry is relatively smaller for bipyrimidine ligands than for taphen ones, probably due to the rigidity of the latter compared to the former. The energies were calculated for the two different pathways (Figure 4.29) and are presented in Figure 4.30.

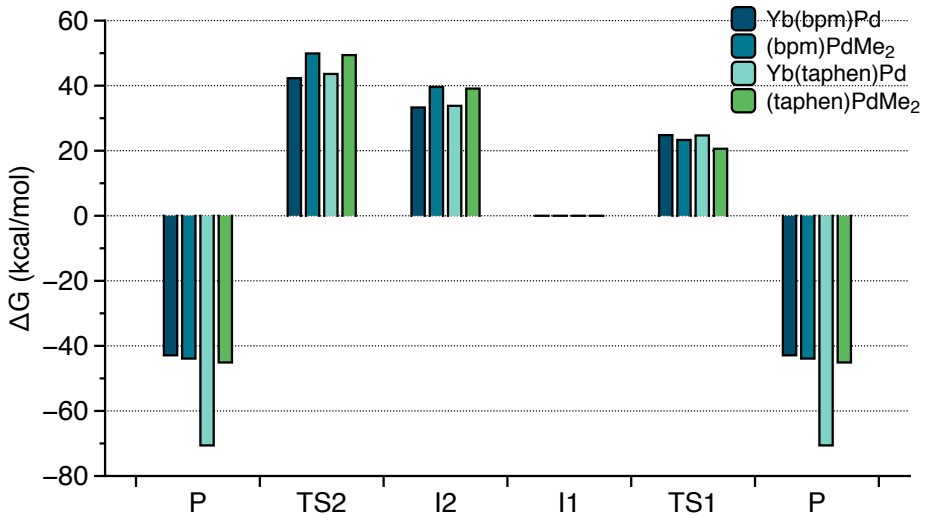

Figure 4.30: Gibbs enthalpy of different complexes taking I1 as a reference at the ωB97X-D2/BS2 level, the names have been defined in Figure 4.29

The energies of the different TS are similar depending on the complexes at stake. There is a stabilisation of the TS2and I2 molecules (>5 kcal/mol) passing from the monometallic

to the bimetallic complexes. But, this difference does not change the order of the reaction, as in toluene the pathway 1 (TS1) is favored over the pathway 2 (TS2). Moreover, the TS1 stability is slightly decreased from the mono-metalic to the bimetallic complex: $\Delta G_{TS1}((bpm)PdMe_2) < \Delta G_{TS1}(Yb(bpm)Pd)$. This difference could induce a slower reductive elimination in the case of bimetallic complexes than in the case of monometallic complexes. However, it is thin and cannot explain the observed experimental distinction between *Yb(taphen)Pd* and *Yb(bpm)Pd*. The electronic structure of the latter has to play a role in the increase of ΔG_{TS1}. The frontier orbitals of *Yb(taphen)Pd* at the TS1 geometries are pictured in Figure 4.15.

SOMO	LUMO	LUMO+1
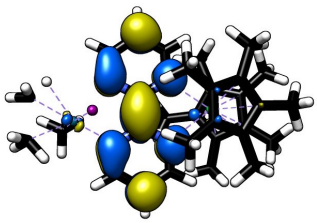	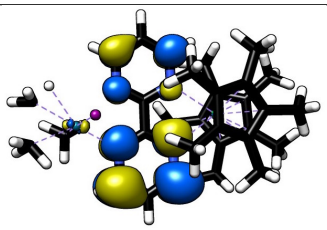	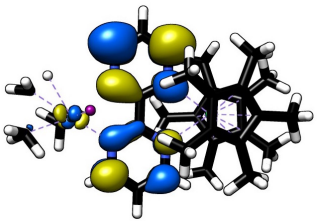
- 0.2080	0.0051	0.0180

Table 4.15: Molecular orbitals of TS1 at the ωB97X-D2/BS2 level of theory and their respective energies in eV

The Pd-N distortion, observed in the DFT optimised structure of TS1, is modifying the symmetry of the π_1^* and π_3^* of bipyrimidine (LUMO and LUMO+1 in Figure 4.15). The LUMO and LUMO+1 orbitals of *Yb(taphen)PdMeI* become slightly asymetric in TS1. If the ground state of the molecule involves both π_1^* and π_3^* of bipyrimidine as it is the case for bipyridine complexes of ytterbium[27,83,85] and as it was shown for *Yb(bpm)Pd*, TS1 might be higher in energy for *Yb(bpm)PdMeI* than for *Yb(taphen)PdMeI*. Contrary to bpm, taphen does not possess a low-lying excited states that might get involved in further stabilisation of a Pd^{IV} species.

DMRG calculations could become very useful in this particular scenario: by enabling larger active space, studying this mechanism at the DMRG level could bring more accurate values for the energy than at the DFT level. Such calculations are currently being investigated in collaboration with M. Reiher[91] (ETH Zurich).

4.3 Towards the design of a new ligand

The case of bipyrimidine and taphen has shown that the ligand is crucial in order to stabilise certain reactive intermediates, or to promote reductive elimination selectively. Getting a better understanding of the ligand design that could be placed in a bimetallic fashion could trigger new developments for the synthesis of bimetallic molecules with lanthanide and palladium. As a result, other ligands were used, such as dipyrido[3,2-a:2',3'-c]phenazine (dppz) and the 2-(2-pyrimidil)benzimidazolate (Ind-H) ligand. Both ligands vary from bipyrimidine and taphen in different ways. The synthesis and characterisation of both molecules will be discussed and further lead to a computational evaluation of different ligands in order to promote electron density on the palladium itself.

4.3.1 The dipyrido[3,2-a:2',3'-c]phenazine ligand

The dipyrido[3,2-a:2',3'-c]phenazine ligand (dppz) has been used extensively in photochemistry and is known for its tendency of well delocalising electrons. However, the use of this ligand for poly-metallic clusters has been rather limited (to the best of our knowledge there is no entry in the CCDC over poly-metallic complexes of dppz). As such using the phenanthroline core of dppz to coordinate the TM centre and then using the nitrogens present on the edge of the molecule to coordinate the Yb centre would be a novel use of dppz and could create new hetero-metallic compounds. The reaction of one equivalent of dppz to (tmeda)$PdMe_2$ led to the formation of a fine orange/red powder. This powder was used in order to synthesise poly-metallic molecules with $Cp^*_2Yb(OEt_2)$. The brownish/back solution was crystallised at $-40\,^{o}C$ and tiny dark crystals were suitable for X-Ray diffraction studies (Figure 4.31).

This molecule contains two ytterbium and one palladium centres. The two ytterbium ions are coordinated in a non-covalent way to the two carbons near the nitrogen, as they are looking for more than one atom to bind to (for geometry comparison see Table 4.16). The deformation of the dppz itself indicates an electron transfer to the ligand. The X-Ray data did not enable the confirmation of hydrogen atoms near the ytterbium. Their presence was proved as in thf, $Cp^*_2Yb(thf)_2$ and free $(dppz)PdMe_2$ were gathered. When changing the

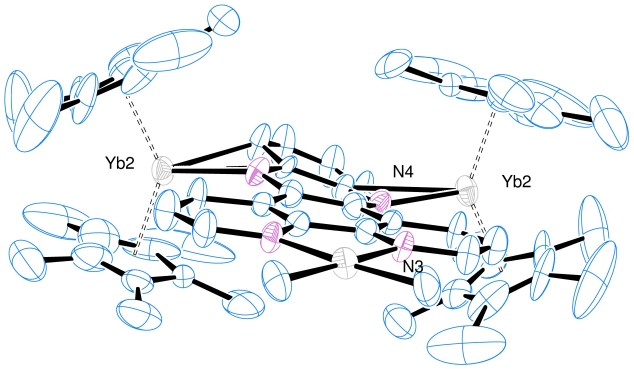

Figure 4.31: ORTEP of the X-Ray diffraction structure of *Yb(dppz)Pd*

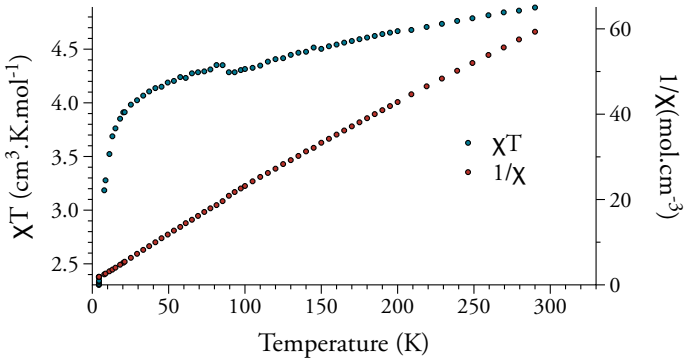

Figure 4.32: Temperature dependent magnetic data for *Yb(dppz)Pd* from 5 K to 300 K at 0.5 T $1/\chi$ vs T is given as filled red dots, χT vs. T as filled blue dots

solvent for toluene the complex could be formed again, indicating an equilibrium between the trimeric form and the palladium complex depending on the solvent. The magnetism of *Yb(dppz)Pd* at room temperature showed two Yb^{III} consistent with the deformation of the dppz moiety (see spectrum Figure 4.32).

In order to compare the strength of the bond between the ytterbium centres and the dppz complex, quantum chemistry calculations were performed. The geometry optimisations were more complicated than what was expected from the previous calculations as the geometry did not successfully reproduce experimental results (Table 4.16).

On one hand, using all-electron calculations and different spin state for the molecule, the resulting geometry is different from what is expected from the crystallographic structure. On the other hand, the use of a large core ECP calculation was able to partially recover the distances found in the crystallographic structure. This difference probably lies in the difficult electronic structure of the complex that the pseudopotential masked by putting

Distance (Å)	*Yb(dppz)Pd*	Singlet	Triplet	Quintet	LC-ECP
Yb-N (avg)	2.28(1)	2.377	2.389	2.391	2.328
Yb-C (dppz)	2.81(2)	3.190	3.153	3.402	2.711
Yb-Yb	7.08	7.508	7.497	7.533	6.931
Yb-Pd	8.13	7.792	7.851	7.551	8.303
Pd-C (Me) (avg)	2.05(1)	2.036	2.038	2.041	2.038
Pd-N (avg)	2.13(1)	2.130	2.134	2.159	2.154

Table 4.16: Comparison between the experimental structure of *Yb(dppz)Pd* and the theoretical structures optimised at the PBE-D3 level of theory with ZORA2 or LC-ECP at different spin states (singlet, triplet and quintet) where avg stands for average

a_2		b_2	
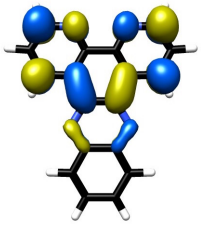	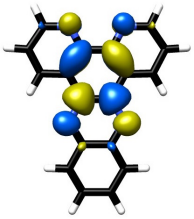	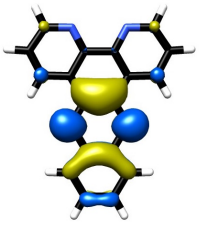	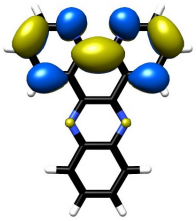
π_1^*	π_2^*	π_3^*	π_4^*
0.01	0.01	1.16	0.81

Table 4.17: Molecular orbitals of neutral dppz and their natural occupation in the ground state for dppz dianion at the CASSCF(14,[2,2,3,3])

the 4f electrons in the core of the pseudopotential.

In order to understand the distorted geometric structure, dppz radical anion and dppz singlet dianion were studied at the CASSCF level, after a geometry optimisation of neutral dppz at the PBE-D3/ZORA2 level. As pyridine and phenanthroline, the point group of dppz is C_{2v}. The valence orbitals of neutral dppz contains four π^* orbitals, four lone pairs and two π orbitals. The natural occupation of each orbital was calculated in the ground state for the singlet dianion at the CASSCF(14,[2,2,3,3]) level and are shown in Table 4.17.

The addition of two electrons on the dppz moiety leads to an electronic structure involving the π_4^* and π_3^* orbital. The resulting electronic structure is for 93% $\pi_3^{*\uparrow}\pi_4^{*\downarrow}$. This could explain the non planar structure observed experimentally. The two b_2 π^* orbitals are located in two distinct parts of dppz: the geometric structure of the dppz ligand could be distorted between the two positions of the electrons. Excited states for the singlet biradical dppz found one low lying singlet of electronic structure π_3^{*2}, located 0.2 eV (0.41 eV)

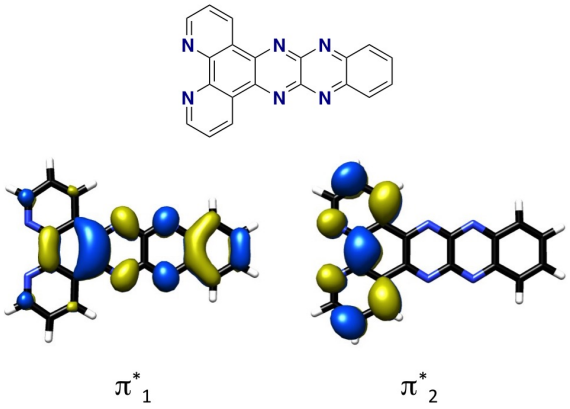

Figure 4.33: Molecular orbitals of dpq-QX

below (above) the ground state at the CASPT2 (CASSCF) level of theory. The presence of these two quasi-degenerate states could trigger multi-reference in the ground state for dppz complexes containing ytterbium.

The dppz ligand presents one other advantage compared to bpm: the presence of two lanthanides coordinated to the ligand that could easily decoordinate. This facile decoordination could be used during reactivity: changing the solvent could change the overall reactivity of the complex. But, it could also induce problems, as the lanthanide could react with the reagent and not act as an electron donor to the palladium. As such, the addition of MeI only resulted in the formation of $(\mathrm{dppz})\mathrm{PdMe}_2$ and the reaction between MeI and the ytterbium complex.

A ligand with the same structure than dppz, but that would possess two nitrogens for the bonding of the two lanthanide complexes, such as the one describe recently by Neves *et al.*[92] (dpq-QX) could stabilise the bonding of the two lanthanide centres on the ligand itself. A CASSCF/CASPT2(18,[3,3,3,3]) calculation on the singlet dianion dpq-QX showed that the electronic structure of this molecule involved two low-lying states (Figure 4.33): $\pi_1^{*\,2}$ and $\pi_1^{*\uparrow}\pi_2^{*\downarrow}$. The use of this ligand for the synthesis of more stable hetero-bimetallic complexes is currently under study.

4.3.2 The 2-(2-pyrimidil)benzimidazolate ligand

The classification of Green[64] define all the previous ligands as L2 type ligand for the palladium side of the bimetallic complexes. Using instead LX ligands could create a new

type of behaviour. The 2-(2-pyrimidil)benzimidazolate ligand presents on one side a LX and on the other a L2 binding site. This ligand (Ind-H) has been associated with ruthenium complexes recently[93] and its use in organometallic chemistry is limited to this sole example. The ligand (Ind-H) was synthesised according to existing procedures[93] and was characterised by X-Ray diffraction studies. Addition of this ligand to a solution of $(\mathrm{tmeda})\mathrm{PdMe}_2$ in acetonitrile gave a fine yellow powder. Upon diffusion in a pyridine and pentane mixture at room temperature, this powder gave yellow needle crystals of the complex (Ind)PdMe(py) that were suitable for X-Ray diffraction studies (Figure 4.34). Despite our best efforts, attempt to synthesise the bimetallic *Yb(Ind)Pd* were unsuccessful, but are still being investigated.

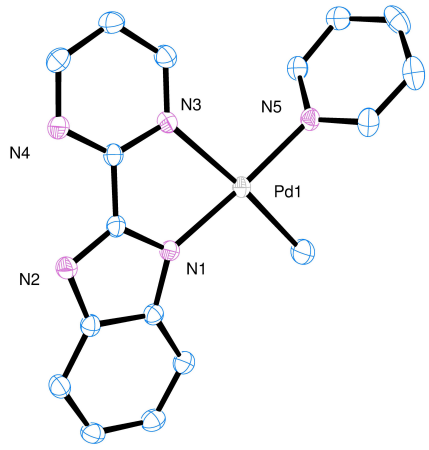

Figure 4.34: ORTEP of the X-Ray diffraction structure of (Ind)PdMe(py)

The valence molecular orbitals of the anionic Ind ligand have been represented in Table 4.18. The electronic structure of the ligand radical dianion was then studied using CASSCF - CASPT (13,[2,2,4,3]). The ground state of the molecule involves two different π^* orbitals of the anionic Ind ligand. It is a mixture of 50 % $n_1^2 n_2^{\uparrow} \pi_1^{*\uparrow} \pi_2^{*\downarrow}$ and 50 % $n_1^{\uparrow} n_2^2 \pi_1^{*\uparrow} \pi_2^{*\downarrow}$. The involvement of the two states in a 50/50 ratio is interesting as it could mean that both states can be involved during catalysis.

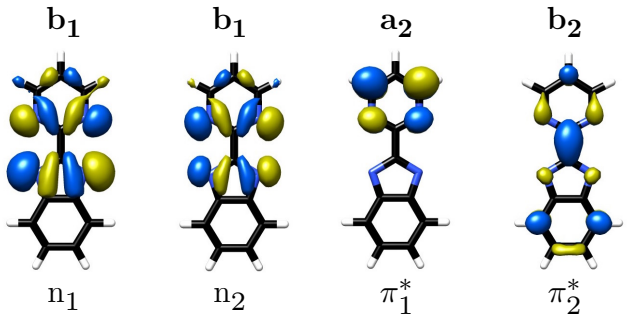

Table 4.18: Valence molecular orbitals of Ind at the CASSCF(13,[2,2,4,3]) level of theory

4.3.3 The optimal ligand design ?

As shown previously, the design of the ligand is critical in order to enhance the reactivity of the complex. This design relies on three specific aspects:

- The simplicity of the ligand synthesis;
- The simplicity of the ligand reduction: in order to promote the electron transfer the ligand should be easily reduced, which limit the study to π delocalised systems;
- The availability of the electron for the TM: the electronic spin density on the TM itself should get the highest possible in order to promote interesting reactivity.

Using chemical instincts and the help of organic chemists specialised in the synthesis of N-heteroaromatic compounds, the first two points are very easy to analyse. The computational tool can help to analyse the electronic spin density on the palladium centre. Obviously, this density will depend on the geometry of the complex and hence on its crystal field splitting. In a first approximation, square planar complexes were studied with different ligands proposed by A. Hammer (Msc Student) and Y. Bourne-Branchu (PhD student in C. Gosmini and G. Danoun's group (Laboratoire de Chimie Moléculaire)) as easy ligands to synthesise (Figure 4.35).

Three classes can be distinguished: the ligands with a base bipyrimidine, the ligand with one pyrimidine and a five members cycle containing either an oxygen or a nitrogen and bigger π systems. Comparing different substituent groups on the bipyrimidine could resolve the influence of electro-attractor or donor groups on the density of palladium. Changing one pyrimidine with another cycle with hetero-atoms will be interesting as oxygen is known

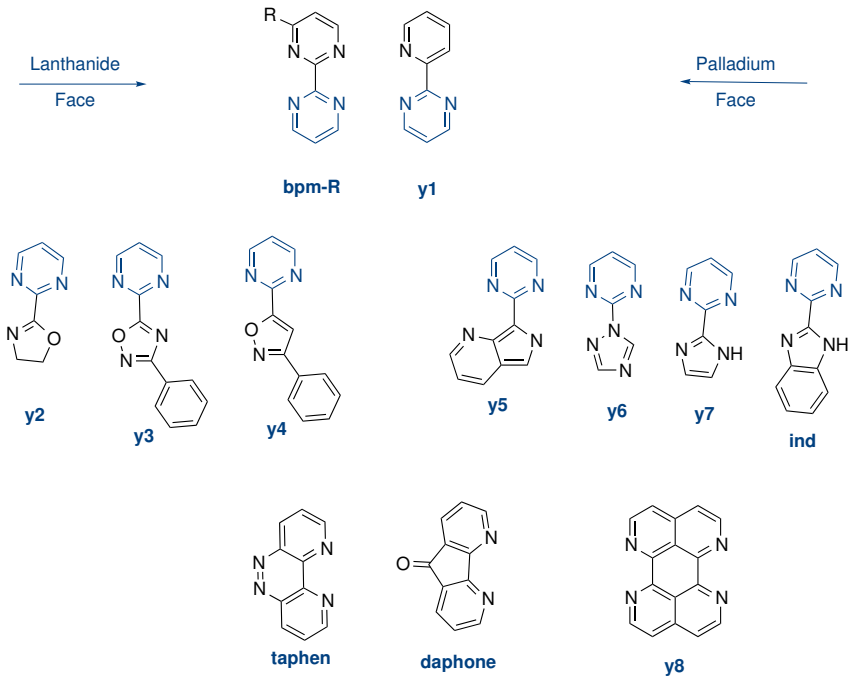

Figure 4.35: Scheme of the different ligands proposed by A. Hammer and Y. Bourne-Branchu, the arrow indicates the lanthanide and the palladium coordination sites

to create strong bonds with lanthanides. Moreover, the influence of the delocalisation of the cycle will be tested with the third class of compounds.

As the cost of the calculation is important for lanthanide complexes (for the optimisation/single point cycles), the calculations were performed on the palladium complexes. The palladium complex was optimised in its neutral form and a single point calculation was performed on the optimised geometry in its radical anionic form. The Lœwdin population was analysed using different density functionals and the results are shown in Figure 4.36.

To check the functional dependency of the results, the calculations were performed using three different functionals: M06-2X, PBE0-D3BJ and ωB97X-D3. From these graphs different general conclusions can be drawn:

- Effect of electro attractor or electro donor groups: compared to bpm-OMe and bpm, bpm-CN has a higher spin density, which indicates that electro attractor groups increase the spin density on the palladium itself compared to electro-donor groups such as OMe which reduces the spin density on the palladium centre. This is in agreement with a comparison between y7 and Ind that shows that Ind has a lower spin density on

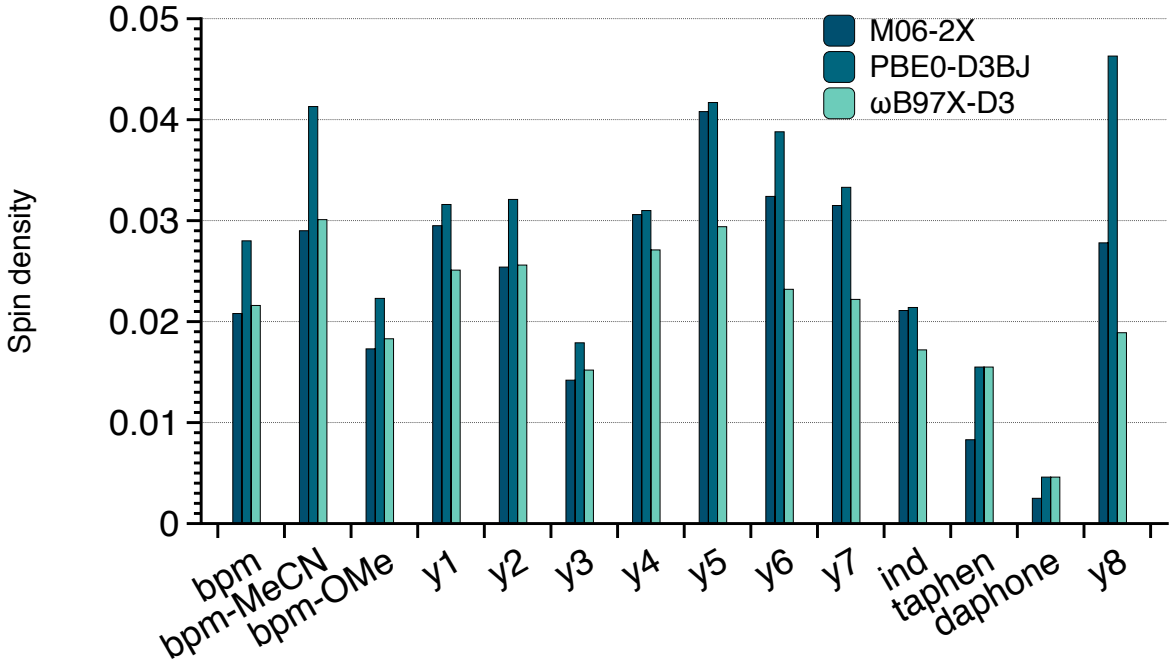

Figure 4.36: Lœwdin spin density on the palladium for the radical complexes using different density functionals M06-2X, ωB97X-D3, PBE0-D3BJ

the palladium ion, *i.e.* that the increase in delocalisation of the π system reduces the spin density on the palladium;

- Effect of the Green's type of ligand: it is hard to conclude for this type of effects. Compared to bpm, y1 has lower spin density on the palladium using PBE0-D3BJ and ωB97X-D3 (M06-2X gives the same spin density for both compounds). On the contrary, compared to y3, y4 has a higher spin density on the palladium. This indicates that depending on the molecular orbitals of the ligands, the effect in passing from a L2 to a LX will be different.

Depending on the density functional, several ligands have a high spin density on the palladium. While M06-2X is known not to be accurate for its density values[94], ωB97X-D3 is known to predict accurate densities and polarisabilities for aromatic systems[95]. Using this functional, three molecules have a spin density approaching 0.03: y5, y4 and bpm-MeCN. These molecules could be interesting candidates for the synthesis of bimetallic complexes of lanthanide.

4.4 Conclusion and perspective

Several multi-metallic complexes bearing a redox-non innocent ligand, a lanthanide and a TM complex have been synthesised and studied using both experimental and quantum chemical tools. The study was focussed on the use of two ligands bipyrimidine and taphen, analogues of bipyridine and phenanthroline, which are known to induce interesting electronic structure with ytterbium complexes. Bimetallic complexes, *Yb(bpm)Pd* and *Yb(taphen)Pd* have been synthesised and their electronic structure presented a radical delocalised on the π^* system of the neutral ligand with a strong interaction with the ytterbium ion for bipyrimidine and no interaction for taphen. The electronic structure of the radical ligand was evaluated at the CASSCF level of theory and showed significant differences between taphen and bpm: while the latter has a multi-reference character on its π^* orbitals, the former does not. This triggered a difference in reactivity. For bpm, the intermediate $\mathrm{Pd}^{+\mathrm{IV}}$ complex was stable, while for taphen the complex decomposed very easily.

As a result, the design of the ligand determines whether the electron could be used by the palladium moiety for further reactivity. In order to study this influence, the design of the ligand was varied and further quantum chemistry analyses led to the evaluation of different ligands that could be of interest in the synthesis of bimetallic molecules. These ligands among others are under study.

The metal side of the bimetallic complex has also been varied, with platinum or nickel and did not show a strong influence of the metal on the electronic structure of the complex. Reactivity studies are being undertaken, in order to understand the reactivity difference between these complexes, as it has been shown that for bimetallic complexes different reaction mechanisms were characterised for platinum and palladium[18]. Further characterisation of bimetallic molecules bearing a cobalt complex on one side and a lanthanide on the other are also under study, as it has been shown that such complexes present interesting magnetic properties[96].

Finally, the lanthanide electron transfer could be modified by playing on the lanthanide ion at stake: a stronger reducing agent than ytterbium such as samarium and thulium

could increase the electron transfer and further lead to different behaviours for reaction mechanisms, or magnetic properties.

References

[1] H. B. Kagan, *Tetrahedron* **2003**, *59*, 10351–10372.

[2] P. Sehnal, R. J. K. Taylor, I. J. S. Fairlamb, *Chem. Rev.* **2010**, *110*, 824–889.

[3] N. M. Camasso, M. S. Sanford, *Science* **2015**, *347*, 1218–1220.

[4] V. Lyaskovskyy, B. de Bruin, *ACS Catal.* **2012**, *2*, 270–279.

[5] O. R. Luca, R. H. Crabtree, *Chem. Soc. Rev.* **2013**, *42*, 1440–1459.

[6] V. K. K. Praneeth, M. R. Ringenberg, T. R. Ward, *Angew. Chem. Int. Ed. Engl.* **2012**, *51*, 10228–10234.

[7] D. C. Powers, T. Ritter, *Nat. Chem.* **2009**, *1*, 302–309.

[8] Y. Halpin, M. T. Pryce, S. Rau, D. Dini, J. G. Vos, *Dalton Trans.* **2013**, *42*, 16243–16254.

[9] D. L. J. Broere, L. L. Metz, B. de Bruin, J. N. H. Reek, M. A. Siegler, J. I. van der Vlugt, *Angew. Chem. Int. Ed. Engl.* **2015**, *54*, 1516–1520.

[10] J. I. van der Vlugt, *Eur. J. Inorg. Chem.* **2011**, *2012*, 363–375.

[11] S. Bestgen, C. Schoo, C. Zovko, R. Köppe, R. P. Kelly, S. Lebedkin, M. M. Kappes, P. W. Roesky, *Chem. Eur. J.* **2016**, *22*, 7115–7126.

[12] M. N. Hopkinson, B. Sahoo, J.-L. Li, F. Glorius, *Chem. Eur. J.* **2014**, *20*, 3874–3886.

[13] J. C. Tellis, D. N. Primer, G. A. Molander, *Science* **2014**, *345*, 433–436.

[14] D. L. J. Broere, D. K. Modder, E. Blokker, M. A. Siegler, J. I. van der Vlugt, *Angew. Chem. Int. Ed. Engl.* **2016**, *55*, 2406–2410.

[15] A. L. Liberman-Martin, R. G. Bergman, T. D. Tilley, *J. Am. Chem. Soc.* **2013**, *135*, 9612–9615.

[16] A. L. Liberman-Martin, D. S. Levine, W. Liu, R. G. Bergman, T. D. Tilley, *Organometallics* **2016**, *35*, 1064–1069.

[17] J. A. Terrett, J. D. Cuthbertson, V. W. Shurtleff, D. W. C. MacMillan, *Nature* **2015**, *524*, 330–334.

[18] M. G. Pfeffer, B. Schäfer, G. Smolentsev, J. Uhlig, E. Nazarenko, J. Guthmuller, C. Kuhnt, M. Wächtler, B. Dietzek, V. Sundström, S. Rau, *Angew. Chem. Int. Ed. Engl.* **2015**, *54*, 5044–5048.

[19] K. Murata, A. Inagaki, M. Akita, J.-F. Halet, K. Costuas, *Inorg. Chem.* **2013**, *52*, 8030–8039.

[20] M. Braumüller, M. Schulz, D. Sorsche, M. Pfeffer, M. Schaub, J. Popp, B.-W. Park, A. Hagfeldt, B. Dietzek, S. Rau, *Dalton Trans.* **2015**, *44*, 5577–5586.

[21] M. Wächtler, J. Guthmuller, S. Kupfer, M. Maiuri, D. Brida, J. Popp, S. Rau, G. Cerullo, B. Dietzek, *Chem. Eur. J.* **2015**, *21*, 7668–7674.

[22] K. Murata, K. Saito, S. Kikuchi, M. Akita, A. Inagaki, *Chem. Commun.* **2015**, *51*, 5717–5720.

[23] K. Mori, M. Kawashima, H. Yamashita, *Chem. Commun.* **2014**, *50*, 14501–14503.

[24] M. Serratrice, L. Maiore, A. Zucca, S. Stoccoro, I. Landini, E. Mini, L. Massai, G. Ferraro, A. Merlino, L. Messori, M. A. Cinellu, *Dalton Trans.* **2016**, *45*, 579–590.

[25] D. J. Schwartz, G. E. Ball, R. A. Andersen, *J. Am. Chem. Soc.* **1995**, *117*, 6027–6040.

[26] V. Chandrasekhar, J. Goura, J. Brambley, P. Goddard, C. Topping, R. Suriya Narayanan, A. K. Bar, *Dalton Trans.* **2016**, *45*, 9235–9249.

[27] G. Nocton, C. H. Booth, L. Maron, R. A. Andersen, *Organometallics* **2013**, *32*, 5305–5312.

[28] G. Nocton, W. W. Lukens, C. H. Booth, S. S. Rozenel, S. A. Medling, L. Maron, R. A. Andersen, *J. Am. Chem. Soc.* **2014**, *136*, 8626–8641.

[29] G. Nocton, L. Ricard, *Chem. Commun.* **2015**, *51*, 3578–3581.

[30] T. Nagai, H. Tomizawa, K. Sugahara, Y. Takeda, K. Ishida, *J. Mol. Struct.* **1999**, *478*, 211–218.

[31] T. J. King, J. A. H. MacBride, M. Muir, P. M. Wright, *J. Chem. Soc. Chem. Commun.* **1983**, *8*, 425–426.

[32] M. S. Khan, A. Haque, M. K. Al-Suti, P. R. Raithby, *J. Organomet. Chem.* **2015**, *793*, 114–133.

[33] P. K. Byers, A. J. Canty, B. W. Skelton, A. H. White, *J. Chem. Soc. Chem. Commun.* **1986**, *23*, 1722–1724.

[34] M. Lersch, M. Tilset, *Chem. Rev.* **2005**, *105*, 2471–2526.

[35] A. J. Canty, *Dalton Trans.* **2009**, *47*, 10409–10417.

[36] A. J. Canty, *Acc. Chem. Res.* **1992**, *25*, 83–90.

[37] P. K. Byers, A. J. Canty, *J. Chem. Soc. Chem. Commun.* **1988**, *10*, 639–641.

[38] J. M. Racowski, N. D. Ball, M. S. Sanford, *J. Am. Chem. Soc.* **2011**, *133*, 18022–18025.

[39] K. Muñiz, *Angew. Chem. Int. Ed. Engl.* **2009**, *48*, 9412–9423.

[40] A. J. Hickman, M. S. Sanford, *Nature* **2012**, *484*, 177–185.

[41] S. R. Whitfield, M. S. Sanford, *J. Am. Chem. Soc.* **2007**, *129*, 15142–15143.

[42] J. J. Topczewski, M. S. Sanford, *Chem. Sci.* **2014**, *6*, 70–76.

[43] A. R. Mazzotti, M. G. Campbell, P. Tang, J. M. Murphy, T. Ritter, *J. Am. Chem. Soc.* **2013**, *135*, 14012–14015.

[44] L. M. Mirica, J. R. Khusnutdinova, *Coord. Chem. Rev.* **2013**, *257*, 299–314.

[45] Q. Liu, X. Dong, J. Li, J. Xiao, Y. Dong, H. Liu, *ACS Catal.* **2015**, *5*, 6111–6137.

[46] X. Hu, *Chem. Sci.* **2011**, *2*, 1867.

[47] S. Z. Tasker, E. A. Standley, T. F. Jamison, *Nature* **2014**, *509*, 299–309.

[48] B. M. Rosen, K. W. Quasdorf, D. A. Wilson, N. Zhang, A.-M. Resmerita, N. K. Garg, V. Percec, *Chem. Rev.* **2011**, *111*, 1346–1416.

[49] Y. Aihara, N. Chatani, *J. Am. Chem. Soc.* **2014**, *136*, 898–901.

[50] J. R. Bour, N. M. Camasso, M. S. Sanford, *J. Am. Chem. Soc.* **2015**, *137*, 8034–8037.

[51] C. G. Riordan, *Science* **2015**, *347*, 1203–1204.

[52] S. Kanoktanaporn, J. A. H. MacBride, *J. Chem. Soc. Perkin Trans. 1* **1978**, 1126.

[53] T. Cheisson, A. Auffrant, G. Nocton, *Organometallics* **2015**, *34*, 5470–5478.

[54] S. Demir, J. M. Z'arozny, M. Nippe, J. R. Long, *J. Am. Chem. Soc.* **2012**, *134*, 18546–18549.

[55] D. J. Berg, J. M. Boncella, R. A. Andersen, *Organometallics* **2002**, *21*, 4622–4631.

[56] S. G. Fox, R. D. Gillard, *Polyhedron* **1988**, *7*, 349–352.

[57] M. Reiher, O. Salomon, B. Artur Hess, *Theor. Chem. Acc.* **2001**, *107*, 48–55.

[58] M. Swart, M. Gruden, *Acc. Chem. Res.* **2016**, *49*, 2690–2697.

[59] A. Rosa, A. W. Ehlers, E. J. Baerends, *J. Phys. Chem.* **1996**, *100*, 5690–5696.

[60] R. Z. Khaliullin, E. A. Cobar, R. C. Lochan, A. T. Bell, M. Head-Gordon, *J. Phys. Chem. A* **2007**, *111*, 8753–8765.

[61] P. R. Horn, E. J. Sundstrom, T. A. Baker, M. Head-Gordon, *J. Chem. Phys.* **2013**, *138*, 134119.

[62] P. R. Horn, Y. Mao, M. Head-Gordon, *Phys. Chem. Chem. Phys.* **2016**, *18*, 23067–23079.

[63] A. R. E. Mountain, N. Kaltsoyannis, *Dalton Trans.* **2013**, *42*, 13477–13486.

[64] M. Green, *J. Organomet. Chem.* **1995**, *500*, 127–148.

[65] K. Müller, C. Faeh, F. Diederich, *Science* **2007**, *317*, 1881–1886.

[66] T. Furuya, A. S. Kamlet, T. Ritter, *Nature* **2011**, *473*, 470–477.

[67] C. N. Neumann, T. Ritter, *Angew. Chem. Int. Ed. Engl.* **2015**, *54*, 3216–3221.

[68] M. G. Campbell, T. Ritter, *Chem. Rev.* **2015**, *115*, 612–633.

[69] H. Shigehisa, E. Nishi, M. Fujisawa, K. Hiroya, *Org. Lett.* **2013**, *15*, 5158–5161.

[70] M. Rueda-Becerril, O. Mahé, M. Drouin, M. B. Majewski, J. G. West, M. O. Wolf, G. M. Sammis, J.-F. Paquin, *J. Am. Chem. Soc.* **2014**, *136*, 2637–2641.

[71] Q. Shao, Y. Huang, *Chem. Commun.* **2015**, *51*, 6584–6586.

[72] L. An, Y.-L. Xiao, Q.-Q. Min, X. Zhang, *Angew. Chem. Int. Ed. Engl.* **2015**, *54*, 9079–9083.

[73] Z. Yuan, H.-Y. Wang, X. Mu, P. Chen, Y.-L. Guo, G. Liu, *J. Am. Chem. Soc.* **2015**, *137*, 2468–2471.

[74] K. L. Hull, W. Q. Anani, M. S. Sanford, *J. Am. Chem. Soc.* **2006**, *128*, 7134–7135.

[75] M. Ahrens, G. Scholz, T. Braun, E. Kemnitz, *Angew. Chem. Int. Ed. Engl.* **2013**, *52*, 5328–5332.

[76] S. Enthaler, *Angew. Chem. Int. Ed. Engl.* **2014**, *53*, 2716–2721.

[77] C. J. Burns, R. Andersen, *J. Chem. Soc. Chem. Commun.* **1989**, 136–137.

[78] M. L. Cole, G. B. Deacon, P. C. Junk, K. Konstas, *Chem. Commun.* **2005**, 1581–1583.

[79] Z. Xie, Z. Liu, F. Xue, T. C. Mak, *J. Organomet. Chem.* **1996**, *539*, 127–130.

[80] T. Birk, K. S. Pedersen, C. A. Thuesen, T. Weyhermüller, M. Schau-Magnussen, S. Piligkos, H. Weihe, S. Mossin, M. Evangelisti, J. Bendix, *Inorg. Chem.* **2012**, *51*, 5435–5443.

[81] S. Labouille, C. Clavaguéra, F. Nief, *Organometallics* **2013**, *32*, 1265–1271.

[82] M. D. Walter, C. J. Burns, P. T. Matsunaga, M. E. Smith, R. A. Andersen, *Organometallics* **2016**, *35*, 3288–3497.

[83] C. H. Booth, M. D. Walter, D. Kazhdan, Y.-J. Hu, W. W. Lukens, E. D. Bauer, L. Maron, O. Eisenstein, R. A. Andersen, *J. Am. Chem. Soc.* **2009**, *131*, 6480–6491.

[84] V. Goudy, A. Jaoul, M. Cordier, C. Clavaguéra, G. Nocton, *J. Am. Chem. Soc.* **2017**, *139*, 10633–10636.

[85] C. H. Booth, D. Kazhdan, E. L. Werkema, M. D. Walter, W. W. Lukens, E. D. Bauer, Y.-J. Hu, L. Maron, O. Eisenstein, M. Head-Gordon, R. A. Andersen, *J. Am. Chem. Soc.* **2010**, *132*, 17537–17549.

[86] I. M. Pendleton, M. H. Pérez-Temprano, M. S. Sanford, P. M. Zimmerman, *J. Am. Chem. Soc.* **2016**, *138*, 6049–6060.

[87] D. M. Crumpton-Bregel, K. I. Goldberg, *J. Am. Chem. Soc.* **2003**, *125*, 9442–9456.

[88] C. Duecker-Benfer, R. van Eldik, A. J. Canty, *Organometallics* **1994**, *13*, 2412–2414.

[89] P. K. Byers, A. J. Canty, M. Crespo, R. J. Puddephatt, *Organometallics* **1988**, *7*, 1363–1367.

[90] T. Furuya, D. Benitez, E. Tkatchouk, A. E. Strom, P. Tang, W. A. Goddard III, T. Ritter, *J. Am. Chem. Soc.* **2010**, *132*, 3793–3807.

[91] K. H. Marti, M. Reiher, *Phys. Chem. Chem. Phys.* **2011**, *13*, 6750–6759.

[92] F. da Silva Miranda, A. M. Signori, J. Vicente, B. de Souza, J. P. Priebe, B. Szpoganicz, N. S. Gonçalves, A. Neves, *Tetrahedron* **2008**, *64*, 5410–5415.

[93] M. Haga, M. Ishizuya, T. Kanesugi, T. Yutaka, D. Sakiyama, J. Fees, W. Kaim, *Indian Journal of Chemistry* **2003**, *42A*, 2290–2299.

[94] M. G. Medvedev, I. S. Bushmarinov, J. Sun, J. P. Perdew, K. A. Lyssenko, *Science* **2017**, *355*, 49–52.

[95] S. Maekawa, K. Moorthi, *J. Chem. Eng. Data* **2014**, *59*, 3160–3166.

[96] J. W. Sharples, D. Collison, *Coord. Chem. Rev.* **2014**, *260*, 1–20.

If we ever reach the point where we think we thoroughly understand who we are and where we came from, we will have failed.

— Carl Sagan *The varieties of scientific experience*

General conclusion

Lanthanide molecules have a vast electron transfer reactivity. Both divalent samarium and ytterbium are capable of transferring one electron to organic or organometallic molecules. While divalent samarium triggers radical reactions that have been used for decades, divalent ytterbium stabilises intermediate mixed-valent compounds with an electronic structure accounting for a reduced and a neutral ligand (two different configurations for the ytterbium ion: $4f^{13}$ and $4f^{14}$).

N-heterocycles present the advantage of being able to store electrons inside their π aromatic systems. However, the electronic structure of radical N-hetero-aromatics is still poorly understood. Phenanthroline radical for instance has a multi-configurational ground state, involving its lone pair and its π^* orbitals. While this does not pose problem to understand the reactivity of this compound with lanthanide complexes, it raises the question whether theoretical calculations can be of use to understand lanthanide complexes bearing phenanthroline radical.

Phenanthroline complexes of samarium are known to be in equilibrium between their monomeric radical and their σ-dimeric forms. Contrary to what was expected from the electronic structure of phenanthroline radical, there was no significant difference between CASSCF and DFT methods for the monomer. On the contrary, the electronic structure of the dimer was poorly evaluated at the DFT level and only led to spin contamination from the biradicaloid species. This spin contamination was related to the HF-exchange percentage: only at low HF-exchange percentage spin contamination is found. This can be related to the 4f orbitals population that is evolving depending on the HF-exchange percentage. The UV-visible spectrum of the equilibrium between the radical monomer and the σ-dimer showed peaks corresponding to phenanthroline radical. As a result, TDDFT and EOM-CCSD calculations were performed but did not match the experimental UV-visible spectrum. Indeed, the presence of a multi-configurational ground state prevents both types

of calculation from being accurate and only CASSCF calculations were able to reproduce the experimental UV-visible spectrum. Spin contamination in the evaluation of the σ-dimer and the electronic structure of phenanthroline radical questions the formation of a σ-dimer in the solid state for packing reasons, as the π dimer could also be present in solution. This type of equilibrium between a σ-dimer, a π dimer and a radical monomer could lead to a better understanding of radical reactions and, by design, to covalent bonds themselves. This is currently being investigated using EPR analyses.

While N-heterocycles present several low-lying states, benzophenone only presents one. Upon addition of a reducing agent such as SmI_2, benzophenone can be reduced to the ketyl radical which can dimerise and form a pinacol complex. This coupling reaction was investigated using experimental and theoretical analyses. The stability of the radical species was dependent on the solvent as in thf and acetonitrile only the dimeric form is stable while in pyridine the monomeric ketyl radical was characterised. Quantum chemical data was able to distinguish thf and pyridine but there was a strong dependance on the density functional for the evaluation of ΔG.

These two samarium complexes bearing radical ligands were reacted with persistent radical such as tempo or with N-heteroaromatic molecules. The reaction with tempo either with the benzophenone ketyl or the phenanthroline radicals leads to the separation of a neutral benzophenone or phenanthroline and coordination of a tempo anion on the samarium ion. The reaction mechanism for phenanthroline complexes of samarium was investigated at the DFT and CASSCF levels of theory and showed that the electron transfer happens step-wise: tempo first coordinates on the lanthanide center, and this ion serves as a bridge for transferring the electron from phenanthroline to tempo. After addition of another equivalent of tempo on $Cp^*_2Sm(tempo)$, tempo coordinates to the lanthanide ion which promotes the departure of a Cp^* radical molecule. Contrary to $Cp^*_2Sm(tempo)$, $Cp^{ttt}_2Sm(tempo)$ does not promote such departure, probably due to the sterical crowding surrounding the lanthanide ion. The reaction with N-heterocycles was studied using the ketyl radical complex. A selective Minisci coupling was observed and has been studied using UV-visible spectra and quantum chemical analyses. While the mechanism is still not entirely known and is still being investigated, the final molecule synthesised could be of high interest as a ligand in the

field of lanthanide chemistry. Its use in this specific field is under study in our group and has led to a collaboration with the group of Camp (CPE Lyon).

N-heterocycles present also other advantages, as they can serve as electronic bridges between several molecular edifices. They can be used in the design of multi-metallic molecules involving on one side a divalent lanthanide ion and on the other a TM catalyst. The molecule thus created could be used as an advanced catalyst, where the TM center could be assisted by the radical ligand itself.

Such design was investigated using ytterbium as the lanthanide and palladium as the TM. Two ligands were chosen for their close vicinity with bipyridine and phenanthroline: bipyrimidine and taphen. The two molecules synthesised were able to stabilise differently Pd^{IV} intermediates and the relationship between this stabilisation and the molecular orbitals of the radical ligands was discussed. Indeed, bipyrimidine radical has one low lying state that interferes during the reductive elimination and stabilises further the Pd^{IV} intermediate. The study on the ligand design was initiated using bigger π system such as dppz, and a different coordination mode to the palladium center with Ind. Based on these results, the design of the ligand was further evaluated using DFT methods and it was possible to propose new designs for bridging N-heteroaromatic ligands. Our group is currently trying to isolate bimolecular edifices bearing N-heterocycles with other metal than palladium such as nickel, platinum and cobalt, and several N-heteroarenes are considered as the bridging ligands. The development of new N-heterocycles is also being investigated in collaboration with the group of Gosmini and Danoun (Ecole Polytechnique (Palaiseau)).

Despite these important results, this study was faced with numerous challenges. On the experimental side, it is difficult to characterise completely lanthanide complexes. First of all, divalent lanthanide complexes are reactive towards oxidants such as O_2, and good care is necessary to isolate any complex presenting such a motif. The use of pure samples for further analysis is of crucial importance in order to measure correctly the magnetic or EPR behaviour. The paramagnetism induced by the lanthanide ion can also be responsible of broads and unusable ^1H NMR as it was the case, for instance, with benzophenone complexes of SmI_2 and for the analysis of the Minisci reaction with SmI_2. In these cases the use of other analyses such as UV-visible is necessary but gives, sometimes, less information than

a ^{1}H NMR. In addition, the oxidation state of the lanthanide centre is not always obvious and its analysis require the use of several techniques such as EPR, magnetism and UV-visible experiments. Finally, divalent lanthanide molecules have not been fully characterised, and it is still difficult to know experimentally if the lanthanide electronic configuration is $4f^{n}$ or $4f^{n-1}5d^{1}$. Progress are being made in this specific area with the research performed by our group in collaboration with the groups of Le Guennic (Université de Rennes), Maury (ENS Lyon) and Duboc (Université Joseph Fourrier (Grenoble)).

On the theoretical side, quantum chemical calculation depends on the method chosen and the approximations considered. This manuscript showed how all-electron relativistic calculations (using either ZORA or DKH2 hamiltonians) can be used in a systematic way to treat lanthanide. However, it could be of interest to evaluate the difference of these calculations with the more accurate X2C model. Calculations at the DFT level have been evaluated in Chapter 2 and compared with experiments. It has been shown that the density functional had a large influence on the expected results. This difference is difficult to analyse globally, and has to be seen as a case by case scenario. It is notable however to see that increasing the HF-exchange is increasing the 5d population for examples detailed in Chapter 2. In this context, the use of *ab initio* calculations such as OO-MP2, CCVB or DLPNO-CCSD as routine standards could lead to significant improvement for these calculations. This is currently under study in collaboration with the group of Head-Gordon (UC Berkeley). The degeneracy of the 4f orbitals or the electronic structure of radical N-hetero-aromatics is also not treated exactly by DFT. CASSCF can be used to study the electronic structure of lanthanide bearing radical N-hetero-aromatics ligands but the limitations of CASSCF, *i.e.* the small number of orbitals to include in the active space, restrain the electronic structure to a set of orbitals. If this set of orbitals are not chosen properly, this could lead to erroneous results. That is why, in this study, CASSCF calculations were compared to experimental data when available. Additionally, the inclusion of dynamic correlation through the use of CASPT2 or NEVPT2 methods is not always easy, as for all-electron lanthanide calculations, this can rise the memory demand of the calculation. Current development such as DMRG can improve the accuracy of quantum chemistry calculations with lanthanide complexes

and lead to better electronic structure evaluations. A collaboration with M. Reiher (ETH Zurich) is currently being established to perform these calculations.

In conclusion, the reduction processes that occur in lanthanide chemistry are rich and are still poorly understood. This manuscript, far from being exhaustive, detailed the use and the performance of combined experimental and theoretical work in order to understand, evaluate and improve electron transfer using lanthanide complexes. It is our understanding that new developments in this field will pass through their combined use. The numerous collaborations developed throughout this study will improve the understanding and the theoretical treatments of lanthanide complexes.

Small molecules such as carbon dioxyde or methane can be activated using selective reducing agents. Recycling these molecules is of crucial interest for the world as they are partly responsible for the global warming. During this thesis, several reactions were conducted between SmI_2 and carbon dioxyde. While the reduction of carbon dioxyde occurs, it was difficult to analyse the resulting products. The use of SmI_2 in carbon dioxyde reactions could lead to an expansion of lanthanide use in an industrial context and further improve the existing industrial processes.

Appendices

A

Experimental section

General considerations

All reactions were performed using standard Schlenk-line techniques or in a dry-box ($O_2 <$ 0.1 ppm, $H_2O <$ 0.1 ppm). All glassware was dried at 130°C for at least 12 h prior to use. Toluene, pentane, diethyl ether, thf, and pyridine were dried over sodium. Toluene-d8 was dried over sodium while thf-d8 was dried and stored over molecular sieves. Acetonitrile and CD_3CN were dried over CaH_2 and distilled prior to use. All the solvents were degassed prior to use.

^{1}H NMR spectra were recorded on Bruker Advance III-300 MHz. ^{1}H chemical shifts are in δ units relative to TMS. Magnetic susceptibility measurements were made for all samples at 0.5, and 20 kOe in a 7 T Cryogenic SX600 SQUID magnetometer. Diamagnetic corrections were made using Pascals constants.

The electrochemical experiments were performed using a VERSATAT potentiostat/galvanostat electrode cell using a carbon disk as working electrode, a Ag gauze as the counter electrode, and a reference electrode. Measurements were made with a concentration of about 3 mM. Tetrabutylammonium tetrafluoroborate salt served as electrolyte (concentration 0.12 M).

UV-visible spectra were recorded in 300-1000 nm range at room temperature on an Agilent Cary 60 Spectrometer in 1 or 10 mm quartz cuvettes with solvent background correction.

Single crystals were mounted on a Kapton loop using a Paratone N oil. An APEX II CCD BRUKER detector and a graphite Mo-KÎ± monochromator were used for the data acquisition. All measurements were done at 150 K and a refinement method was used for solving the structure. The structure resolution was accomplished using the SHELXT-2014[1] program and the refinement was done with the SHELXL-2014[2] program. The structure solution and the refinement were achieved with the PLATON software[9]. Finally, pictures of the compound structure were obtained using the Ortep-III software[3]. During the refinement steps, all atoms – except hydrogens – were refined anisotropically. The position of the hydrogens was determined using residual electronic densities which are calculated by a Fourier difference. Finally, in order to obtain a complete refinement, a weighting step followed by multiples loops of refinement was done.

Chapter 2

The benzophenone (bph), phenanthroline (phen), and chalcone ligands were bought from Sigma-Aldrich and sublimed before use.

$(\mathbf{I_2Sm(bph)(thf)_3)_2}$: Thf was added at room temperature to a mixture of bph (22.5 mg, 0.12 mmol) and SmI_2 (50 mg, 0.12 mmol). The solution was stirred for a couple of hours and a fine precipitate started to form. The solution was filtrated and put at -40°C overnight. Pale yellow crystals were isolated and were suitable for X-Ray diffraction studies. Elemental analyses were performed on the crystals but came back twice with problematic results, that could account for a decomposition of the product during travel.

$(\mathbf{ISm(bph)_2(MeCN))_2}$: Acetonitrile was added at room temperature to a mixture of bph (22.5 mg, 0.12 mmol) and SmI_2 (50 mg, 0.12 mmol). The solution was stirred for a couple of hours and turned from green to yellow. Pale yellow crystals were isolated at room temperature and were suitable for X-Ray diffraction studies.

$(\mathbf{I_2Sm(chalcone)(thf)_3)_2}$: Thf was added at room temperature to a mixture of chalcone

(14 mg, 7 mmol) and SmI_2 (30 mg, 0.07 mmol). The solution was stirred for a couple of hours and the solution was put at -40°C overnight. Pale yellow crystals were isolated and were suitable for X-Ray diffraction studies.

Chapter 3

The tempo molecule was bought from Sigma-Aldrich and sublimed before use. $Cp^*_2Sm(OEt_2)$[4], Cp^{ttt}_2Sm[5], $Cp^*_2Sm(phen)$ and $Cp^{ttt}_2Sm(phen)$[6] were synthesised according to existing procedures.

Reaction between one equivalent of Cp^*_2Sm and tempo: Toluene was added to a mixture of one equivalent of tempo (13 mg, 8 mmol) and one equivalent of $Cp^*_2Sm(OEt_2)$ (40 mg, 9 mmol). The solution was stirred for a couple of hours at room temperature. The resulting orange-yellow solution was put at -40°C, and yellow blocks of $(Smtempo_3)_2$ were isolated and were suitable for X-Ray diffraction analysis and corresponded to the structure already available in the litterature[7]. Addition of another equivalent of tempo (13 mg, 8 mmol) to the orange yellow solution triggered the precipitation of a fine yellow power that was analysed as $(Smtempo_3)_2$ by X-Ray diffraction analysis.

$Cp^{ttt}_2Sm(tempo)$: Toluene was added to a mixture of one equivalent of tempo (10 mg, 0.06 mmol) and one equivalent of Cp^{ttt}_2Sm (40 mg, 0.06 mmol). The solution was stirred for a couple of hours at room temperature. The resulting red solution was put at -40°C, and red plate crystals were isolated and suitable for X-Ray diffraction experiments.
^1H NMR (δ, 295K, Tol-d8): 23.70 (s, 1H, $Cp^{ttt}-H$), 21.08 (s, 1H, Cp^{ttt}), 4.92 (s, 6H, tempo), 3.35 (s, 1H, tempo), 3.08 (s, 1H, tempo), 2.92 (s, 1H, tempo), 2.33 (s, 18H, Cp^{ttt}), 0.61 (s, 6H, tempo), 0.25 (s, 18H, Cp^{ttt}), -8.42 (s, 18H, Cp^{ttt})

$Cp^*Sm(tempo)_2(phen)$: Toluene was added to a mixture of tempo (19 mg, 12 mmol) and $Cp^*_2Sm(phen)$ (24 mg, 0.04 mmol). The solution turned deep red and crystals were

isolated and suitable for X-Ray diffraction experiments.
^{1}H NMR (δ, 295K, Tol-d8): 9.08 (s, free phen), 8.75 (s, 2H, phen), 8.31 (s, free phen), 7.84 (s, 2H, phen), 7.63 (s, free phen), 6.92 (s, 2H, phen), 2.47 (s, 12H, tempo), 0.44 (s, 15H, Cp*), -2.57 (s, 12H, tempo)

I_2Sm(tempo): Thf was added to a mixture of tempo (9 mg, 0.06 mmol) and $(I_2Sm(bph)(thf)_3)_2$ (31 mg, 0.03 mmol). The solution turned deep red and crystals were isolated and suitable for X-Ray diffraction experiments.

I_2Sm(phenO)$(MeCN)_3$: Phenanthroline (9.0 mg, 0.05 mmol) was added to a solution of SmI_2 (20 mg, 0.05 mmol) and benzophenone (9.1 mg, 0.05 mmol) in pyridine. The solution turned from black purple to yellow after a few minutes stirring at room temperature. A layer of pentane was added on top of the pyridine solution, and yellow block crystals were extracted but were not suitable for X-Ray diffraction experiments. After removal of the solvent, the solution was placed in acetonitrile. After a few days at - 40^{o}C yellow block crystals were isolated and were suitable for X-Ray diffraction experiments.
Anal. Calculated for $C_{41}H_{31}N_6O_1I_2Sm_1$: C, 47.91; H, 3.04; N, 8.18. Found : C, 48.23; H, 3.28; N, 5.76.

Minisci reaction between benzophenone and phenanthroline with SmI_2: Acetonitrile was added to a mixture of benzophenone (225 mg, 1.24 mmol), phenanthroline (223 mg, 1.24 mmol) and SmI_2 (500 mg, 1.24 mmol). The solution turned rapidly red. After 10 hours stirring at room temperature, the yellow solution was put under reduced pressure in order to remove the solvent. Then, a 0.1 M HCl solution was put on the residual solid, and an extraction was performed with dichloromethane. The organic phase was washed with water until the washing were no longer acid, and was finally dried with $MgSO_4$. The solvent was removed and the compound was gathered as a yellow powder (33 % yield). Recrystallisation of the powder in EtOH gave colourless yellow crystals suitable for X-Ray diffraction analysis.
^{1}H NMR (δ, 295K, $CDCl_3$): 9.05 (s, 1H), 8.13 (d, 1H), 8.04 (d, 1H), 7.51 (m, 1H), 7.40 (d, 1H), 7.33 (s, 1H), 7.26 (m, 4H), 7.14 (m, 6H), 5.16 (s, 1H)

Kinetic study in acetonitrile: The initial concentration of each reagent in the previous reaction was varied from 2.5 to 7.4 mmol/L. The same procedure was also used for SmI_2 varying its initial concentration from 2.5 to 5 mmol/L while the concentration of benzophenone and phenanthroline was not varied (4 mmol/L). The decomposition of the red intermediate (560 nm) was followed by UV-visible spectroscopy from the time the reaction was launched to at least 3 times the half-life of this intermediate. The decomposition led to a decrease in the peak corresponding to the intermediate at 560 nm. This decrease was fitted with exponentials using Datagraph[8], and the half-life of the intermediate was then obtained.

Chapter 4

The bipyrimidine, a gift from Pr. Richard Andersen (UC Berkeley), was sublimed, and used as it was once sublimed. The 4,5,9,10-tetraazaphenanthrene (taphen)[9], dipyrido[3,2-a:2',3'-c]phenazine (dppz)[10], and 2-(2-pyrimidyl)benzimidazolate (Ind)[11] ligand, the $(tmeda)PdMe_2$[12], and $Cp^*_2Yb(OEt_2)$[13] complexes were synthesised according to published procedures. $(taphen)PdCl_2$ was synthesised following one procedure for similar complexes[14].

$\mathbf{Cp^*_2Yb(taphen)YbCp^*_2}$, *Yb(taphen)Yb*: Toluene was added to a mixture of $YbCp^*_2(OEt_2)$ and taphen. After stirring a few hours at room temperature the dark purple solution was put in the freezer at -40°C. Dark purple crystal were isolated and were suitable for X-Ray diffraction studies.
^{1}H NMR (δ, 295K, thf-d8): 259.86 (s, 1H, taphen) 91.82 (2H, s, taphen) 58.96 (3H, s, taphen) 4.72 (30H, s, Cp*) 4.85 (30H, s, Cp*)

$\mathbf{(taphen)PdMe_2}$: Thf was added at room temperature to a mixture of $(tmeda)PdMe_2$ (83 mg, 0.30 mmol) and taphen (60 mg, 0.30 mmol) at room temperature. After stirring for a couple of hours, the stirring is stopped and the reaction mixture is let stand overnight. The

resulting red needles are isolated, washed with pentane with 85 % yield (81 mg, 0.26 mmol). Anal. Calculated for $C_{12}H_{12}N_4Pd$: C, 45.23; H, 3.80; N, 17.58. Found : C, 45.13; H, 3.64; N, 17.38.

$Cp^*_2Yb(taphen)PdMe_2(toluene)$, *Yb(taphen)Pd*: Toluene was added at room temperature to a mixture of the red crystals of $(taphen)PdMe_2$ (70 mg, 0.22 mmol, 1 eq) and the green crystals of $Cp^*_2Yb(OEt_2)$ (114 mg, 0.22 mmol, 1 eq). After stirring for several hours, the stirring is stopped and the purple reaction mixture is let stand overnight at -40°C. After one night, dark purple needles were isolated with 48 % yield (90 mg, 0.11 mmol).
^{1}H NMR (δ, 295K, thf-d8): 73.87 (s, 2H, taphen), 13.44 (s, 30H, Cp*), -8.46 (s, 6H, Pd-CH3), -135.13 (s, 2H, taphen), -295.69 (s, 2H, taphen)
Anal. Calculated for $C_{32}H_{42}N_4PdYb$: C, 50.42; H, 5.56; N, 7.35. Found : C, 50.59; H, 5.15; N, 8.45.

$Cp^*_2Yb(taphen)PdMe_3I$, *Yb(taphen)PdMeI*: Pentane was added at room temperature to 1 equivalent of $Cp^*_2Yb(taphen)PdMe_2(toluene)$. MeI (excess) in cold acetone was then added to the solution, and the resulting dark solution was stirred for several minutes before being cooled at -40°C. Black needles were isolated and were analysed by X-Ray diffraction analysis. The fast decomposition of this compound in toluene-d8 did not allow a ^{1}H NMR characterisation but led to red crystals of 7 that were suitable for X-Ray Diffraction analysis.

$Cp^*_2YbMe_2PdtaphenYbCp^*_2$, *Yb(taphen)PdYb*: Toluene was added over a mixture of the black crystals of **3** and $YbCp^*_2(OEt_2)_2$ at room temperature. The mixture turned rapidly dark purple, and the compound was isolated by recrystallisation in toluene/pentane at -40°C to yield black needle crystals (55 % yield) that were suitable for X-Ray diffraction analysis.
Elemental analyses were performed twice on the crystals but the resulting values were not in agreement with the calculated ones, probably due to the decomposition of the sample upon travel.

$Cp^*_2YbMe_2Pd(tmeda)$: Toluene was added at room temperature to a mixture of $(tmeda)PdMe_2$ (20 mg, 0.08 mmol) and the green crystals of $Cp^*_2Yb(OEt_2)$ (60 mg, 0.08 mmol). After stirring for several hours, the stirring is stopped and the purple reaction mixture is let stand overnight at -40°C. After one night, blue block crystals were isolated.

$(bpm)PdMe_2$: thf was added to a mixture of $(tmeda)PdMe_2$ (120 mg, 0.47 mmol, 1 eq) and bipyrimidine (62 mg, 0.40 mmol, 1.2 eq) at room temperature. After stirring for a couple of hours, the stirring is stopped and the red reaction mixture is let still overnight. The resulting red needles are isolated, washed with pentane with 68 % yield.
Anal. Calculated for $C_{10}H_{12}N_4Pd$: C, 40.76; H, 4.10; N, 19.01. Found : C, 40.93; H, 4.18; N, 18.80.

$Cp^*_2Yb(bpm)PdMe_2(toluene)$, *Yb(bpm)Pd*: A cold solution of the green crystals of $Cp^*_2Yb(OEt_2)$ (37 mg, 0.07 mmol, 1 eq) in toluene was added to a cold solution of the red needles of $(bpm)PdMe_2$ (21 mg, 0.07 mmol, 1 eq). The resulting brown reaction mixture is let still overnight at -40°C. After one night, dark brown blocks were isolated with 69 % yield.
^{1}H NMR (δ, 295K, Tol-d8): 256.32 (s, 2H, bpm), 6.03 (s, 6H, Pd-CH3), 5.91 (s, 30H, Cp*), -3.97 (s, 2H, bpm), -159.39 (s, 2H, bpm).
Anal. Calculated for $C_{30}H_{42}N_4PdYb$: C, 48.81; H, 5.73; N, 7.59. Found : C, 46.98; H, 5.73; N, 4.72.

$Cp^*_2Yb(bpm)PdMe_3I$, *Yb(bpm)PdMeI*: Toluene was added at room temperature to 1 equivalent of $Cp^*_2Yb(bpm)PdMe_2(toluene)$. MeI (1 eq) was added to the cold solution and then let at -40°C. Brown needles were isolated.
^{1}H NMR (δ, 295K, Tol-d8): 264.52 (s, 2H, bpm), 6.34 (s, 15H, Cp*), 5.99 (s, 15H, Cp*), 4.70 (s, 2H, bpm), -0.82 (s, 6H, Pd-CH3), -11.55 (s, 3H, Pd-CH3), -168.40 (s, 2H, bpm).
Anal. Calculated for $C_{31}H_{45}N_4IPdYb + 0.5(C_7H_8)$: C, 44.74; H, 5.33; N,6.05. Found : C, 45.02; H, 4.28; N, 6.05.

$(\mathbf{Cp^*_2Yb})_\mathbf{2}(\mathbf{dppz})\mathbf{PdMe_2}$, *Yb(dppz)Pd*: Toluene was added at room temperature to a mixture of $\mathrm{Me_2Pddppz}$ (34mg, 0.08 mmol) (orange/red solid) and $\mathrm{YbCp^*_2(OEt_2)_2}$ (84 mg, 0.16 mmol). The resulting black/brown mixture was stirred for a few hours and let stand overnight at -40°C. Small black needles were isolated and were suitable for X-Ray diffraction studies. Elemental analyses were performed twice on the crystals but the resulting values were not in agreement with the calculated ones, probably due to the decomposition of the sample upon travel.

^{1}H NMR (δ, 295K, Tol-d8): 196.15 (s, 2H, dppz), 129.21 (s, 2H, dppz), 36.59 (s, 2H, dppz), 14.74 (bs, 6H, $\mathrm{PdMe_2}$), 11.60 (s, 2H, dppz), -1.32 (bs, 60H, $\mathrm{YbCp^*}$).

$(\mathbf{Ind})\mathbf{PdMe_2}$: Acetonitrile was added to a mixture of the Ind-H ligand (15 mg, 0.08 mmol) and $(\mathrm{tmeda})\mathrm{PdMe_2}$ (20 mg, 0.08 mmol). After stirring over 12 hours, the resulting pale powder was gathered, and dried. Crystallisation in a pyridine and pentane mixture led to yellow block crystals that were suitable for X-Ray diffraction analysis.

References

[1] G. M. Sheldrick, *Acta Cryst.* **2015**, *A71*, 3–8.

[2] G. Sheldrick, *Acta Cryst.* **2015**, *C71*, 3–8.

[3] L. J. Farrugia, *J. Appl. Cryst.* **2012**, *45*, 849–854.

[4] D. J. Berg, C. J. Burns, R. A. Andersen, A. Zalkin, *Organometallics* **1989**, *8*, 1865–1870.

[5] G. Nocton, L. Ricard, *Dalton Trans.* **2014**, *43*, 4380–4387.

[6] G. Nocton, L. Ricard, *Chem. Commun.* **2015**, *51*, 3578–3581.

[7] W. J. Evans, J. M. Perotti, R. J. Doedens, J. W. Ziller, *Chem. Commun.* **2001**, 2326–2327.

[8] I. Visual Data Tools, Datagraph, **2017**.

[9] R. Nasielski-Hinkens, M. Benedek-Vamos, *J. Chem. Soc. Perkin Trans. 1* **1975**, 1229–1229.

[10] J. E. Dickeson, L. A. Summers, *Aust. J. Chem.* **1970**, *23*, 1023–1027.

[11] M. Haga, M. Ishizuya, T. Kanesugi, T. Yutaka, D. Sakiyama, J. Fees, W. Kaim, *Indian Journal of Chemistry* **2003**, *42A*, 2290–2299.

[12] W. De Graaf, J. Boersma, W. Smeets, A. L. Spek, *Organometallics* **1989**, 2907–2917.

[13] T. D. Tilley, R. A. Andersen, B. Spencer, H. Ruben, A. Zalkin, D. H. Templeton, *Inorg. Chem.* **1980**, *19*, 2999–3003.

[14] K. Ha, *Zeitschrift für Kristallographie - New Crystal Structures* **2013**, *228*, 365–366.

Abstract

Ce travail de thèse s'est intéressé aux transferts d'électron dans des complexes de lanthanide. Les lanthanides ont la capacité dans leur degré d'oxydation II de pouvoir transférer sélectivement un électron à une molécule organique. Ce type de réaction a été décrite par le passé pour des complexes faisant intervenir un ytterbium et des ligands de type bipyridine et phénanthroline. Le but de cette étude est de comprendre les transferts d'électrons dans ces molécules, en caractérisant la molécule $Cp^*_2Sm(phen)$ et en la faisant réagir avec un radical organique. Ce type de réactivité donnera lieu à un transfert d'électron qui sera par la suite utilisé pour transférer des électrons à des métaux de transition.

Dans le premier chapitre, la trame du manuscrit est installée, et les différentes méthodes théoriques sont mises en avant. Les lanthanides sont des éléments lourds ce qui signifie que les effets relativistes sont importants pour ces composés. Aussi, différentes méthodes doivent être utilisées pour tenir compte de ces effets : un RECP ou des hamiltoniens relativistes du type ZORA ou DKH2. De plus, les méthodes de type DFT ont été utilisées depuis plus de 20 ans pour comprendre le fonctionnement de complexes de lanthanide. Cependant, les orbitales 4f des lanthanides sont dégénérées, ce qui signifie que la DFT ne décrit pas correctement la structure électronique du lanthanide et que des méthodes de type CASSCF sont nécessaires pour arriver à l'élucider. Ce type de problématique est intégré à deux exemples, détaillés dans ce premier chapitre. Dans le cas de la tétraméthylbiphosphinine, le samarium peut réduire le ligand alors que dans le cas de l'ytterbium le ligand n'est pas réduit. Cette différence a été analysée par DFT et CASSCF et il a été montré que l'on pouvait relier cette modulation à un changement d'énergie orbitalaire entre l'ion lanthanide et le ligand. Le deuxième exemple a traité de complexes de lutécium et d'ytterbium méthyle. Contrairement au complexe de lutécium celui d'ytterbium ne peut activer le méthane. Des calculs CASSCF ont permis de montrer que dans le cas de l'ytterbium, le méthyl n'était pas un anion mais un radical et que l'ytterbium ne réduisait pas le méthane. Ce type de structure électronique, très différente de celle obtenue par des méthodes de type DFT, permet de mieux comprendre le fonctionnement de ce composé.

Dans le deuxième chapitre, une étude théorique est décrite concernant le complexe de $Cp^*_2Sm(phen)$. Une analyse comparative de différentes fonctionnelles de la densité a été fait et comparé aux résultats expérimentaux de dimérisation du composé. Cette étude a permis de montrer une forte corrélation entre la contamination de spin, le pourcentage d'échange HF et les comparaisons énergétiques avec l'expérience. Ces résultats ont permis

de mettre en évidence que dans le cas de fonctionnelle à haut pourcentage d'échange HF, les résultats théoriques étaient proche de l'expérience. De plus, des comparaisons entre les spectres expérimentaux UV-visible et les spectres d'absorption théoriques ont été réalisées en utilisant une variété de fonctionnelles de la densité (TDDFT) et de méthodes ab initio. Ces deux types de méthodes ne permettent pas d'avoir des résultats théoriques proches de l'expérience. Cependant, l'utilisation de méthodes du type CASSCF permet de rétablir une correspondance entre spectre expérimental et spectre simulé. Cela indique que la structure électronique de l'état fondamental de la phénanthroline radical est multiconfigurationnel. Ces résultats ont été ensuite appliqués à la simulation de l'équilibre entre la benzophénone radical et la benzophénone dimérique.

Dans le chapitre 3, les informations recueillies dans le chapitre 2 pour la structure électronique du complexe de samarium phénanthroline radical ont été utilisées afin de tester la réactivité de ce composé vis à vis du radical tempo. La réactivité du complexe de samarium a montré un transfert d'électron de la phénanthroline radical vers le tempo radical grâce à un mécanisme à l'intérieur de la sphère de coordination du samarium. Des réactions de type "réactions induites stériquement" ont été démontrées et étudiées en utilisant la DFT et les techniques de type CASSCF. Finalement, les complexes de samarium benzophénone radical ont été réagi avec de la phénanthroline et de nouveaux types de couplage entre la benzophénone et la phénanthroline ont pu être découverts, notamment grâce à une activation C-H.

Dans le chapitre 4, le transfert d'électron découvert dans le chapitre 3 a été utilisé pour transférer un électron jusqu'à un métal de transition. De nouveaux types de molécules bimétalliques ont été synthétisés et caractérisés en utilisant l'outil théorique et expérimental. La réactivité de deux complexes bimétalliques a été comparée, et a montré que selon le ligand transférant l'électron au métal de transition, la stabilisation d'état d'oxydation métastable n'était pas aussi facile. Finalement, de nouveaux ligands ont été proposés, certains permettant de stocker plus d'un électron sur le cycle aromatique. Ces ligands sont actuellement en cours d'étude. De plus, une étude théorique prédictive a été réalisée pour analyser une petite quantité de ligand. Cette étude a permis de proposer certains ligands avec un fort potentiel de transfert d'électron sur le métal de transition.

En conclusion, cette étude a pu montrer que les transferts d'électron dans des complexes de lanthanide peuvent donner des informations quant à la structure électronique de ligands N-hétérocycliques aromatiques. L'électron stocké sur ces ligands peut être utilisé et transféré sur d'autres molécules comme tempo ou des complexes organométalliques. De multiples études sont en cours afin d'améliorer les processus découverts et afin d'en comprendre les rouages.

université PARIS-SACLAY
ÉCOLE DOCTORALE
Sciences chimiques : molécules, matériaux, instrumentation et biosystèmes

Titre : Transferts d'électron dans des complexes de lanthanide: une étude combinée de chimie expérimentale et théorique

Mots clefs : éléments f, lanthanide, chimie quantique, radicaux, structure électronique

Résumé : Comprendre les réactions biologiques requiert l'utilisation de composés capables de transférer des électrons de manière sélective et de stabiliser des intermédiaires réactionnels. Ce travail s'est intéressé à la conception et à la réactivité de complexes de lanthanide divalents qui ont ce type de propriétés.
Dans un premier temps, la réduction de deux molécules organiques, la phénanthroline et la benzophenone, a été étudiée. Les données thermodynamiques obtenues avec la phénanthroline ont permis de construire un ensemble de données de références de différentes fonctionnelles de la densité. Des méthodes de type TDDFT et CASSCF ont été ensuite mises en œuvres afin de reproduire les spectres UV-visibles.
Par la suite, les radicaux benzophenone et phénanthroline ont été utilisés afin de réaliser des réactions radicalaires. L'utilisation du radical tempo a permis de réaliser des réactions de réduction induite par les effets stériques des complexes. La compétition entre la benzophenone et la phénanthroline a également été étudiée et a permis de réaliser des couplages de type Minisci, qui sont inédits pour des complexes de lanthanides.
Enfin, la réduction de composés organométalliques via un ligand N-hétérocyclique a été réalisée. Deux de ces composés ont été comparés vis à vis de la stabilisation de complexes de palladium au degré d'oxydation $+IV$. L'importance du ligand a été de plus étudiée grâce à des calculs CASSCF et DFT qui ont montré que certains types de ligands permettaient un transfert électronique plus direct jusqu'au palladium.

Title : Electron transfers in lanthanide complexes: a combined study of experimental and computational chemistry

Keywords : f elements, lanthanide, quantum chemistry, radicals, electronic structure

Abstract : Understanding biological reactions require the use of molecules that can transfer electrons selectively and stabilise key intermediates. This work is interested into the design and the reactivity of divalent lanthanides that possess this kind of property.
Firstly, organic molecules, *i.e.* phenanthroline and benzophenone, were reduced by samarium complexes. The thermodynamic data obtained for phenanthroline reduction was used to perform a benchmark study on different density functionals. TDDFT and CASSCF methods were then used to understand the electronic structure of the complexes and compared to the UV-visible spectrum of the molecules.
Then, benzophenone ketyl and phenanthroline radicals have been used to perform radical reactions. Reactions with tempo led to already observed sterically induced reduction which mechanism was investigated. The competition between phenanthroline and benzophenone led to Minisci couplings that were never described with lanthanide complexes.
Finally, the electron was transferred to organometallic species containing palladium via a bridge N-heterocycle ligand. Two of such species were compared towards the stabilisation of palladium at the IV^{th} oxidation state. The importance of the ligand was further assessed by a combination of DFT and CASSCF calculations showing that certain ligands enabled a more direct transfer towards the palladium centre.

Université Paris-Saclay
Espace Technologique / Immeuble Discovery
Route de l'Orme aux Merisiers RD 128 / 91190 Saint-Aubin, France